Politecnico di Milano

School of Civil, Environmental and Land Management Engineering

Master of Science in Civil Engineering – Structures

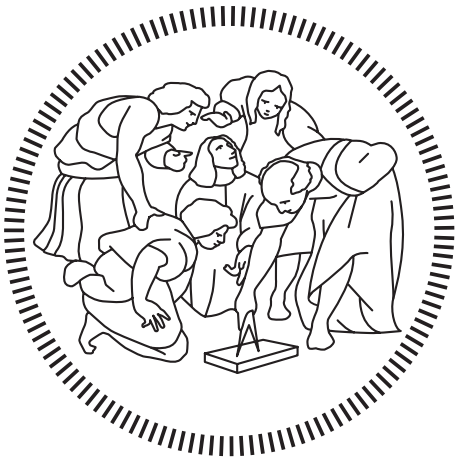

MECHANICAL MODELING OF STRANDED CABLES AND ASSESSMENT OF THEIR SELF-DAMPING PROPERTIES FOR AEOLIAN VIBRATIONS APPLICATIONS

Author:
Stefano Corazza
968080

Supervisor
Prof. Francesco Foti

Co-Supervisor
Prof. Luca Martinelli

Academic Year 2021 – 2022

"This is the key of modern science and is the beginning of the true understanding of nature. This idea. That to look at the things, to record the details, and to hope that in the information thus obtained, may lie a clue to one or another of a possible theoretical interpretation."

Richard P. Feynman,
in "The Character of Physical Law", 1965

Abstract

The present work focuses on the mechanical modeling of the bending behavior of metallic stranded cables. Starting from a description of the hysteretic moment-curvature law of the cross sections, a theoretical model for the self-damping is developed and applied to a widespread typology of overhead electrical line conductors, namely the ACSR conductors.
The first part of the thesis deals with the modeling of the combined action of tensile and bending loads, with emphasis on the applications of different radial pressures transmission models and stick-slip mechanical laws for multilayer conductors under flexure.
A novel generalization of the problem through closed-form coefficients expressions describing the admissible domain of the wire axial force is presented.
An ideal bi-linear approximating law for the description of the moment-curvature relationship through closed-form equations is enforced and uniquely defined by the so-called construction parameter. Such coefficient is determined for the different radial pressures transmission models and sliding conditions, for a sample of 15 ACSR cross-sections.
The influence of the construction parameter is then investigated with reference both to the static response of the metallic strand and to its dynamic behavior (i.e. its self-damping properties).
In the second part of the work, the self-damping properties of ACSR conductors are studied by comparing various experimental results with the non-dimensional dissipated power per unit of length of the conductor predicted by an enhanced unified analytical model for both the gross-sliding and micro-slip dissipation mechanisms.
Furthermore, the Energy Balance Principle (EBP) is used to predict the steady-state amplitude of aeolian vibrations of the bare conductor: the results obtained with both empirical and theoretical models for the cable self-damping are compared with field experimental data. The influence of the construction parameter on the aeolian vibrations amplitude is also assessed and parametric analysis are carried out.

Keywords: Aeolian vibrations, Stranded cables, Bending, Wire sliding, Overhead electrical lines, Self-damping, Energy balance principle.

Sommario

Il presente lavoro si focalizza sulla modellazione meccanica del comportamento flessionale di funi metalliche spiroidali. Partendo da una descrizione della legge momento-curvatura per il comportamento isteretico delle sezioni delle funi, viene sviluppato un modello analitico per la descrizione del loro smorzamento proprio. Tale modello viene successivamente applicato ad una tipologia ricorrente di conduttori delle linee elettriche aeree: i conduttori ACSR.
La prima parte della tesi si concentra sulla modellazione della risposta delle funi caricate in modo combinato da azione assiale e momenti flettenti, con particolare attenzione all'applicazione di diversi modelli di trasmissione delle pressioni radiali di contatto e di leggi di scorrimento per conduttori multi-strato soggetti a flessione.
Una nuova generalizzazione del problema attraverso le espressioni in forma chiusa di coefficienti che descrivono il dominio ammissibile dell'azione assiale nei fili è presentata.
Una legge bi-lineare approssimante per la descrizione della relazione momento-curvatura attraverso equazioni in forma chiusa viene applicata e univocamente definita dal cosiddetto parametro costruttivo del conduttore. Questo coefficiente viene determinato per diversi modelli di trasmissione delle pressioni radiali di contatto e per diverse condizioni di scorrimento, per un campione di 15 conduttori ACSR. L'influenza del parametro costruttivo è quindi indagata sia in riferimento alla risposta statica del conduttore che rispetto al suo comportamento dinamico (lo smorzamento proprio).
Nella seconda parte del lavoro, le proprietà di smorzamento proprio dei conduttori ACSR vengono investigate attraverso il confronto di diversi risultati sperimentali con le previsioni teoriche di potenza dissipata adimensionale per unità di lunghezza ottenute attraverso l'applicazione di un modello analitico unificato per due diversi meccanismi di dissipazione: il micro-scorrimento e il macro-scorrimento dei fili.
In aggiunta, le ampiezze di vibrazioni eoliche del solo conduttore vengono predette attraverso l'applicazione del Metodo del Bilancio Energetico: i risultati ottenuti attraverso l'utilizzo di modelli empirici e del modello analitico di smorzamento proprio vengono confrontati con i risultati di campagne sperimentali sul campo. L'influenza del parametro costruttivo sull'ampiezza di vibrazione eolica viene anche valutata e delle analisi parametriche sono esguite.

Parole Chiave: Vibrazioni eoliche, Funi spiroidali, Flessione, Scorrimento dei fili, Linee elettriche aeree, Smorzamento proprio, Principio del bilancio energetico.

Acknowledgments

First of all, I would like to express my truest gratitude to Prof. Francesco Foti and Prof. Luca Martinelli for their constant guidance and support during several months of work. They permitted me to learn a lot from them and have been examples of dedication and passion in everything they do.

A special thanks goes to my parents who sustained me in every step of my life and made me the person I am today.
Thanks to my family and to my friends, especially to Leonardo, with whom I've been sharing this path during the last five years.
Finally, thanks to all the people I've met, that permitted me to grow both on personal and professional side.
After five years of university career, it's time to conclude this journey, full of everlasting memories.

Contents

List of Figures

List of Tables

Chapter 1

Introduction

1.1 The Considered Problem

Metallic stranded cables are widely employed structural members. Their use in several engineering applications has become very diffused, due to their large flexibility and high strength associated with light weight. Due to their good electric conductivity they are also employed for overhead electrical transmission lines. The most widespread typology of metallic stranded cable for overhead high voltage lines (OHL) is the so-called Aluminium Conductor Steel Reinforced (ACSR).
As evidenced by extensive analytical and numerical investigations (e.g. in (Papailiou, 1997), (Hong et. al, 2005), (Lalonde et al., 2017)), whenever a strand is bent, an axial force gradient is generated along the length of the wires. Such gradient makes the wires prone to sliding with respect to the neighboring ones and is counteracted by the tangential friction forces acting on the internal contact surfaces between the wires. The possible activation of these sticking/sliding frictional interfaces makes the bending behavior of strands inherently non-linear and non-holonomic (Foti and Martinelli, 2018b).
As a consequence, bending vibrations of stranded cables are characterized by a hysteretic damping mechanism (see e.g. (Hard and Holben, 1967),(Claren and Diana, 1969)).
The self-damping is a physical characteristic of the conductor that defines its capacity to dissipate energy internally while subjected to vibrations. For conventional stranded conductors, energy dissipation can be attributed partly to inelastic effects within the body of the wires (hysteresis damping at the molecular level) but mostly to frictional damping, due to small relative movements between overlapping individual wires, as the conductor flexes with the vibration modal shape (CIGRE, 2011).
Conductor self-damping is generally not specified by the manufacturer and can be determined through measurements performed on a laboratory test span. Semi-empirical methods are available and allow to estimate the self-damping parameters of conventional stranded conductors without testing them.
The drawback is that these methods often lead to different results, depending on both the test method and end-conditions, as well as measurement errors (CIGRE, 2011).
Moreover, the measurements of conductor self-damping are difficult because the dissipated power is very small. In fact, usual order of magnitude of the dissipated power per unit of length for typical testing conditions of common ACSR conductors ranges between 0.1-100 mW/m, depending on the frequency of excitation.
With the great interest and concern regarding the vibration of overhead conductors, there is a growing requirement for reliable information on the self-damping characteristics of conductors. This necessity is related to the emphasis on the improvement of existing methods

for investigating and controlling the problem. Cable self-damping is a principal factor in determining the response of a conductor to alternating forces induced by the wind.
The self-damping data are used for the computations of wind-induced conductor vibrations mostly through deterministic methods based on the Energy Balance Principle (EBP).
However, stochastic approaches for the modeling of aeolian vibrations by considering the wind as a narrow band stochastic process are also possible (see e.g. (Foti et al., 2020)) and permit to overcome the principal drawback of the EBP, that is, the mono-modal oscillations assumption.
The most important source of vibrations of overhead electrical conductors is aeolian vibration, i.e. the name associated, in the field of transmission lines engineering, to Vortex Induced Vibrations (VIV). Aeolian vibrations are caused by the alternate shedding of Karman vortices from the top and bottom of the line's conductor, and can take place when a smooth wind flow of 1 to 7 m/s interacts with such a conductor (EPRI, 2006).
Aeolian vibrations are one of the major cause of fatigue failures of conductors, that may occur at points where the flexural motion of the cable is constrained against transverse vibrations (e.g. suspension clamps) (Rocha et al., 2021). Failures of overhead electrical conductors lead to power interruption, thus to economic losses, people discomfort and serious injuries.
Recently, several research works are trying to reproduce the fretting conditions that occur at the wire scale through fretting fatigue tests on individual wires, which provides a better understanding of such phenomenon. In order to describe the stress state that leads to wires failure, combined effect of both alternating tension loading and alternating bending should be investigated (Omrani et al., 2021).
With practical engineering interest of a predictive and optimized maintenance of critical regions of overhead electrical lines, the accurate assessment of aeolian vibrations amplitudes for the prediction of fatigue life of components (see e.g. (Mendonça et al., 2021)) underlies the necessity of an in-depth study of the cyclic bending behavior of conductors.
To this aim, a complete characterization of their moment-curvature response is of paramount importance. As a part of this research work, novel closed-form expressions for the computation of the construction coefficient c_0 (i.e. the parameter fully describing the bi-linear approximating M-χ law) have been derived.
The first part of the work fits into this context throughout the investigation of the influence of c_0 parameter on the cross-sectional response of multilayer conductors under bending. On this behalf, different radial transmission pressures models and physically-sound sliding conditions (see e.g. (Carodu, 2013)) are enforced and applied to a sample of widespread ACSR conductors. The characteristics of the interwire sticking/sliding dissipative mechanism have also been extrapolated in past researchers' works in order to characterize the hysteretic behavior of the strand. The following evidences have been found:

- in the high-curvature regime, wires tend to slip with respect to the neighboring ones and the power dissipation is mainly due gross-sliding mechanism (Goudreau et al., 1998)(Foti and Martinelli, 2018a);
- for low curvatures, the wires of the strand tend to stick together and the dissipation is mainly due to micro-slip phenomena at the contact surfaces, as it has been suggested e.g. in (Goudreau et al., 1998).

An analytical formulation developed by Foti and Martinelli (2018b), on the basis of a well-established mechanical model of the strand (Foti and Martinelli, 2016a, 2016b), has permitted to distinguish between the two different dissipation mechanisms which can take place before and after the activation of the interwire sticking/sliding phenomenon, namely the Micro-Slip and Gross-Sliding dissipation mechanisms.

The aim of the second part of the present work is to apply such enhanced unified analytical model for the cable self-damping to several experimental results of the literature, in order to assess its capability to describe the real dynamic behavior of cables and to address in-depth considerations on the predictions of the possible transition between the two dissipation mechanisms.

1.2 Objectives

The following objectives are pursued in this thesis:

1. state of the art review of overhead transmission lines aeolian vibrations phenomenon and conductors self-damping;
2. description of the cross-sectional response of metallic strands, solution of the axial-torsional problem and of the non-linear bending problem;
3. analysis of various radial transmission pressures models and comparison of their predictions for a sample of 15 ACSR conductors. Computation of approximated radial contact forces on the pointwise distributed radial contact patches, for the same conductors sample;
4. enforcement of two novel sliding conditions between wires of multilayer conductors under bending. Expression of different slip conditions through a couple of coefficients (a and b) governing the form of the differential equation that describes the wire axial force limit domain;
5. description of the moment-curvature hysteretic behavior of stranded cables through a perfect bi-linear approximating law fully defined by the so-called construction parameter c_0 and implementation of a novel approach for the determination of such coefficient in a closed form;
6. determination of a range of values of c_0 for the sample of 15 ACSR conductors of different stranding and assessment of its influence on both the static response of the metallic strand (application to a well-known bending test results coming from the literature) and to its dynamic response (i.e. ACSR conductors Self-Damping);
7. Application of an analytical model for the self-damping of ACSR conductors and comparison of the theoretical predictions for different values of the construction parameter with experimental results coming from the literature;
8. Identification of the possible transition between Micro-Slip and Gross-Sliding dissipation mechanisms, and assessment of a theoretical threshold on the basis of the analytical model formulated according to a new parametrisation;
9. Implementation of the Energy Balance Principle for the assessment of aeolian vibrations amplitude for the case of bare conductor. Analysis of the influence of various parameters, i.e. the loading ratio, friction coefficient, turbulence intensity, stiffness reduction factor and construction parameter;
10. Comparison between the predictions of the non-dimensional vibration amplitude evaluated by means of both empirical and theoretical self-damping models with available experimental results obtained through free-field tests.

1.3 Overview

The present thesis is arranged in six different chapters. After this introduction, the state of the art is presented in Chapter 2. The phenomenon of aeolian vibrations is discussed, as well as the geometry and some construction aspects regarding overhead transmission line conductors. Then, the experimental measurements commonly adopted for the determination of conductors Self-Damping are described. Finally, empirical and theoretical models of the literature for the characterization of cables self-damping are reviewed.
Chapter 3 analyses the cross-sectional response of stranded cables. Lateral and Radial contact conditions are assessed, starting from well-known equations of the literature. Different radial transmission pressures models are implemented, and their predictions are compared with reference to a sample of 15 ACSR conductors cross-sections. Approximated values of the radial contact forces are also computed by considering contact patches as pointwise distributed. Both the axial-torsional problem and the bending problem are assessed. The moment curvature law is approximated through an ideal bi-linear relationship, fully defined by the construction parameter c_0 of each cable. A novel approach for the generalization of different stick-slip mechanical laws is presented. The influence of different radial pressure models and sliding conditions on the construction parameter c_0 is then investigated and linear interpolations of the construction parameters as a function of the strand diameter are provided for different stranding classes.
Additionally, the static response of the strand is studied with reference to a well-documented bending test, for different values of the construction parameter.
Chapter 4 deals with the Self-Damping of ACSR conductors. After the presentation of an enhanced unified analytical model for the description of the self-damping, experimental results coming from various testing campaigns are compared with the predictions of the theoretical models describing different dissipation mechanisms (i.e. Micro-Slip and Gross-Sliding).
The influence of the construction coefficient on the Micro-Slip and Gross-Sliding dissipation mechanisms predictions of the dissipated power is studied, with reference to different cartesian and bi-logarithmic planes.
In Chapter 5 the Energy Balance Principle (EBP) for the assessment of the aeolian vibrations amplitude of overhead electrical line (ACSR) conductors is applied. Experimental results are compared with the predictions of non-dimensional vibration amplitude obtained though the theoretical self-damping model previously applied and through empirical damping models. The influence of the construction parameter c_0 on the prediction of the non-dimensional amplitude of vibration is also investigated.
Finally, in Chapter 6, the conclusions of such work are drawn, the possible drawbacks are evidenced and some future developments are proposed.

Chapter 2

State of the Art

In this chapter, existing literature about stranded cable and their self-damping properties is discussed. Section 2.1 is focused on the description of the phenomenon of aeolian vibrations, while Section 2.2 deals with the basic geometrical and mechanical characterization of the overhead transmission line conductors, with emphasis on a widely diffused conductors typology, namely the Aluminium Conductor Steel Reinforced (ACSR).
In Section 2.3, the experimental testing methodologies for the determination of the cable Self-Damping properties, according to current engineering practice, are described, while in Section 2.4 different self-damping models of the literature are presented.
In particular, subsection 2.4.1 deals with the description of the most diffused empirical models for the cable self-damping, while in Subsection 2.4.2 several theoretical models developed in the past years are presented.

2.1 Aeolian vibrations

Aeolian vibration is the name associated, in the field of transmission lines engineering, to *Vortex Induced Vibrations* (VIV). This type of vibration due to wind forces is caused by the alternate shedding of Karman vortices from the top and bottom of the line's conductor.
Aeolian vibrations are one of the major cause of fatigue failures of conductors. They occur when a smooth wind flow of 1 to 7-10 m/s interacts with a conductor; they are observed in 3-150 Hz frequency range and have peak-to-peak amplitudes of up to one conductor diameter D (EPRI 2006). However, with reference to the non-dimensional single-peak antinode vibration amplitude A (that will be extensively used in the following part of this work), the application of the Energy Balance Principle (EBP) generally shows that aeolian vibrations are characterized by values of A/D up to the order of 1 (for frequency $f \to 0$).
Initially, the frequency f of vortex shedding is related to the velocity V of the incoming flow and to the diameter D of the conductor, through the Strouhal equation:

$$f_{VS} = St \cdot \frac{V}{D} \tag{2.1}$$

where St is the Strouhal number, that ranges between 0.18-0.22.
Conductor vibration causes localized bending which, depending on its level, may cause, sometimes in a short period of time, fatigue failures of the conductor strands at the suspension clamps or at the clamps of spacers, dampers, and other devices installed on the conductor, such as items associated with the support and protection of the conductor itself. Figure 2.1 shows an example of fatigue failure of the conductor strands at the suspension clamp.
Aeolian vibration is most serious when the conductor tensions are high, the spans are long, the terrain is smooth, and wind occours with frequent, low-to-moderate, steady amplitude (EPRI 2006).

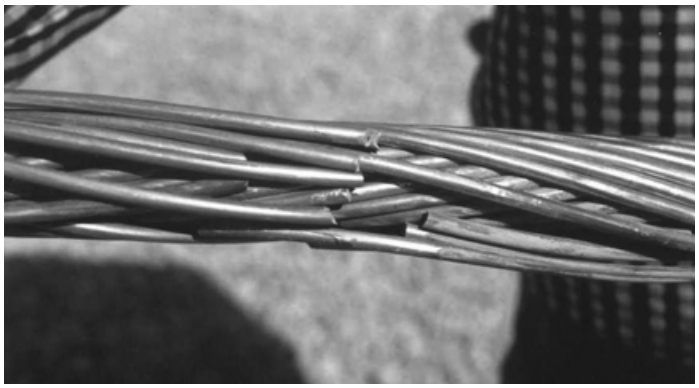

Figure 2.1. Fatigue failure of conductor strands at the suspension clamp (EPRI, 2006).

Aeolian vibrations can be clearly distinguished from other two types of wind-induced vibrations: *galloping* and *subspan oscillations*. Galloping is characterized by low frequencies and high amplitudes of vibration (up to several times the sag of the cable), occurring mainly in the cross-wind direction. It is a vertical oscillation of the conductor span in one or a few loops, but it usually incorporates other less visible twisting, lateral and longitudinal motions. Galloping is usually caused by moderately strong, steady crosswinds (wind velocity over 15 m/s) and it is a form of instability due to the unstable shape assumed by the conductors when they are covered with ice.

Subspan oscillations occur for bundled conductors only and are caused by the wake produced by the windward conductor on the leeward one. For this reason this phenomenon is referred to as wake induced oscillations. They are characterized by intermediate frequency of the order of a few Hz and amplitude of the order of the conductor spacing in the bundle. The motion occurs in moderate to strong winds, usually in the range from 7 to 18 m/s.

Table 2.1. Types of wind-induced vibrations, adapted from (EPRI, 2006).

Descriptor	**Aeolian Vibration**	**Galloping**	**Wake-induced Oscillation**
Types of Overhead Lines Affected	All	All	Bundled conductors lines
Approx. Frequency Range (Hz)	3–150	0.08–3	0.15–10
Approx. Vibration Amplitude Range[1]	0.01–1	5–300	0.5–80
Wind Character	Steady	Steady	Steady
Wind Velocity	1 to 7 m/s	7 to 18 m/s	4 to 18 m/s
Conductor Surface	Bare or uniformly iced	Asym. ice deposit	Bare, dry
Approx. Time for severe damage	3 months–20+ years	1–48 hours	1 months–8+ years

[1]:Peak-to-Peak amplitude expressed in conductor diameters D.

The severity of aeolian vibration can be assessed through design rules based on past experience. Measurements on existing lines can also be performed to assess conditions, using special-purpose measuring instruments.
Another way is to use an analytical approach to simulate the aeolian vibration behavior of the conductor and eventually the behavior of conductor plus damping devices. This approach can be used to investigate alternatives in the design or retrofit process and, being aware of its limits, also in the direct design of the damping system for a new line.
The most used analytical models are based on the Energy Balance Principle (EBP), and they give an estimate of an upper bound to the expected vibratory motions. The EBP approach requires that the energy dissipated by the conductor and other devices used for its support and protection and the energy input from the wind are known as a function of the vibration frequency and amplitude.
Besides the use of a deterministic approach based on the EBP, a stochastic approach for the modeling and investigation of aeolian vibrations is also possible (see e.g. Foti et al., 2020). The Energy Balance Principle is indeed based on the simplifying assumption of mono-modal oscillations. However, typical aeolian vibration records clearly show that several modes can be simultaneously excited due to wind variations in time and along the span. On these regards, random vibration analysis permits to overcome the basic assumption of mono-modal vibrations by modeling wind forces as a narrow band stochastic process and with arbitrary cross-correlation in space (Foti et al., 2020).

2.1.1 Excitation

Aeolian vibration is a form of instability generated by the wind blowing on conductors; it is concerned with the details of the flow, which interacts with the motion of the conductor. Aeolian vibration is closely related on the wind side, to the vortex-shedding phenomenon and its energy input to the structure and, on the conductor side, to its damping ability. The uniform flow of air or water across a stationary, rigid cylinder whose axis is normal to the streamwise direction has been studied by many investigators; Strouhal (1878) and Von Karman (1912) were among the first to do so. Various flow regimes can evolve, depending on the Reynolds number Re.
This dimensionless number is defined as follows:

$$Re = \frac{VD}{\nu} \tag{2.2}$$

where D is the cylinder diameter, V is the velocity of the incoming wind flows and ν represents the kinematic viscosity of the fluid, that can also be expressed as:

$$\nu = \frac{\mu}{\rho} \tag{2.3}$$

where μ is the dynamic viscosity of the fluid and ρ is its density.
Figure 2.2 shows the various flow regimes as a function of the Reynolds number. It is clear that vortex shedding is continuous from $Re = 40$ to $Re = 300000$. This range of Re includes that which corresponds with light to moderate winds blowing across overhead conductors (Vecchiarelli, 1997). Reynolds number values are computed using the conductor diameter.
Vortex shedding generates alternating forces that act in the transverse direction of the flow (lift forces). The frequencies of the vortex shedding can be approximately computed by the Strouhal formula (Equation 2.1). When the body is fixed, the lift forces are generally out of phase or unsynchronized, hence the net lift force is small. The motion of the conductor (assumed as a cylinder) in the transverse direction may be initiated when the velocity of the flow is such that the vortex-shedding frequency f_{VS} is close to the natural vibration frequency f_n of the conductor itself.

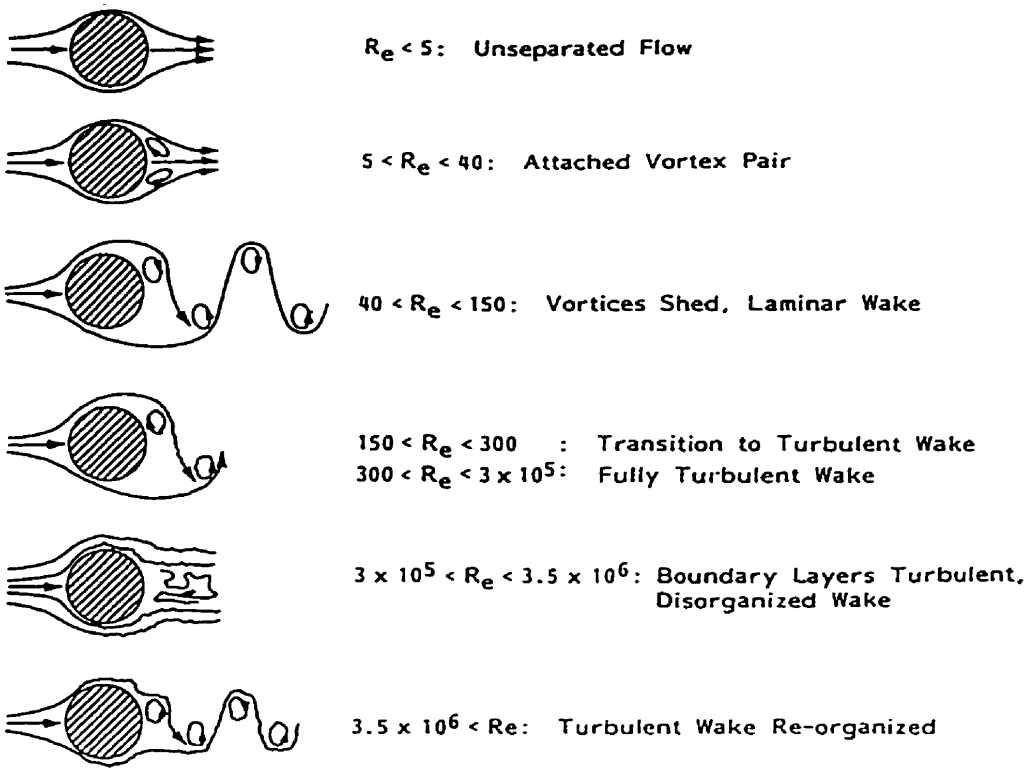

Figure 2.2. Regimes of fluid flow across a stationary circular cylinder (Vecchiarelli, 1997),(Lienhard, 1966).

In such case, the conductor motion can (Vecchiarelli, 1997):

- subsequently increase the strength of the shed vortices, so that the magnitudes of the vortex-induced lift forces along the conductor are amplified;
- enhance the spanwise correlation of vortex shedding, that causes vortex-induced lift forces to act in phase and become synchronized;
- change the vortex-shedding frequency f_{VS} to equal or almost equal f_n, consequently the Strouhal law is violated and the conductor takes control over the shedding phenomenon, resulting in synchronization. This is the so-called lock-in phenomenon, because f_{VS} remains anchored to f_n in a velocity interval denoted as lock-in range.

As a consequence of these effects, the conductor can experience a significant level of vibration. Aeolian vibrations lead to conductor fatigue. The latter is caused by the cyclic bending of the conductors where their motion is restrained, but it is not a bending fatigue situation. In fact, the fatigue mechanism of vibrating conductors is a highly localized phenomenon called *fretting fatigue*: it occurs on the outer surface of the wires because of the cyclic micro-slip induced by the conductor motion (EPRI, 2006). Figure 2.3 shows an example of wear damage and fretting marks on an ACSR conductor after a fatigue testing.
An in-depth knowledge and modeling of the conductor mechanics as well as its self-damping is necessary to address a quantitative approach that permits to assess the conductor fatigue phenomenon (see e.g. (Azevedo, 2009),(Redford, 2018)) and predict more clearly its remaining lifetime (Mendonća, 2021).

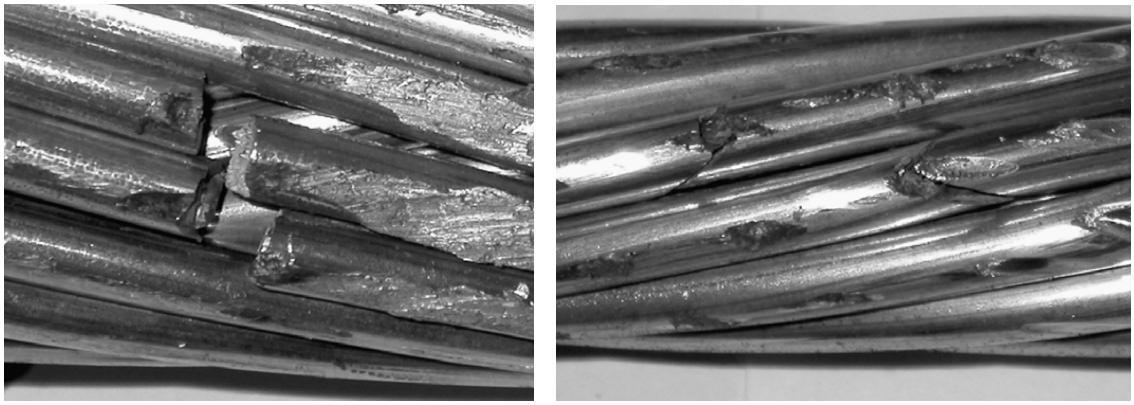

(a) Wear damage on external layer.

(b) Elliptical fretting marks on internal layer.

Figure 2.3. General view of an ACSR conductor after the fatigue testing (Azevedo, 2009).

2.2 Overhead transmission line conductors

Conductors of an overhead power line are stranded cables. They are considered the most important part of the entire line, since their function is to transfer electric power. Strands are made of helical wires, which are twisted around an initially straight core and grouped in concentric layers. Wire ropes, in turn, are obtained by helically twisting and grouping metallic strands. The *core* wire can be of the same material or different with respect to the external twisted wires. In fact, overhead conductors can be realized with different combination of materials, resulting in different strength-to-weight ratios. The latter is the main mechanical parameter used to select the proper conductor for every specific application.

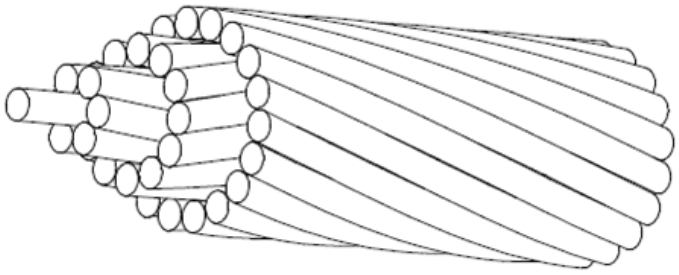

Figure 2.4. Structure of a typical conductor (EPRI, 2006).

Conductor characteristics also include conductance, diameter, strength, weight and thermal expansion coefficient, as well as stress-strain, creep and thermal loss-of-strength characteristics. Proper conductor selection takes into account the interaction of these characteristics with requirements of the electrical line: its voltage, capacity and load factor, the terrain it will cross and the environmental loads that it must withstand.
All standard overhead conductors are concentric-lay, i.e. the strand axis cylinders for all layers are concentric with the core. All standard overhead conductors are reverse-lay as well. This means that the direction of rotation of each layer is made opposite to that of the layer below (Rawlins, 2005).
It is worth noticing that using stranded conductors permits them to be flexible enough to be reeled for shipping, and makes them more tolerant of minor damage than solid rods would be. It also possible to manufacture conductors in great lengths, even though the maximum size of ingots or spool loads, involved in the manufactoring process, may limit the weight of individual component strands.
Helical lay, and concentric lay, in particular, is used to realize fully the flexibility offered by multiple strand construction. Reverse lay improves the conductor's structural integrity by defining the space for each layer. Moreover, use of reverse lay reduces the torque created in conductors when they are tensioned (which can cause problems during stringing) and improves electrical characteristics (such as self-inductance and ac resistance). More detailed information can be found e.g. in (Rawlins, 2005).

2.2.1 Conductor Geometry

Conductors are specified by type, size and stranding. The electrical conductance that is required in a conductor determines its equivalent area in 1350 alloy aluminum, as minimum value.

The most used types of conductors are herein listed (EPRI, 2006):

- *Aluminium Stranded Conductor* (ACS) and *All Aluminium Conductor* (AAC) are composed by commercially pure aluminium. They are suitable for short spans in distribution networks, due to their relative low strength-to-weight ratio.
- *All Aluminum Alloy Conductor* (AAAC) and *Aluminum Alloy Stranded Conductor* (AASC) are composed by an aluminum-magnesium alloy, that ensures a higher strenght.
- *Aluminum Conductor Alloy Reinforced* (ACAR), where same conductance is shought through combination of 1350 alloy with higher strength.
- *Aluminum Conductor Steel Reinforced* (ACSR) and *Aluminum Alloy Conductor Steel Reinforced* (AACSR), in which the minimum aluminium area is combined with various area of steel to obtain different conductor strengths. ACSR is the most commonly used conductor type.

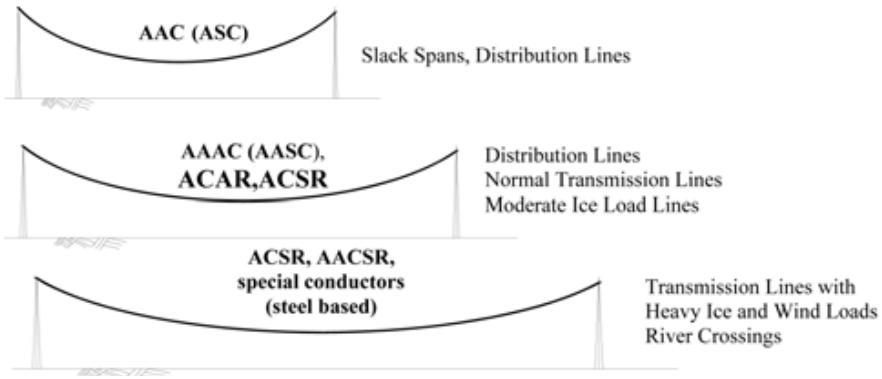

Figure 2.5. Typical use of bare conductors (EPRI, 2006).

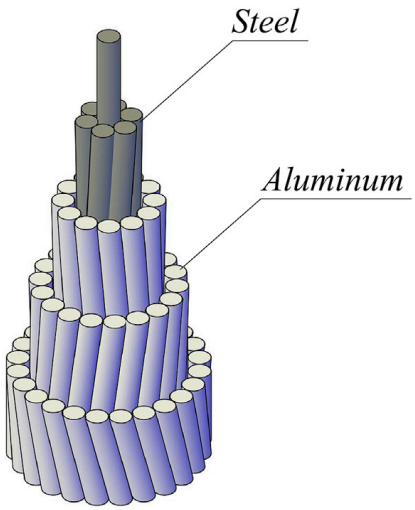

Figure 2.6. Schematic representation of the internal structure of a 54/7 ACSR conductor (Foti and Martinelli, 2018a).

Let us now introduce for convenience a numbering notation for the different layers of wires. In particular, let us denote with $i = 0$ the core wire, and let us count in ascending order the layers of wires starting from the one which is in contact with the core (i.e. $i = 1$).
In conductors where all wires have the same diameter, the number of wires in the i-th layer is $n_i = 6 \cdot i$ and the outside diameter of the layer is $D_i = (1 + 2 \cdot i) \cdot d$, where d is the wire diameter. Thus we have $D_i = (1 + n_i/3) \cdot d$.
In conductors where the strands of the outer layers have a different diameter from the core wire, the number of wires in the outer part still increases by six from layer to layer.
So that the following relationship (*concentric-lay rule*) is applied to these layers (Rawlins, 2005).

$$D_i = (1 + n_i/3) \cdot d_i \tag{2.4}$$

The pitch of the strand helices is called "*length of lay*" in conductor practice, and the ratio of the length of lay of a layer of strands to the outside diameter of that layer is called the "*lay ratio*" of the layer.
Lay ratio for conventional conductors are specified in various standards. Figure 2.7 shows the lay ratios for aluminium layers given in (ASTM, 1980) and (IEC, 1966) standards. It is evident that lay ratios less than 10 are prohibited, so that interference shouldn't occur, except in layers of less than 9 strands. Furthermore, both standards permit substantial gaps to occur, especially in the inner layers.

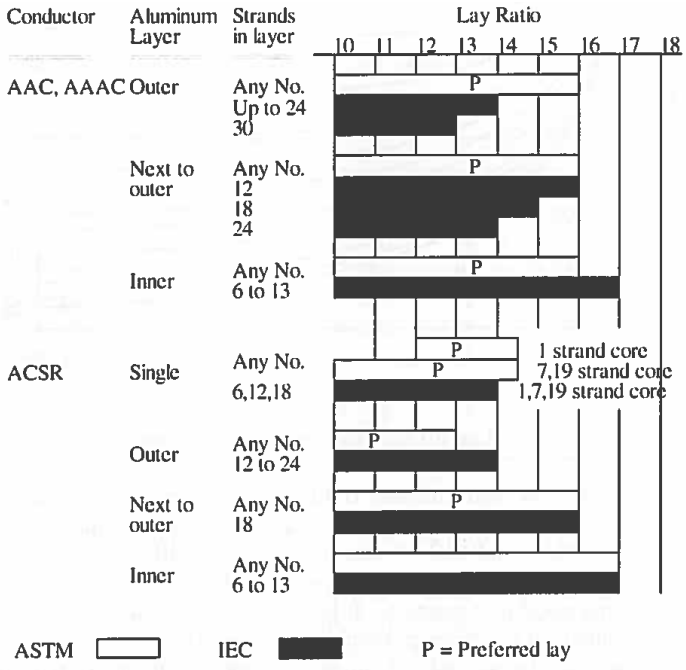

Figure 2.7. Lay ratios permitted by ASTM and IEC standards (Rawlins, 2005).

2.3 Experimental Measurements of the Self-Damping

In this section, different test procedures for the measurements of the cable self-damping are reviewed, with reference to indoor laboratory spans.

2.3.1 General considerations

The variation of ambient temperature inside laboratory spans is minimal and should be suitably controlled (values up to 0.2°C/h are considered acceptable). For consistent results, a span length greater than 40m is recommended, even if satisfactory results can be obtained with spans in the range of 30m. For shorter spans, a critical role on the results is given by the influence of the termination losses and the distribution of the tensile load between the conductor strands (CIGRE, 2011).
The free span length may affect the number of vibration modes that can be detected on conductors. In fact, large conductors may require a higher starting frequency than would be necessary, due to insufficient free span length. For instance, on a 50m span, when the conductor is tensioned at 20% RTS, the minimum of ten loops, required for a suitable measurement resolution, can be obtained with a frequency of 12 Hz. The minimum value of loops would be achieved with a frequency of 6 Hz using a 100m span.
Another important issue is related to termination portion of the span length. In fact, the test span shall be strung between two massive blocks with a weight not lower than 10 percent of the ultimate tensile strength of the largest conductor to be tested. Each block should be a single piece, generally made of reinforced concrete, and solidly connected with the concrete floor slab. The stiffness of these blocks should be as high as possible in order to minimize the losses and provide the maximum reflection of the waves.
Figure 2.8 shows an example of laboratory test span.

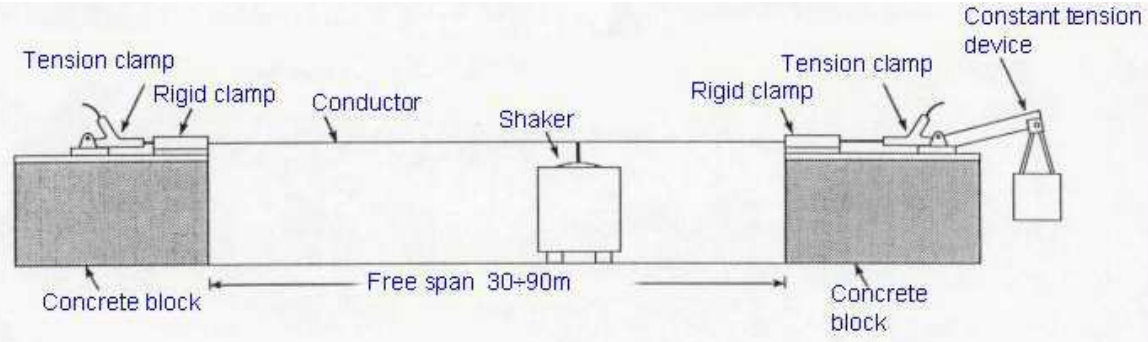

Figure 2.8. Test span for conductor self-damping measurements (CIGRE, 2011).

The test span should also have the capability of maintaining a constant conductor tension. The latter is measured by a load cell located between the tension device and the dead end clamp. Terminating fixtures and rigid clamps should be of sufficient stiffness to ensure that energy losses do not occur beyond the extremities of the free span.
One important aspect that should be considered, is related to the large dissipation of energy that occurs near the end of the span. Preference should be given to a test arrangement which would minimize energy dissipation at the span end terminations. If there is uncertainty about this, the energy should be assessed and eventually accounted for, unless using the Inverse Standing Wave Ratio (ISWR) method.
The termination losses may be minimized by terminating the conductor by a flexure member, such as a wide, flat bar of sufficient strength to accommodate the span tension but also

flexible enough in the vertical direction to allow it to bend readily and to avoid bending the conductor through a sharp radius of curvature where it would normally enter the clamp.

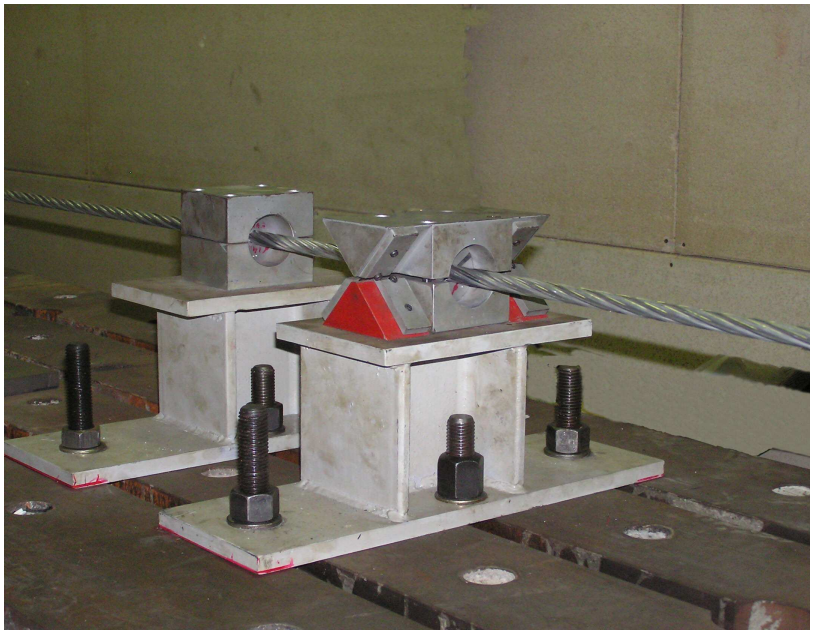

Figure 2.9. Pivoted clamp and rigid clamp at span extremity (CIGRE, 2011).

Vibrations of the conductor are usually excited through an electro-dynamic shaker or hydraulic actuators. The shaker should be able to provide a suitable sinusoidal force to the test span, so that the alternating movement is a simple harmonic, with a distortion level of less than 5%. It is required that both vibration amplitude and frequency are controlled to an accuracy of ±2% (CIGRE, 2011). The use of computers and dedicated software, for the shaker control and for the data acquisition, reduction and elaboration, is considered as a normal practice.
Furthermore, the shaker should be placed within one of the end loops of the span, but not necessarily at an anti-node. This location also makes it possible to excite greater amplitudes even if a rigid connection between the shaker and the conductor is used. In this condition, shaker forces are generally low.
It is worth noticing that, the armature of the shaker can be connected to the test span either rigidly or by the use of a flexible connection. However, the fixture shall be as light as possible in order to avoid the introduction of unwanted inertial forces and to prevent that, at the higher frequencies, the force needed to vibrate that mass plus the shaker armature will be beyond the capability of the shaker system.
To avoid distortion of the mode shape in the conductor vibration, the clamp mass must be as low as possible and, in resonance conditions, the phase between force and acceleration, at the driving point, must be as close as possible to 90 deg. In this case, the force applied by the shaker has its minimum and equals the damping force. For angles different from 90 deg, inertia and elastic components are also present and these give rise to distortions. The shaker connection shall be instrumented for force and vibration level measurements. The latter is generally made using accelerometers, but also velocity transducers and displacement transducer can be used.

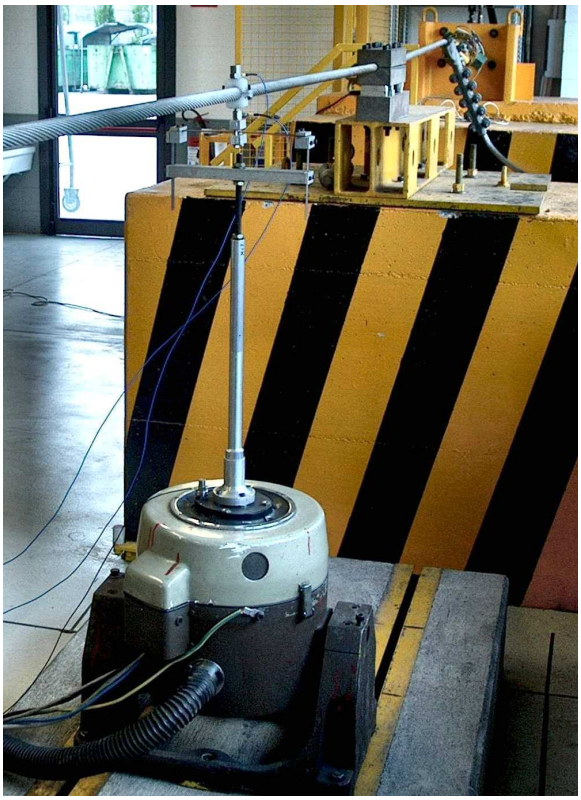

Figure 2.10. Example of electrodynamic shaker (CIGRE, 2011).

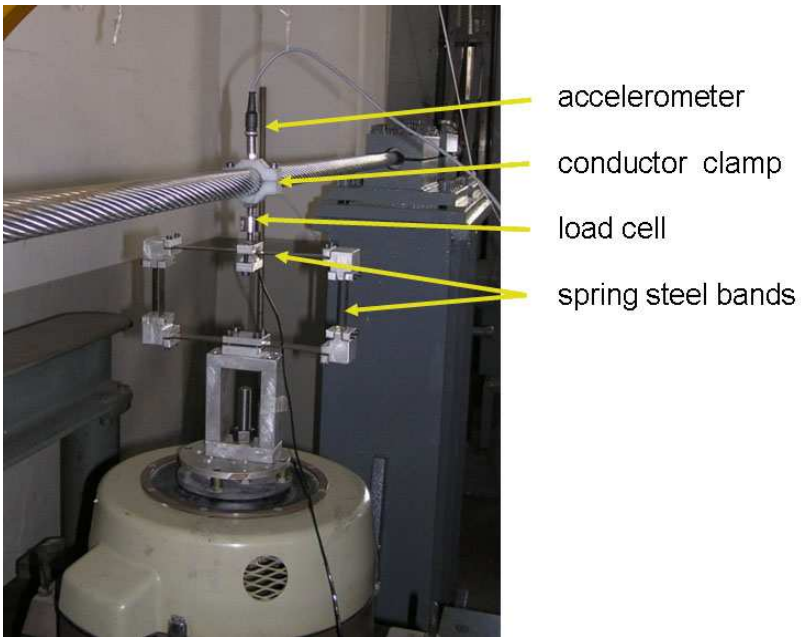

Figure 2.11. Flexible connection between shaker and conductor (CIGRE, 2011).

Due to the large number of symbols that will be adopted in the following subsections for the description of the test procedures, a table with the nomenclature is herein proposed.

Table 2.2. Nomenclature of the involved quantities.

Symbol	Nomenclature	Unit
E_{diss}	Energy dissipated by the system	Joule
E_{kin}	Kinetic energy of the cable	Joule
F	Force transmitted by the exciter, peak value	N
u	Antinode cable displacement	mm
u_f	Cable displacement at the force application point	mm
θ	Phase between F and u_f	deg
l	Span length	m
λ	Wavelength	m
T	Conductor tension	N
ω	Circular frequency	rad
f	Frequency	Hz
m	Conductor mass per unit of length	kg/m
n	Number of vibrating loops in the span	-
ξ	Non-dimensional hysteretic damping coefficient	-
h	Non-dimensional viscous damping coefficient ($h = 0.5\xi$)	-
a_i	Cable vibration single amplitude at the i-th node	mm
S_i	Inverse standing wave ratio (ISWR) at loop i	-
$\sqrt{Tm}$	characteristic impedance of the conductor	Ns/m

The test methods herein described for the determination of the dissipated power per unit of length, require that the conductor reaches a resonant condition, with the exception of the ISWR method for which tuning the span to resonance, although preferable, is not strictly necessary. As a general comment, the natural frequencies of the span may be estimated by applying the taut string model. The following equation holds:

$$f = \frac{1}{\lambda} \cdot \sqrt{\frac{T}{m}} = \frac{n}{2l} \cdot \sqrt{\frac{T}{m}} \tag{2.5}$$

Equation 2.5 provides a good starting point for finding resonances, even if conductor stiffness and the presence of the shaker on the span may influence the vibration modes, i.e. modify the natural frequencies.

2.3.2 Power Method

The power method allows to determine the dissipation characteristics of a conductor by the measurement of both the force and the vibration level imparted to the test span at the point of attachment to the shaker. The conductor, tensioned on the experimental span, is forced to vibrate at one of its resonant frequencies, with both amplitude and frequency being controlled by means of the driving system.
The non-dimensional viscous damping coefficient h, can be calculated by dividing the energy introduced in the conductor E_{diss} by the total kinetic energy of the conductor E_{kin}, where E_{diss} and E_{kin} are average energies "per cycle" of vibration. It holds:

$$h = \frac{1}{4\pi} \frac{E_{diss}}{E_{kin}} \tag{2.6}$$

If a displacement transducer is used at the forcing point, then the dissipated energy E_{diss} can be computed as follows (Diana et al., 2000),(CIGRE, 2011):

$$E_{diss} = \frac{P}{f} = \frac{\pi\, F\, u_f\, f\, \sin(\theta)}{f} = \pi\, F\, u_f\, \sin(\theta) \tag{2.7}$$

While the kinetic energy of the conductor is given by:

$$E_{kin} = \frac{1}{4} m\, l\, u^2\, \omega^2 \tag{2.8}$$

For normal conductors, the non-dimensional damping coefficient h ranges between 0.0001 and 0.001.
Some general considerations and conclusions concerning with the capability of the power method are here collected:

- the power method is simple and requires a limited number of measurement points;
- on the other hand, all the extraneous dissipation is part of the total calculation of the conductor self-damping. As a consequence, special care must be devoted to reduce all these extraneous loss sources or to account for them.
- The loops at the ends of the span and at the shaker connection behave differently from the rest of the span, having an energy dissipation that can be much higher than that of all of the rest of the span (see e.g (Noiseux, 1988)). The end losses can be determined by comparing the power inputs for two spans of different lengths identically terminated. Where it is not convenient to change the span length, it is necessary to minimize these losses or to use the ISWR method.

2.3.3 Inverse Standing Wave Ratio Method

The ISWR method determines the power dissipation characteristics of a conductor by the measurement of nodal and antinodal amplitudes on the span at each tunable harmonic.
In order to understand the principle involved in this method, it is necessary to trace the waves leaving the vibration shaker as they are reflected at the span ends. Assuming that the shaker is attached near one of the span terminations, it will induce impulses that will travel to the far end of the span and then return as reflected waves.
If no losses are present in the system, the incident and reflected waves are equal. Perfect nodes will be formed where the two waves meet and pass, so that zero motion will exist at the nodes. The anti-nodes will have an amplitude equal to the sum of the incident and reflected waves. If losses are present in the system, on the contrary, motion will appear at the nodes. The amplitude of this motion will be the difference between the incident and the reflected waves. The ratio between nodal amplitude and anti-nodal amplitude is indicative of the dissipation within the system. Where low span losses are present, very precise measurements are necessary for determining nodal amplitude. These measurements may be a problem (CIGRE, 2011).

The total power dissipated by the conductor can be computed from the following equation (Diana et al., 2000),(CIGRE, 2011):

$$P = \frac{V^2}{2}\sqrt{Tm}\,S_i \tag{2.9}$$

where:

- $\sqrt{Tm}$ is the characteristic impedance of the conductor;
- $V = \omega\, u$ is the antinode vibration velocity;
- $S_i = a_i/u$ is the inverse standing wave ratio (ISWR) of loop i;

Performing two measurements in two different nodes j and k, the power dissipated by the conductor between these loops will be:

$$P = P_k - P_j \tag{2.10}$$

Therefore the energy dissipated by the conductor between these two nodes can be expressed as:

$$E_{diss,k,j} = (P_k - P_j)\frac{2\pi}{\omega} \tag{2.11}$$

The kinetic energy between the two nodes is given by:

$$E_{kin} = \frac{1}{2}u^2\,\omega^2\frac{m}{4}\frac{2\pi}{\omega}\sqrt{\frac{T}{m}}\,n_v \tag{2.12}$$

where n_v is the number of antinodes between nodes k and j.
The value of the non-dimensional self-damping coefficient can be computed by the following equation:

$$h = \frac{S_k - S_j}{\pi\, n_v} \tag{2.13}$$

where S_k and S_j are the ISWR respectively at loop k and j.
Some general considerations and conclusions concerning with the capability of the ISWR method are here collected:

- An advantage of this method is that the measured dissipation relates to the considered portion of conductor only. As a consequence, the estimated self-damping value is not affected by the influence of span terminations and shaker-conductor connection;
- A critical aspect regards the measurement of the vibration amplitude in two different nodes vibrating under steady state condition. In fact, the exact node positions should be detected and the displacements to be measured are very small (on the order of a few micrometers);
- Special care must be devoted in avoiding horizontal and torsional motion of the cable in the test procedure, because the node vibration has a component only in the same vertical direction as the antinode vibration, with zero component in the horizontal and torsional directions.;
- In order to obtain the conductor self-damping, the aerodynamic losses should be subtracted by the measured total damping.

2.3.4 Decay Method

The decay method permits to determine the dissipation properties of a conductor by the measurement of the decay rate of the amplitude of motion of a span following a period of forced vibration at a natural frequency and fixed test amplitude. The rate of decay is a function of the system losses: in fact, where low dissipation levels are present, decay times are long.
Such method, if correctly employed, can give an estimation of the Self-damping values in a large range of vibration amplitudes in one trial. Moreover, it is quick and easy, requiring, in its simplest form, just one transducer measuring the decay.
However, as in the Power method, all the extraneous dissipation is part of the total calculation of the conductor self– damping. It is necessary to minimize all these extraneous loss sources or accounting for them. When this is not possible the use of the ISWR method is recommended (CIGRE, 2011).
Decay rate is recorded and expressed in terms of logarithmic decrement, i.e. the natural logarithm of the amplitude ratio of two successive cycles of vibration.
The logarithmic decrement δ can be computed as follows:

$$\delta = \frac{1}{n_c}\frac{Y_a}{Y_z} \tag{2.14}$$

where n_c is the number of cycles between the two cycles considered, Y_a and Y_z are the single antinode amplitude of the first and last cycle considered respectively.
The power dissipated by the conductor can be then computed according to the following equation:

$$P = \frac{1}{2} f\, m \cdot V_a^2 \cdot L \cdot \delta \tag{2.15}$$

where V_a is the antinode velocity at the initial antinode amplitude.
The non-dimensional damping coefficient is hence:

$$h = \frac{\delta}{2\pi} \tag{2.16}$$

The decay record may take the form of a series of steps occurring at the fundamental frequency of the test span. The particular shape of the steps will depend upon where the vibration is sensed and will obviously be more pronounced in highly damped spans.
The main advantage of the decay method is the possibility of a wide range of testing amplitudes in one trial, while it is not recommended for test spans with unknown end and drive point losses.

Comparison

As a general comment, the Inverse Standing Wave Ratio Method and Power Method are considered costly to equip and tedious to perform. On the contrary, the Decay Method is relatively easy to understand and perform, and requires minimal instrumentation. When damping is low, the Decay Method has good accuracy and resolution while both the Power Method and the ISWR Method suffer reduced accuracy. As a consequence, the decay test may be a suitable complement to these methods. However, when conductor damping is low the relative effect of other damping sources is larger and therefore the ISWR method may be considered advantageous (CIGRE, 2011).

2.4 Models for the cable self-damping

In this section, different models for the cable self damping of the literature are presented. Subsection 2.4.1 deals with the description of the empirical approach that is currently adopted for the evaluation of the cable self-damping, whereas in subsection 2.4.2 different theoretical models proposed in the literature are described.
A new analytical model developed by (Foti and Martinelli, 2018a, 2018b), will be extensively described in a fully dedicated section (4.1) and will be later on applied.

2.4.1 Empirical Models

The current engineering practice for the evaluation of the cable self-damping is based on an empirical approach. Forced vibration tests are typically performed on laboratory test spans, with length in the order of 30–90 m, according to two widely accepted international standards (CIGRE, 1979), (IEEE, 1993).
Several laboratories around the world have performed conductor self-damping measurements in accordance with the above mentioned standards. However, large disparities in self-damping predictions have been found among the results supplied by the various laboratories.
The causes of these disparities can been identified into the following main points:

1. The different typology of test method adopted for the dissipated power measurements (*Power Test Method* (PM), *Inverse Standing Wave Ratio Test Method* (ISWR), *Decay Test Method*);

2. The different conductor conditioning before the test;

3. The different manufacturing processes of the conductor;

4. The different span end conditions (restraints) set up in the various test laboratories (such as rigid clamps, pivoted clamps, flexure members);

5. The different types of connection between the electro-dynamic shaker and the conductor (rigid or flexible) and the different location of the power input point along the span.

The experimental data are usually fitted through the following power law:

$$P_d = k\frac{A^l\, f^m}{T^n} \tag{2.17}$$

where A (m) is the single-peak antinode vibration amplitude, T (kN) is the tension in the cable and f (Hz) is the vibration frequency. Different sets of exponents (l,m,n) have been determined by different research groups and are reported in Table 2.3. This discrepancies are related to the reasons previously identified. The proportionality coefficient k that appears into Equation 2.17 can be conveniently evaluated through the following empirical rule, valid for the case of *Aluminium Conductors Steel Reinforced* (ACSR):

$$k = \frac{D}{\sqrt{m \cdot RTS}} \tag{2.18}$$

where D is the conductor diameter, expressed in mm, RTS is the Rated Tensile Strength of the conductor, expressed in kN and m is the mass per unit of length of the cable, expressed in kg/m. The proportionality coefficient k is dimensional. Typical values of k for common conductors are in the range of $k \in [1.5, 2.5]$ and its dependence upon the strand diameter D will be later on investigated (see Subsection 3.6.3).

Table 2.3. Exponents of the empirical power law measured by different research groups.

Reference	l	m	n	Measurement Technique
Noiseux (1991)	2.44	5.63	2.76	ISWR[1]
Mech. Lab. Politecnico di Milano (2000)	2.43	5.50	2.00	ISWR[1]
Tompkings et al. (1956)	2.43	5.5	2	ISWR[1]
Rawlins (1983)	2.2	5.4	-	ISWR[1]
Mocks and Schmid (1989)	2.45	5.38	2.4	PM[2] (pivoted end)
Kraus and Hagedorn (1991)	2.47	5.38	2.8	PM[2] (pivoted end)

[1]: Inverse Standing Wave Ratio
[2]: Power Method

2.4.2 Theoretical Models

During the past years, several theoretical models for the cable self-damping have been proposed. The development of reliable and physically sound models for the self-damping of stranded cables has two main advantages:

- the reduction of the uncertainties typically related to the application of empirical damping models (see subsection 2.4.1);
- the reduction of the need for expensive and time consuming experimental tests on laboratory spans or instrumented lines (see also the previous section 2.3).

As already anticipated in Chapter 1, the internal damping of transmission line conductors can be attributed partly to inelastic effects within the body of the wires but mostly to frictional damping, due to small relative displacements between the wires of the strand (see e.g. (Claren and Diana, 1969)).
Based on this evidence, various theoretical models have been proposed in the literature to characterize the power dissipated during the flexural oscillations of conductors, under a physically sound mechanical description of the internal damping mechanisms.
One of the first theoretical models on the cable self-damping was proposed by Noiseux (1992). He modeled the conductor as a taut beam and accounted for its energy dissipation by means of a complex bending stiffness describing the hysteretic behavior of the cross-sections. An experimentally calibrated hysteretic loss factor was then used to control the energy dissipation.
Hardy (1990) studied the stick-slip frictional behavior of the external layer of wires of the strand through the well-known Amontons–Coulomb friction law. He also calculated the energy dissipated when a sinusoidal deflection is imposed to the cable centerline. However, his model is limited to the description of the dissipation mechanism involved by the full-slip of external wires (i.e. the so-called gross-sliding dissipation mechanism).
Goudreau et al. (1998) generalized Hardy's model by taking into account also the tangential compliance of the contact surfaces between wires. Such choice led to the possible occurrence of the so-called micro-slip dissipation mechanism. The theoretical dissipated power per unit of length according to Goudreau's model can be expressed through the following power law:

$$P_d = k\frac{A^3 f^7}{T^4} \tag{2.19}$$

Such power law exponents are significantly higher than those determined experimentally from the tests in the laboratory spans (see Tab. 2.3).

Expressions of the proportionality coefficient k were not provided, though.
Rawlins (2009) developed a model to evaluate the cable self-damping starting from the analysis of the internal contact surfaces between the wires of the strand. Such model is not restricted to the slip-state of the wires in the outermost layer of the conductor (on the contrary to Goudreau's one); however, it neglects the gross-sliding dissipation mechanisms due to the activation of the wire sliding.
Rawlins' model can be conveniently cast in the following form that simplifies the comparison with Eq. 2.17.

$$P_d = k_0(T)\,\frac{A^2\,f^5}{T^2} + k_1(T)\,\frac{A^3\,f^7}{T^3} \tag{2.20}$$

where $k_0(T)$ and $k_1(T)$ are two dimensional coefficients, depending both on the geometrical-mechanical properties of the strand and on the axial force T (Foti and Martinelli, 2018b).
The first term of Eq. 2.20 is only due to the hysteretic material damping in the wires of the conductor, while the second one represents the effect of the frictional dissipation due to the micro-slip between the wires of the strand.
Rawlins has also proposed a procedure for the estimation of the coefficients $k_0(T)$ and $k_1(T)$, starting from the results of standard laboratory measurements of self-damping. However, a quite poor agreement between the theoretical and experimentally determined values of such coefficients is found.
Possible motivations of this conclusion can be associated to the main drawbacks of Rawlins' model. The latter are stated as follows:

1. Experimental tests have shown that the material damping in the wires is almost negligible if compared with the frictional dissipation due to interwire sliding phenomenon. Rawlins' formulation, on the contrary, highlights importance for both physical mechanisms.

2. Rawlins' formulation neglects the hysteretic dissipation due to the gross-sliding between the wires of the strand. Such mechanism can indeed give a significant contribution to the overall self-damping of the conductor, on the basis of the amplitude and frequency of vibration.

Based on the results of the quasi-static bending tests on short cables collected by (Godinas, 1999), Guerard and Lilien (2011) derived the following proportionality relation for the conductor dissipated power:

$$P_d:\ P_d \propto (C_* T)^{\delta+1/2}\frac{A^3\,f^7}{T^4} \tag{2.21}$$

where C_* is a unitary dimensional coefficient and $\delta = 0.25$ is a parameter determined from static bending tests.
Exponents of such power law are close to the ones obtained by Goudreau et al. (1998) but higher than those obtained from experimental tests, which are collected in Table 2.3.
Finally, Foti and Martinelli (2018a, 2018b) have proposed a unified enhanced analytical model for the description of the cable self-damping, starting from a in-depth modeling of the mechanical behavior of such structures.
A unified non-dimensional expression for the estimation of the energy dissipated when the strand cross section is subjected to alternate bending has been obtained. The knowledge in closed-form of such dissipated energy has then been used to retrieve an analytical estimate of the dissipated power per unit length of the conductor, i.e. P_d.
This model will not be further discussed here, but it will be extensively described in section 4.1, since it will be conveniently applied all along Chapter 4.

Chapter 3

Modeling of the strand cross-sectional response

In this chapter, the cross-sectional response of stranded cable is assessed. The linear axial-torsional problem and the nonlinear bending problem are analyzed. Specific attention is devoted to the application of different models for the transmission of radial contact pressures, as well as for the formulation and implementation of different stick-slip mechanical laws.
A subsection is dedicated to the definition of the moment-curvature relationship through a construction parameter c_0 that accounts for the internal geometry of the strand, and it is typical of each conductor. As a consequence of the application of different models (both for the pressures transmission and for the stick-slip law), different values of c_0 are obtained and compared for each case. An application on the static response of the conductors is assessed.
In Section 3.1 the geometry of the strand is analyzed and useful quantities are introduced.
Section 3.2 deals with the description of the contact patches typologies, as well as their numerical applications for the various ACSR conductors cross-sections.
Section 3.3 is about the formulation of the mechanical model of both at the wire level and at the strand level, with the assessment of the cross-sectional response.
In Section 3.4 the solution of the linear axial-torsional problem is developed, with particular interest on the presentation of three different radial contact pressure models, namely model A,B and C and to their comparison in terms of predicted results (Subsection 3.4.2).
Section 3.5 deals with the solution of the nonlinear bending problem for the strand. Different stick-slip mechanical models are enforced, and a novel generalization of the problem through closed-form coefficient expressions is presented (Subsection 3.5.3). An entire subsection is dedicated to the formulation of the moment-curvature relationship trough an "ideal" bi-linear approximating law fully defined by the c_0 coefficient (Subsection 3.5.4).
In Section 3.6 the procedures for the evaluation of the construction parameter c_0 through various user-coded programs are assessed. In particular, both a numerical evaluation and a closed form solution are proposed.
Section 3.7 deals with the numerical applications for the evaluation of the model coefficients in the case of different radial contact pressures transmission models and stick-slip mechanical laws.
Results are discussed, analyzed and compared for the various stranding and conductors typologies.
Furthermore, Section 3.8 collects a case study of the literature related to the description of the mechanical response of an ACSR Drake conductor subject to a bending test. The influence of c_0 parameter is investigated as well.
Finally, in Section 3.9 some interesting conclusions are drawn.

3.1 Geometry of the Strand

Overhead electrical conductors are spiral strands. The latter are made of metallic wires with a round-shaped cross section. The wires are helically twisted around a central straight wire, and grouped in concentric layers. The central wire is commonly known as core wire or "king" wire. Wires in a layer are typically characterized by the same geometrical and material properties, so that the symmetry of the strand with respect to its centerline is ensured.
A mathematical description of the internal structure of the strand can be provided within a so-called *Strand-attached Reference System* (SRS). The following right-handed orthogonal axes x_i are then introduced:

- x_1, that coincides with the strand centerline;
- x_2 and x_3, that are orthogonal axes on a strand cross-section, so that they are both orthogonal to x_1.

The SRS is shown in Figures 3.1a and 3.1b.
Each wire centerline (locus of wire centroids) is represented as a circular helix in the SRS. It can be completely characterized through a couple of geometric parameters: the radius R, and the pitch P. A positive sign is conventionally assigned to the pitch of helices which are twisted around the strand axis according to the right-hand rule.
In the next developments, the pitch of the strand helices will be indicated as "length of lay" (i.e. the term commonly used in conductor practice), while the ratio of the length of lay of a layer of strands to the outside diameter of that layer (P_j/D_j) is called the "lay ratio" of the layer.
As discussed in Section 2.2, wires of adjacent layers are generally laid in opposite directions, according to the reverse-lay construction.

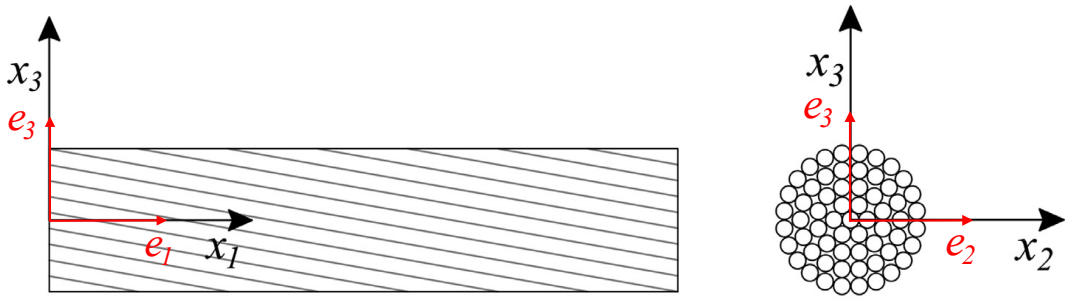

(a) Side view of the spiral strand.

(b) Cross-section of the strand.

Figure 3.1. Reference system of the strand, adapted from (Foti and Martinelli, 2016a).

A position vector $\boldsymbol{x}_w$ can be adopted to identify the points of the wire centerline. The following equation holds:

$$\boldsymbol{x}_w(\theta) = \frac{P}{2\pi}(\theta - \theta_0)\,\boldsymbol{e}_1 + R\cos(\theta)\,\boldsymbol{e}_2 + R\sin(\theta)\,\boldsymbol{e}_3 \tag{3.1}$$

where θ is the swept angle, i.e. the angle which the projection of the position vector on the plane $x_1 = 0$ defines with the direction of the axis x_2.
θ_0 is the value of the swept angle at $x_1 = 0$.
The orientation of the wire cross-section can be described by introducing on the wire centerline the local Serret–Frenet unit vectors $\boldsymbol{f}_i(\theta)$, where $\boldsymbol{f}_1(\theta)$ is the tangent unit vector, $\boldsymbol{f}_2(\theta)$ is

the normal unit vector and $\boldsymbol{f}_3(\theta)$ is the binormal unit vector of the wire centerline. These can be evaluated starting from Eq. 3.1 and related to the unit vectors $\boldsymbol{e}_i$ of the SRS through a rotation tensor $\boldsymbol{\Lambda}_w(\theta)$, as follows:

$$\boldsymbol{f}_i(\theta) = \boldsymbol{\Lambda}_w(\theta)\boldsymbol{e}_i \qquad i \in [1,3] \tag{3.2}$$

It is now necessary to define the *lay angle* α. The latter is the constant angle which the tangent unit vector $\boldsymbol{f}_1$ defines with the strand axis x_1.
The components of the rotation tensor $[\boldsymbol{\Lambda}_w(\theta)]_{\boldsymbol{e}}$ can now be expressed as follows:

$$[\boldsymbol{\Lambda}_w(\theta)]_{\boldsymbol{e}} = \begin{bmatrix} \cos(\alpha) & 0 & \sin(\alpha) \\ -\sin(\alpha)\sin(\theta) & -\cos(\theta) & \cos(\alpha)\sin(\theta) \\ \sin(\alpha)\cos(\theta) & -\sin(\theta) & -\cos(\alpha)\cos(\theta) \end{bmatrix} \tag{3.3}$$

The lay angle α is related to the radius and pitch of the helix by means of the following equation:

$$\alpha = \arctan\left(\frac{2\pi R}{P}\right) \tag{3.4}$$

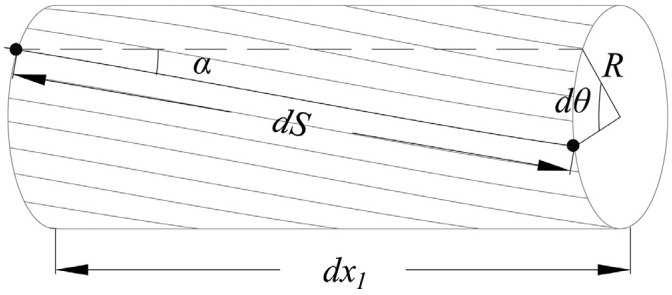

Figure 3.2. Length of an infinitesimal segment dS of the wire centerline (Foti and Martinelli, 2016a).

It is possible to provide an equivalent description of the wire centerline by means of an arc-length coordinate S, that is a smooth mapping (i.e. of class C^1).
By considering an infinitesimal segment of the helix, dS, and its developed length dx_1, according to Figure 3.2, the following differential relations can be obtained:

$$\sin(\alpha)dS = Rd\theta \tag{3.5a}$$

$$\cos(\alpha)dS = dx_1 \tag{3.5b}$$

Let us now focus on the strand cross-section, with reference to Figure 3.3, and consider a generic point P belonging to the strand cross-section.

- The position of point P is described with respect to the centroid of the wire to which it belongs, through the polar coordinates r and φ;
- Then, its position is transformed into the SRS.

Neglecting the difference between the wire cross-section and its projection on the strand cross-section, a generic point P is described by the following position vector:

$$\boldsymbol{x}(\theta, r, \varphi) = \frac{P}{2\pi}(\theta - \theta_0)\,\boldsymbol{e}_1 + \Big(R\cos(\theta) + r\,\cos(\varphi)\Big)\,\boldsymbol{e}_2 + \Big(R\sin(\theta) + r\,\sin(\varphi)\Big)\,\boldsymbol{e}_3 \tag{3.6}$$

with $\varphi \in [0, 2\pi]$ and $r \in [0, d/2]$, where d is the wire diameter.

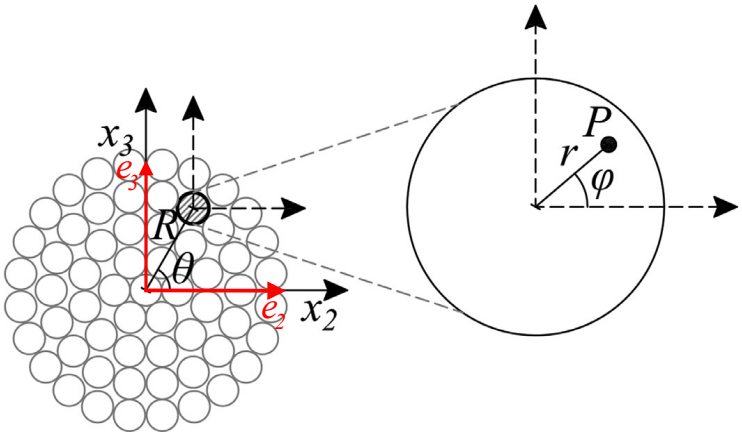

Figure 3.3. Polar coordinate system of the wire cross-section, adapted from (Foti and Martinelli, 2016a).

With reference to the arc-length coordinate S, the variation of the local unit vectors $\boldsymbol{f}_i(\theta(S))$ along the wire centerline, is given by the well-known Serret-Frenet equations:

$$\frac{d\boldsymbol{f}_1(S)}{dS} = \kappa\, \boldsymbol{f}_2(S) \tag{3.7a}$$

$$\frac{d\boldsymbol{f}_2(S)}{dS} = \tau\, \boldsymbol{f}_3(S) - \kappa\, \boldsymbol{f}_1(S) \tag{3.7b}$$

$$\frac{d\boldsymbol{f}_3(S)}{dS} = -\tau\, \boldsymbol{f}_2(S) \tag{3.7c}$$

The symbols κ and τ are the curvature and the torsion of the wire centerline, that can be evaluated as follows:

$$\kappa = \frac{\sin^2(\alpha)}{R} \tag{3.8a}$$

$$\tau = \frac{\sin(\alpha)\cos(\alpha)}{R} \tag{3.8b}$$

It is worth noticing that, the radius of normal curvature of the wire centerline ρ_w is defined as the inverse of the wire curvature:

$$\rho_w = \frac{1}{\kappa} = \frac{R}{\sin^2(\alpha)} \tag{3.9}$$

The equations 3.7 can be also used to express the derivative of the rotation tensor $\boldsymbol{\Lambda}_w$ with respect to S. The following equation is easily obtained:

$$\frac{d\boldsymbol{\Lambda}_w(S)}{dS} = \boldsymbol{\Lambda}_w(S)\, \boldsymbol{\Omega}_w \tag{3.10}$$

where $\boldsymbol{\Omega}_w$ is a skew-symmetric tensor whose components in the local basis can be expressed as:

$$[\boldsymbol{\Omega}_w]_{\boldsymbol{f}} = \begin{bmatrix} 0 & -\kappa & 0 \\ \kappa & 0 & -\tau \\ 0 & \tau & 0 \end{bmatrix} \tag{3.11}$$

3.2 Description of the contact patches

The wires of the strand interact between themselves at the internal contact surfaces, where friction forces are present. These tend to contrast relative interwire displacements, allowing for the transmission of tangential stresses between wires when the strand is loaded. In general, a wire can be:

1. in contact with the neighbors belonging to the same layer. This condition can be referred to as lateral or circumferential contact mode;
2. in contact with the neighbors belonging to the adjacent layers. This condition is named as radial contact mode.
3. in contact with the neighbors belonging both to the same layer and to the adjacent layers. This is the case of mixed contact mode.

Mixed contacts cannot be treated by neglecting the elastic tangential compliance of contact patches. This fact is related to the nature of the problem, that is intrinsically statically indeterminate on the strand cross-section, hence, a specific constitutive law is necessary (see e.g. (Foti and Martinelli, 2019)).
In the following, we will focus on the description of the radial and lateral (circumferential) contact modes, that will be treated in subsections 3.2.2 and 3.2.1 respectively.

3.2.1 Lateral Contact Mode

Figure 3.4 shows a scheme of the lateral contact between wires of the outermost layer of the conductor.

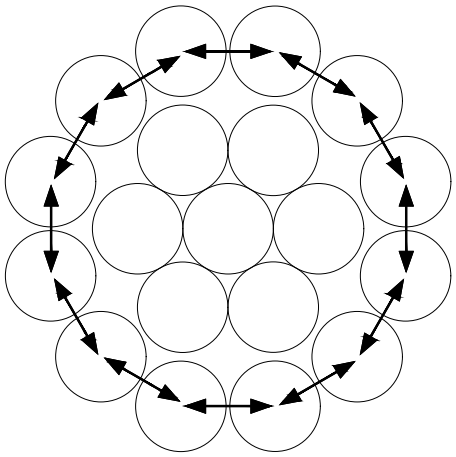

Figure 3.4. Lateral contact mode.

In the past years, some authors did analyze the geometric conditions for the occurrence of lateral contact (Costello, 1990), (Rawlins, 2005) with reference to the case of a straight strand without imperfections. In this ideal case, the friction forces tend to contrast the onset of relative intra-layer displacements (intra-layer sliding). The contact takes place along continuous lines and the normal forces on the contacting surfaces are hoop actions, depending only on the geometry and the stresses of the layer components (Foti and Martinelli, 2016b). However, it is worth noting that typical strand constructions allow for interlayer clearances

(Feyrer 2015, Rawlins, 2005). Moreover, even if the theoretical geometrical conditions for lateral contact are satisfied, intra-layer gaps can be generated by manufacturing imperfections and strand ageing or by the loading process of the strand.
In order to have compact packing, Rawlins (2005) has shown that the lay angle α and the lay ratio P/D of a certain layer of wires, must satisfy the following two nonlinear equations.

$$\sin\left(\frac{2\pi\zeta}{P}-\frac{\varphi'}{2}\right)\cdot\cos\left(\frac{2\pi\zeta}{P}-\frac{\varphi'}{2}\right)=-\frac{2\pi\zeta}{P}\cdot\left[\frac{1}{\frac{\pi d}{P}\cdot\left(\frac{D}{d}-1\right)}\right]^2 \tag{3.12}$$

$$\sin^2\left(\frac{2\pi\zeta}{P}\right)=\frac{d^2-4\,\zeta^2}{(D-d)^2}=\frac{\left(\frac{\pi\,d}{P}\right)^2-\left(\frac{2\pi\zeta}{P}\right)^2}{\left(\frac{\pi\,d}{P}\right)^2\cdot\left(\frac{D}{d}-1\right)^2} \tag{3.13}$$

These equations in the unknowns $2\pi\zeta/P$ and P/D must be solved numerically, due to their nonlinearity. As an alternative, the following equation yields a good approximation of the exact theoretical lay ratios (reported in Figure 2.7).

$$\frac{P}{D}=\frac{1}{1+\frac{3}{n}}\cdot\frac{\pi}{\sqrt{\left(\frac{n^2}{9}-1\right)\tan^2\left(\frac{\pi}{n}\right)-1}} \tag{3.14}$$

It is worth noticing that Equation 3.14 does not apply to the inner-most layer, with $n = 6$. In this case it yields an infinite lay ratio, corresponding to $\alpha = 0$ deg, i.e. to straight wires. However, from a user point of view, for a given conductor, the number of wires in each layer is known, as well as the outer diameter D and the wires diameter d. Thus, Eq. 3.14 may be used to obtain the lay ratio for each layer. This leads to the pitch P of the helix formed by a strand in the layer and to the maximum lay angle α (corresponding to contacting wires). Indeed, for a circular helix, lay angle α, wrapped on a cylinder of diameter $(D - d)$, and pitch length P, one has the well-known formula:

$$\tan(\alpha)=\frac{\pi(D-d)}{P} \tag{3.15}$$

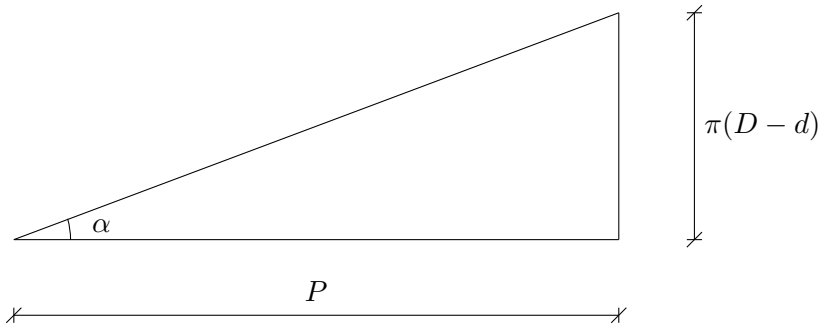

Figure 3.5. Lay angle determination scheme.

As already mentioned, eq. 3.14 doesn't apply to the innermost layer (i.e. $i = 1$). This means that the formula cannot be applied to 6/1 conductors.
In such cases, another equation proposed by Foti and Martinelli 2019 can be adopted.
One has that the maximum admissible lay angle for the first layer of wires is given by:

$$\alpha_{0,max,adm}=\arccos\left(\sqrt{\frac{\tan^2(\frac{\pi}{2}-\frac{\pi}{m})}{(1+\xi_0^{-1})^2-1}}\right) \tag{3.16}$$

where $m = 6$ is the number of wires in the first layer of the conductor and

$$\xi_0 = \frac{d_{w0}}{d_{c0}} \tag{3.17}$$

is the ratio between the diameter of the external wires and the one of the core. If radial contact is present, the latter should be lower than one.
In the following table, calculations for the typical conductor cross-sections are performed, in order to assess whether or not the lateral contact mode can take place, for each layer of wires. In particular, the maximum admissible lay angle $\alpha_{max,adm}$ is computed through the equations 3.14 and 3.15, $\forall i > 1$, while Eq. 3.16 is used for $i = 1$.
It is worth noticing that Eq. 3.16 predicts an admissible lay angle equal to zero, if the diameters of steel and aluminium wires are equal (that is the case of the 6/1 conductors studied in this work) or in the case in which both the core and the first layer of wires are characterized by the same material, involving wires of equal diameters. The latter is the case of multi-layer conductors considered in the present work, because there are always 7 steel wires with the same diameter in the center of the cable, that are the core and the first layer.
The lay angle $\alpha_{max,adm}$ is compared with the actual one (α) obtained via Equation 3.4. In this last case, the value of the preferred helix pitch is adopted (P_p), leading to a preferred value of the lay angle (α_p), according to the ASTM standard (1).
However, for the seek of completeness, the assessment of the lateral contact conditions for the various ACSR conductors is also performed by adopting the maximum and minimum values of the lay angles, always with reference to the ASTM standard.
This comparison is conveniently reported into Appendix C.
Lateral contact cannot take place if the angle $\alpha_{max,adm}$ is greater than α, because a small gap between wires belonging to this layer is present. In this case, contact may be considered as radial contact between adjacent layers.
This consideration can be analytically formulated stating that the geometric condition ensuring lateral contact in the reference configuration of the strand, for the generic layer of wires i, is:

$$\alpha_{p,i} \geq \alpha_{max,adm,i} \tag{3.18}$$

The results of the computations are reported in the tables 3.1-3.5.
It is also worth noticing since now that the lay angles α and $\alpha_{max,adm}$ of the various layer are independent from the conductor typology, and they depend only upon the stranding.
As it can be seen, lateral contact is usually present only between the first layer of wires ($i = 1$) and the core wire ($i = 0$).

Table 3.1. Lateral contact condition for 6/1 conductors. Preferred lay angle.

Code Word	Stranding	$D\,(mm)$	$n_L\,(-)$	$d_{st}\,(mm)$	$d_{al}\,(mm)$	$\alpha_{max,adm}$	α_p	Lateral Contact
Innermost Layer $i = 1$.								
Sparrow	6/1	8.01	1	2.67	2.67	0.00	9.15	**Yes**
Pigeon	6/1	12.75	1	4.25	4.25	0.00	9.15	**Yes**
Penguin	6/1	14.31	1	4.77	4.77	0.00	9.15	**Yes**

Table 3.2. Lateral contact condition for 26/7 conductors. Preferred lay angle.

Code Word	Stranding	$D\,(mm)$	$n_L\,(-)$	$d_{st}\,(mm)$	$d_{al}\,(mm)$	$\alpha_{max,adm}$	α_p	Lateral Contact
Outermost Layer $i = 3$.								
Partridge	26/7	16.28	3	2.00	2.57	16.33	13.52	**No**
Hawk	26/7	21.80	3	2.68	3.44	16.33	13.52	**No**
Drake	26/7	28.10	3	3.45	4.44	16.33	13.52	**No**
Middle Layer $i = 2$.								
Partridge	26/7	16.28	3	2.00	2.57	14.56	10.53	**No**
Hawk	26/7	21.80	3	2.68	3.44	14.56	10.53	**No**
Drake	26/7	28.10	3	3.45	4.44	14.56	10.53	**No**
Innermost Layer $i = 1$.								
Partridge	26/7	16.28	3	2.00	2.57	0.00	4.79	**Yes**
Hawk	26/7	21.80	3	2.68	3.44	0.00	4.79	**Yes**
Drake	26/7	28.10	3	3.45	4.44	0.00	4.79	**Yes**

Table 3.3. Lateral contact condition for 48/7 conductors. Preferred lay angle.

Code Word	Stranding	$D\,(mm)$	$n_L\,(-)$	$d_{st}\,(mm)$	$d_{al}\,(mm)$	$\alpha_{max,adm}$	α_p	Lateral Contact
Outermost Layer $i = 4$.								
Carillon	48/7	30.48	4	2.84	3.66	16.79	14.11	**No**
Gatineau	48/7	33.00	4	3.08	3.96	16.79	14.11	**No**
Bersfort	48/7	35.60	4	3.32	4.27	16.79	14.11	**No**
Layer $i = 3$.								
Carillon	48/7	30.48	4	2.84	3.66	16.33	11.50	**No**
Gatineau	48/7	33.00	4	3.08	3.96	16.33	11.50	**No**
Bersfort	48/7	35.60	4	3.32	4.27	16.33	11.50	**No**
Layer $i = 2$.								
Carillon	48/7	30.48	4	2.84	3.66	14.55	10.53	**No**
Gatineau	48/7	33.00	4	3.08	3.96	14.55	10.53	**No**
Bersfort	48/7	35.60	4	3.32	4.27	14.55	10.53	**No**
Innermost Layer $i = 1$.								
Carillon	48/7	30.48	4	2.84	3.66	0.00	4.79	**Yes**
Gatineau	48/7	33.00	4	3.08	3.96	0.00	4.79	**Yes**
Bersfort	48/7	35.60	4	3.32	4.27	0.00	4.79	**Yes**

Table 3.4. Lateral contact condition for 54/7 conductors. Preferred lay angle.

Code Word	Stranding	$D\,(mm)$	$n_L\,(-)$	$d_{st}\,(mm)$	$d_{al}\,(mm)$	$\alpha_{max,adm}$	α_p	Lateral Contact
Outermost Layer $i = 4$.								
Duck	54/7	24.21	4	2.69	2.69	16.87	14.24	**No**
Crow	54/7	26.28	4	2.92	2.92	16.87	14.24	**No**
Curlew	54/7	31.59	4	3.51	3.51	16.87	14.24	**No**
Layer $i = 3$.								
Duck	54/7	24.21	4	2.69	2.69	16.54	11.70	**No**
Crow	54/7	26.28	4	2.92	2.92	16.54	11.70	**No**
Curlew	54/7	31.59	4	3.51	3.51	16.54	11.70	**No**
Layer $i = 2$.								
Duck	54/7	24.21	4	2.69	2.69	15.50	10.94	**No**
Crow	54/7	26.28	4	2.92	2.92	15.50	10.94	**No**
Curlew	54/7	31.59	4	3.51	3.51	15.50	10.94	**No**
Innermost Layer $i = 1$.								
Duck	54/7	24.21	4	2.69	2.69	0.00	4.79	**Yes**
Crow	54/7	26.28	4	2.92	2.92	0.00	4.79	**Yes**
Curlew	54/7	31.59	4	3.51	3.51	0.00	4.79	**Yes**

Table 3.5. Lateral contact condition for 72/7 conductors. Preferred lay angle.

Code Word	Stranding	$D\,(mm)$	$n_L\,(-)$	$d_{st}\,(mm)$	$d_{al}\,(mm)$	$\alpha_{max,adm}$	α_p	Lateral Contact
Outermost Layer $i = 5$.								
Falcon	72/7	37.69	5	2.51	3.77	16.95	17.81	**Yes**
Nelson I	72/7	40.60	5	2.71	4.06	16.95	17.81	**Yes**
Nelson II	72/7	43.20	5	2.88	4.32	16.95	17.81	**Yes**
Layer $i = 4$.								
Falcon	72/7	37.69	5	2.51	3.77	16.74	15.74	**No**
Nelson I	72/7	40.60	5	2.71	4.06	16.74	15.74	**No**
Nelson II	72/7	43.20	5	2.88	4.32	16.74	15.74	**No**
Layer $i = 3$.								
Falcon	72/7	37.69	5	2.51	3.77	16.19	11.39	**No**
Nelson I	72/7	40.60	5	2.71	4.06	16.19	11.39	**No**
Nelson II	72/7	43.20	5	2.88	4.32	16.19	11.39	**No**
Layer $i = 2$.								
Falcon	72/7	37.69	5	2.51	3.77	13.74	10.27	**No**
Nelson I	72/7	40.60	5	2.71	4.06	13.74	10.27	**No**
Nelson II	72/7	43.20	5	2.88	4.32	13.74	10.27	**No**
Innermost Layer $i = 1$.								
Falcon	72/7	37.69	5	2.51	3.77	0.00	4.79	**Yes**
Nelson I	72/7	40.60	5	2.71	4.06	0.00	4.79	**Yes**
Nelson II	72/7	43.20	5	2.88	4.32	0.00	4.79	**Yes**

3.2.2 Radial Contact Mode

According to the radial contact mode, each wire is assumed in contact with those of the adjacent layers (interior and/or exterior) and the friction forces contrast relative inter-layer displacements (sliding). Figure 3.6 shows a scheme of the radial contact mode.

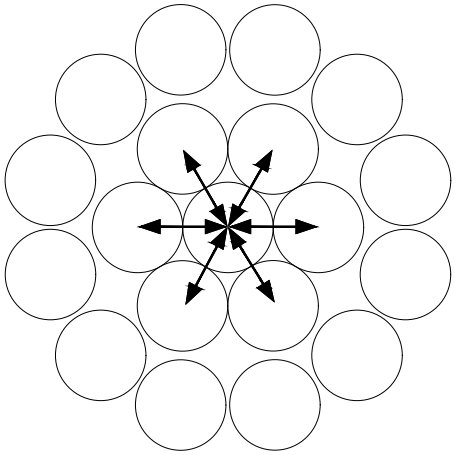

Figure 3.6. Radial contact mode.

The contacts in the case of radial mode are as follows:

- the innermost layer is in contact with the core wire along a continuous helix;
- all the other layers are characterized by interlayer contact surfaces that are pointwise distributed along helical paths (i.e. contact helices).

By neglecting changes in the internal geometry of the strand with respect to its reference configuration we have that:

- the contact helix of a generic wire with the internal layer is characterized by the same pitch of the wire centerline and helix radius equal to $R_{C,int} = R_i - d_i/2 = R_i - r_i$;
- the contact helix of a generic wire with the external layer is characterized by the same pitch of the wire centerline and helix radius equal to $R_{C,ext} = R_i + d_i/2 = R_i + r_i$;

where d_i and r_i are the wire diameter and wire radius of layer i.
The geometric condition ensuring radial contact in the reference configuration of the strand, for the generic layer of wires i, is the counterpart of Eq. 3.18. One simply has:

$$\alpha_i < \alpha_{max,adm,i} \tag{3.19}$$

Distance between contact points

One can obtain an approximate value of the contact forces by multiplying the force per unit of length computed assuming a line contact situation by the distance between contact points at a given interface. For a generic layer i, the quantity of interest is the distance of contact points with layer $i-1$.
Cardou (2013) has shown that this distance, calculated on the contact helix of layer i (i.e. on a wire outer fiber which is in contact with layer $i-1$) is given by:

$$d_{Ci} = \frac{2\pi\, R_{C,i}}{n_{i-1}} \frac{\cos(\alpha''_{i-1})}{\sin(\alpha'_i + \alpha''_{i-1})} \tag{3.20}$$

where:

- R_{Ci} is the radius of the contact cylinder between layers i and $i-1$, that is $R_{C,int} = R_i - r_i$;
- n_{i-1} is the number of wires of the $(i-1)$-th layer;
- α'_i and α''_{i-1} are slightly different angles from the corresponding lay angles. The reason is that they correspond to the wire "fibre" which is on the contact cylinder and not to the centerline. These fibers are helical curves having practically the same lay length as the center line helix. However, because the contact cylinder radius is slightly different than the lay cylinder radius (as already pointed out), the helix angle is also different.

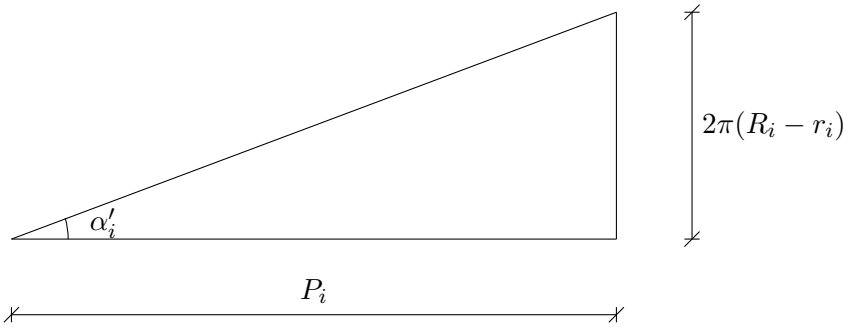

Figure 3.7. Determination of angle α'_i.

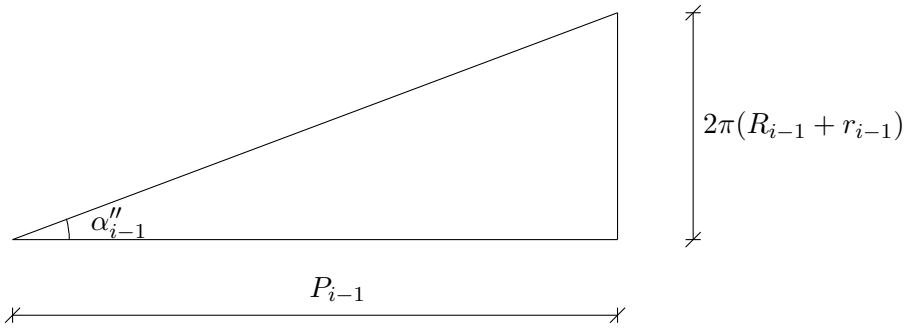

Figure 3.8. Determination of angle α''_{i-1}.

If the difference between the angles α'_i and α''_{i-1} (measured on the contact cylinder) and the lay angles α_i and α_{i-1} is neglected, one gets the following equation (Chouinard, 1994):

$$d_{Ci} = \frac{2\pi\, R_{Ci}}{n_{i-1}} \frac{\cos(\alpha_{i-1})}{\sin(\alpha_i + \alpha_{i-1})} \tag{3.21}$$

A different expression was proposed by Papailiou (1995). In his work, contact point distance is measured on the centerlines of layer i or $i-1$. The distance of contact points measured on the contact helix of layer i is given by:

$$d_{Ci} = \frac{2\pi R_{Ci}}{n_{i-1}} \cdot \frac{(1-\gamma_i^2)\,\cos(\alpha_{i-1})}{(1+\gamma_i)\,\sin(\alpha_{i-1})\,\cos(\alpha_i) + (1-\gamma_i)\sin(\alpha_i)\,\cos(\alpha_{i-1})} \tag{3.22}$$

where $\gamma_i = r_i/R_{Ci}$, having denoted with r_i the wire radius of layer i.
If the wire radius is small with respect to the contact cylinder radius R_{Ci} (i.e. $\gamma_i \to 0$), then Eq. 3.21 and Eq. 3.22 are identical.
It is worth noticing that, in multilayer conductors this equation may apply only to the outer layers. In fact, for the contacts between the core wire and the first layer of wires, one has: $R_C = r$, leading to $\gamma = 1$ and the equation is meaningless.
As previously recalled, the innermost layer (i.e. $i = 1$) is in contact with the core wire along a continuous helix. For this reason, distances between contact points at the interface between the core wire and the first layer are not here computed, just because they are not assumed to be pointwise distributed.
The distances between contact points are computed according to Equations 3.20, 3.21 and 3.22 and reported in tables 3.6-3.9, for different stranding.

Table 3.6. Distances (mm) between contact points for 26/7 conductors.

Code Word	$D\,(mm)$	$n_{i-1}\,(-)$	$\gamma\,(-)$	$R_c\,(mm)$	$d_{C,i}$ (Eq 3.20)	$d_{C,i}$ (Eq 3.21)	$d_{C,i}$ (Eq 3.22)
Contacts between layer $i = 2$ and layer $i = 3$.							
Partridge	16.28	10	0.231	5.57	8.16	8.44	8.24
Hawk	21.80	10	0.231	7.46	10.93	11.30	11.03
Drake	28.10	10	0.231	9.62	14.09	14.57	14.22
Contacts between layer $i = 1$ and layer $i = 2$.							
Partridge	16.28	6	0.428	3.00	12.38	11.85	11.55
Hawk	21.80	6	0.428	4.02	16.59	15.88	15.48
Drake	28.10	6	0.428	5.18	21.37	20.44	19.92

Table 3.7. Distances (mm) between contact points for 48/7 conductors.

Code Word	$D\,(mm)$	$n_{i-1}\,(-)$	$\gamma\,(-)$	$R_c\,(mm)$	$d_{C,i}$ (Eq 3.20)	$d_{C,i}$ (Eq 3.21)	$d_{C,i}$ (Eq 3.22)
Contacts between layer $i = 3$ and layer $i = 4$.							
Carillon	30.48	16	0.158	11.04	9.72	9.89	9.80
Gatineau	33.00	16	0.158	12.54	10.99	11.16	11.07
Bersfort	35.60	16	0.158	13.52	11.84	12.04	11.93
Contacts between layer $i = 2$ and layer $i = 3$.							
Carillon	30.48	10	0.231	7.38	11.65	12.34	11.73
Gatineau	33.00	10	0.231	8.58	13.43	14.13	13.52
Bersfort	35.60	10	0.231	9.25	14.47	15.23	14.57
Contacts between layer $i = 1$ and layer $i = 2$.							
Carillon	30.48	6	0.428	3.72	15.86	14.91	13.81
Gatineau	33.00	6	0.428	4.62	19.07	18.25	17.78
Bersfort	35.60	6	0.428	4.98	20.56	19.67	19.17

Table 3.8. Distances (mm) between contact points for 54/7 conductors.

Code Word	$D\,(mm)$	$n_{i-1}\,(-)$	$\gamma\,(-)$	$R_c\,(mm)$	$d_{C,i}$ (Eq 3.20)	$d_{C,i}$ (Eq 3.21)	$d_{C,i}$ (Eq 3.22)
Contacts between layer $i = 3$ and layer $i = 4$.							
Duck	24.21	18	0.143	9.42	7.26	7.36	7.31
Crow	26.28	18	0.143	10.22	7.88	7.98	7.94
Curlew	31.59	18	0.143	12.29	9.47	9.60	9.54
Contacts between layer $i = 2$ and layer $i = 3$.							
Duck	24.21	12	0.200	6.73	8.63	8.98	8.68
Crow	26.28	12	0.200	7.30	9.36	9.74	9.42
Curlew	31.59	12	0.200	8.78	11.25	11.72	11.33
Contacts between layer $i = 1$ and layer $i = 2$.							
Duck	24.21	6	0.333	4.04	15.77	15.53	15.90
Crow	26.28	6	0.333	4.38	17.12	16.86	17.26
Curlew	31.59	6	0.333	5.27	20.58	20.27	20.75

Table 3.9. Distances (mm) between contact points for 72/7 conductors.

Code Word	$D\,(mm)$	$n_{i-1}\,(-)$	$\gamma\,(-)$	$R_c\,(mm)$	$d_{C,i}$ (Eq 3.20)	$d_{C,i}$ (Eq 3.21)	$d_{C,i}$ (Eq 3.22)
Contacts between layer $i = 4$ and layer $i = 5$.							
Falcon	37.69	21	0.125	15.08	7.72	7.85	7.79
Nelson I	40.60	21	0.125	16.25	8.32	8.46	8.40
Nelson II	43.20	21	0.125	17.28	8.85	9.00	8.93
Contacts between layer $i = 3$ and layer $i = 4$.							
Falcon	37.69	15	0.167	11.31	10.08	10.18	10.18
Nelson I	40.60	15	0.167	12.19	10.86	10.97	10.97
Nelson II	43.20	15	0.167	12.96	11.55	11.67	11.67
Contacts between layer $i = 2$ and layer $i = 3$.							
Falcon	37.69	9	0.250	7.54	13.23	14.03	13.89
Nelson I	40.60	9	0.250	8.13	14.26	15.12	14.36
Nelson II	43.20	9	0.250	8.64	15.17	16.08	15.28
Contacts between layer $i = 1$ and layer $i = 2$.							
Falcon	37.69	6	0.500	3.77	16.12	15.12	13.89
Nelson I	40.60	6	0.500	4.07	17.39	16.32	15.01
Nelson II	43.20	6	0.500	4.32	18.49	17.35	15.94

As a general conclusion, it is possible to observe that Eq. 3.20 and Eq. 3.22 give quite close results for each interface of the various conductor cross-sections.
Eq. 3.21 predicts in general higher values for the distances between contact points. However, the overestimation decreases as the evaluation of the distances moves to the outer interfaces. As a matter of fact, γ coefficient depends only upon the stranding typology.
Finally, the calculated distances between contact points will conveniently used later on, in order to compute the approximate values of the radial contact forces at the various interfaces of each conductor cross-section considered in the present work.

3.3 Mechanical Model of the Strand

In this section, the mechanical model of stranded cables is presented. First, the mechanical model of a single wire according to the classical theory of curved thin rods is assessed in Subsection 3.3.1. Afterwards, the cross-sectional response of the whole strand is investigated in Subsection 3.3.2. Additionally, Subsection 3.3.3 deals with a kinematic model of the strand, that is conveniently introduced in order to evaluate the axial force in the wires (Subsection 3.3.4).

3.3.1 Wire Mechanical Model

Wires are the basic components of the strand and can be considered as curved thin rods. They can be described according to the classic theory of Kirchhoff–Clebsch–Love (KCL) (Love, 1944) under the following assumptions:

1. elastic material;
2. small displacements of the cross-section;
3. small rotations of the cross-section.

Under the previous assumptions, the cross-sections remain plane and normal to the deformed centerline of the rod, so that a linear strain field is assumed. Shear deformability is considered negligible due to the inherent slenderness and flexibility of typical metallic wires. Finally, variation of the strand internal geometry with respect to the reference (undeformed) configuration are disregarded.
It is convenient to study the mechanical response of wires within a moving reference frame centered on the centroid of the cross section and with axes directed as the Serret–Frenet unit vectors, $\boldsymbol{f}_i(S)$, with $i = 1, 2, 3$, function of the arc-length coordinate S (Section 3.1). In this context, the vectors $\boldsymbol{f}_i$ identify a set of principal axes for round wire cross sections. The generalized stresses of the curved thin rod model are defined as the axial force, F_{w1}, the torsional moment M_{w1} and the bending moments M_{w2} and M_{w3}.
These are the moments acting with respect to the directions of the vectors $\boldsymbol{f}_i$.
The generalized strains (i.e. the work-conjugated quantities) are:

- the wire axial strain ε_w, that is the elongation of the wire centerline;
- the mechanical curvatures χ_{wi} $(i = 1, 2, 3)$, that are collected into the vector $\boldsymbol{\chi}_w$, expressed in Equation 3.23a

The well-known kinematic equations are here re-written, in a more concise matrix notation, as it follows:

$$\boldsymbol{\chi}_w(S) = \sum_{i=1}^{3} \chi_{wi}(S)\boldsymbol{f}_i(S) = \frac{d\boldsymbol{\varphi}_w}{dS} + \boldsymbol{\Omega}_w\,\boldsymbol{\varphi}_w \tag{3.23a}$$

$$\boldsymbol{\varphi}_w(S) = \sum_{i=1}^{3} \varphi_{wi}(S)\boldsymbol{f}_i(S) \tag{3.23b}$$

where $\boldsymbol{\Omega}_w$ is the tensor defined in Equation 3.11 and components $\varphi_{wi}(S)$ of the vector $\boldsymbol{\varphi}_w(S)$ represent the cross sectional rotations about the moving reference system of the wire.

The constitutive equations according to Love's formulation and under the assumption of round cross section read:

$$F_{w1} = EA_w\,\varepsilon_w \tag{3.24a}$$

$$M_{w1} = \frac{EI_w}{1+\nu}\,\chi_{w1} \tag{3.24b}$$

$$M_{w2} = EI_w\,\chi_{w2} \tag{3.24c}$$

$$M_{w3} = EI_w\,\chi_{w3} \tag{3.24d}$$

where:

- E is the Young modulus of the material;
- ν is the Poisson coefficient of the material;
- A_w is the area of the cross-section;
- I_w is the second are moment of the wire cross-section about its principal inertia axes.

Let us now consider a generic system of external forces $\boldsymbol{t}(S)$ and couples $\boldsymbol{m}(S)$ per unit length of the wire centerline and define the vectors of internal actions as follows:

$$\boldsymbol{F}_w(S) = \sum_{i=1}^{3} F_{wi}(S)\boldsymbol{f}_i(S) \tag{3.25a}$$

$$\boldsymbol{M}_w(S) = \sum_{i=1}^{3} M_{wi}(S)\boldsymbol{f}_i(S) \tag{3.25b}$$

The indefinite equilibrium equations can be written as:

$$\frac{d\boldsymbol{F}_w}{dS} + \boldsymbol{\Omega}_w\,\boldsymbol{F}_w + \boldsymbol{t} = \boldsymbol{0} \tag{3.26a}$$

$$\frac{d\boldsymbol{M}_w}{dS} + \boldsymbol{\Omega}_w\,\boldsymbol{M}_w + \boldsymbol{f}_1 \times \boldsymbol{F}_w + \boldsymbol{m} = \boldsymbol{0} \tag{3.26b}$$

where the symbol $\times$ is used to denote the vectorial product.
As a general comment, the shear forces F_{w2} and F_{w3} can only be evaluated a-posteriori through the equilibrium equation. This is a consequence of the model formulation, because shear forces are not generalized stresses in such model, as it happens in the classical case of Euler-Bernoulli beam theory.

3.3.2 Cross Sectional Response of the Strand

The mechanical response of the strand cross-section can be described in terms of the resultant axial force $N_s(x_1, t)$, the torsional moment $M_{s1}(x_1, t)$ and the bending moments $M_{si}(x_1, t)$, with $i = 1, 2$.
Neglecting the shear deformability, one can describe the kinematics of the strand according to the classic Euler-Bernouilli beam theory.
Considering an infinitesimal segment of the strand of length dx_1, the axial strain of the strand can be defined starting from the relative axial displacement du_s (Figure 3.9), as follows:

$$\varepsilon_s(x_1, t) = \frac{du_s}{dx_1} \tag{3.27}$$

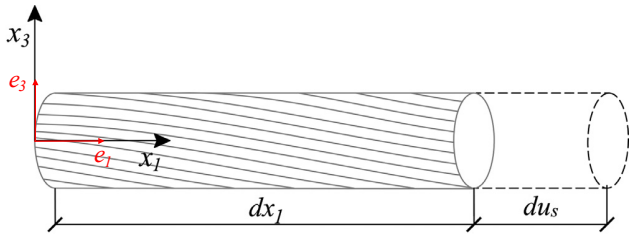

Figure 3.9. Axial elongation for an infinitesimal portion of the strand, adapted from (Foti and Martinelli, 2016a).

Considering the same infinitesimal segment of the strand of length dx_1, one can also introduce the relative rotation $d\psi_s$ (Figure 3.10), so that the bending curvature can be computed as follows:

$$\chi_s = \frac{d\psi_s}{dx_1} \tag{3.28}$$

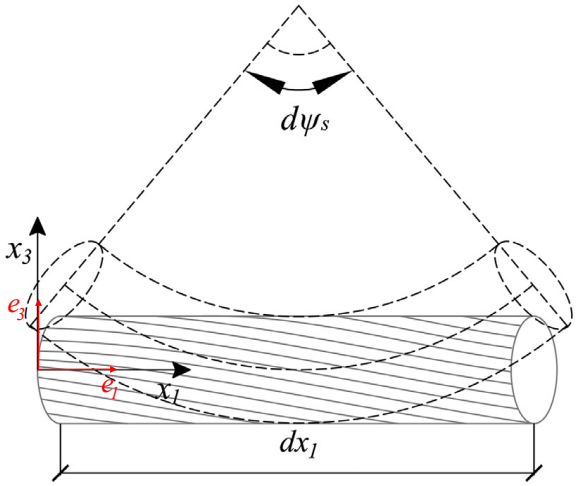

Figure 3.10. Bending curvature for an infinitesimal portion of the strand, adapted from (Foti and Martinelli, 2016a).

The virtual work per unit of length of the strand δW_s can be expressed as:

$$\delta W_s = N_s \delta\varepsilon_s + \sum_{i=1}^{3} M_{si} \delta\chi_{si} = \boldsymbol{\sigma}_{\boldsymbol{s}}^{\boldsymbol{T}} \delta\boldsymbol{\varepsilon}_{\boldsymbol{s}} \tag{3.29}$$

where $\boldsymbol{\sigma_s}$ and $\boldsymbol{\varepsilon_s}$ are column vectors that collect the work-conjugated stress and strains variables of the strand:

$$[\boldsymbol{\sigma}_s] = [N_s, M_{s1}, M_{s2}, M_{s3}]^T \tag{3.30a}$$

$$[\boldsymbol{\varepsilon_s}] = [\varepsilon_s, \chi_{s1}, \chi_{s2}, \chi_{s3}]^T \tag{3.30b}$$

For the next developments, it is convenient to collect the strand curvatures in a unique vector, according to the following expression:

$$\boldsymbol{\chi_s}(x_1, t) = \sum_{i=1}^{3} \chi_{si}(x_1, t)\boldsymbol{e}_i = \frac{\partial \boldsymbol{\varphi}_s}{\partial x_1} \tag{3.31}$$

where $\boldsymbol{\varphi}_s(x_1, t)$ is the rotation vector of the strand, whose components $\varphi_{si}(x_1, t)$ (in the basis $\boldsymbol{e}_i$) represent the cross-sectional rotations about the SRS axes:

$$\boldsymbol{\varphi}_s(x_1) = \sum_{i=1}^{3} \varphi_{si}(x_1, t)\boldsymbol{e}_i \tag{3.32}$$

The strand resultant axial force and moments can be evaluated by summing up all wire contributions, applying the equilibrium equations.
A vector $\boldsymbol{F}_{wp}$ can be obtained by projecting the generic wire axial force F_{w1} on the *Strand-attached Reference System* (SRS), according to the components of the first column of the tensor $\boldsymbol{\Lambda}_w(\theta)$:

$$\boldsymbol{F}_{wp} = F_{w1}\Big(\cos(\alpha)\boldsymbol{e}_1 - \sin(\alpha)\sin(\theta)\boldsymbol{e}_2 + \sin(\alpha)\cos(\theta)\boldsymbol{e}_3\Big) \tag{3.33}$$

Denoting with m the number of layers and with n_j the number of wires belonging to the j-th layer, one can evaluate the strand axial force through the following equation:

$$N_s = \sum_{j=0}^{m}\sum_{i=1}^{n_j} F_{w,ij}\cos(\alpha_j) \tag{3.34}$$

where the subscript "0" denotes the core wire.
In order to compute the strand resultant moments, it is necessary to project the wire moments on the SRS and then add the contribution coming from the vector $\boldsymbol{F}_{wp}$. The following equations hold:

$$M_{s1} = \sum_{j=0}^{m}\sum_{i=1}^{n_j} \cos(\alpha_j)M_{w1,ij} + \sin(\alpha_j))M_{w3,ij} + R_j\sin(\alpha_j)F_{w1,ij} \tag{3.35}$$

$$\begin{aligned} M_{s2} = \sum_{j=0}^{m}\sum_{i=1}^{n_j} &- \sin(\alpha_j)\sin(\theta_i)M_{w1,ij} - \cos(\theta_i)M_{w2,ij} + \\ &+ \cos(\alpha_j)\sin(\theta_i)M_{w3,ij} + R_j\cos(\alpha_j)\sin(\theta_j)F_{w1,ij} \end{aligned} \tag{3.36}$$

$$\begin{aligned} M_{s3} = \sum_{j=0}^{m}\sum_{i=1}^{n_j} &\sin(\alpha_j)\cos(\theta_i)M_{w1,ij} - \sin(\theta_i)M_{w2,ij} + \\ &- \cos(\alpha_j)\cos(\theta_i)M_{w3,ij} - R_j\cos(\alpha_j)\cos(\theta_j)F_{w1,ij} \end{aligned} \tag{3.37}$$

3.3.3 Kinematics of the Strand

In this subsection the kinematic of the strand is assessed, according to the formulation developed by (Foti and Martinelli, 2016b-2019). The deformation of a generic wire can be computed by relating the strand generalized strains, i.e. the vector $\boldsymbol{\varepsilon_s}$ (Eq. 3.30b), containing the strand axial strain ε_s (Eq. 3.27) and its mechanical curvatures $\boldsymbol{\chi}_s$ (Eq. 3.31), to the generalized strain variables of the wire, defined in Subsection 3.3.1 according to the Kirchhoff-Clebsch-Love theory, i.e. the wire axial strain ε_w and its mechanical curvatures, the latter being collected in the vector $\boldsymbol{\chi}_w$ (Eq. 3.23a).

Evaluation of the wire axial strain

Let us make reference again to Figure 3.9 and adopt an incremental formulation for the sake of simplicity, where the dot symbol denotes the derivative with respect to time t.
When a cross-section of the strand undergoes a small incremental translation $d\dot{u}_s$ along the direction x_1, the points of a generic wire cross-section displace of a quantity $\cos(\alpha)\, d\dot{u}_s$, in the direction of the tangent to the wire centerline.
The incremental wire axial strain $\dot{\varepsilon}_{w,a}(S,t)$ can be expressed as it follows:

$$\dot{\varepsilon}_{w,a}(S,t) = \cos(\alpha)\frac{\partial \dot{u}_s}{\partial S} \tag{3.38}$$

By recalling Eq. 3.5b and exploiting Eq. 3.27, the incremental strain of the points of the wire centerline can be rewritten according to the following expression:

$$\dot{\varepsilon}_{w,a}(S,t) = \cos^2(\alpha)\dot{\varepsilon}_s(x_1(S),t) \tag{3.39}$$

The latter expression only accounts for the effect of axial elongation of the strand.
If a combination of axial load and torsional moment applied is applied at the conductor ends, the mechanical problem becomes axisymmetric. As a consequence, all wires belonging to the same concentric layer behave identically and the hypothesis of preservation of the wire helicoidal geometry can be adopted to study the axial-torsional behavior of the strand (see e.g. (Lanteigne, 1985)).
Considering also the small strains hypothesis and negligible changes in the internal geometry of the strand, the following expression can be derived:

$$\dot{\varepsilon}_{w,at}(S,t) = \dot{\varepsilon}_{w,a}(S,t) + \dot{\varepsilon}_{w,t}(S,t) \tag{3.40}$$

where the incremental torsional wire strain contribution is given by:

$$\dot{\varepsilon}_{w,t}(S,t) = R\sin(\alpha)\cos(\alpha)\dot{\chi}_{s1}(x_1(S),t) \tag{3.41}$$

so that, by recalling Equation 3.39, Eq. 3.40 becomes:

$$\dot{\varepsilon}_{w,at}(S,t) = \cos^2(\alpha)\dot{\varepsilon}_s(x_1(S),t) + R\sin(\alpha)\cos(\alpha)\dot{\chi}_{s1}(x_1(S),t) \tag{3.42}$$

The latter is a linear kinematic equation expressing the incremental axial-torsional contribution of the wire strain.
At this stage it is important to notice that whenever a strand is bent, an incremental axial strain will arise due to a small change in the strand bending curvature.
Two limit kinematic assumptions have been proposed in the literature and have been widely adopted in recent studies. They are the so-called *full-slip* state and *full-stick* state:

1. under the *full-slip* kinematic condition, the external surfaces of the wires are assumed to be perfectly lubricated, such that the strand is modeled as a bundle of individually bent wires (i.e. curved thin rods). The wire length remains unchanged and the displacements in the direction of the strand axis, x_1, are proportional to the distance from a wire diameter parallel to the strand neutral axis of bending. The bending contribution to the axial strain of the wires is then equal to zero, so that the total incremental wire strain coincides with the axial-torsional strain incremental contribution (see Eq. 3.44);

2. under the *full-stick* kinematic condition the wires are ideally welded together, such that any relative displacement among them is prevented. All wires are considered as a part of an "ideal" strand cross section, planar and normal to the deformed centerline of the strand. In this case, the points of the cross section of the wire are subjected to an additional displacement in direction $x_1(S)$ which is proportional to the distance of the wire centroid from the axis x_2. The additional incremental strain due to bending of the strand about x_2 and x_3 axes can be computed respectively as:

$$\dot{\varepsilon}^{stick}_{w,b2}(S,t) = R\cos^2(\alpha)\sin(\theta(S))\dot{\chi}_{s2}(S,t) \tag{3.43a}$$

$$\dot{\varepsilon}^{stick}_{w,b3}(S,t) = R\cos^2(\alpha)\cos(\theta(S))\dot{\chi}_{s3}(S,t) \tag{3.43b}$$

   The total incremental wire strain in the sticking state can be then computed by adding the bending contributions about x_2 and x_3 axes (Eqts. 3.43) to the axial-torsional wire strain increment (Eq. 3.42), according to Eq. 3.45.

The incremental axial strain can be then expressed by distinguishing between *full-slip* and *full-stick* states, according to what was just presented, as it follows:

$$\begin{cases} \dot{\varepsilon}_w(S,t) = \dot{\varepsilon}_{w,at}(S,t) & \text{slipping case} \qquad (3.44) \\ \dot{\varepsilon}_w(S,t) = \dot{\varepsilon}_{w,at}(S,t) + \dot{\varepsilon}^{stick}_{w,bi}(S,t) & \text{sticking case} \quad i=2,3 \qquad (3.45) \end{cases}$$

The total strain is a function of time t and depend upon the past history of the strand, according to the following integral equation:

$$\varepsilon_w(S,t) = \int_0^t \dot{\varepsilon}_w(S,t)dt \tag{3.46}$$

It is also possible to simplify the previous expression by noting that the dependency on the past history of the total strain is only due to the term which describes the strain due to bi-axial bending of the strand. One has:

$$\varepsilon_w(S,t) = \varepsilon^L_w(S,t) + \varepsilon^{NL}_w(S,t) \tag{3.47}$$

where:

$$\varepsilon^L_w(S,t) = \varepsilon_{w,at}(S,t) = \cos^2(\alpha)\varepsilon_s(x_1(S),t) + R\sin(\alpha)\cos(\alpha)\chi_{s1}(x_1(S),t) \tag{3.48}$$

and the nonlinear part of the total strain is given by:

$$\varepsilon^{NL}_w(S,t) = \varepsilon^{stick}_{w,bi}(S,t) = \int_0^t \dot{\varepsilon}^{stick}_{w,bi}(S,t)dt\,, \quad \text{with i=2,3} \tag{3.49}$$

Evaluation of the wire curvatures

By assuming that the wire cross section rotates rigidly with the cross section of the strand (Foti and Martinelli, 2016b-2019), the following equation can be conveniently introduced to relate the strand rotation vector, $\boldsymbol{\varphi_s}$ (see Eq. 3.32) to that of a generic wire, $\boldsymbol{\varphi}_w$ (see Eq. 3.23b):

$$\boldsymbol{\varphi}_w(S,t) = \boldsymbol{\Lambda}_w^T(S)\,\boldsymbol{\varphi}_s(x_1(S),t) \tag{3.50}$$

where $\boldsymbol{\Lambda}_w$ is the rotation tensor which relates the orientation of the local Serret-Frenet unit vectors of the wire cross-section with respect to the basis $\boldsymbol{e}_i$ of the SRS, already introduced in Section 3.1 (see Eqts. 3.2 and 3.3).
At this stage, by recalling the definition of the mechanical curvatures of the strand (Eq. 3.31) and the useful differential relation reported in Eq. 3.5b, one can express the derivatives of the wire rotations with respect to S in the following manner:

$$\frac{\partial \boldsymbol{\varphi}_w}{\partial S} = \cos(\alpha)\boldsymbol{\Lambda}_w^T(S)\,\chi_s(x_1(S),t) + \frac{d\boldsymbol{\Lambda}_w^T}{dS}\boldsymbol{\varphi}_s(x_1(S),t) \tag{3.51}$$

By solving Eq. 3.50 for $\boldsymbol{\varphi_s}$ and substituting in Eq. 3.51, and recalling Eq. 3.10, the following equation is readily obtained:

$$\frac{\partial \boldsymbol{\varphi}_w}{\partial S} = \cos(\alpha)\boldsymbol{\Lambda}_w^T(S)\,\chi_s(x_1(S),t) - \boldsymbol{\Omega_w}(S)\boldsymbol{\varphi}_w(S,t) \tag{3.52}$$

By recalling Eq. 3.23a, Eq.3.52 permits to obtain the following result:

$$\boldsymbol{\chi}_w(S,t) = \cos(\alpha)\boldsymbol{\Lambda}_w^T(S)\boldsymbol{\chi_s}(x_1(S),t) \tag{3.53}$$

so that the vector collecting the mechanical curvatures of a generic wire of the strand is fully related to the one collecting the mechanical curvatures of the entire strand.

3.3.4 Evaluation of the axial force in the wires

It is now convenient to focus on the determination of the expression of the resultant axial force on the wire cross-section, that will be useful for the next developments of this work.
The resultant axial force on the generic wire cross-section can be expressed as:

$$F_{w1}(x_1(S),t) = \int_{A_w} \sigma(S,t)dA_w \tag{3.54}$$

where:

$$\sigma(S,t) = E\varepsilon(S,t) \tag{3.55}$$

is the normal stress at a generic point of the wire cross-section, evaluated under the assumption of linear elastic thin rods.
After some straightforward substitutions, one can express the the axial force acting on the wire cross-section as the sum of a linear contribution F_{w1}^L related only to the axial-torsional contribution of the strain, and a non-holonomic non-linear one, F_{w1}^{NL}, representing the contribution due to bending of the strand to the axial force of a generic wire in case of full-stick kinematic assumption.
The equation simply reads:

$$F_{w1}(x_1(S),t) = F_{w1}^L(x_1(S),t) + F_{w1}^{NL}(x_1(S),t) \tag{3.56}$$

The linear component of the wire axial force can be evaluated as it follows:

$$F_{w1}^{L}(x_1(S),t) = \int_{A_w} E\Big[\cos^2(\alpha)\varepsilon_s(x_1(S),t) + R\sin(\alpha)\cos(\alpha)\chi_{s1}(x_1(S),t)\Big]dA_w \tag{3.57}$$

but due to the polar symmetry of the round wire section, the contribution of the torsional curvature of the strand is null, so that the above expression can be rewritten as:

$$F_{w1}^{L}(x_1(S),t) = EA_w\ \cos^2(\alpha)\varepsilon_s(x_1(S),t) \tag{3.58}$$

On the other hand, the non-linear component of the wire axial force can be evaluated through the following more general expression:

$$F_{w1}^{NL}(x_1(S),t) = \int_{A_w} E\,\varepsilon_w^{NL}(S,t)dA_w \tag{3.59}$$

By summing up the two contributions presented in Eqts. 3.58 and 3.59, one can finally obtain the total axial force in a generic wire F_{w1}.

Remark

It is worth noticing that the contribution of the non-linear component of the wire axial force (F_{w1}^{NL}) averaged on a generic layer of wires, gives a resultant almost equal to zero.
By recalling Eq. 3.34 it is in fact possible to express the strand axial force N_s.
The stresses normal to the strand cross-section are defined on each wire through the projection $\sigma\ \cos(\alpha)$. So that, by denoting with m the total number of layers and with n_j the number of wires in the j-th layer, the strand axial force can be computed as:

$$N_s(x_1,t) = \sum_{j=0}^{m}\Big[n_j\ \cos^3(\alpha_j)EA_{wj}\Big]\varepsilon_s(x_1(S),t) + \sum_{j=0}^{m}\Big[\cos(\alpha_j)\sum_{i=1}^{n_j}F_{w1}^{NL}(x_1(S),t)\Big] \tag{3.60}$$

The second term of the previous equation has the physical meaning of an additional contribution to the strand resultant axial force, related to the bending of the strand.
Such term is strictly equal to zero both under *full-slip* state and *full-stick* state (see Foti and Martinelli, 2016a).
Preliminary analysis developed by Foti in his PhD thesis (18) show that such term can be neglected in most practical applications, leading to the introduction of the following convenient approximation:

$$N_s \cong \sum_{j=0}^{m}\Big[n_j\ \cos^3(\alpha_j)EA_{wj}\Big]\varepsilon_s \tag{3.61}$$

Hence, as an important conclusion, the contribution of the nonlinear component of the wire axial force averaged on the entire cross-sections of the strand, practically returns a null contribution of the axial force on the strand.

3.4 Axial-torsional Problem

In this Section the axial-torsional mechanical model of the strand is presented.
The experimental evidence clearly shows that the axial-torsional behavior of metallic stranded cables is essentially linear under typical service loading conditions (Foti and de Luca di Roseto, 2016),(Foti and Martinelli, 2019). This is an important difference with respect to the bending problem, which is by far more complex to solve due to its intrinsic non-linear and non-holonomic nature. The latter will be assessed in the next Section (3.5).

3.4.1 Stiffness Matrix

According to the previous developments, the generalized strains of the generic wire can be evaluated according to Equation 3.47 and 3.53. Due to the linearity property of the axial-torsional problem, the wire axial strain can be here conveniently introduced in integral form, i.e. it is not necessary to rely on an incremental formulation, as it was previously done in Paragraph 3.3.3.
Once the wire generalized strains have been introduced, by direct application of the linear constitutive laws (Eqts. 3.24), it is immediate to obtain the resultant generalized forces (i.e. axial force and bending moments) acting on the cross-section of the generic wire.
Then, the strand cross-sectional resultants can be conveniently computed by straightforward application of Equations 3.34, 3.35, 3.36 and 3.37.
Let us now focus on the derivation of the stiffness matrix for the axial-torsional problem and consider a strand loaded by an axial force N_s and a torsional moment M_{s1} only.
In this context, a common hypothesis is to assume that the cross-sections remain plane, so that the kinematic filed can be described by means of the axial strain ε_s and of the torsional curvature χ_{s1}.
The vectors of generalized stresses and strains in this particular case are simply:

$$[\boldsymbol{\sigma}_s] = [N_s, M_{s1}]^T \tag{3.62a}$$

$$[\boldsymbol{\varepsilon_s}] = [\varepsilon_s, \chi_{s1}]^T \tag{3.62b}$$

At this stage, one can write the elastic energy of the strand per unit of length, by expressing it as a quadratic form, introducing the stiffness matrix of the strand section $\boldsymbol{K}_s$.
The elastic energy per unit of length of the strand reads:

$$\frac{dU}{dx_1} = \frac{1}{2}\boldsymbol{\sigma}_s^T\, \varepsilon_s = \frac{1}{2}\boldsymbol{\varepsilon}_s^T\, \boldsymbol{K}_s\, \boldsymbol{\varepsilon}_s \tag{3.63}$$

The axial-torsional stiffness matrix $\boldsymbol{K}_{s,at}$ has to be positive definite and symmetric, as direct consequence of the elasticity assumption. Its structure is herein collected:

$$\boldsymbol{K}_{s,at} = \begin{bmatrix} EA & C_{AT} \\ C_{AT} & GJ \end{bmatrix} \tag{3.64}$$

where EA and GJ denote respectively the axial and torsional stiffness of the strand, while C_{AT} is the axial-torsional stiffness coupling term, that is present due to the direct consequence of the helicoidal geometry of the wires centerlines.
The vector of generalized stresses can then be expressed as follows:

$$\begin{bmatrix} N_s \\ M_{s1} \end{bmatrix} = \begin{bmatrix} EA & C_{AT} \\ C_{AT} & GJ \end{bmatrix} \begin{bmatrix} \varepsilon_s \\ \chi_{s1} \end{bmatrix} \tag{3.65}$$

The axial-torsional cross-sectional stiffness can be expressed according to the following equations (Foti and Martinelli, 2016b):

$$EA = \sum_{j=0}^{m} n_j \, \cos^3(\alpha_j) \, EA_{w,j} \tag{3.66}$$

$$\begin{aligned} GJ = \sum_{j=0}^{m} n_j \Big(& \frac{EI_{w,j}}{1+\nu_j} \Big[\cos^3(\alpha_j) + (1+\nu_j) \sin^2(\alpha_j) \cos(\alpha_j) \Big] \\ & + \sin^2(\alpha_j) \cos(\alpha_j) \, R_j^2 \, EA_{w,j} \Big) \end{aligned} \tag{3.67}$$

$$C_{AT} = \sum_{j=0}^{m} n_j \, R_j \, \sin(\alpha_j) \, \cos^2(\alpha_j) EA_{w,j} \tag{3.68}$$

3.4.2 Radial Contact Pressures Models

In a homogeneous, isotropic bar under axial load, there is no radial stress, while in a conductor under tension, there are clenching forces between layers, i.e. normal forces acting at the contact points between wires (Cardou, 2013). Their presence can be intuitively explained. In fact, the axial force in each wire tends to "straighten up" the helix, and thus tends to induce a decrease of the radius of the lay cylinder. This inward radial motion is blocked by internal layers of wires, thus an interlayer pressure arises.
Such pressure is already present even before the application of the tension T on the strand, because of the stranding process. The contribution of these "residual" clenching forces was highlighted e.g. in (Foti and Martinelli, 2016b), (Frigerio et al., 2016). They can play a significant role in slack stranded cables and the importance of their effects decreases as the axial force acting on the strand increases. Foti and Martinelli have also found that the value of residual radial contact forces heavily influences the reference value of the transition curvature (and corresponding bending moment) from the initial *full-stick* behavior and the *full-slip* regime.
One could account for the effect of the residual radial contact forces R_j acting on the generic j-th layer, by slightly modifying the expressions 3.72a and 3.72b which will be derived in the next paragraph (see (22) for further details).
At the current time there is not a well-established formulation to model such "residual" pressures. In fact, this is still an open research topic. However, residual radial contact forces won't be further considered in the present work.
In this subsection, three different radial contact pressure models of the literature are presented. The predictions of these different models will be then compared for each layer of wires, for various ACSR conductors.

Radial Contact Pressures Model A (P.M. A)

This radial contact pressures model was developed by Foti and Martinelli and originally presented in (22).
Let us consider an infinitesimal wire segment dS. Figure 3.11 shows a scheme of the wire portion subjected to a system of distributed radial forces acting on the contact helices (internal and external).

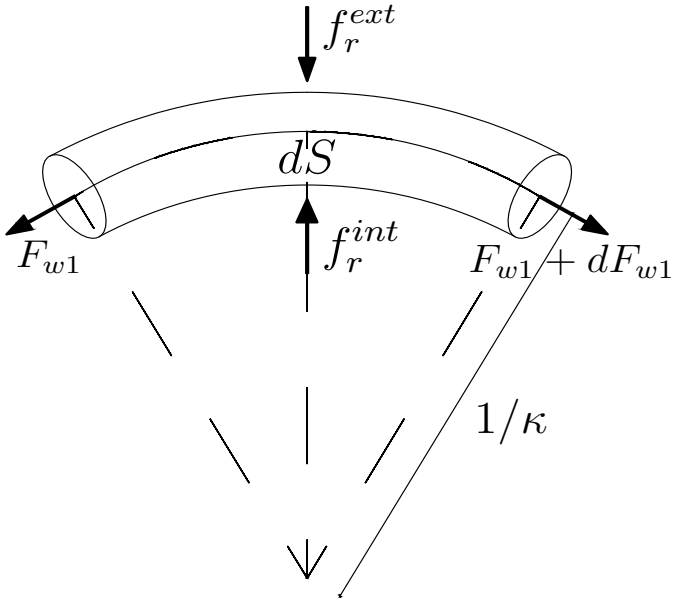

Figure 3.11. Radial forces contributions of an infinitesimal wire segment.

By stating the equilibrium of the infinitesimal wire along the radial directions the following equation is obtained:

$$F_{w1}(S,t)\kappa + c^{ext} f_r^{ext} - c^{int} f_r^{int} = 0 \tag{3.69}$$

where κ denotes the initial curvature of the wire centerline, while c^{ext} and c^{int} are two non-dimensional coefficients that account for the difference between dS and the length of the infinitesimal segments of the contact helices. Foti and Martinelli have expressed this coefficients as follows:

$$c^{int} = 1 - \frac{\kappa\, d}{2} \tag{3.70a}$$

$$c^{ext} = 1 + \frac{\kappa\, d}{2} \tag{3.70b}$$

The radial contact conditions can be studied starting from the literature assumption that all the wires in a layer are subjected to the same external radial contact forces. Hence, the equilibrium in the radial direction at the interface between two generic layers , j and $j-1$ requires that:

$$n_j\, f_{r,j}^{int} = n_{j-1} f_{r,j-1}^{ext} \tag{3.71}$$

where the symbol n_k denotes the number of wires in the k-th layer.
The radial equilibrium equation of a wire (3.69) can then be iteratively solved together with the condition (3.71) starting from the outermost layer (layer m), where the external radial

forces are assumed equal to zero (unloaded strand lateral surface).
The following expressions can be obtained:

$$f_{r,j}^{ext} = \frac{1}{n_j} \sum_{l=j+1}^{m} \Gamma(l,j)\delta_l \, F_{w1,j}^{av} \tag{3.72a}$$

$$f_{r,j}^{int} = \frac{1}{n_j} \, \delta_j \, F_{w1,j}^{av} + \gamma_j \, f_{r,j}^{ext} \tag{3.72b}$$

where $F_{w1,j}^{av}$ is the average axial force of the wires in the j-th layer:

$$F_{w1,j}^{av} = \frac{1}{n_j} \sum_{i=1}^{n_j} F_{w1,ij} \tag{3.73}$$

It is worth noticing that, for the axial-torsional loading scenario only, the average axial force of the wires in the j-th layer exactly coincides with the wire axial force previously determined through Equation 3.58, that is the linear component of the wire axial force.
If a bending deformation is superimposed, then the induced non-linear components of the wire axial forces averaged on the layer of wires is negligible, as already remarked in Subsection 3.3.4.
The function $\Gamma(i,j)$ is defined according to the following equation:

$$\Gamma(l,j) = \Pi_{k=j+1}^{l-1} \gamma_k \tag{3.74}$$

Coefficients δ_j and γ_j which appear in the above equations, depend only on the geometric characteristics of the j-th layer through the non-dimensional coefficients c_j^{int} and c_j^{ext} and the initial curvature of the wire centerline κ_j:

$$\delta_j = \frac{n_j \, \kappa_j}{c_j^{int}} \tag{3.75a}$$

$$\gamma_j = \frac{c_j^{ext}}{c_j^{int}} \tag{3.75b}$$

Radial Contact Pressures Model B (P.M. B)

As the number of layers of typical ACSR conductors increases, the effect of the non-dimensional coefficients c^{ext} and c^{int} on the radial contact pressures tends to become lower. The aim of this part of the work is to rigorously evaluate the consequences of neglecting such coefficients on the radial contact forces values for typical multi-layer ACSR conductors.
On this behalf, one can introduce the following approximated equations:

$$c^{int} \cong 1 \tag{3.76a}$$

$$c^{ext} \cong 1 \tag{3.76b}$$

So that, if the difference between the segment dS of the wire and the length of the infinitesimal segments of the contact helices is disregarded, Radial Pressures Model B is found.
As a direct consequence of the imposition of Eqt.s 3.76, one has: $\delta_j = n_j \, \kappa_j$ and $\gamma_j = 1$.
Equations 3.74 simplifies as it follows:

$$\Gamma(l,j) = \Pi_{k=j+1}^{l-1} 1 \tag{3.77}$$

and the external and internal radial contact forces can be computed much more easily, according to the following equations:

$$f_{r,j}^{ext} = \frac{1}{n_j} \sum_{l=j+1}^{m} \Gamma(l,j) n_l \, \kappa_l \, F_{w1,j}^{av} \tag{3.78a}$$

$$f_{r,j}^{int} = \kappa_j \, F_{w1,j}^{av} + f_{r,j}^{ext} \tag{3.78b}$$

Radial Contact Pressures Model C (P.M. C)

This model was originally developed by Papailiou (1997) and has been later adopted, with minor changes, also by Foti and Martinelli (2016a).
The main difference between this model and the previous ones, is that Papailou's transfer model does not take into account the different number of wires of the layers which are in contact, as it can be see from Fig. 3.12.

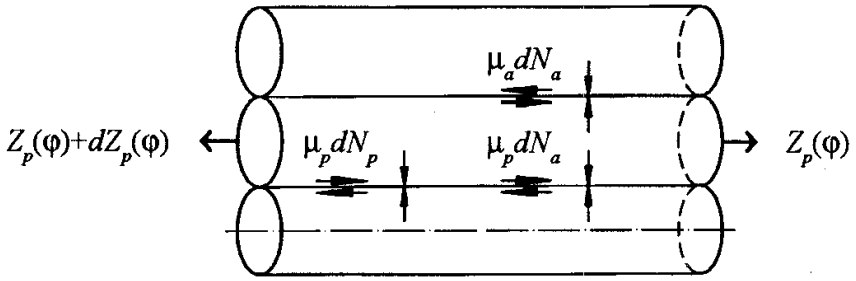

Figure 3.12. Forces acting on a differential wire element in the penultimate layer of a multilayer conductor, from (Papailiou, 1997).

In fact, an approximation is clearly introduced by extending the model he developed for single-layer conductors to the case of multi-layer conductors. By stating the equilibrium in the radial direction at the interface between two generic layers , j and $j-1$, one has:

$$f_{r,j}^{int} = f_{r,j-1}^{ext} \tag{3.79}$$

and the condition directly translates in a drastically different model with respect to the previous two (see also Eq. 3.71).
The basic assumption that is necessary to iteratively solve equation 3.69 is that all wires in a layer are subjected to the same external radial forces.
In this way it is possible to start from the outermost layer, where $f_r^{ext} = 0$ because the surface is unloaded. With the usual notation (m denotes the number of layers and n_j the number of wires in the j-th layer) one gets:

$$f_{r,j}^{ext} = \sum_{l=j+1}^{m} \kappa_l \, F_{w1,l}^{av} \tag{3.80}$$

At this stage, by recalling the definition of the average axial force in wires of the l-th layer (Eq. 3.73) and expression 3.56, one obtains the following equation:

$$f_{r,j}^{ext} = \sum_{l=j+1}^{m} \kappa_l \, F_{w1,l}^{L} + \sum_{l=j+1}^{m} \left(\frac{\kappa_l}{n_l} \sum_{i=1}^{n_l} F_{w1,i}^{NL} \right) \tag{3.81}$$

It is worth noticing that the second term which appears in the previous equation is directly related to the resultant of wire axial forces due to the bending of the strand in each layer and can be neglected without significantly affect the results (Foti and Martinelli, 2016a), as already remarked several times (see Subsection 3.3.4).
So that, Eq 3.81 simplifies as follows:

$$f_{r,j}^{ext} \cong \sum_{l=j+1}^{m} \kappa_l \, F_{w1,l}^{L} \tag{3.82}$$

Due to the simplicity of this model, closed-form expressions for the computation of the radial contact forces as a functions of the strand axial force N_s can be derived in a straightforward manner. From Equations 3.82 and 3.61, the linear component of the wire axial force can be computed as:

$$F_{w1,l}^{L} = \frac{\cos^2(\alpha_l) EA_{wl}}{\sum_{k=1}^{n_w} EA_{wk} \cdot \cos^3(\alpha_k)} N_s = \nu_{w,l} \, N_s \tag{3.83}$$

where n_w denote the total number of wires of the strand.
The non-dimensional coefficient $\nu_{w,l}$ accounts for the characteristics of the internal structure of the strand, and express the non-dimensional axial force in the l-th layer of wires.
By substitution of Eq. 3.83, one finally obtains:

$$f_{r,j}^{ext} \cong \sum_{l=j+1}^{m} \frac{\nu_{w,l}}{\rho_{w,l}} \, N_s \tag{3.84}$$

From the equilibrium equation of the wire in the radial direction one can also obtain the internal radial contact forces:

$$f_{r,j}^{int} = \left(f_{r,j}^{ext} + F_{w1,j} \, \kappa_j \right) \cong \sum_{l=j+1}^{m} \frac{\nu_{w,l}}{\rho_{w,l}} N_s + \kappa_j \, \nu_{w,j} \, N_s \tag{3.85}$$

Numerical Validation Test

In this paragraph, a validation test of the different radial transmission pressures models is performed. Numerical results coming from a finite element model of a stranded cable (see Ref. 65) are compared with the theoretical predictions of the three different radial transmission pressures models (P.M. A, B and C). The composition of the investigated strand is reported in Table 3.10 for the sake of clarity.

Table 3.10. Composition of the Investigated spiral strand.

Layer	n_w	d_w (mm)	P_p (mm)	E (GPa)	ν (-)	θ_0 (deg)
0	1	4.50	0	217	0.28	0
1	6	4.25	-97.44	217	0.28	0
2	12	4.25	231.05	217	0.28	0
3	18	4.25	-322.06	217	0.28	0
4	24	4.25	413.08	217	0.28	0

The external diameter of the strand is equal to $D = 38.50$ mm, its Rated Tensile Strength is $RTS = 1310.475$ kN and the cable is strung at a tension level $T = 0.20 \; RTS$. The finite element model considers pure radial contacts between wires belonging to layers 1-4. However, contact deformability is accounted for, whereas Pressures Models A-C are formulated under

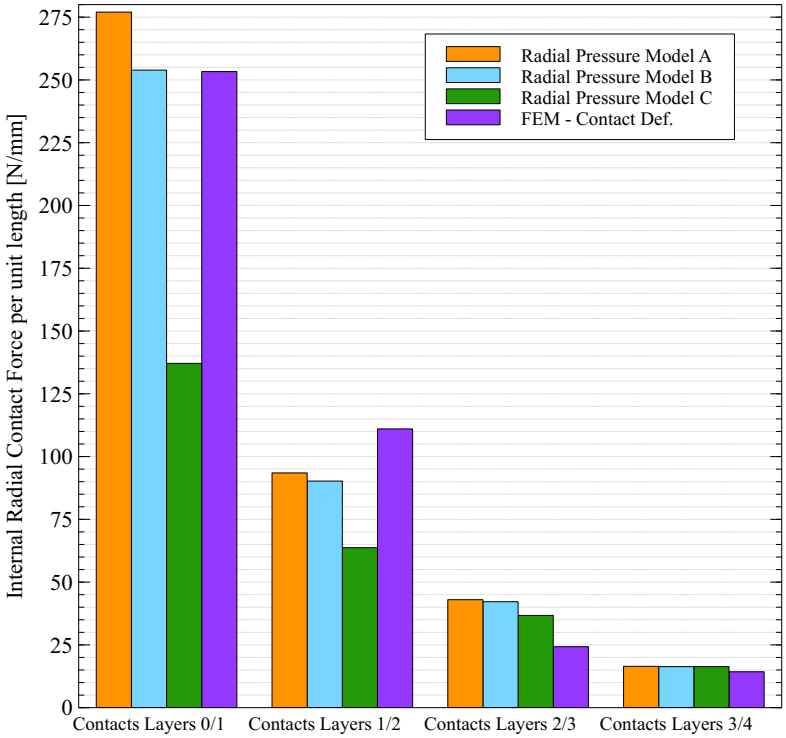

Figure 3.13. Comparison between the internal radial contact force per unit of length predicted by the different models and the FE model results.

the assumption of fully rigid contacts. Additionally, the core wire is considered to be in contact with the first layer of wires, through mixed-type patches (i.e. both radial and lateral contacts). As it can be seen from Fig. 3.13 for what concerns the contacts between the core wire and the first layer, almost perfect correlation between FEM results and P.M. B is present. Additionally, FEM results obtained for contacts between layer 1 and layer 2 are better approximated by P.M.A, while results obtained for contacts between layers 2 and 3 are better approximated by P.M.C. This fact could be related to the contact deformability, which causes radial forces per unit length to be smaller with respect to the fully-rigid model predictions. Theoretical predictions for the contacts between layer 3 and 4 are equally close to FEM results.

Comparison among the different models

In this paragraph the radial pressures transmission models A, B and C are applied to a sample of 15 conductors cross-sections, and their predictions of the internal and external radial contact forces per unit of length are then compared.
The geometrical and mechanical properties of the investigated conductors are reported in Appendix A, whereas their cross-sections schemes are conveniently reported in Appendix B. The following plots show various bar charts for both the prediction of the internal and external radial contact forces per unit of length for the different conductors, distinguished by layers. Radial forces per unit of length are computed by considering an axial force of 1 kN acting on the strand. Due to the linearity property of the axial-torsional problem, the following results can be easily scaled up in order to obtain the corresponding values of the radial contact forces for any magnitude of the axial force N_s acting on the strand.

ACSR 6/1

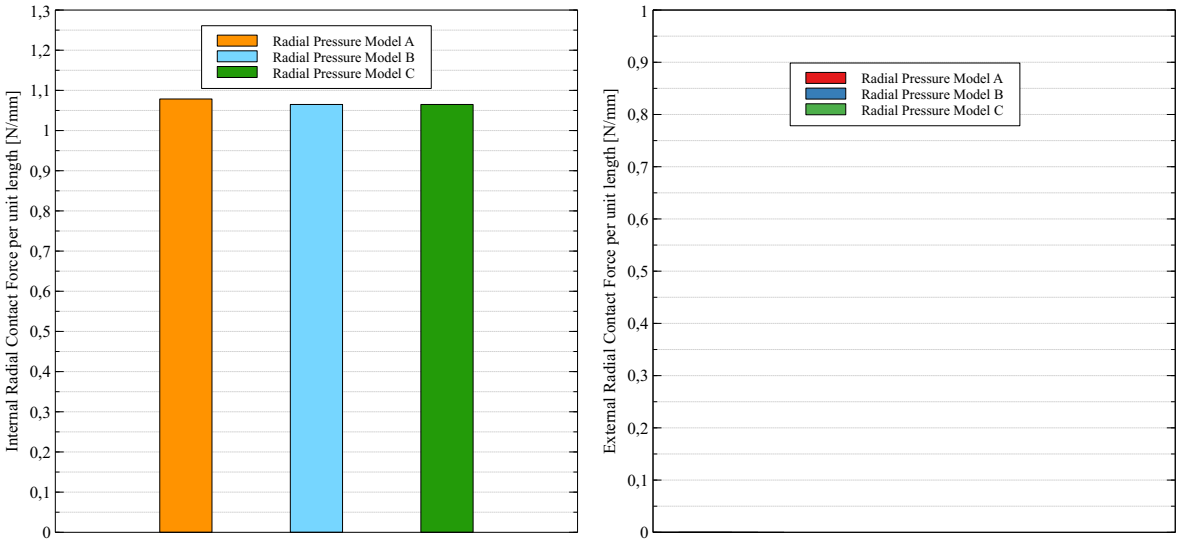

(a) (b)

Figure 3.14. ACSR 6/1 Sparrow: plot of the internal (a) and external (b) radial contact forces per unit of length for the sole layer of wires.

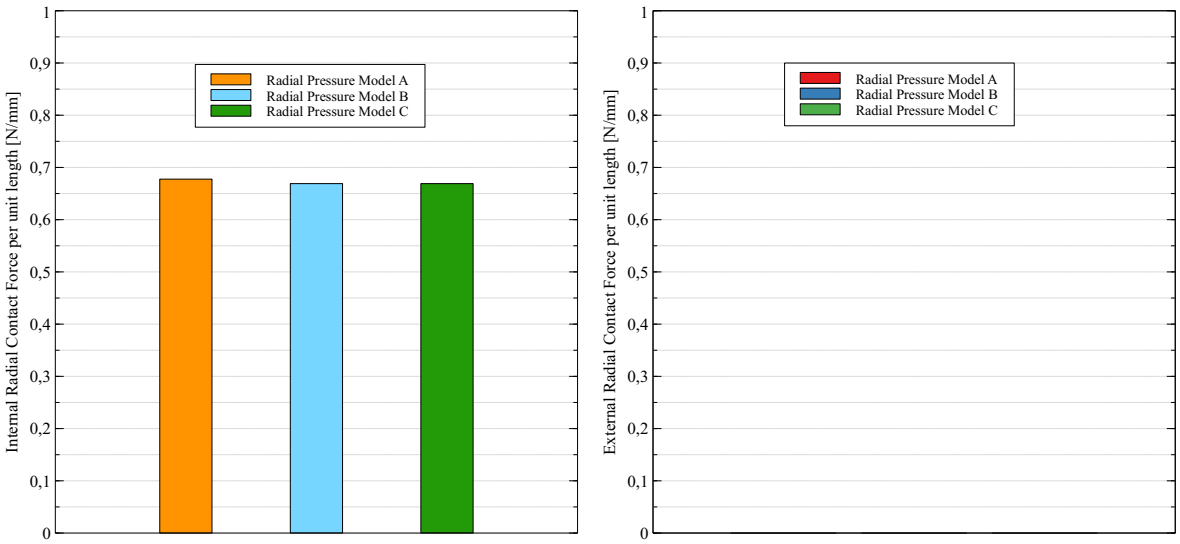

(a) (b)

Figure 3.15. ACSR 6/1 Pigeon: plot of the internal (a) and external (b) radial contact forces per unit of length for the sole layer of wires.

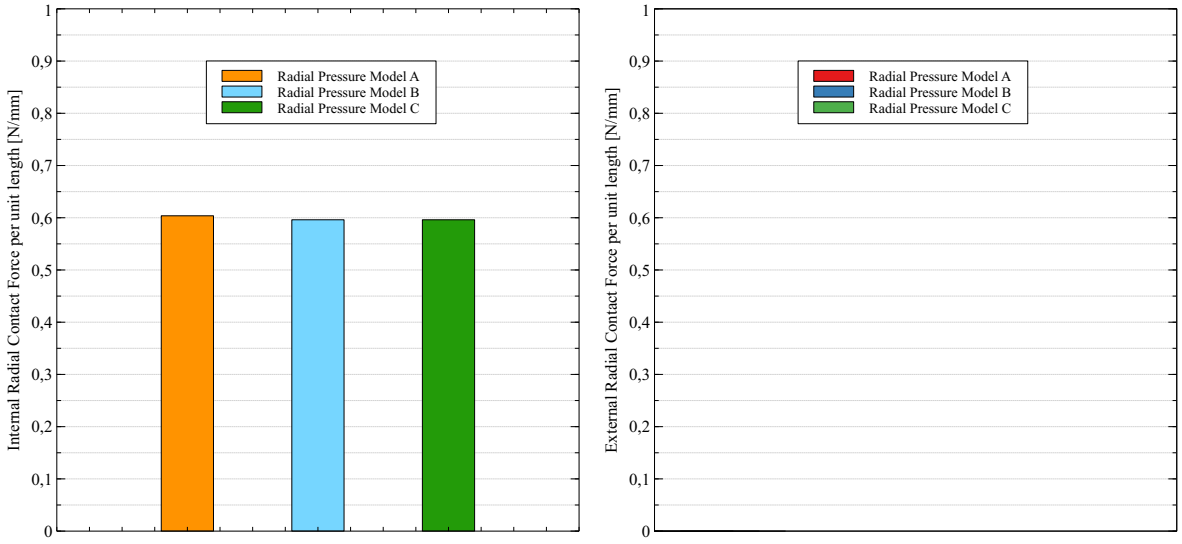

(a) (b)

Figure 3.16. ACSR 6/1 Penguin: plot of the internal (a) and external (b) radial contact forces per unit of length for the sole layer of wires.

ACSR 26/7

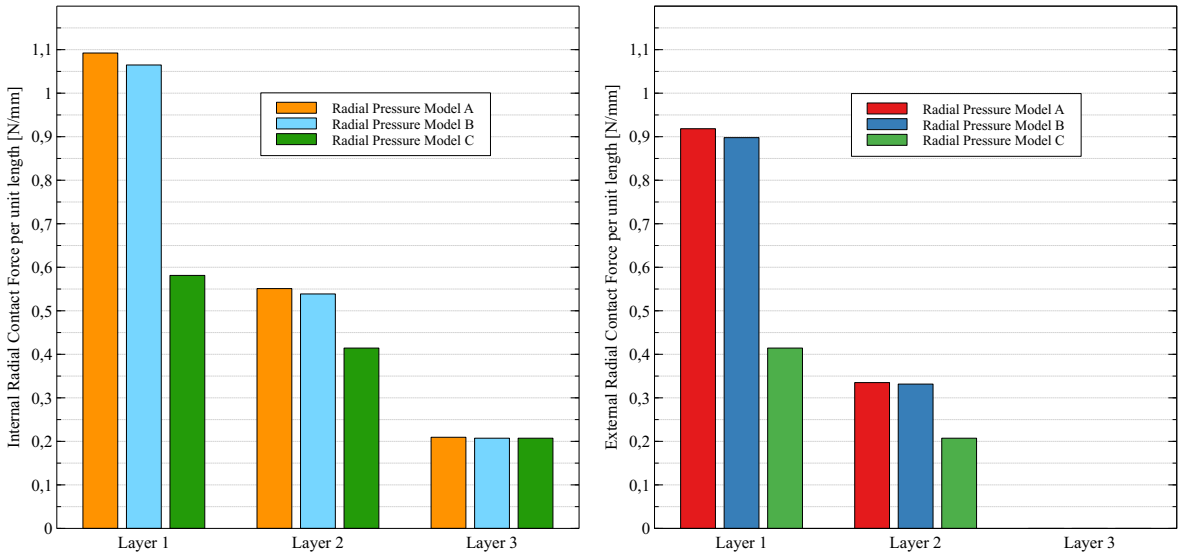

(a) (b)

Figure 3.17. ACSR 26/7 Partridge: plot of the internal (a) and external (b) radial contact forces per unit of length for the three layers of wires.

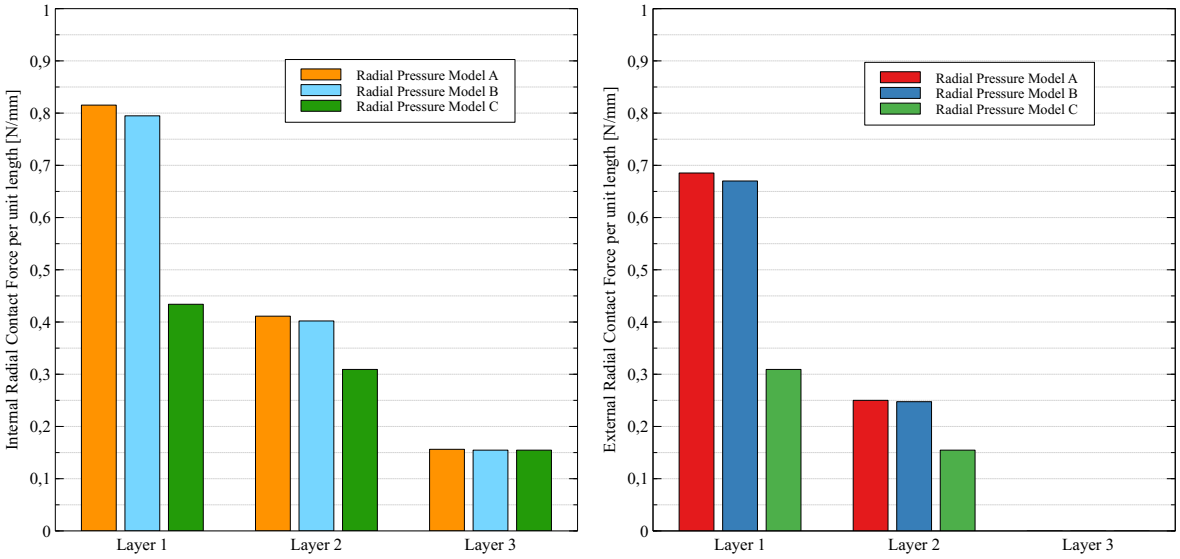

(a) (b)

Figure 3.18. ACSR 26/7 Hawk: plot of the internal (a) and external (b) radial contact forces per unit of length for the three layers of wires.

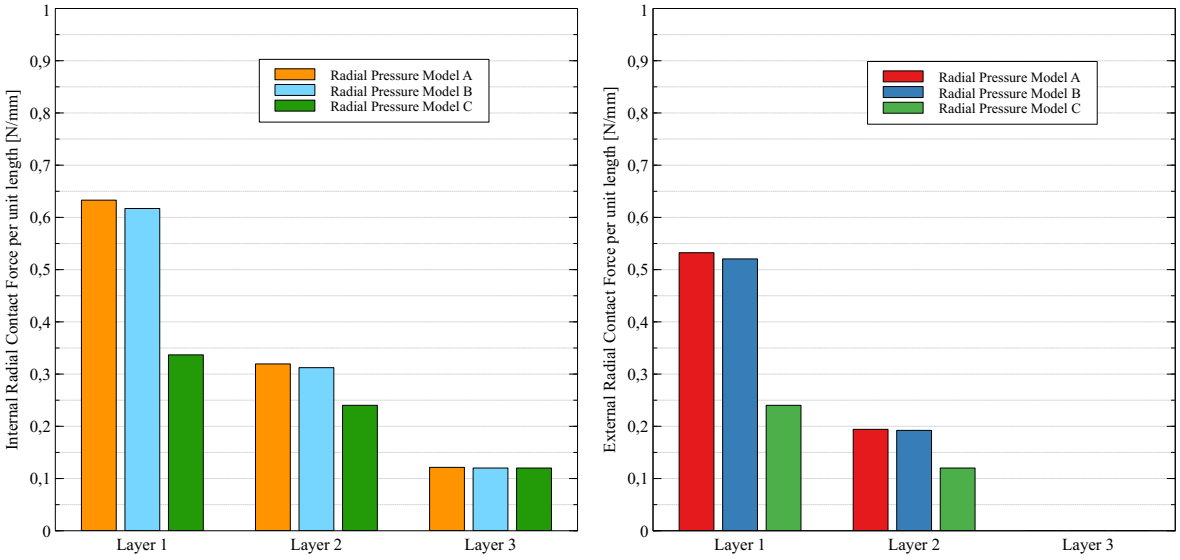

(a) (b)

Figure 3.19. ACSR 26/7 Drake: plot of the internal (a) and external (b) radial contact forces per unit of length for the three layers of wires.

ACSR 48/7

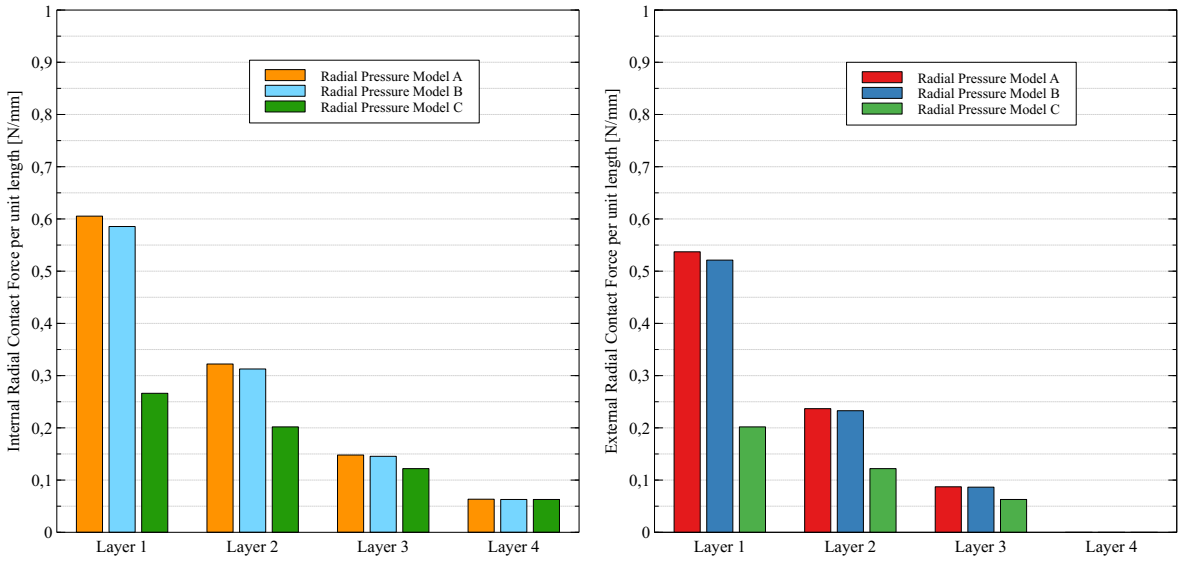

(a) (b)

Figure 3.20. ACSR 48/7 Bersfort: plot of the internal (a) and external (b) radial contact forces per unit of length for the four layers of wires.

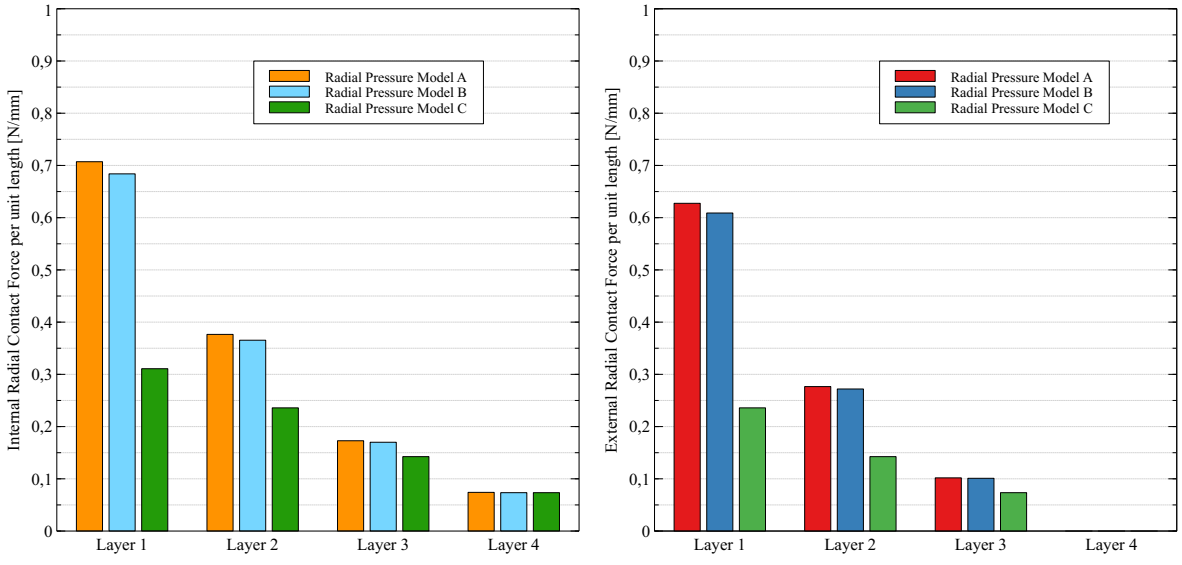

(a) (b)

Figure 3.21. ACSR 48/7 Carillon: plot of the internal (a) and external (b) radial contact forces per unit of length for the four layers of wires.

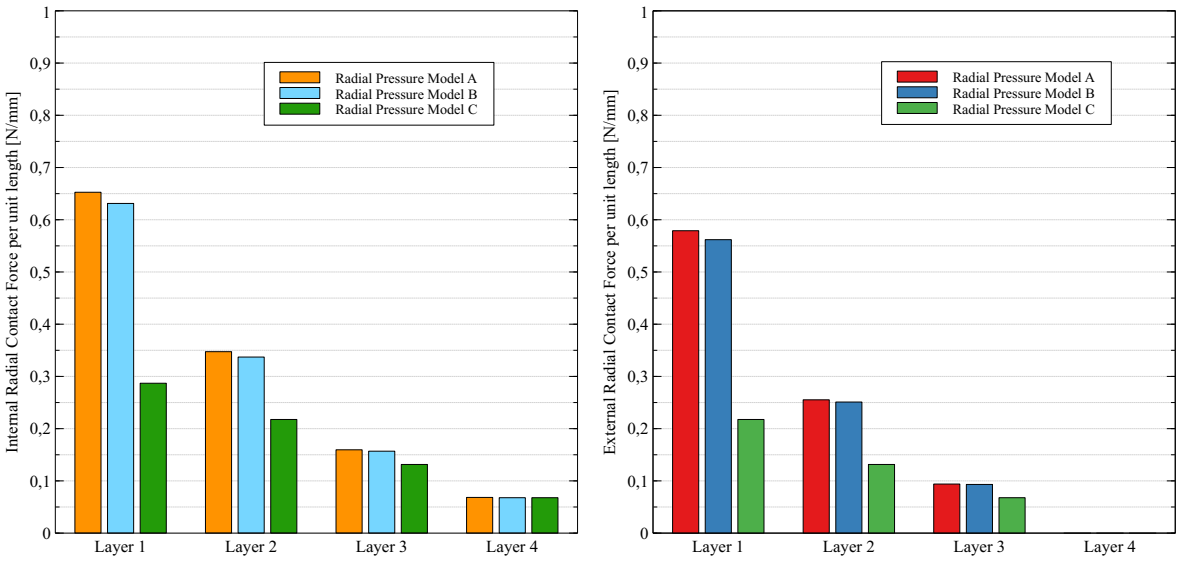

(a) (b)

Figure 3.22. ACSR 48/7 Gatineau: plot of the internal (a) and external (b) radial contact forces per unit of length for the four layers of wires.

ACSR 54/7

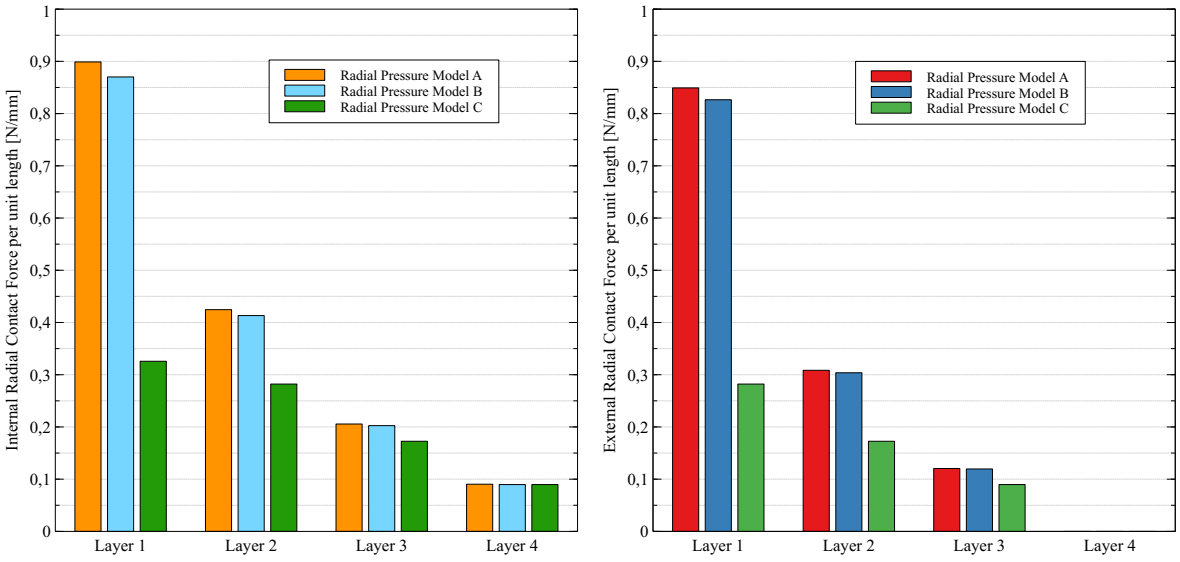

(a) (b)

Figure 3.23. ACSR 54/7 Duck: plot of the internal (a) and external (b) radial contact forces per unit of length for the four layers of wires.

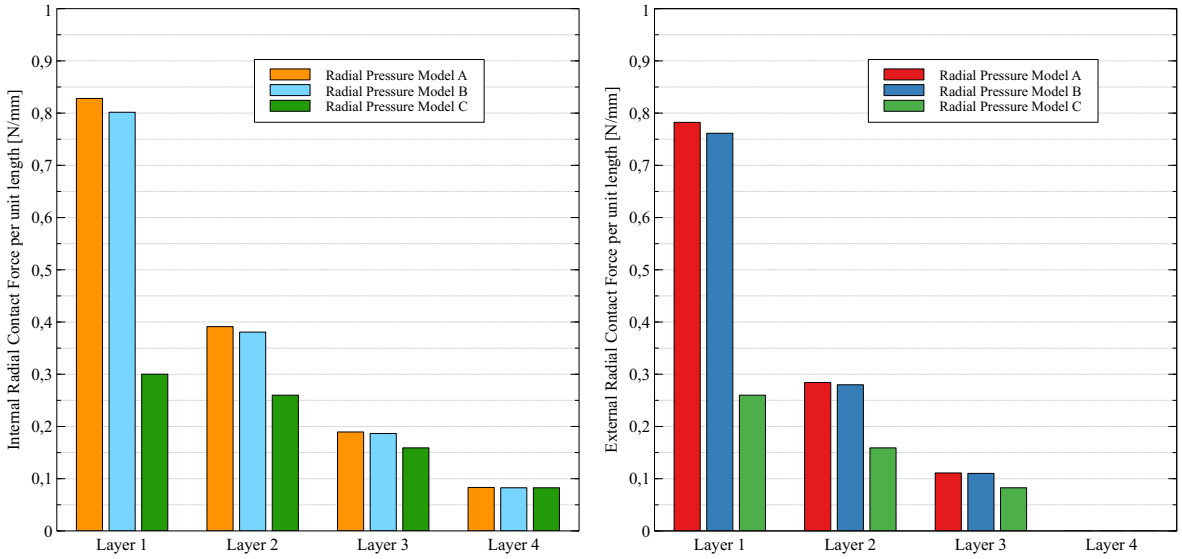

(a) (b)

Figure 3.24. ACSR 54/7 Crow: plot of the internal (a) and external (b) radial contact forces per unit of length for the four layers of wires.

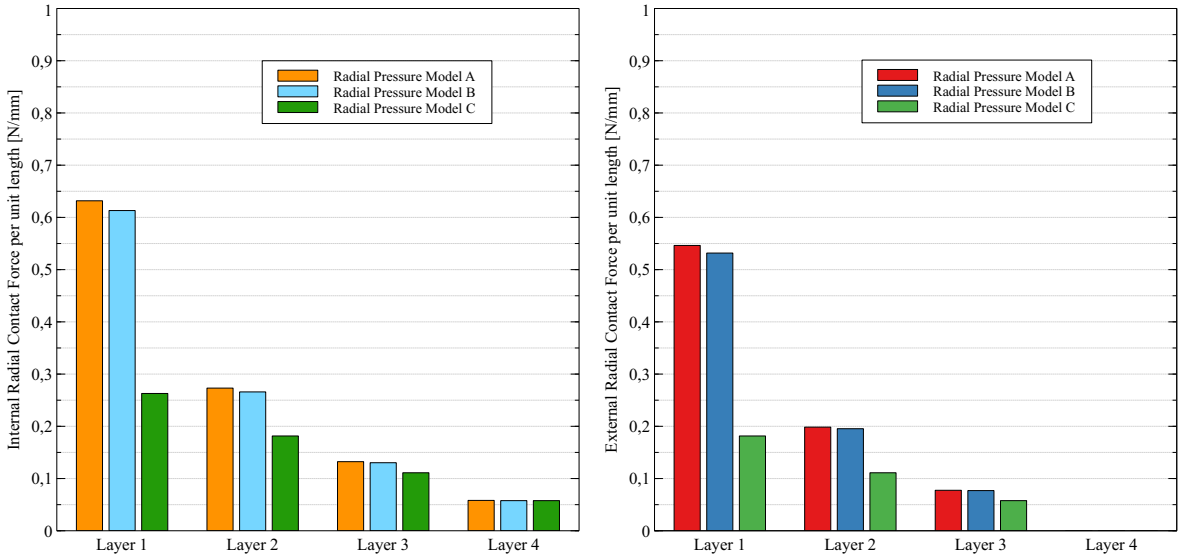

(a) (b)

Figure 3.25. ACSR 54/7 Curlew: plot of the internal (a) and external (b) radial contact forces per unit of length for the four layers of wires.

ACSR 72/7

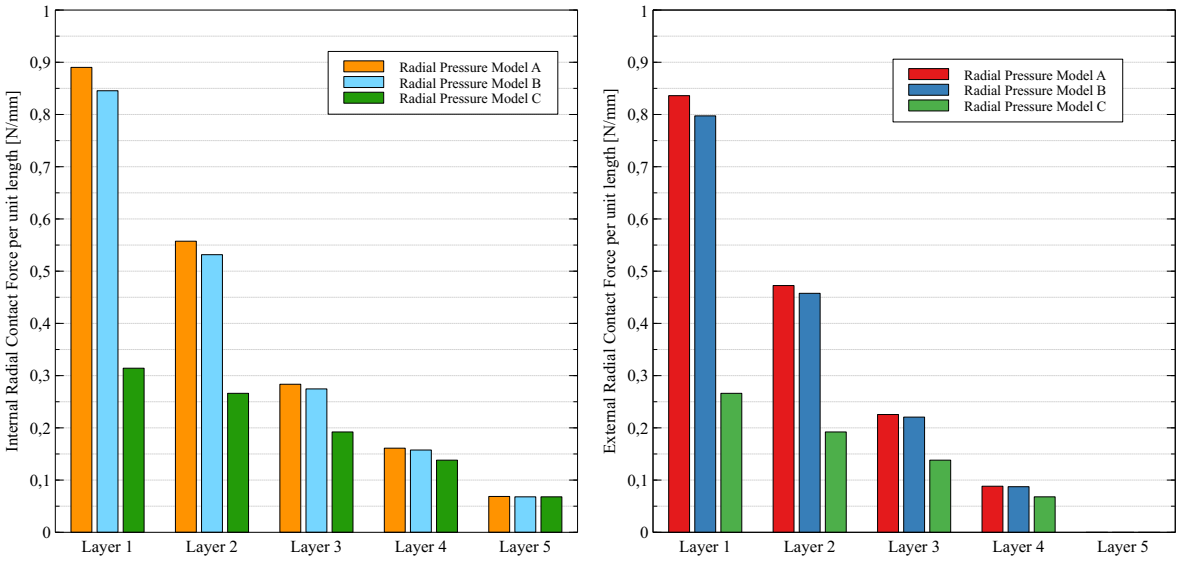

(a) (b)

Figure 3.26. ACSR 72/7 Falcon: plot of the internal (a) and external (b) radial contact forces per unit of length for the five layers of wires.

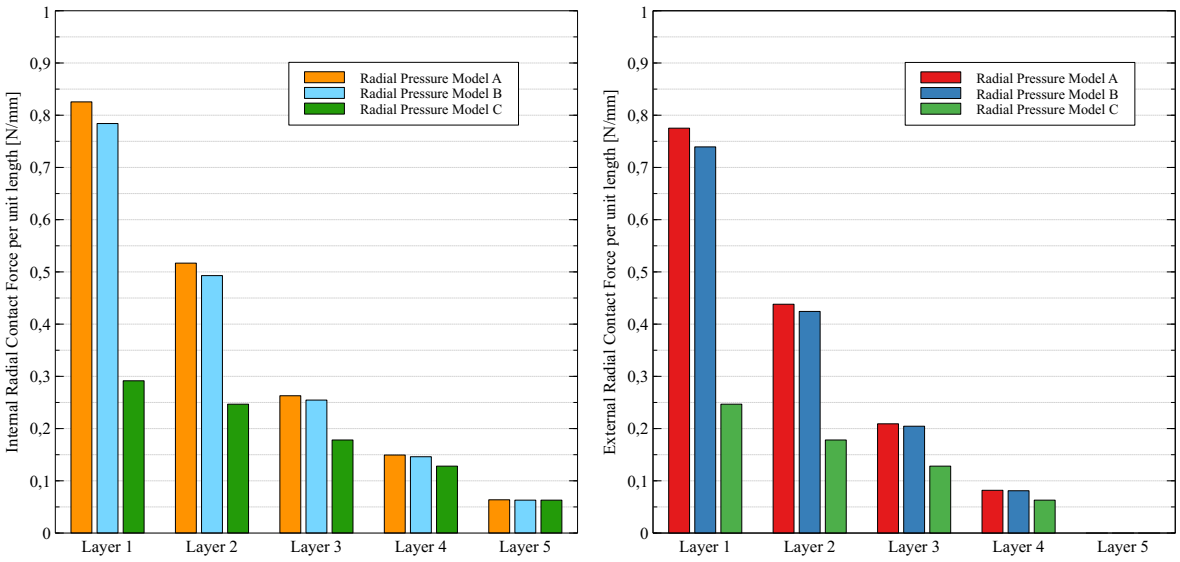

(a) (b)

Figure 3.27. ACSR 72/7 Nelson I: plot of the internal (a) and external (b) radial contact forces per unit of length for the five layers of wires.

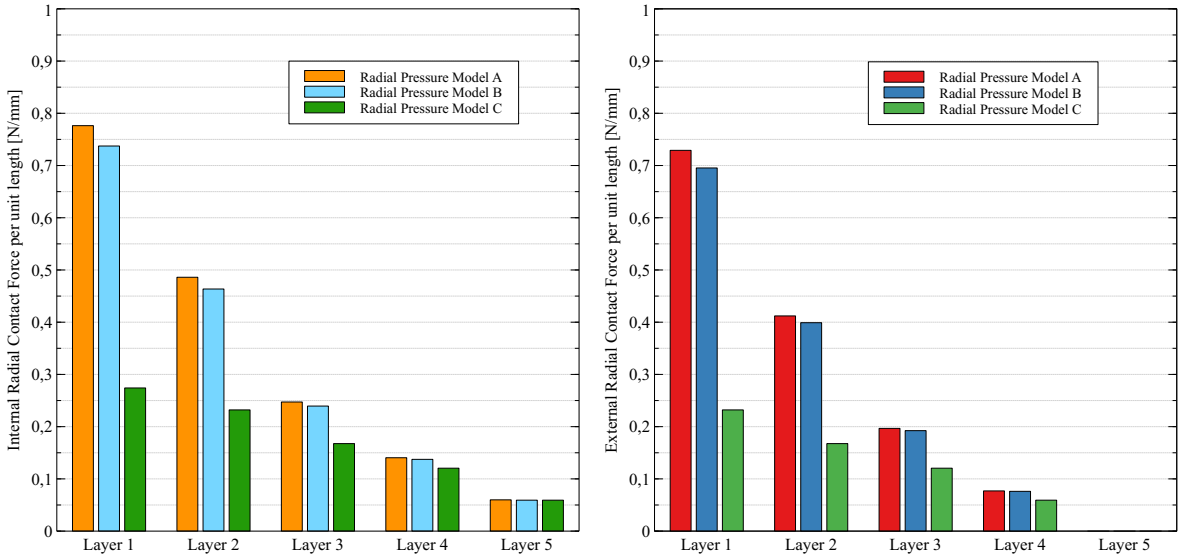

(a) (b)

Figure 3.28. ACSR 72/7 Nelson II: plot of the internal (a) and external (b) radial contact forces per unit of length for the five layers of wires.

From the previous figures, interesting conclusions can be drawn:

- As a trivial consideration, all the pressures models correctly predict null external radial forces per unit of length on the outermost layer of wires;
- Radial Pressures Model C is systematically underestimating both the external and internal radial contact forces per unit of length at each layer of the conductors cross-sections, except for the internal radial force per unit of length of the outermost layer, that coincides to the one predicted by the Pressure Model B for all the conductor typologies. As a particular case, 6/1 conductors present just one layer of wires, for which pressure models B and C give the same results;
- Radial Pressures Model A and B are predicting quite close results in every situation. The difference between their predictions is mostly important in the innermost layer, where the influence of correction coefficients c^{int} and c^{ext} is higher;
- The relative difference between the predictions of Radial Pressures Models A and B is practically constant for each layers of conductors belonging to the same stranding class, both for the internal and external radial contact forces per unit of length. The maximum relative difference is encountered for the internal redial contact force per unit of length of 72/7 ACSR conductors and it is equal to 5.02%;
- Radial Pressures Model B is way more simple than P.M. A but can still be conveniently applied with good approximation for the analysis of multillayer strands, predicting the internal and external radial contact forces per unit of length with a relative percentage difference respectively of 5.02% and 4.63% at most (corresponding to the case of ACSR 72/7 conductors, layer $j = 1$). In the case of ACSR 54/7 conductors, such difference lowers down to 3.20% and 2.67% respectively for the internal and external contact forces per unit of length of the first layer of wires. Furthermore, such relative difference reaches its minimum for the outermost layer of the analyzed conductors, being less than 1% for both the external and internal radial forces per unit of length;

- The relative difference between Radial Pressures Models A and C is practically constant for each layers of conductors belonging to the same stranding class, both for the internal and external radial contact forces per unit of length. Such difference is particularly relevant for the innermost layer of multilayer strands. For ACSR 54/7 and 72/7 conductors, P.M. A predicts forces per unit length even 3 times larger than the ones predicted by P.M. C, that is, a relative difference of 64.70% and 68.17% respectively for the internal and external radial forces per unit of length in the case of 72/7 conductors. Such values becomes 63.76% and 66.78% in the case of 54/7 conductors (respectively for the internal and external contact forces per unit of length of the first layer of wires);
- Due to its more complex formulation, Pressures Model A appears to be the most accurate among the three that were compared. In fact, a closer agreement was generally found between the FEM results and the predictions obtained through the Pressures Model A, especially for inner layers of wires.

3.4.3 Approximated Radial Contact Forces

In this Subsection, the approximated radial contact forces acting at the interfaces of the different layers of wires are computed.
In particular, the approximated values of such contact forces can be obtained by multiplying the radial force per unit of length computed assuming a line contact situation (i.e. results obtained in Subsection 3.4.2) by the distance between contact points at a given interface (that was computed in Subsection 3.2.2 for each interface of the various conductors).
Three different models for the radial pressures transmission were used, as well as three different formulae for the computation of the distances between contact points (Eqts. 3.20, 3.21 and 3.22).
This means that a total of 9 possibilities for the estimation of the radial contact forces (both internal and external) at each interface arise.
Results of the approximated radial contact forces are collected in the bar charts shown in Fig.s 3.35-3.52. Each figure collects the results of either the external approximated forces or the internal approximated forces of a specific ACSR conductor, computed by applying the three radial pressure models (namely P.M. A, B and C) and the three distance formulae (Carodu's, Chouinard's and Papailou's ditances). Each subplot refers to a specif layer of that conductor.
Results of the approximated radial contact forces are also reported in tabular form for the sake of convenience in Appendix D.

Remarks

It is worth noticing that:

- distances between contact points are not computed for the case of 6/1 conductors and for the first layer (i.e $i = 1$) of multilayer strands. This is due to the fact that contact patches between the core and the first layer of wires are assumed to be continuous and not pointwise distributed (see Sec. 3.2.2 for further details). As a consequence, approximated radial contact forces are not computed for such cases;

- external approximated radial contact forces on the outermost layer of wires are null, as a trivial consequence of the fulfillment of the different radial pressure models equilibrium equations. For this reason, external radial contact forces for the outermost layer of each conductor are not reported in the following figures, being zero;

- approximated radial contact forces are computed by considering the generic strand loaded with an axial force of 1 kN. Due to the linearity property of the axial-torsional problem, the following results can be easily scaled up in order to obtain the corresponding values of the approximated radial contact forces for any magnitude of the axial load N_s acting on the strand;

- approximated radial contact forces are here computed by passing from the radial contact forces per unit of length (i.e. f_r^{int} and f_r^{ext}) to the normal contact forces acting on contact points between adjacent layers (direct consequence of the alternate lays of multilayer conductors). For this reason, internal and external approximated radial forces will be referred to as P^{int} and P^{ext}, meaning that they act on contact points between conductor layers.

ACSR 26/7

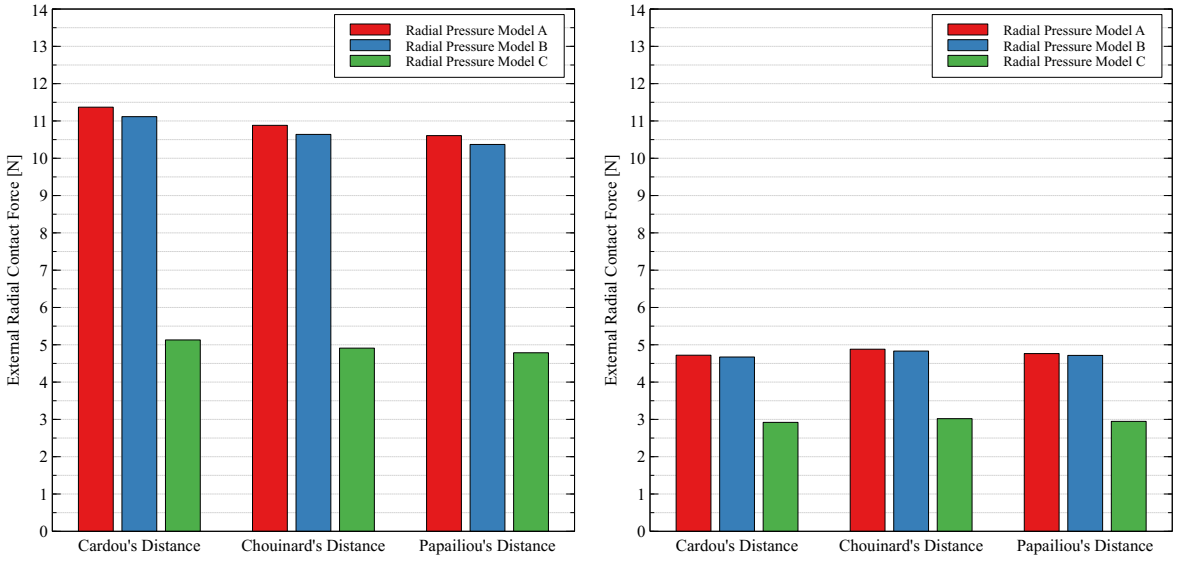

(a) Layer 1. (b) Layer 2.

Figure 3.29. ACSR 26/7 Partridge: plot of P^{ext} for the different layers.

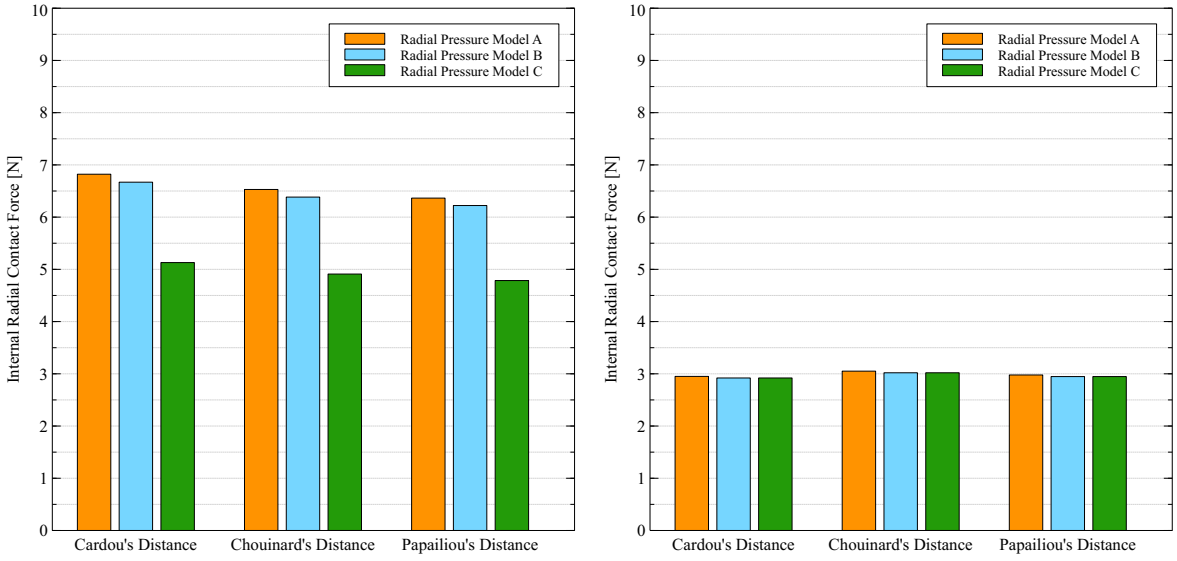

(a) Layer 2. (b) Layer 3.

Figure 3.30. ACSR 26/7 Partridge: plot of P^{int} for the different layers.

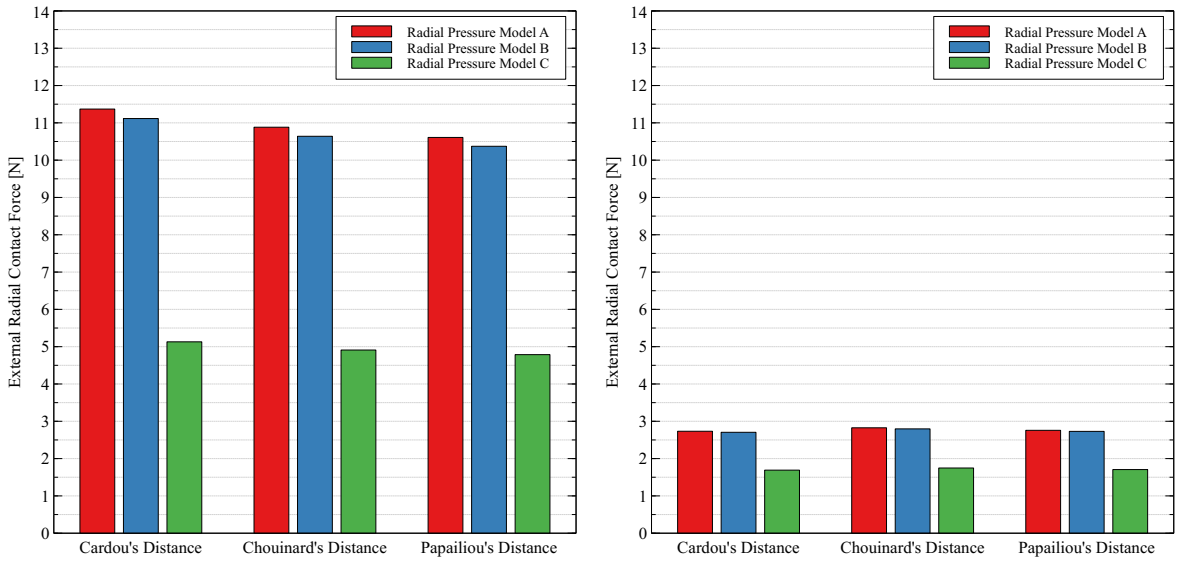

(a) Layer 1. (b) Layer 2.

Figure 3.31. ACSR 26/7 Hawk: plot of P^{ext} for the different layers.

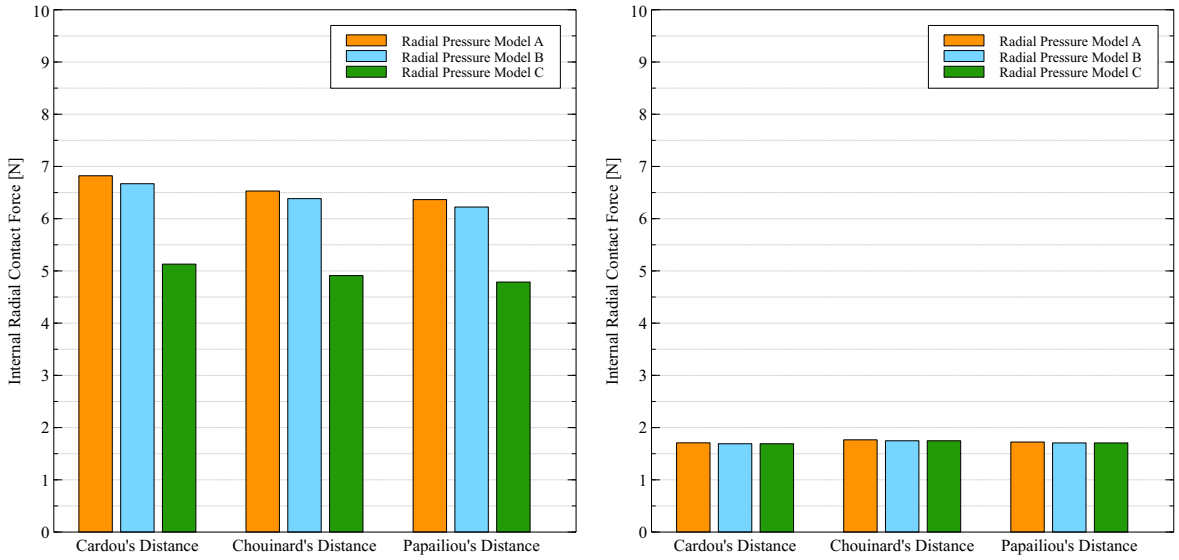

(a) Layer 2. (b) Layer 3.

Figure 3.32. ACSR 26/7 Hawk: plot of P^{int} for the different layers.

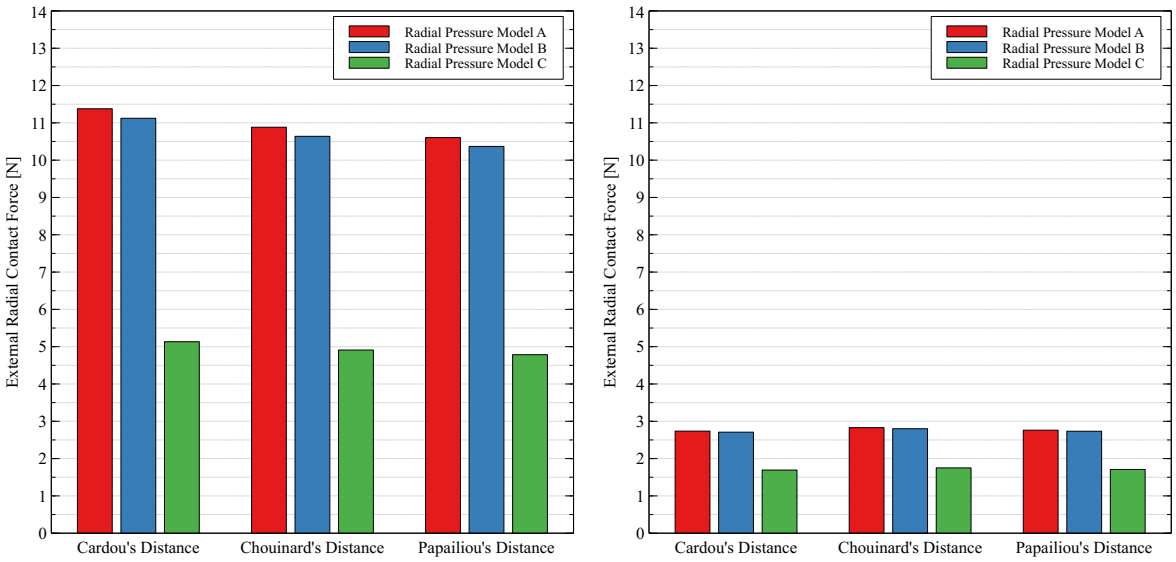

(a) Layer 1. (b) Layer 2.

Figure 3.33. ACSR 26/7 Drake: plot of P^{ext} for the different layers.

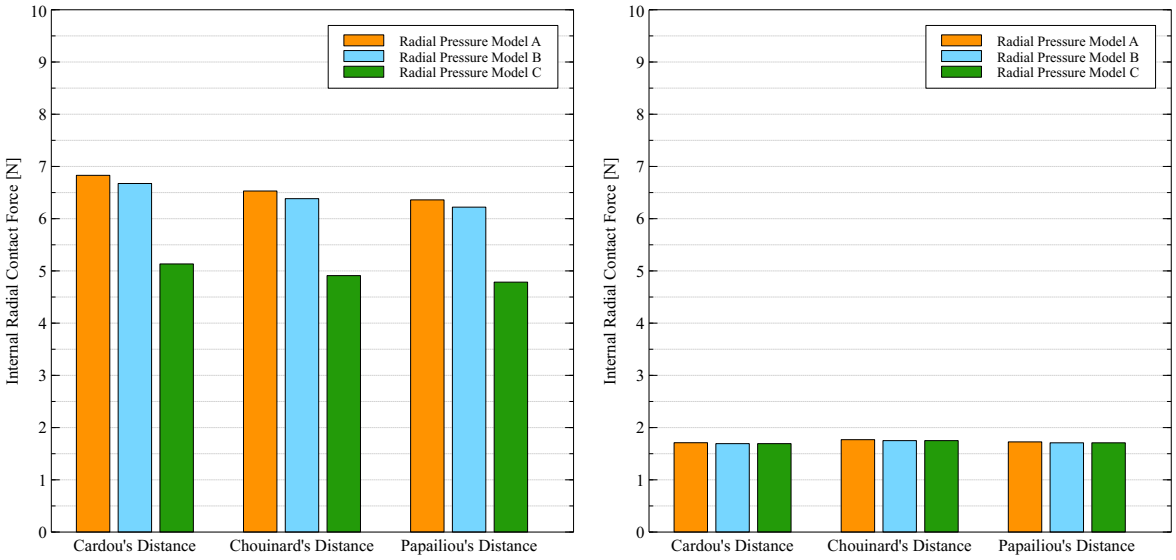

(a) Layer 2. (b) Layer 3.

Figure 3.34. ACSR 26/7 Drake: plot of P^{int} for the different layers.

ACSR 48/7

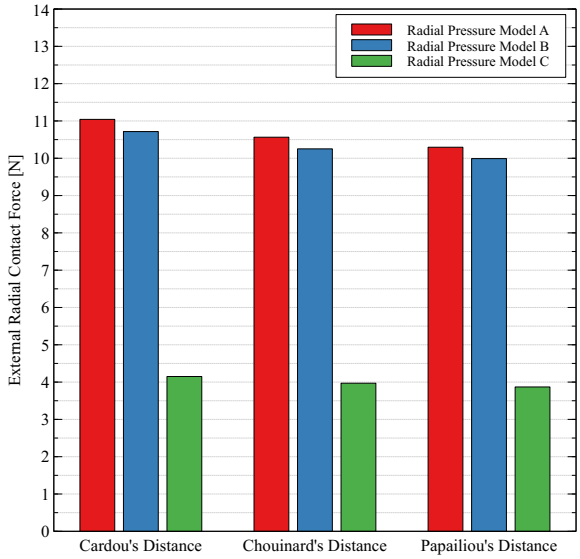

(a) Layer 1.

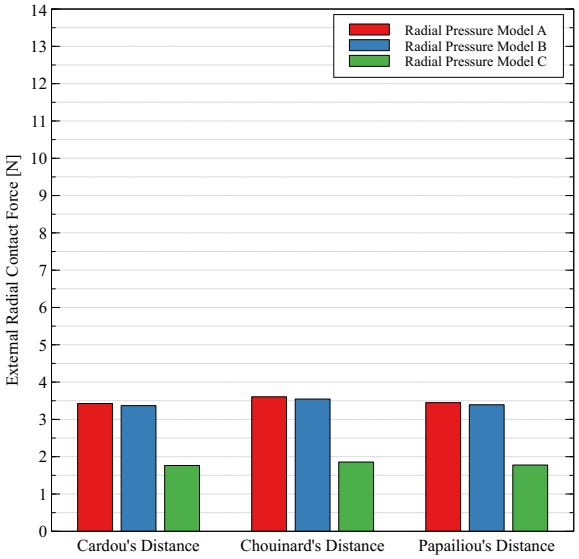

(b) Layer 2.

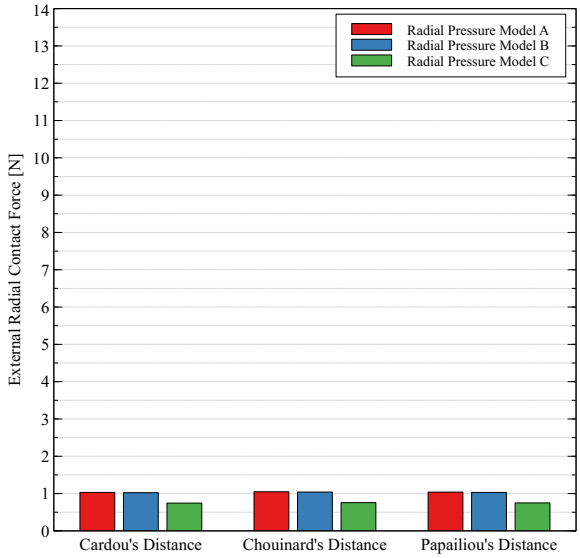

(c) Layer 3.

Figure 3.35. ACSR 48/7 Bersfort: plot of P^{ext} for the different layers.

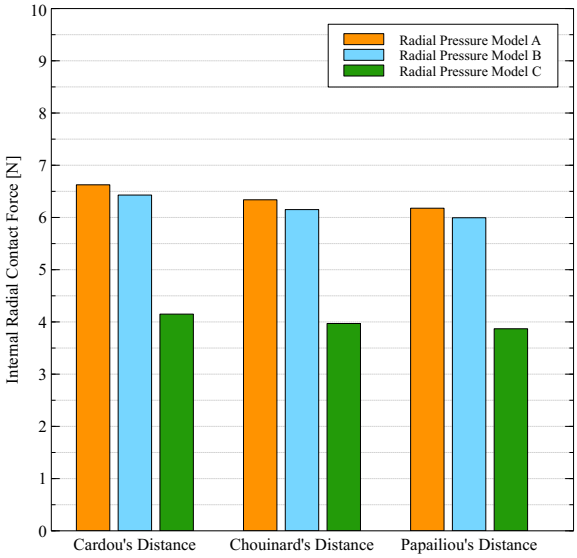

(a) Layer 2.

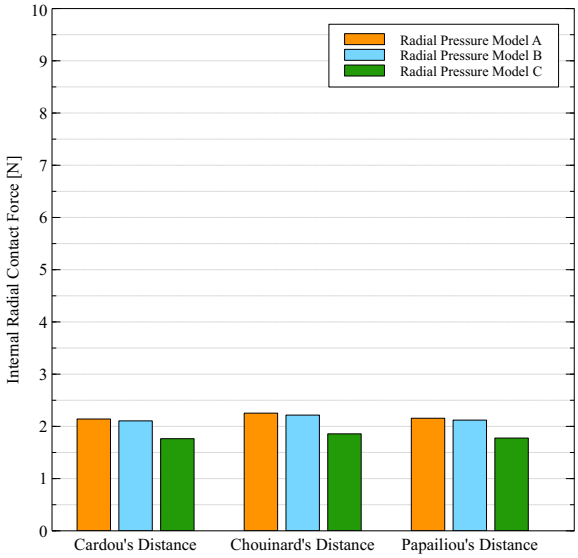

(b) Layer 3.

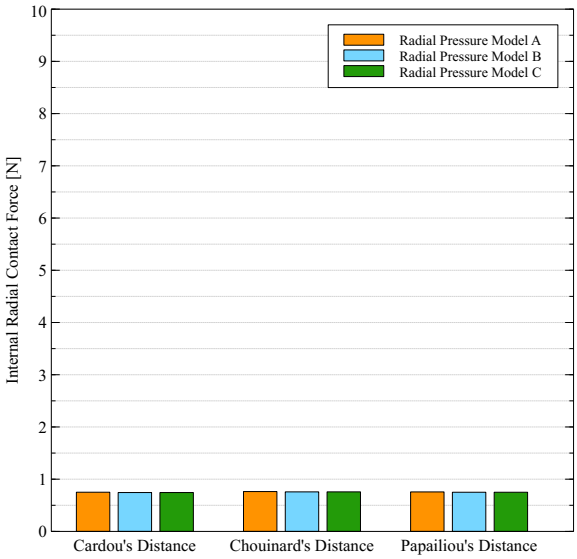

(c) Layer 4.

Figure 3.36. ACSR 48/7 Bersfort: plot of P^{int} for the different layers.

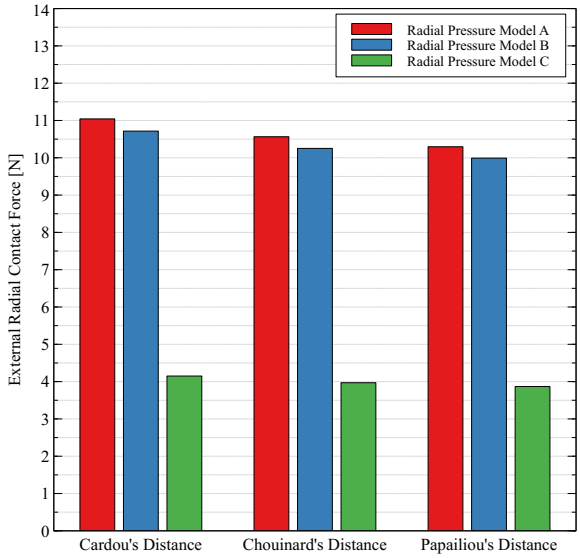

(a) Layer 1.

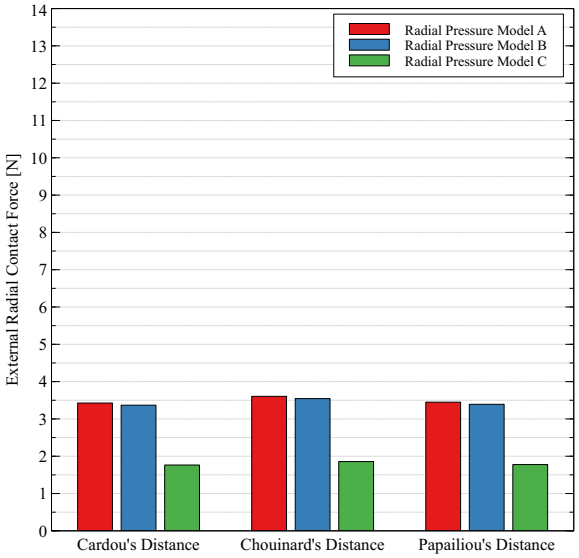

(b) Layer 2.

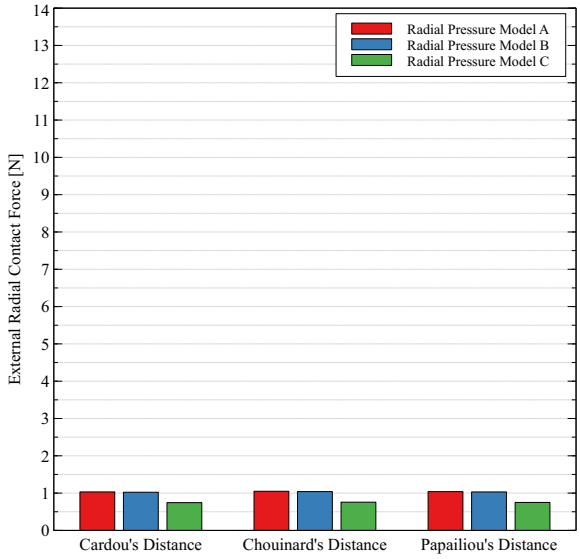

(c) Layer 3.

Figure 3.37. ACSR 48/7 Carillon: plot of P^{ext} for the different layers.

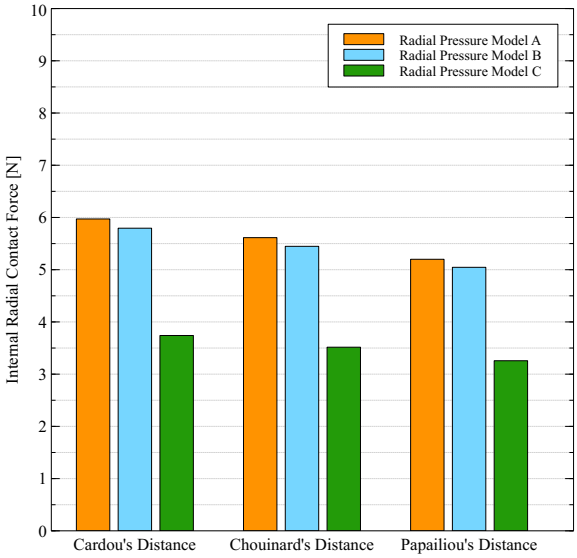

(a) Layer 2.

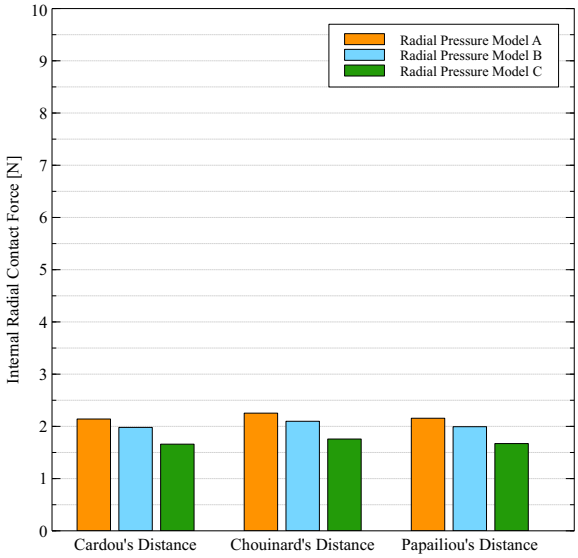

(b) Layer 3.

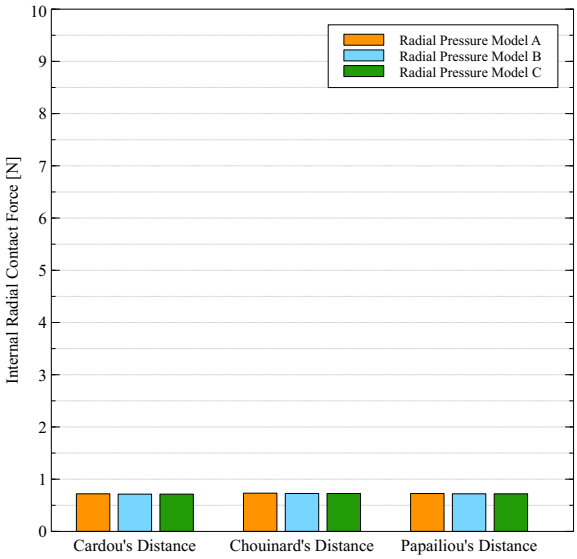

(c) Layer 4.

Figure 3.38. ACSR 48/7 Carillon: plot of P^{int} for the different layers.

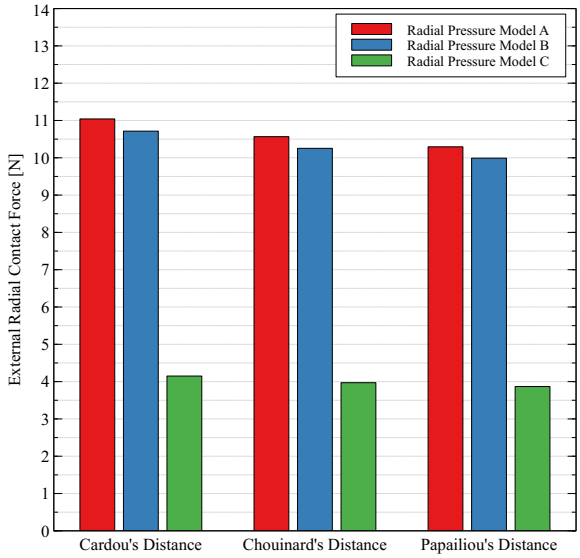

(a) Layer 1.

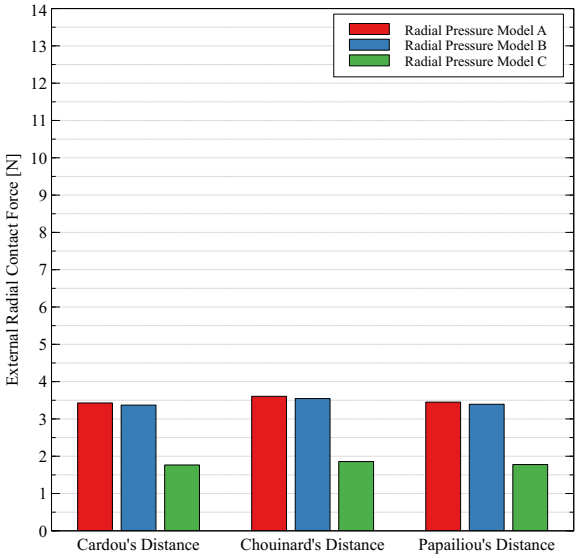

(b) Layer 2.

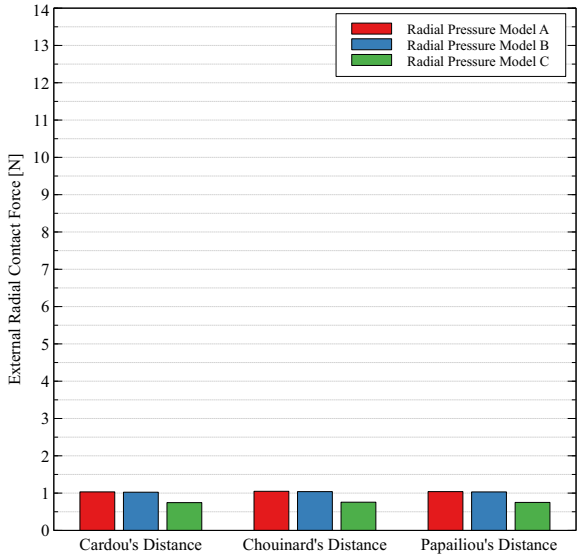

(c) Layer 3.

Figure 3.39. ACSR 48/7 Gatineau: plot of P^{ext} for the different layers.

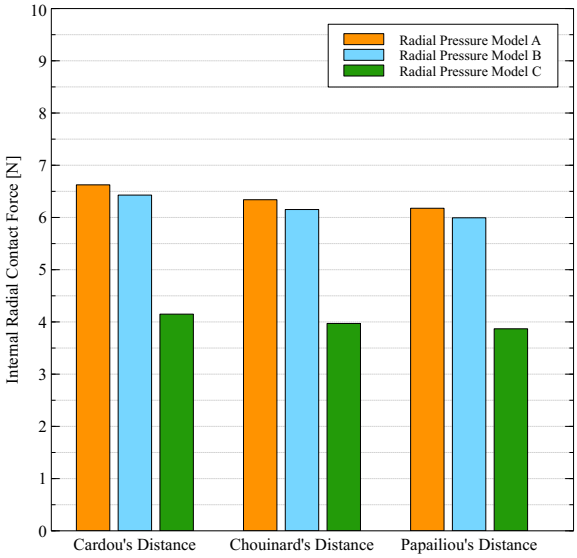

(a) Layer 2.

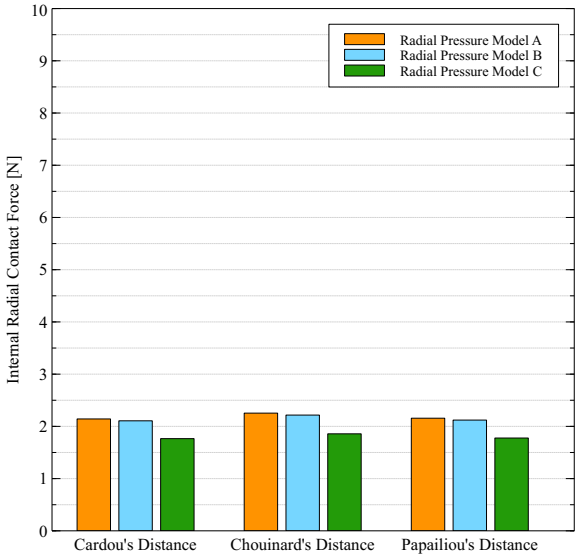

(b) Layer 3.

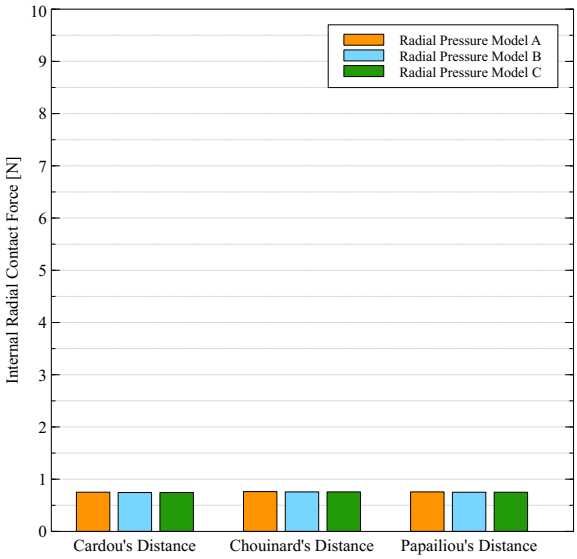

(c) Layer 4.

Figure 3.40. ACSR 48/7 Gatineau: plot of P^{int} for the different layers.

ACSR 54/7

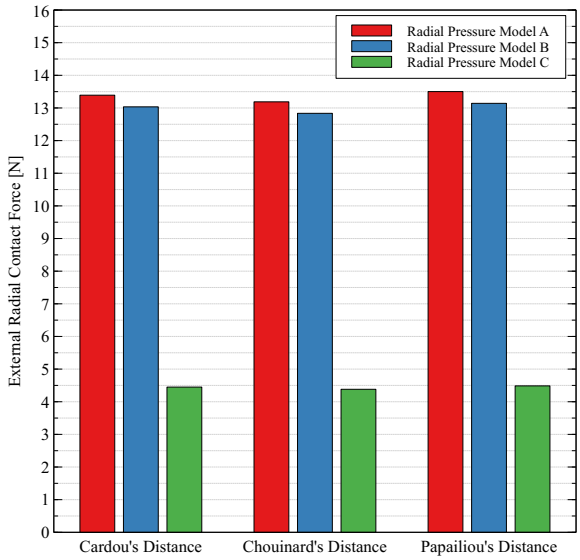

(a) Layer 1.

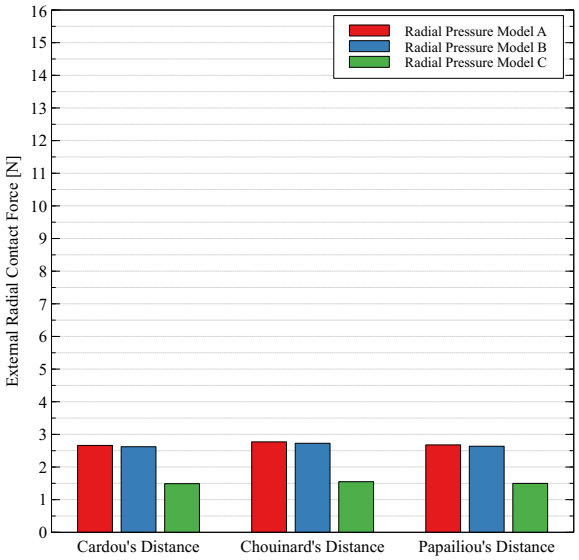

(b) Layer 2.

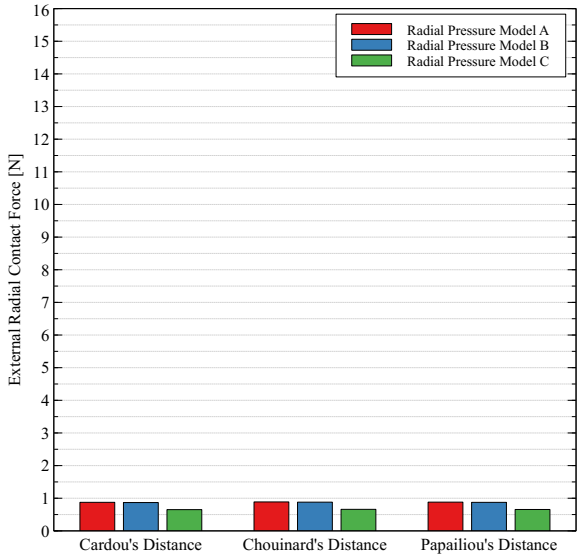

(c) Layer 3.

Figure 3.41. ACSR 54/7 Duck: plot of P^{ext} for the different layers.

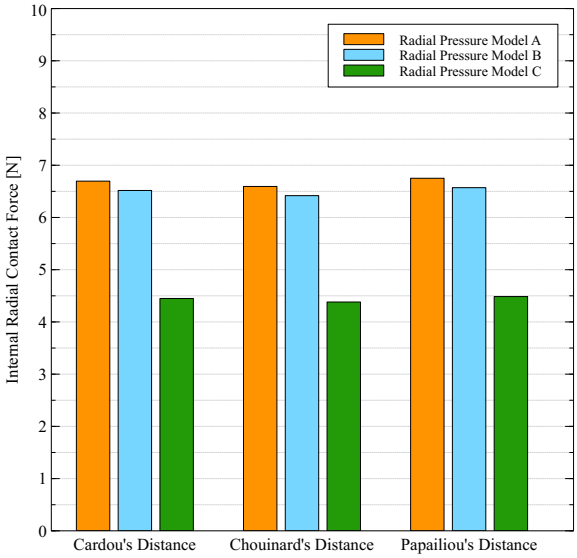

(a) Layer 2.

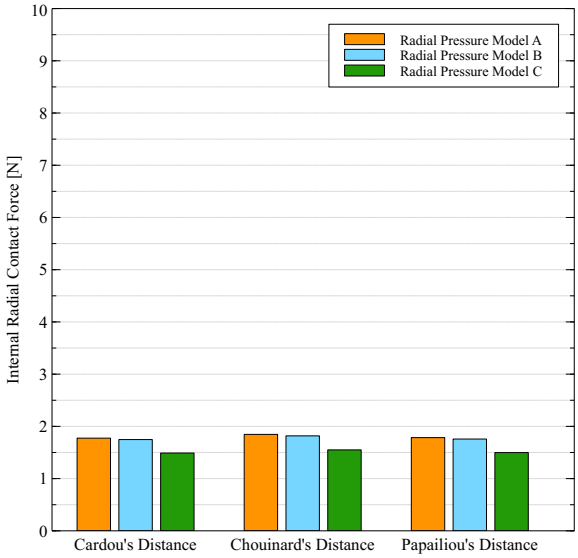

(b) Layer 3.

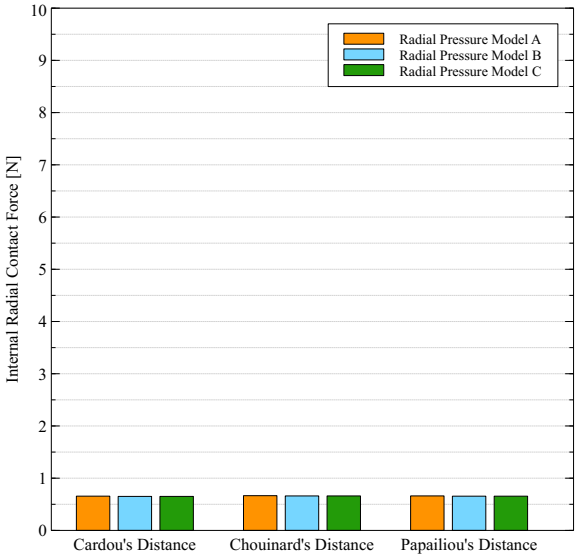

(c) Layer 4.

Figure 3.42. ACSR 54/7 Duck: plot of P^{int} for the different layers.

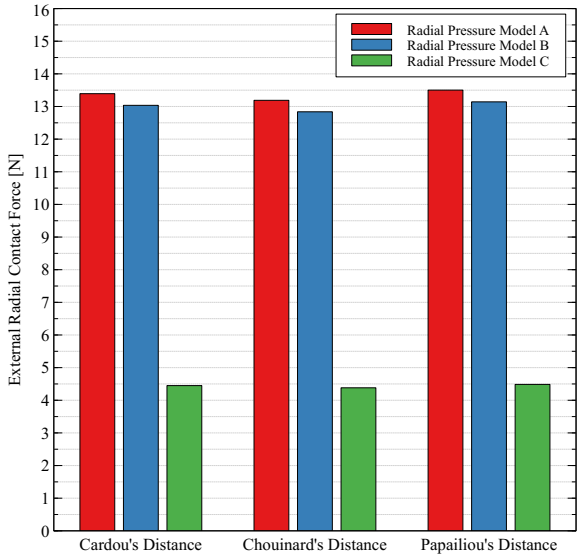

(a) Layer 1.

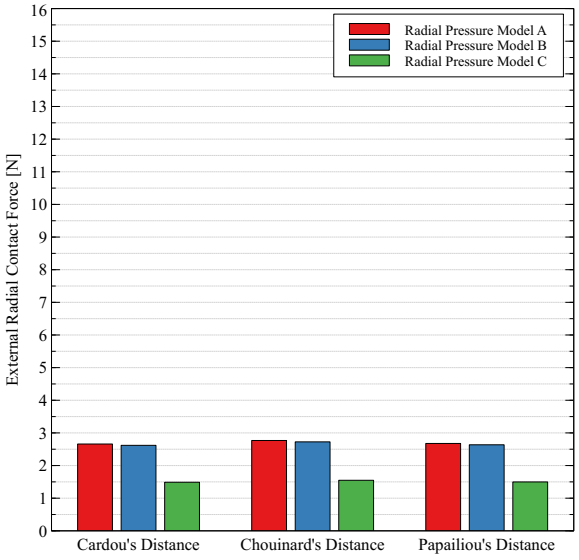

(b) Layer 2.

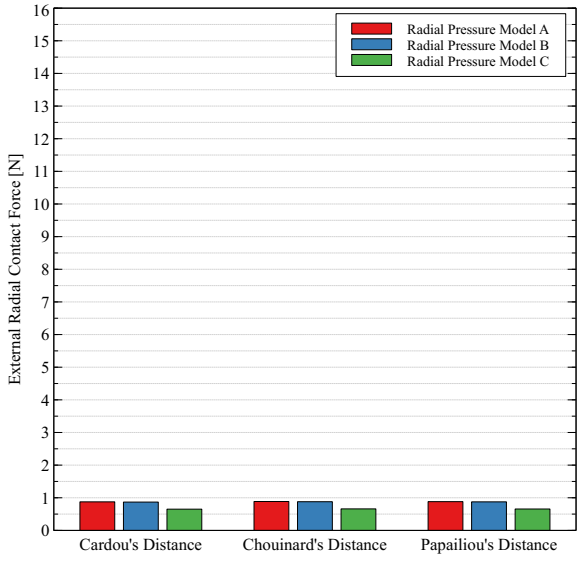

(c) Layer 3.

Figure 3.43. ACSR 54/7 Crow: plot of P^{ext} for the different layers.

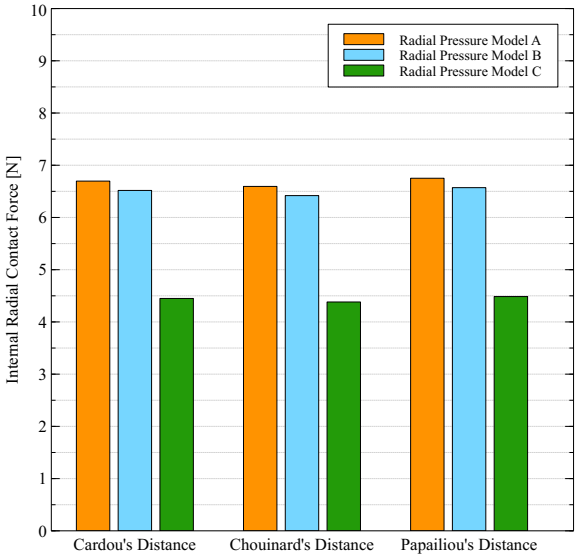

(a) Layer 2.

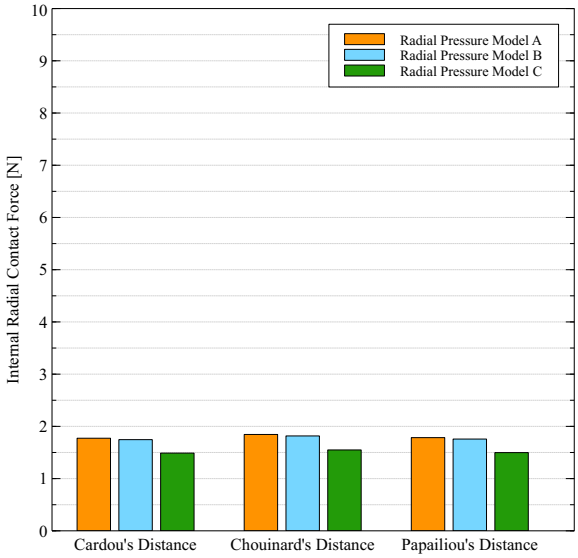

(b) Layer 3.

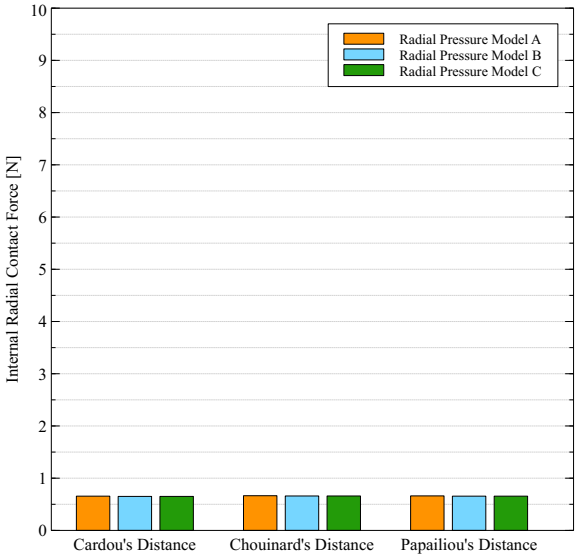

(c) Layer 4.

Figure 3.44. ACSR 54/7 Crow: plot of P^{int} for the different layers.

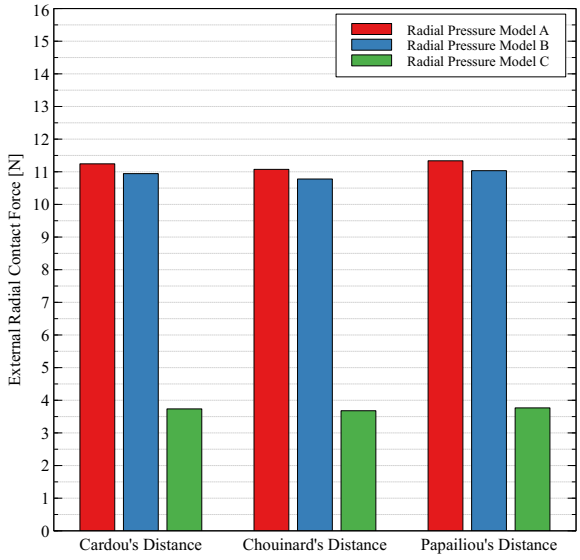

(a) Layer 1.

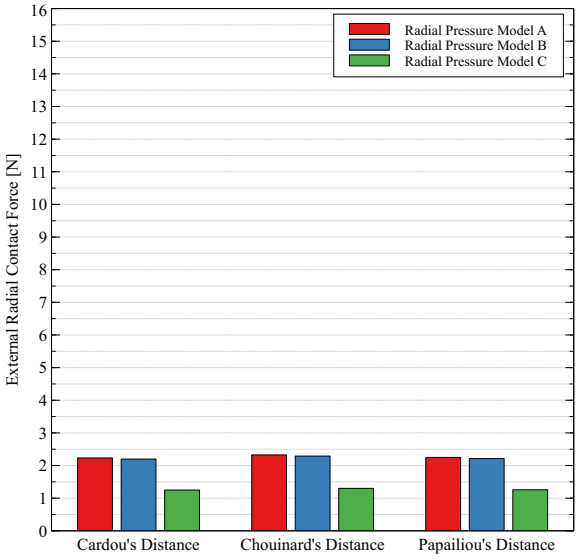

(b) Layer 2.

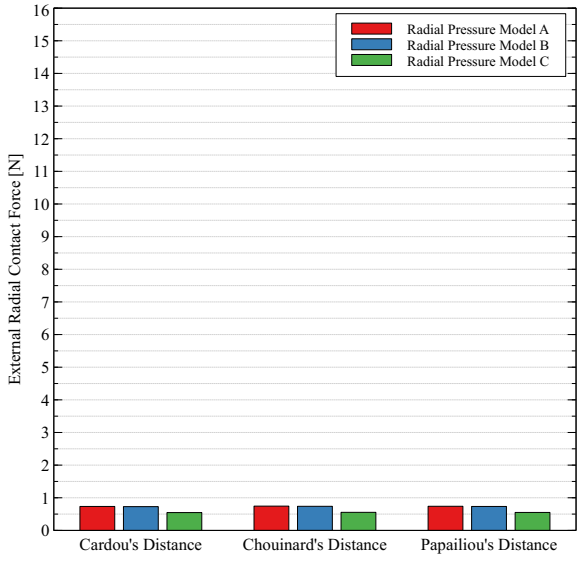

(c) Layer 3.

Figure 3.45. ACSR 54/7 Curlew: plot of P^{ext} for the different layers.

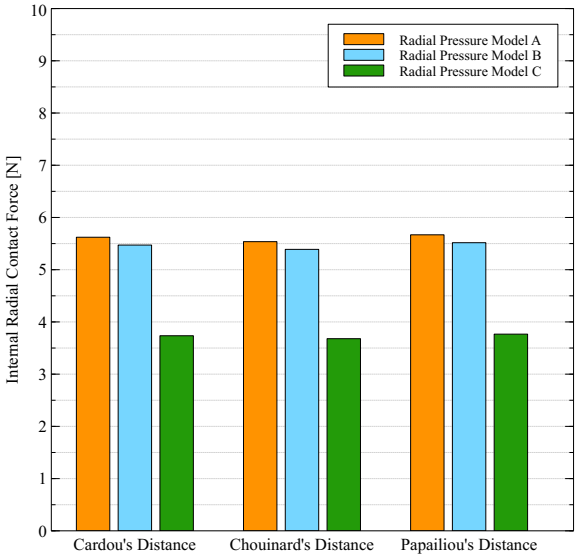

(a) Layer 2.

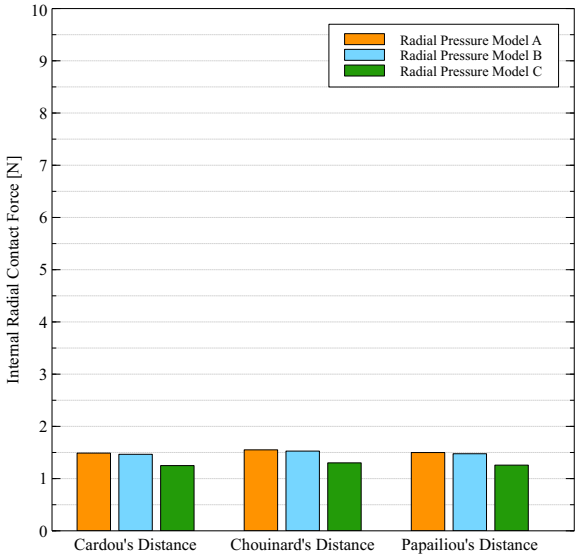

(b) Layer 3.

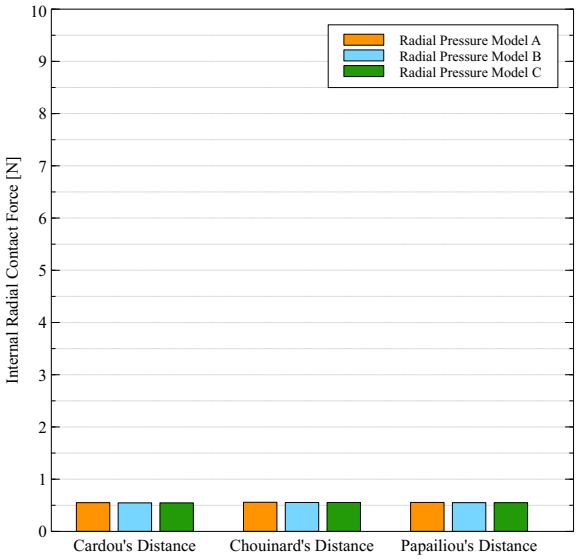

(c) Layer 4.

Figure 3.46. ACSR 54/7 Curlew: plot of P^{int} for the different layers.

ACSR 72/7

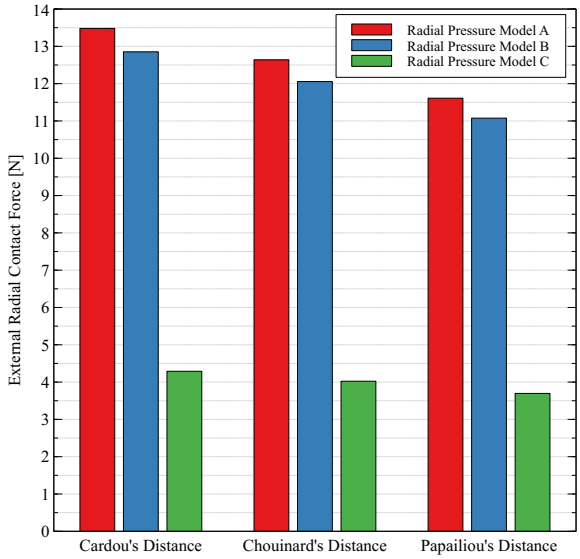

(a) Layer 1.

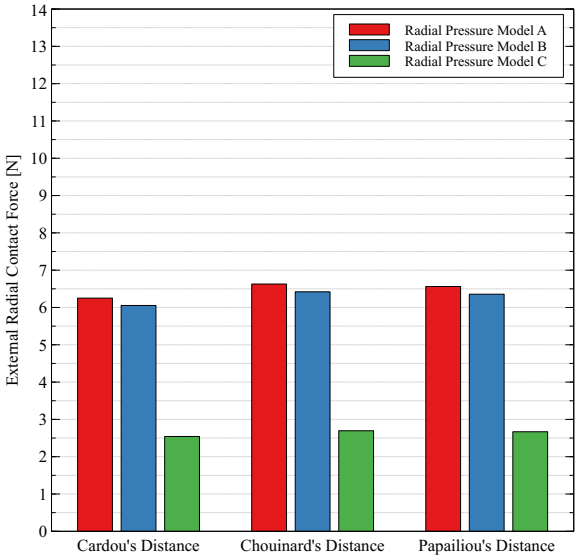

(b) Layer 2.

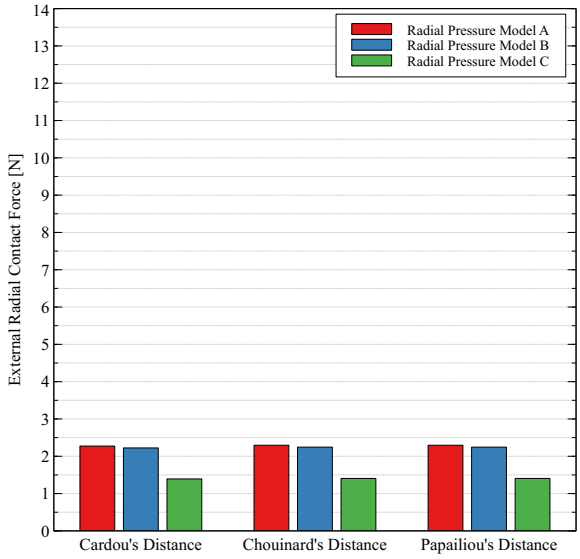

(c) Layer 3.

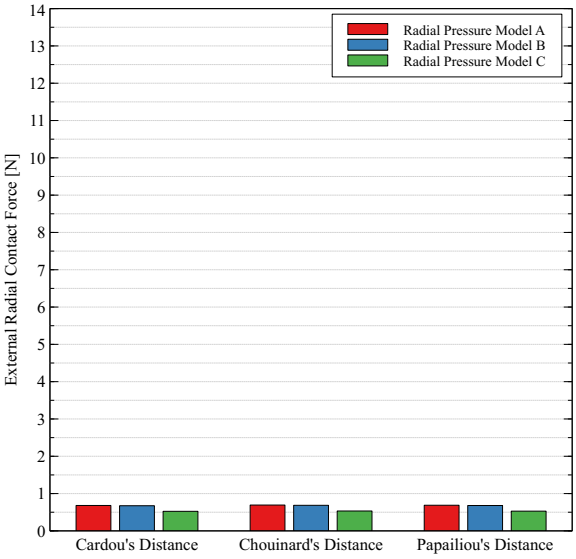

(d) Layer 4.

Figure 3.47. ACSR 72/7 Falcon: plot of P^{ext} for the different layers.

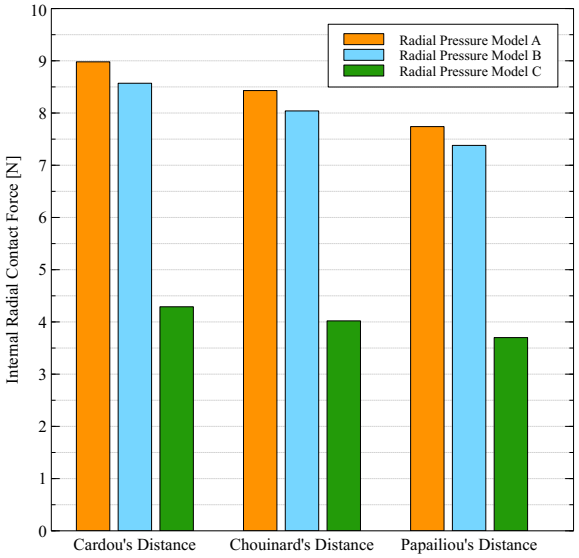

(a) Layer 2.

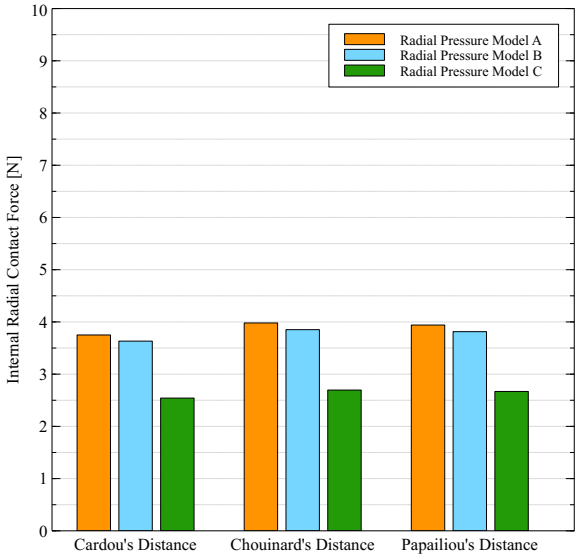

(b) Layer 3.

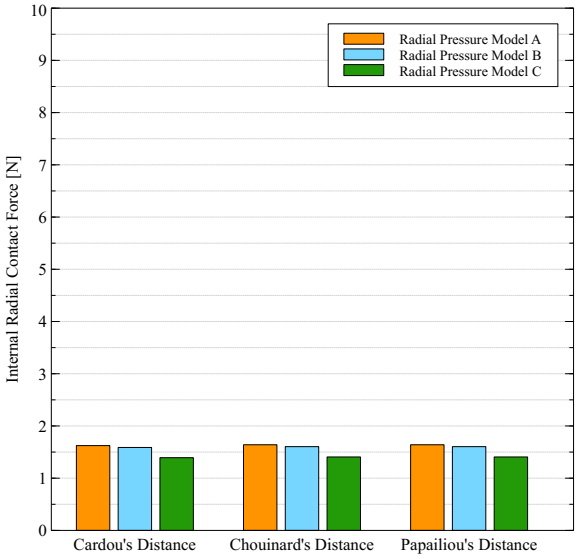

(c) Layer 4.

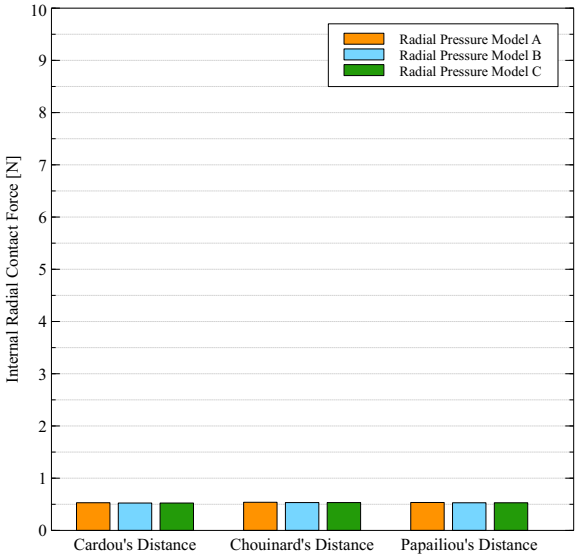

(d) Layer 5.

Figure 3.48. ACSR 72/7 Falcon: plot of P^{int} for the different layers.

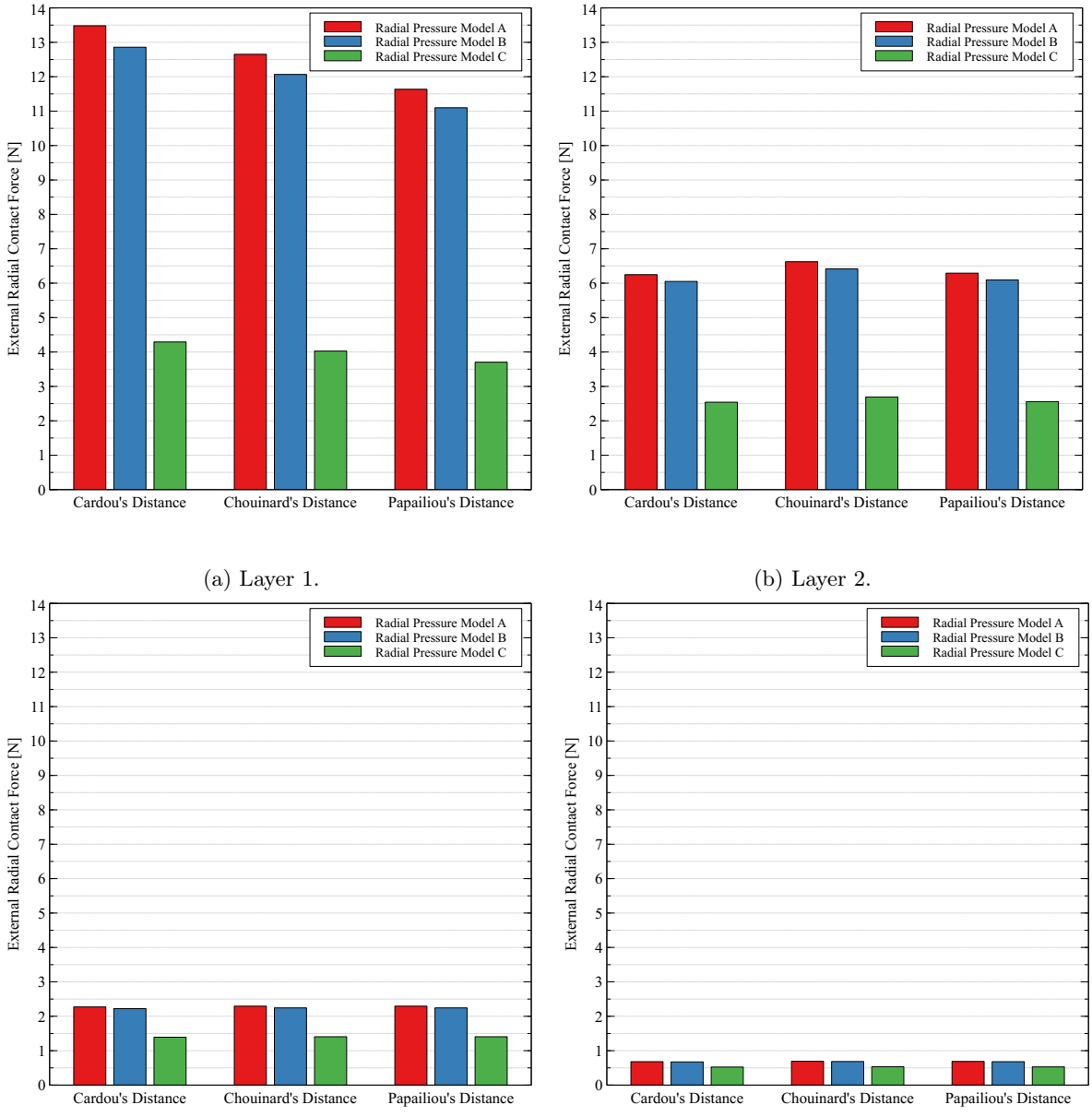

(a) Layer 1.

(b) Layer 2.

(c) Layer 3.

(d) Layer 4.

Figure 3.49. ACSR 72/7 Nelson I: plot of P^{ext} for the different layers.

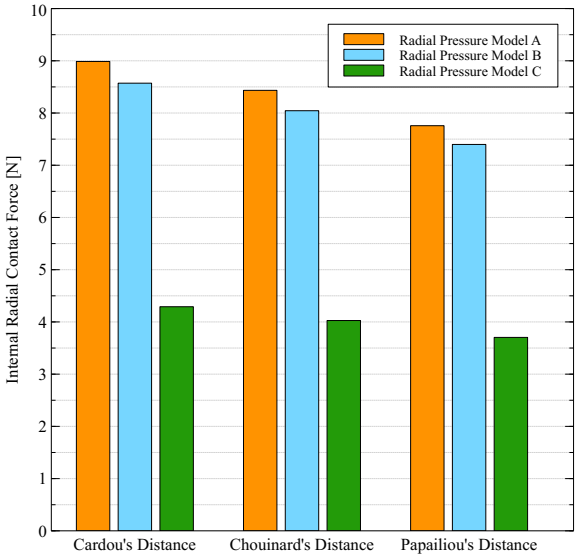

(a) Layer 2.

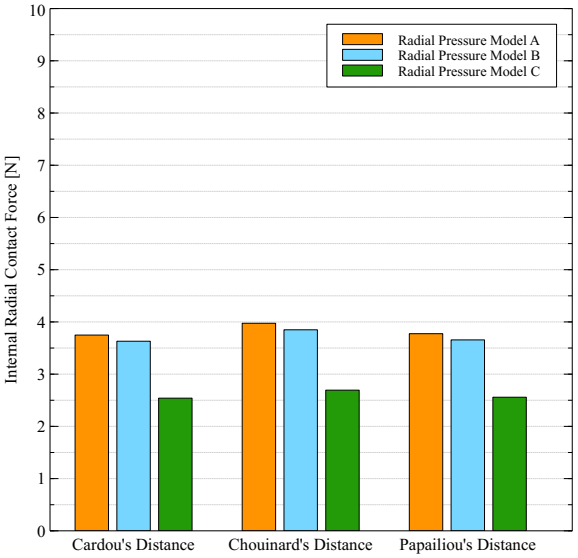

(b) Layer 3.

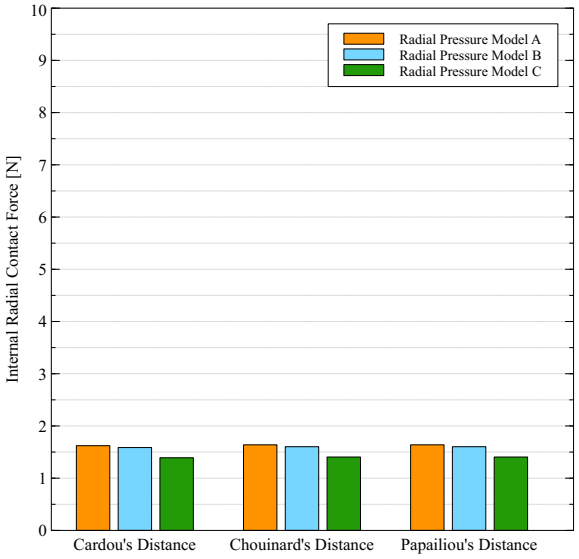

(c) Layer 4.

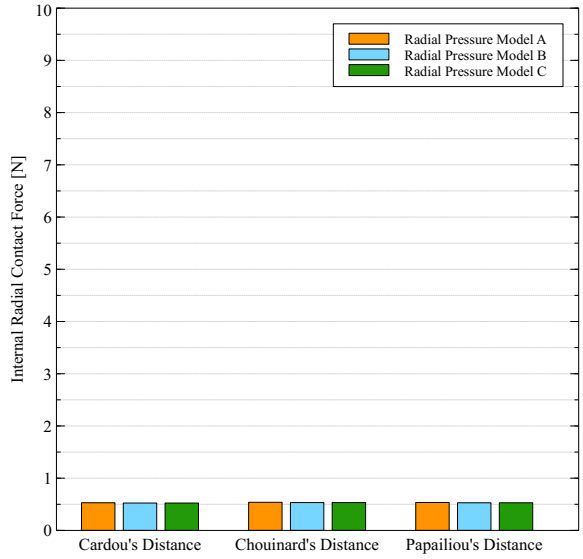

(d) Layer 5.

Figure 3.50. ACSR 72/7 Nelson I: plot of P^{int} for the different layers.

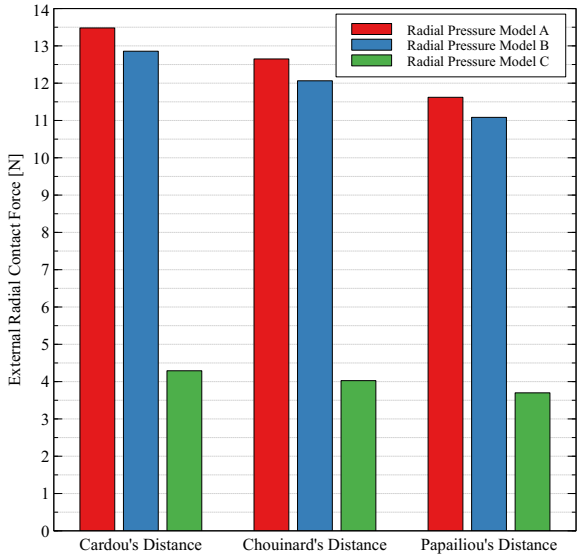

(a) Layer 1.

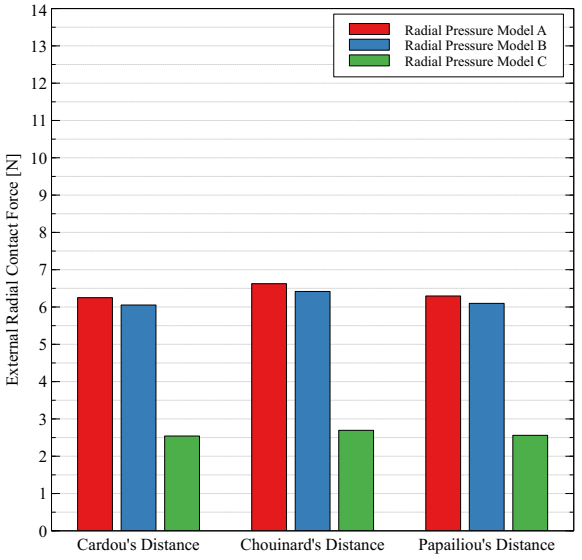

(b) Layer 2.

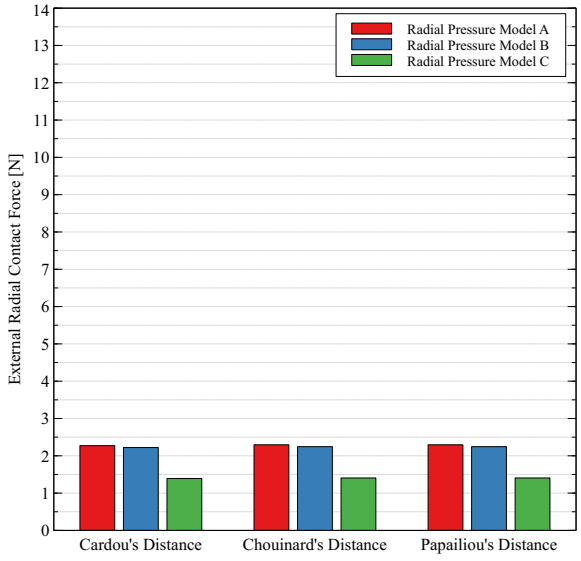

(c) Layer 3.

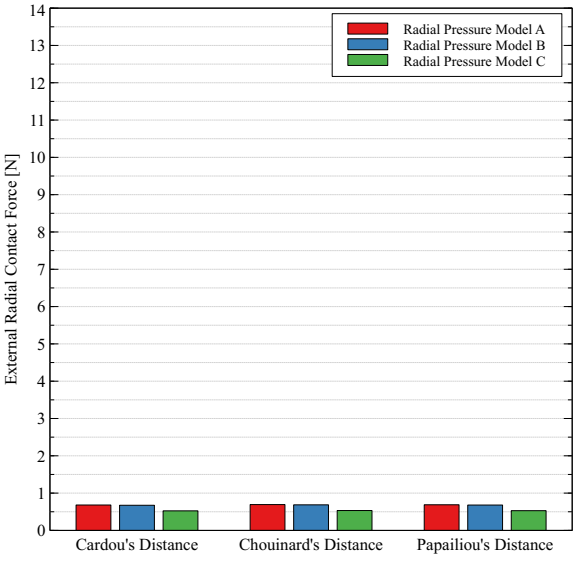

(d) Layer 4.

Figure 3.51. ACSR 72/7 Nelson II: plot of P^{ext} for the different layers.

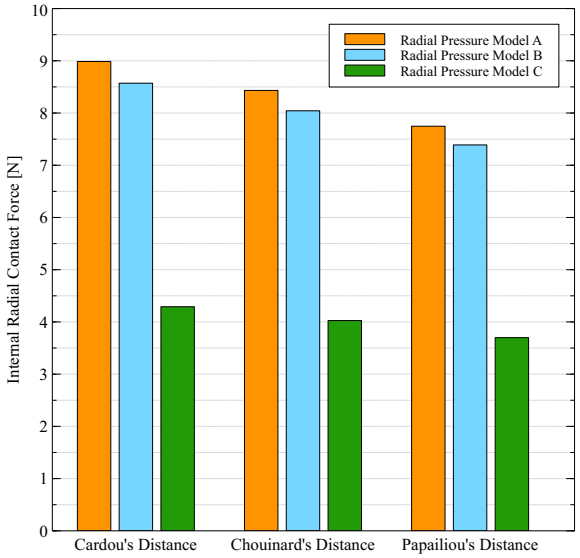

(a) Layer 2.

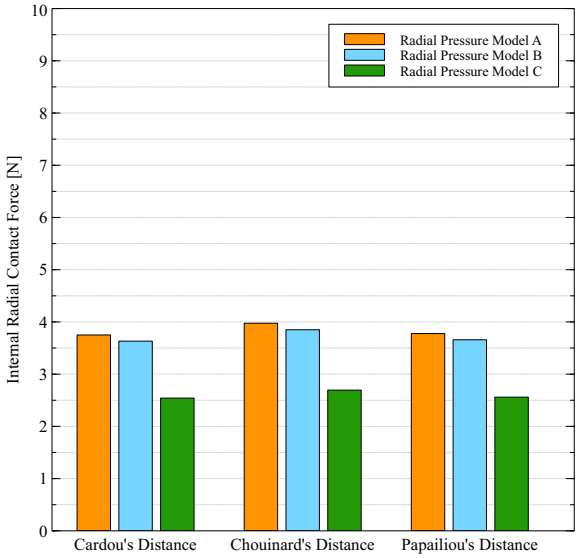

(b) Layer 3.

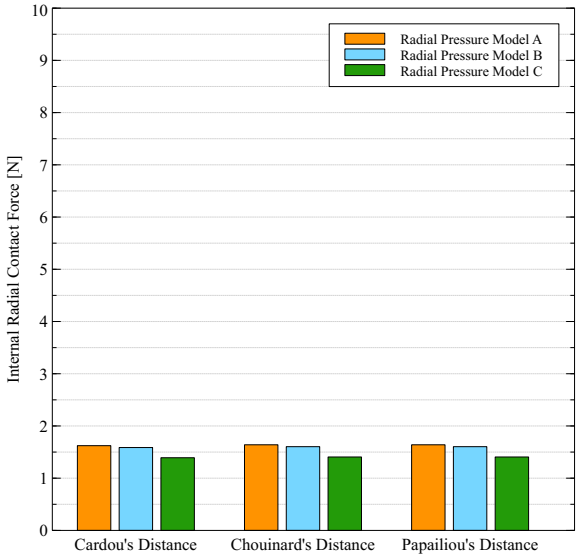

(c) Layer 4.

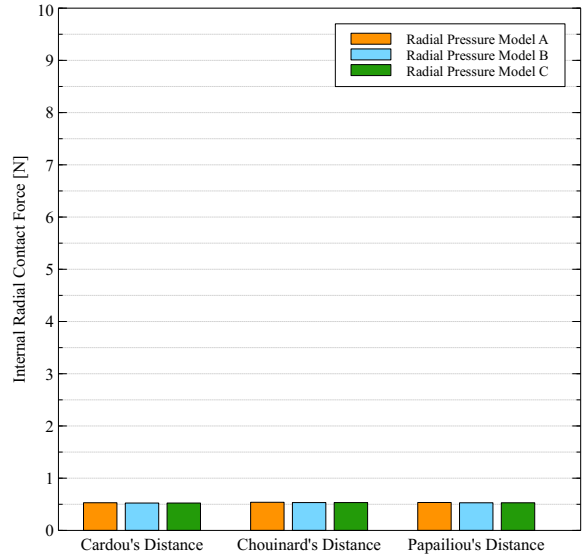

(d) Layer 5.

Figure 3.52. ACSR 72/7 Nelson II: plot of P^{int} for the different layers.

Comments

Some comments about the results collected in the previous graphs are herein proposed:

- considerations already evidenced about the general trend of the predictions of the different radial pressures transmission models (A,B and C) hold and are confirmed by the previous plots(see Subsection 3.4.2 for further details);
- considerations already evidenced about the general trend of the values of the contact points distances obtained through the different equations (Eqts. 3.20, 3.21 and 3.22) hold and are confirmed by the previous plots (see Subsection 3.2.2 for further details);
- as a matter of fact, the biggest difference in between the nine combinations is due to the underestimation of the radial contact forces per unit of length obtained with the Radial Pressures Model C;
- the slight overestimation of the distance between contact points obtained through Cardou's equation encountered for the innermost layer, decreases as the number of layers of the conductor increases,
- predictions of P^{int} and P^{ext} for intermediate layers obtained with P.M.s A and B tend to even out if combined with the contact points distances computed with Cardou's and Papailiou's equations;
- for the innermost layer of any conductor, maximum values of the approximated internal and external radial contact forces (P^{int} and P^{ext}) are obtained by combining Radial Contact Pressures Model A (see Paragraph 3.4.2) with the distance between contact points computed with Cardou's equation (Eq. 3.20);
- for the innermost layer of any conductor, minimum values of the approximated internal and external radial contact forces (P^{int} and P^{ext}) are obtained by combining Radial Contact Pressures Model C (see Paragraph 3.4.2) with the distance between contact points computed with Papailiou's equation (Eq. 3.22);
- for the intermediate layer of any conductor, maximum values of the approximated internal and external radial contact forces (P^{int} and P^{ext}) are obtained by combining Radial Contact Pressures Model A (see Paragraph 3.4.2) with the distance between contact points computed with Chouinard's equation (Eq. 3.21);
- for the intermediate layer of any conductor, minimum values of the approximated internal and external radial contact forces (P^{int} and P^{ext}) are obtained by combining Radial Contact Pressures Model C (see Paragraph 3.4.2) with the distance between contact points computed with Cardou's equation (Eq. 3.20);
- as a particular result, internal approximated radial contact forces P^{int} for the outermost layer of wires of any conductor are almost equally predicted by the nine different combinations adopted;
- as a particular result, external approximated radial contact forces P^{ext} for the outermost layer of wires of any conductor appear to lose the dependence upon the distance formula, and to vary according to the radial pressures model characteristics only (that is, P.M.s A and B gives practically the same results, whereas P.M.C slightly underestimates the values of the radial contact forces).

3.5 Bending Problem

In this section, the bending problem of metallic stranded cables is assessed.
Its intrinsic nonlinear and non-holonomic features result in a more complex discussion with respect to the solution of the axial-torsional loading scenario, discussed in Section 3.4.
A brief characterization of the flexural stiffness properties during the bending process is provided in Subsection 3.5.1, whereas the formulation of the tangent stiffness matrix within the context of iterative solution strategies for nonlinear structural problems is assessed in Subsection 3.5.2. One of the most important part of the entire author's research work is collected in Subsection 3.5.3, in which different stick-slip mechanical models for multilayer conductors under bending are implemented. A procedure for the obtainment of closed-form expression of two coefficients governing the differential equation describing the wire axial force limit domain is proposed. A generalization of such procedure is then retrieved.
Finally, Subsection 3.5.4 deals with the description of the moment-curvature law of metallic stranded cables. An ideal bi-linear approximating relation is used to describe the hysteretic behavior of such structures, fully defined by the so-called construction parameter c_0.
The procedures for the computation of such parameter will be addressed in the next Section (3.6).

3.5.1 Flexural Stiffness

Whenever a conductor is bent, interactions among adjacent wires occur at internal contact surfaces. Here friction forces tend to contrast relative movement of internal wires, i.e. the interwire displacements, so that transmission of tangential stresses between wires can take place (*full-stick* condition). When the forces which tend to activate the sliding are greater than the frictional ones, then, a wire can undergo to relative displacement with respect to the neighbors. This process can proceed up to the situation for which all the wires are in the so called *full-slip* condition (see e.g. (Foti and Martinelli, 2016a, 2016b)).
Hence, the bending of the strand is a non-linear problem, due to the variable axial strain caused by bending itself (see Eq. 3.43) Equations 3.86 and 3.87 are the most simple expressions that allow for the determination respectively of the maximum and minimum bending stiffness of the conductor.

$$EI_{max} = \sum_i E_i \, I_i \tag{3.86}$$

$$EI_{min} = \sum_i E_i \, I_{0i} \tag{3.87}$$

where E_i and I_i are respectively the Young's modulus and the moment of inertia of the i-th wire. The i-th moment of inertia I_i can be computed as:

$$I_i = I_{0i} + A_i \, d_i^2 \tag{3.88}$$

where I_{0i} is the moment of inertia of wire i relative to its own axis, A_i is the area of the wire and d_i is the distance from the wire's neutral axis to the conductor's neutral axis. With reference to figure 3.53, d_i is defined as follows:

$$d_i = r_n \, \sin(\alpha_i) \tag{3.89}$$

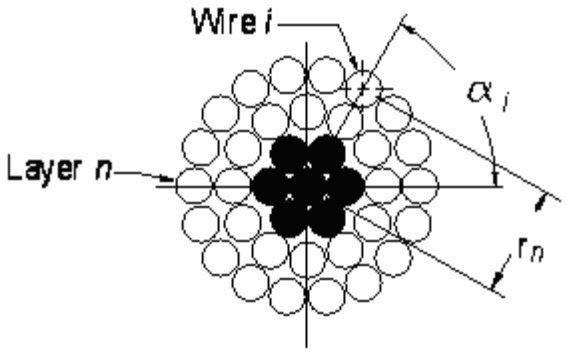

Figure 3.53. Conductor cross section: parameters for bending stiffness calculation (EPRI, 2006).

According to the model proposed by Foti and Martinelli (22), the upper and lower limit values of the tangent bending stiffness can be evaluated through equations 3.90 and 3.91. At small values of the curvature, friction forces are large enough to overcome the axial force gradient along the wire, and all the wires are are ideally welded together such that any relative displacement among them is prevented (*full-stick* state). The strand cross section can be modeled as a planar rigid body, leading the bending stiffness to reach its maximum theoretical value:

$$EI_{max} = EI_{min} + \sum_{j=1}^{m} \frac{n_j}{2} \cos^3(\alpha_j) EA_{w,j} R_j^2 \tag{3.90}$$

If the external surfaces of the wires can be assumed perfectly lubricated, the strand behaves as a bundle of independent curved thin rods (*full-slip* state). The kinematics of each individual wire is described by means of the planar rigid body assumption, and the minimum theoretical value of the flexural stiffness is attained:

$$EI_{min} = \sum_{j=0}^{m} \frac{n_j}{2} \cos(\alpha_j) EI_{w,j} \Big(1 + \cos^2(\alpha_j) + \frac{\sin^2(\alpha_j)}{1+\nu_j}\Big) \tag{3.91}$$

It is worth notice that, as a consequence of the deformability of the internal contact interfaces between the wires, the calculated values of the maximum theoretical value of the flexural stiffness EI_{max} tend to overestimate the bending stiffness of the strands in the small curvature regime. This tendency has been recently recognized by different researchers (Baumann and Novak 2017), (Paradis and Legeron 2011). A stiffness reduction factor β (with: $\beta \in [0, 1]$), can then be introduced to approximately account for this effect. So that an effective maximum flexural stiffness of the strand can be defined as follows;

$$EI_{max,ef} = \beta\, EI_{max} \tag{3.92}$$

For typical ACSR conductors, β can be in the range 0.5-0.95.
The transition from the *full-stick* (i.e from small curvature regime) to the *full-slip* (i.e. to large curvature regime) cross sectional behavior depends on the possible activation of relative displacements between the wires and is inherently non-linear and non-holonomic.

3.5.2 Tangent Stiffness Matrix

The tangent stiffness matrix $\boldsymbol{K}_s$ is important to be evaluated within the context of displacement-based iterative solution strategies for nonlinear structural problems.
The tangent stiffness matrix relates the variations of the generalized cross sectional stress and strain variables and can be evaluated by taking the derivatives of the stress-strain relationships:

$$\boldsymbol{K_s} = \frac{\partial \boldsymbol{\sigma}_s}{\partial \boldsymbol{\varepsilon}_s} \tag{3.93}$$

where $\boldsymbol{\sigma}_s$ and $\boldsymbol{\varepsilon}_s$ are the vectors of generalized stresses and strains, respectively (see Eqts. 3.30). As it was previously discussed, the nonlinearities are only due to the contribution of the wire axial strain components which are due to the bending of the strand.
The cross-sectional tangent stiffness matrix can be expressed as the sum between a constant contribution, evaluated under the assumption of *full-slip* kinematic condition, and an additional term, that generally varies during the analysis and account for the interwire sliding phenomenon (22).

$$\boldsymbol{K}_s = \boldsymbol{K}_{s,slip} + \boldsymbol{K}_{s,add} \tag{3.94}$$

The constant contribution can be expressed as it follows:

$$\boldsymbol{K}_{s,slip} = \begin{bmatrix} EA & C_{AT} & 0 & 0 \\ C_{AT} & GJ & 0 & 0 \\ 0 & 0 & EI_{min} & 0 \\ 0 & 0 & 0 & EI_{min} \end{bmatrix} = \begin{bmatrix} \boldsymbol{K_{s,at}} & \boldsymbol{0} \\ \boldsymbol{0} & \boldsymbol{K_b} \end{bmatrix} \tag{3.95}$$

where $\boldsymbol{K_{s,at}}$ is the axial-torsional stiffness matrix (already expressed in Eq. 3.64) and $\boldsymbol{K_b}$ is the stiffness matrix containing the minimum and maximum flexural stiffness of the strand along the principal diagonal:

$$\boldsymbol{K_b} = \begin{bmatrix} EI_{min} & 0 \\ 0 & EI_{min} \end{bmatrix} \tag{3.96}$$

The additional contribution of the stiffness matrix $K_{s,add}$ is non-symmetric and can be generally written in the following form:

$$\boldsymbol{K_{s,add}} = \begin{bmatrix} 0 & 0 & k_{13} & k_{23} \\ 0 & 0 & k_{14} & k_{24} \\ 0 & 0 & k_{33} & 0 \\ 0 & 0 & 0 & k_{44} \end{bmatrix} \tag{3.97}$$

It is worth noting that out-of-diagonal terms of the matrix can be neglected without significantly affecting the convergence properties of the numerical solution, in the context of iterative solution strategies for nonlinear structural problems.
The expression of the direct stiffness terms k_{33} and k_{44} can be found in (Foti and Martinelli, 2016b).

3.5.3 Stick-Slip Mechanical Models

Sliding conditions of wires in multilayer conductors under bending have been studied by some authors under different literature assumptions. Such hypothesis substantially differs for the tangential contact forces direction (i.e. the friction forces direction) that arise at the wire interfaces, as reported e.g. in (Cardou, 2013).
To the author's knowledge, a rigorous comparison between the different slip conditions assumptions on the strand bending response has never been assessed.
This fact is due to the lack of a general formulation that would permit to study the different hypothesis under a general framework.
The aim of this part of the present work is to build such general framework, on the basis of a generalization of the procedure already developed in (Foti and Martinelli, 2016a).
First of all, the analytical formulation for the obtainment of the closed-form expressions of the coefficients governing the wire axial force limit domain differential equation is presented.
In the second part, different sliding conditions from the literature are analyzed and implemented. As a novel result, two additional sliding conditions are proposed.
Finally, a straightforward generalization of such closed-form expressions through two additional parameters is proposed.

Formulation development

Let us refer just for the sake of simplicity to Radial Contact Pressure Model A. This is not a specialization of the problem and will not cause any lack of generality in the following derivations. Let us consider an infinitesimal wire segment dS. Figure 3.54 shows a scheme of the wire portion subjected to a system of distributed radial and tangential forces acting on the contact helices (internal and external).

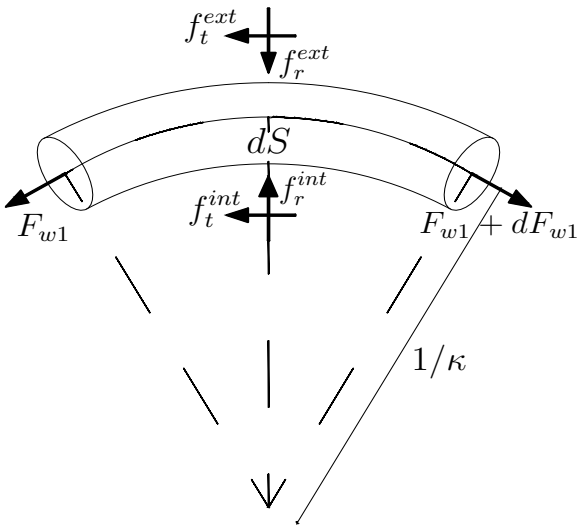

Figure 3.54. Equilibrium of an infinitesimal wire segment.

By stating the equilibrium of the infinitesimal wire segment along the tangential and radial directions, the following equations are obtained:

$$\frac{\partial F_{w1}}{\partial S} - c^{ext} f_t^{ext} - c^{int} f_t^{int} = 0 \tag{3.98a}$$

$$F_{w1}(S,t)\kappa + c^{ext} f_r^{ext} - c^{int} f_r^{int} = 0 \tag{3.98b}$$

where κ denotes the initial curvature of the wire centerline, while c^{ext} and c^{int} are the non-dimensional coefficients that account for the difference between dS and the length of the infinitesimal segments of the contact helices already introduced in Eqs. 3.70.
At this stage, one can study the wire sliding condition by assuming that the tangential forces per unit of length satisfy the Amontons-Coulomb inequalities:

$$f_t^{ext} \leq \mu^{ext} f_r^{ext} \tag{3.99a}$$

$$f_t^{int} \leq \mu^{int} f_r^{int} \tag{3.99b}$$

where μ^{ext} and μ^{int} indicate the friction coefficient of the external and internal contact surfaces.
Substituting the previous expressions into equation 3.98a, and exploiting f_r^{int} from equation 3.98b one has:

$$\frac{\partial F_{w1}}{\partial S} - c^{ext}\mu^{ext} f_r^{ext} - c^{int}\mu^{int} f_r^{int} \leq 0 \tag{3.100a}$$

$$f_r^{int} = \frac{1}{c^{int}}\Big[F_{w1}\kappa + c^{ext} f_r^{ext}\Big] \tag{3.100b}$$

Substituting Eq. 3.100b into Eq. 3.100a one gets:

$$\frac{\partial F_{w1}}{\partial S} - \mu^{int} F_{w1}\kappa - (\mu^{ext} + \mu^{int}) c^{ext} f_r^{ext} \leq 0 \tag{3.101}$$

Accounting for a possible reversal in the direction of the wire axial force gradient, the following tangential contact condition is obtained:

$$\psi(S,t) = |\frac{\partial F_{w1}}{\partial S}| - \mu^{int} F_{w1}(S,t)\kappa - (\mu^{ext} + \mu^{int}) c^{ext} f_r^{ext} \leq 0 \tag{3.102}$$

It is worth noting that the domain of admissible values of the wire axial forces, at a generic coordinate S is expressed by the function $\psi(S,t)$. In particular (Foti and Martinelli, (2016b)):

- If $\psi(S,t) < 0$, the generic wire is in stick-state because the tangential contact forces are large enough to prevent sliding;
- If $\psi(S,t) = 0$, the generic wire is in slip-state.

so that the sliding conditions can be expressed in the following form:

$$\begin{cases} \psi(S,t) = 0 \\ \dot{\psi}(S,t) = 0 \end{cases} \tag{3.103}$$

By recalling Equation 3.5a one can operate a change of coordinates, expressing dS as:

$$dS = \frac{R d\theta}{\sin(\alpha)} \tag{3.104}$$

Recalling also Eq. 3.8a, the following inequality is readily obtained:

$$|\frac{\partial F_{w1}}{\partial \theta}| - \mu^{int} F_{w1}|\sin(\alpha)| - (\mu^{ext} + \mu^{int}) c^{ext} f_r^{ext} \frac{R}{|\sin(\alpha)|} \leq 0 \tag{3.105}$$

At this stage, recalling that the axial force in the wire can be expressed through Eq. 3.56 and considering that:

$$\frac{\partial F_{w1}^{L}}{\partial S} = 0 \tag{3.106}$$

inequality 3.105 becomes:

$$|\frac{\partial F_{w1}^{NL}}{\partial \theta}| - \mu^{int} F_{w1}^{NL} |\sin(\alpha)| - \mu^{int} F_{w1}^{L} |\sin(\alpha)| - (\mu^{ext} + \mu^{int}) c^{ext}\, f_r^{ext} \frac{R}{|\sin(\alpha)|} \leq 0 \tag{3.107}$$

It is now possible to make reference to the radial forces per unit of length multiplied by the radius of curvature of the wire:

$$\hat{f}_r^{ext} = f_r^{ext} \cdot \rho_w = f_r^{ext} \cdot \frac{1}{\kappa_w} \tag{3.108}$$

So that:

$$f_r^{ext} = \hat{f}_r^{ext} \cdot \kappa_w = \hat{f}_r^{ext} \cdot \frac{\sin^2(\alpha)}{R} \tag{3.109}$$

Substituting into inequality 3.107 one gets:

$$|\frac{\partial F_{w1}^{NL}}{\partial \theta}| - \mu^{int} F_{w1}^{NL} |\sin(\alpha)| - \mu^{int} F_{w1}^{L} |\sin(\alpha)| - (\mu^{ext} + \mu^{int}) c^{ext}\, \hat{f}_r^{ext} |\sin(\alpha)| \leq 0 \tag{3.110}$$

At this point, it is possible to insert Eq. 3.83 in the previous expression, in order to express the linear component of the wire axial force F_{w1}^{L}. Hence:

$$|\frac{\partial F_{w1}^{NL}}{\partial \theta}| - \mu^{int} F_{w1}^{NL} |\sin(\alpha)| - \mu^{int} \nu_w |\sin(\alpha)| - (\mu^{ext} + \mu^{int}) c^{ext}\, \hat{f}_r^{ext} |\sin(\alpha)| \leq 0 \tag{3.111}$$

It is now convenient to express the previous inequality in a more general form, introducing the coefficients a and b.
With reference to a single layer of wires (i.e. for a fixed $j \in [1, m]$, where m denotes the total number of layers), the following scalar equation can be used for reference:

$$|\frac{\partial F_{w1}^{NL}}{\partial \theta}| + a F_{w1}^{NL} + b = 0 \tag{3.112}$$

Comparing Equations 3.111 and 3.112 one finally gets:

$$a = -\mu^{int} |\sin(\alpha)| \tag{3.113a}$$

$$b = -\mu^{int} |\sin(\alpha)| \nu_w - (\mu^{int} + \mu^{ext})\, c^{ext} \cdot \hat{f}_r^{ext} |\sin(\alpha)| \tag{3.113b}$$

Depending on the sign of the gradient of $F_{w1,NL}$, two limit conditions can be derived, namely $F_{w1,NL}^{lim,+}$ and $F_{w1,NL}^{lim,-}$.
If the gradient function has a positive sign, i.e. $\frac{\partial F_{w1}^{NL}}{\partial \theta} > 0$, then the positive limit condition is derived:

$$\frac{\partial F_{w1,NL}^{lim,+}}{\partial \theta} - \mu^{int} F_{w1,NL}^{lim,+} |\sin(\alpha)| - \mu^{int} \nu_w |\sin(\alpha)| - (\mu^{ext} + \mu^{int}) c^{ext}\, \hat{f}_r^{ext} |\sin(\alpha)| = 0 \tag{3.114}$$

whereas if the gradient function has a negative sign, i.e. $\frac{\partial F_{w1}^{NL}}{\partial \theta} < 0$, then the negative limit condition is derived:

$$-\frac{\partial F_{w1,NL}^{lim,+}}{\partial \theta} - \mu^{int} F_{w1,NL}^{lim,+} |\sin(\alpha)| - \mu^{int} \nu_w |\sin(\alpha)| - (\mu^{ext} + \mu^{int}) c^{ext} \hat{f}_r^{ext} |\sin(\alpha)| = 0 \quad (3.115)$$

The general solutions of the previous ordinary differential equations (3.114, 3.115) can be expressed as:

$$F_{w1,NL}^{lim\,\pm}(\theta) = C_0^{\pm} \exp\Big[\pm \mu |\sin(\alpha)| \theta \Big] + C_p \quad (3.116)$$

where C_p is a constant particular solution, linearly depending of the axial force acting on the strand N_s:

$$C_p = N_s \bar{C}_p \quad (3.117)$$

Integration constants C_0^+ and C_0^- should be determined by imposing suitable boundary conditions.
Foti and Martinelli (2016a) have derived the integration constants for the special and interesting case of uniform bending of the strand.
These can be expressed by distinguishing two cases:

1. Bending with tension side on the upper side of the strand.
   The boundary conditions are (with $z = 0, 1, 2, \dots$):

$$C_0^+ = -C_p \exp\Big[-\mu |\sin(\alpha)| (2\pi z) \Big] \quad (3.118a)$$

$$C_0^- = -C_p \exp\Big[+\mu |\sin(\alpha)| (2z+1)\pi \Big] \quad (3.118b)$$

   So that the solutions are expressed as it follows:

$$F_{w1,NL}^{lim,+}(\theta) = N_s \bar{C}_p \Big(1 - \exp\Big[+\mu |\sin(\alpha)| (\theta - 2\pi z) \Big] \Big) \quad (3.119a)$$

$$F_{w1,NL}^{lim,-}(\theta) = N_s \bar{C}_p \Big(1 - \exp\Big[+\mu |\sin(\alpha)| [(2z+1)\pi - \theta] \Big] \Big) \quad (3.119b)$$

2. Bending with tension side on the lower side of the strand.
   The boundary conditions are (with $z = 0, 1, 2, \dots$):

$$C_0^+ = -C_p \exp\Big[-\mu |\sin(\alpha)| (2z+1)\pi \Big] \quad (3.120a)$$

$$C_0^- = -C_p \exp\Big[+\mu |\sin(\alpha)| (2\pi z) \Big] \quad (3.120b)$$

   So that the solutions are expressed as it follows:

$$F_{w1,NL}^{lim,+}(\theta) = N_s \bar{C}_p \Big(1 - \exp\Big[+\mu |\sin(\alpha)| [\theta - (2z+1)\pi] \Big] \Big) \quad (3.121a)$$

$$F_{w1,NL}^{lim,-}(\theta) = N_s \bar{C}_p \Big(1 - \exp\Big[+\mu |\sin(\alpha)| (2\pi z - \theta) \Big] \Big) \quad (3.121b)$$

Let us now introduce the so-called non-dimensional limit functions:

$$N^{lim,\pm}(\theta) = \frac{F^{lim\,\pm}_{w1,NL}(\theta)}{N_s} \tag{3.122}$$

The domain of admissible values for the function F^{NL}_{w1} can be defined according to the following inequality:

$$\min(N^{lim,+}, N^{lim,-}) \leq \frac{F^{lim,\pm}_{w1,NL}}{N_s} \leq \max(N^{lim,+}, N^{lim,-}), \;\; \forall\theta \tag{3.123}$$

For the sake of clarity, the plots of the non-dimensional limit functions versus the swept angle $\theta \in [0, 360]$ deg for the sample of 15 conductors are reported into Appendix E.
The limit domain is represented by the continuous black lines, whereas the red dots indicate the values of the non-dimensional limit functions at the swept angles identifying the wires positions.
It is worth noting that the admissible domains are determined by considering the Radial Contact Pressure Model A and the sliding condition shown in Fig. 3.54, which will be referred to as Sliding Condition 1 in the following developments.
Each single limit domain of the previous graphs is related to the different layers of wires of the strand. The ones with the lowest absolute values of $N^{lim,+}$ and $N^{lim,-}$ are associated with the outer layers, while the ones of the innermost layer are associated with the highest absolute values of non-dimensional limit functions.

Comments

As a general comment, the proposed approach is practically convenient because it permits to obtain the expressions of the coefficients a and b that are used to compute the constant particular solution $\bar{C}_p$ of the ordinary differential equations. In fact, with reference to the general form of the tangential equilibrium equation:

$$|\frac{dF^{NL}_{w1}}{dS}| + aF^{NL}_{w1} + b = 0 \tag{3.124}$$

one can search for the constant particular solution by imposing:

$$F^{NL}_{w1,p} = \bar{C}_p \tag{3.125}$$

so that, by backward substitution, one gets:

$$\bar{C}_p = -\frac{b}{a} \tag{3.126}$$

This means that once both coefficients a and b are known, the constant particular solution can be easily computed regardless both the typology of radial contact pressures model and the particular slip condition (also see Paragraphs 3.5.3 - 3.5.3) that is adopted, i.e. by applying this procedure, there are not specialized expressions of $\bar{C}_p$ depending neither on the different radial pressure models, nor on the imposed slip condition.
In the following pages, different sliding conditions will be treated, in order to determine the closed-form expressions of coefficients a and b for each case.

Sliding Condition 1 (S.C.1)

This sliding condition is the one already adopted, that is shown in Figure 3.55, in which tangential forces are parallel and opposite to the direction of wire sliding. This scheme can be regarded to as a sort of "Pullout" test.
Such sliding condition was introduced by Papailiou (1995) and has been extensively adopted in the following years by many other authors (e.g. (Hong et al., 2005), (Foti and Martinelli, 2016a, 2016b)).
However, condition S.C.1 is difficult to justify physically. In fact, it is difficult to understand why layer $i+1$, being in the slip state, would oppose layer i slip. Thus, condition S.C.1 tends to have a strong retardation effect on inner layer slip.
Additionally, the slip phases are assumed to occur sequentially, without any overlap, from one layer to the next. This hypothesis leads to an advantage, for the mechanical model, that is, slip is complete on one layer, before it starts on the next (Cardou, 2013).

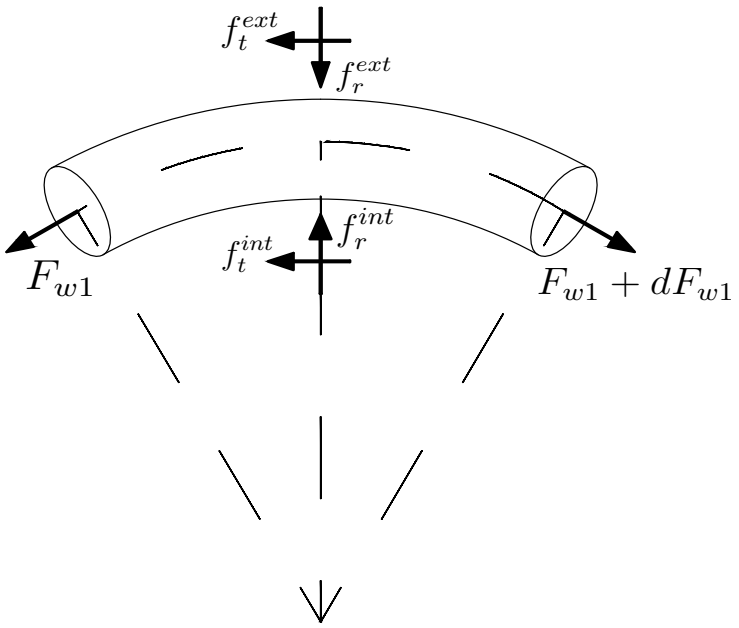

Figure 3.55. Equilibrium of an infinitesimal wire segment, S.C.1.

The equilibrium equations, both along radial and tangential directions, read:

$$\frac{\partial F_{w1}}{\partial S} - c^{ext} f_t^{ext} - c^{int} f_t^{int} = 0 \tag{3.127a}$$

$$F_{w1}(S,t)\kappa + c^{ext} f_r^{ext} - c^{int} f_r^{int} = 0 \tag{3.127b}$$

The previous equations lead to the obtainment of the following coefficients:

$$a = -\mu^{int}|\sin(\alpha)| \tag{3.128a}$$

$$b = -\mu^{int}|\sin(\alpha)|\nu_w - (\mu^{int} + \mu^{ext})\, c^{ext} \cdot \hat{f}_r^{ext}|\sin(\alpha)| \tag{3.128b}$$

Such coefficients were already determined with reference to the explanation of the general procedure previously assessed (Eqts. 3.113a and 3.113b).

Sliding Condition 2 (S.C.2)

This sliding condition describes in a more physical way the sliding process of the wire under the assumption that the sliding starts at the outermost layer of the strand and then "propagates" towards the core. In addition, the slip phases are assumed to occur sequentially, without any overlap, as it occurs in condition S.C.1.
However, in this case, once the sliding is activated, the external tangential force is not directed as the internal one, but points in the opposite direction, that is, along the sliding direction.
The forces acting on an infinitesimal wire segment are shown in Figure 3.56.

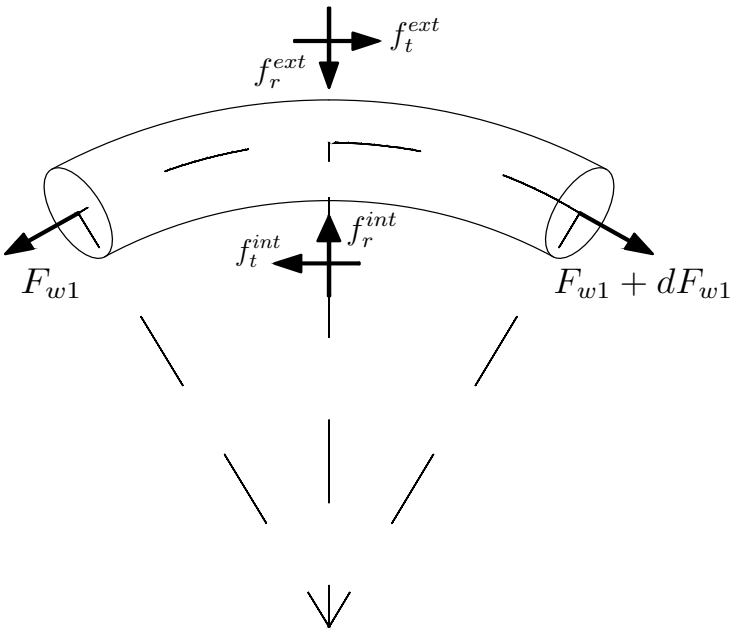

Figure 3.56. Equilibrium of an infinitesimal wire segment, S.C.2.

The equilibrium equations, both along radial and tangential directions, read:

$$\frac{\partial F_{w1}}{\partial S} + c^{ext} f_t^{ext} - c^{int} f_t^{int} = 0 \tag{3.129a}$$

$$F_{w1}(S,t)\kappa + c^{ext} f_r^{ext} - c^{int} f_r^{int} = 0 \tag{3.129b}$$

By repeating the procedure previously shown, one can easily obtain the following coefficients:

$$a = -\mu^{int}|\sin(\alpha)| \tag{3.130a}$$

$$b = -\mu^{int}|\sin(\alpha)|\nu_w - (\mu^{int} - \mu^{ext})\, c^{ext} \cdot \hat{f}_r^{ext}|\sin(\alpha)| \tag{3.130b}$$

It is worth noting that the only modification with respect to the previous Sliding Condition is the sign of the external friction coefficient. If $\mu^{int} = \mu^{ext}$, then the previous equations simplify as follows:

$$a = -\mu^{int}|\sin(\alpha)| \tag{3.131a}$$

$$b = -\mu^{int}|\sin(\alpha)|\nu_w = a\nu_w \tag{3.131b}$$

Sliding Condition 3 (S.C.3)

Sliding condition S.C.3 makes reference to the direction of tangential contact forces described by sliding condition S.C.1. However, an important difference is present. In fact, an angle $\beta_i^{ext} = \alpha_i + \alpha_{i+1}$ is present and defines the inclination of the external tangential contact force with respect to the axis of the wire.
The symbol α_i have been adopted to denote the lay angles of the i-th layer of wires. Such condition was presented for the first time in (Cardou, 2013).
This angle β^{ext} depends on the relative motion of the material points in contact.
In fact it is formed because layer $i+1$ is already slipping on layer i. The forces acting on an infinitesimal wire segment are shown in Figure 3.57.

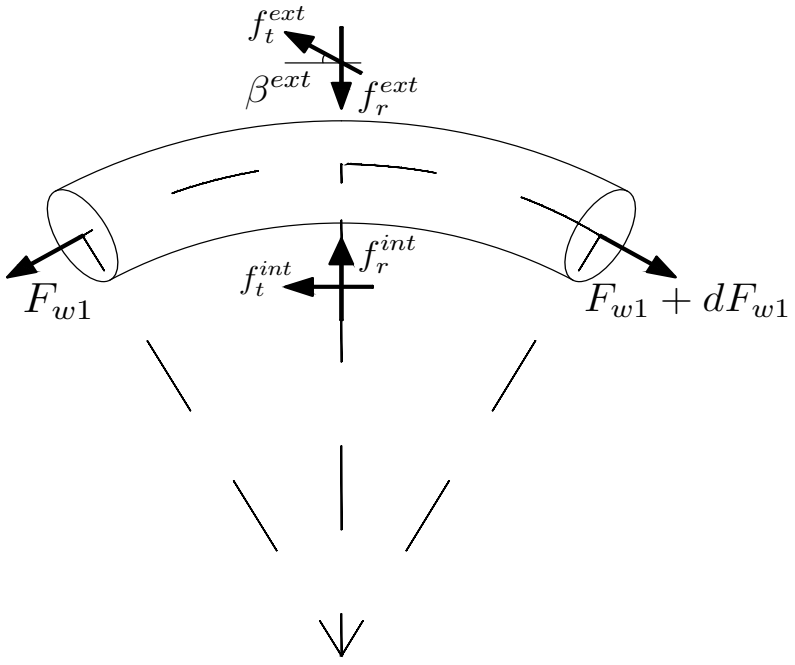

Figure 3.57. Equilibrium of an infinitesimal wire segment, S.C.3.

The equilibrium equations, both along radial and tangential directions, read:

$$\frac{\partial F_{w1}}{\partial S} - c^{ext} f_t^{ext} \cos(\beta^{ext}) - c^{int} f_t^{int} = 0 \tag{3.132a}$$

$$F_{w1}(S,t)\kappa + c^{ext} f_r^{ext} - c^{int} f_r^{int} = 0 \tag{3.132b}$$

By repeating the procedure previously shown, one can easily obtain the following coefficients:

$$a = -\mu^{int}|\sin(\alpha)| \tag{3.133a}$$

$$b = -\mu^{int}|\sin(\alpha)|\nu_w - \left(\mu^{int} + \mu^{ext}\cos(\beta^{ext})\right) c^{ext} \cdot \hat{f}_r^{ext}|\sin(\alpha)| \tag{3.133b}$$

In this case, the modification is just related to the external friction coefficient μ^{ext}.

Sliding Condition 4 (S.C.4)

Sliding condition S.C.4 considers the direction of the external tangential contact force as in sliding condition S.C.2, with the addition of the angle β^{ext} that is formed with respect to the axis of the wire, for the same reason explained in S.C.3.
The enforcement of this sliding condition arises from the need to rigorously quantify the influence of the angle β^{ext} on the bending behavior of multilayer strands, under a more physically-sound slip process (that is, S.C.2).
The forces acting on an infinitesimal wire segment are shown in Figure 3.58.

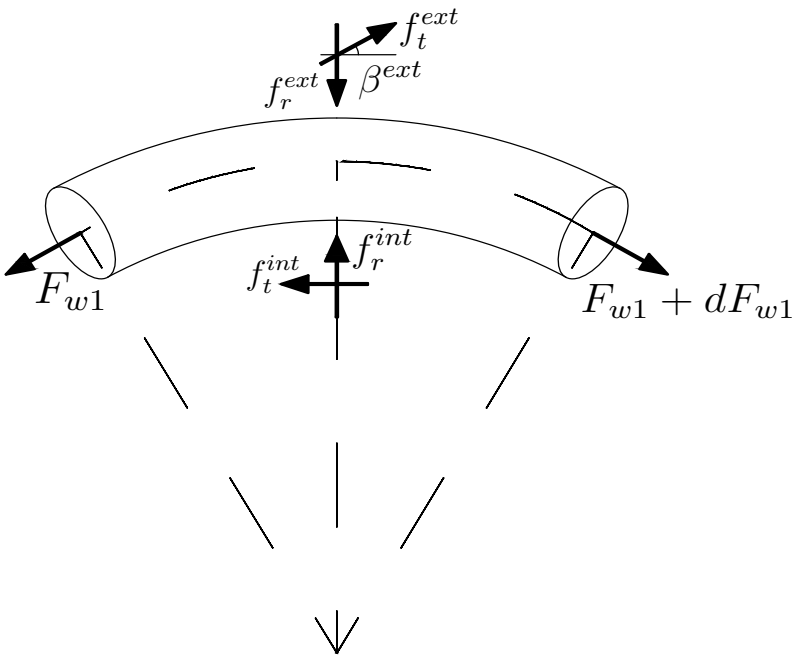

Figure 3.58. Equilibrium of an infinitesimal wire segment, S.C.4.

The equilibrium equations, both along radial and tangential directions, read:

$$\frac{\partial F_{w1}}{\partial S} + c^{ext} f_t^{ext} \cos(\beta^{ext}) - c^{int} f_t^{int} = 0 \tag{3.134a}$$

$$F_{w1}(S,t)\kappa + c^{ext} f_r^{ext} - c^{int} f_r^{int} = 0 \tag{3.134b}$$

By repeating the procedure previously shown, one can easily obtain the following coefficients:

$$a = -\mu^{int}|\sin(\alpha)| \tag{3.135a}$$

$$b = -\mu^{int}|\sin(\alpha)|\nu_w - \left(\mu^{int} - \mu^{ext}\cos(\beta^{ext})\right) c^{ext} \cdot \hat{f}_r^{ext}|\sin(\alpha)| \tag{3.135b}$$

Sliding Condition 5 (S.C.5)

This sliding condition is here presented for the first time within this context, to the author's knowledge. This slip condition arises from the direct consequence of the real sliding process of wires. In fact, it is reasonable that slips of layer i slightly modifies the relative motion with respect to layer $i-1$. Thus, the corresponding friction force direction is also slightly modified.
S.C.5 is based on the S.C.3. However, an angle of inclination $\beta_i^{int} = \alpha_i + \alpha_{i-1}$ is present on the internal tangential contact force.
On the external tangential contact force, it acts and an angle $\beta_i^{ext} = \alpha_i + \alpha_{i+1}$.
The forces acting on an infinitesimal wire segment are shown in Figure 3.57.

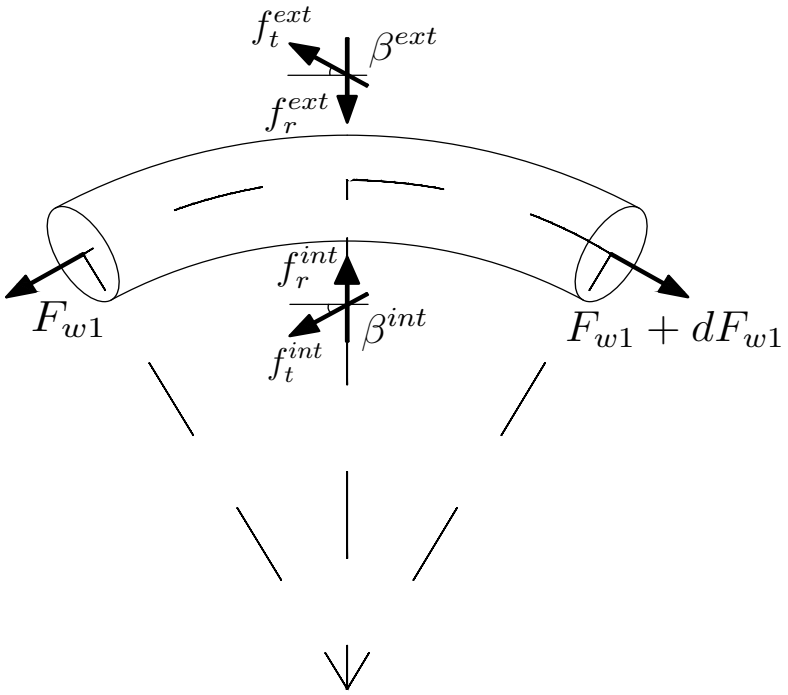

Figure 3.59. Equilibrium of an infinitesimal wire segment, S.C.5.

In this case the equilibrium equations, both along radial and tangential directions, read:

$$\frac{\partial F_{w1}}{\partial S} - c^{ext} f_t^{ext} \cos(\beta^{ext}) - c^{int} f_t^{int} \cos(\beta^{int}) = 0 \tag{3.136a}$$

$$F_{w1}(S,t)\kappa + c^{ext} f_r^{ext} - c^{int} f_r^{int} = 0 \tag{3.136b}$$

By repeating the procedure previously shown, one can easily obtain the following coefficients:

$$a = -\mu^{int} |\sin(\alpha)| \cos(\beta^{int}) \tag{3.137a}$$

$$b = +a\,\nu_w - \left(\mu^{int} \cos(\beta^{int}) + \mu^{ext} \cos(\beta^{ext})\right) c^{ext} \cdot \hat{f}_r^{ext} |\sin(\alpha)| \tag{3.137b}$$

Sliding Condition 6 (S.C.6)

This sliding condition is here presented for the first time within this context, to the author's knowledge, and is the counterpart of S.C.5, already discussed.
S.C.6 is based on the S.C.4. However, the angle of inclination $\beta_i^{int} = \alpha_i + \alpha_{i-1}$ is also present on the internal contact force.
On the external tangential contact force, it acts and an angle $\beta_i^{ext} = \alpha_i + \alpha_{i+1}$.
This condition can be regarded to as the most physically-sound sliding process, because when the wire is sliding, both internal and external tangential forces follow the relative motion of the material points in contact.
Additionally, the external tangential contact force points towards the sliding direction.
The forces acting on an infinitesimal wire segment are shown in Figure 3.60.

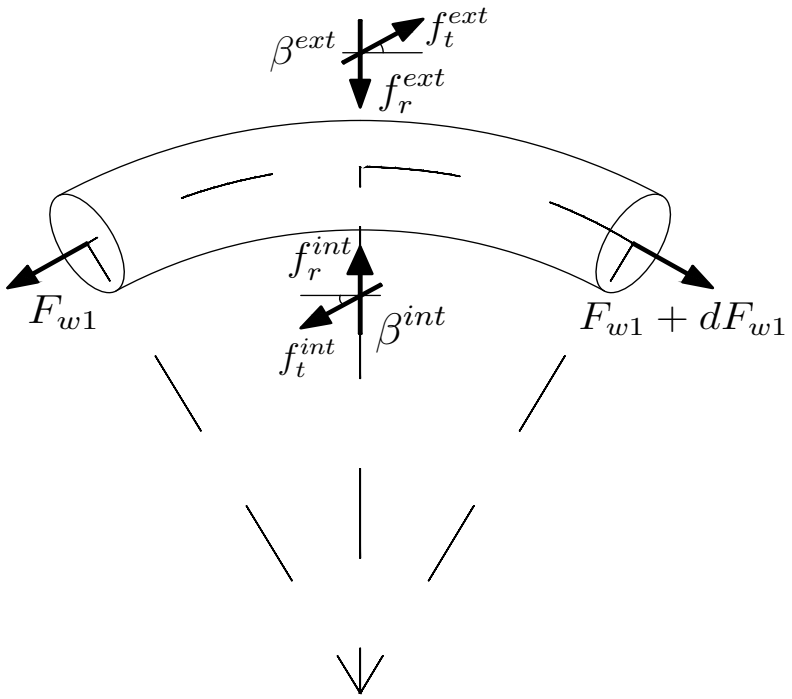

Figure 3.60. Equilibrium of an infinitesimal wire segment, S.C.6.

In this case, the equilibrium equations, both along radial and tangential directions, read:

$$\frac{\partial F_{w1}}{\partial S} + c^{ext} f_t^{ext} \cos(\beta^{ext}) - c^{int} f_t^{int} \cos(\beta^{int}) = 0 \tag{3.138a}$$

$$F_{w1}(S,t)\kappa + c^{ext} f_r^{ext} - c^{int} f_r^{int} = 0 \tag{3.138b}$$

By repeating the procedure previously shown, one can easily obtain the following coefficients:

$$a = -\mu^{int} |\sin(\alpha)| \cos(\beta^{int}) \tag{3.139a}$$

$$b = +a\,\nu_w - \left(\mu^{int} \cos(\beta^{int}) - \mu^{ext} \cos(\beta^{ext})\right) c^{ext} \cdot \hat{f}_r^{ext} |\sin(\alpha)| \tag{3.139b}$$

Comments

It is worth noting that all the different sliding conditions that were presented, can be applied to different radial contact pressure models, namely P.M. A, B and C.
As a general comment, if the difference between the segment dS of the wire and the length of the infinitesimal segments of the contact helices is neglected (i.e. the Radial Pressure Model B is used), different results in terms of admissible wire axial force domain are found. These can be obtained by exploiting the same results obtained with the Radial Pressure Model A, but neglecting the correction coefficients expressed by Equations 3.70, that is imposing them to a unitary value:

$$c^{int} = 1 \tag{3.140a}$$

$$c^{ext} = 1 \tag{3.140b}$$

So that the coefficients a and b for each case can be derived in a straightforward way.
By adopting the proposed formulation, one should provide the non dimensional radial contact force per unit of length (i.e. the radial contact force per unit of length normalized by the strand axial force and multiplied by the radius of curvature of the wire).
In the case of Radial Contact Pressure Model C one gets:

$$\hat{f}_r^{ext} \cong \sum_{l=j+1}^{m} \frac{\nu_{w,l}}{\rho_{w,l}\,\kappa_{w,l}} \tag{3.141}$$

Foti and Martinelli (2016a) have shown that the particular solution of the differential equations 3.114 and 3.115, in the case of the radial contact pressure model C with the Sliding Condition S.C.1, has the following expression:

$$\bar{C_p} = -\Big(\nu_w + 2\rho_w \sum_{l=j+1}^{m} \frac{\nu_{w,l}}{\rho_{w,l}}\Big) \tag{3.142}$$

This can be easily verified by adopting the expression of a and b coefficients previously found (Eq. 3.128a and 3.128b), by inserting the expression of $\hat{f}_r^{ext}$ according to the Radial Pressure Model C, that is reported in Eq. 3.141.
Table 3.11 shows the values of the constant particular solution $\bar{C_p}$ computed in both ways, according to the P.M. C and S.C. 1, for an ACSR 48/7 Bersfort conductor.

Table 3.11. Results of $\bar{C_p}$ for the ACSR 48/7 Bersfort conductor.

Constant Particular Solution $\bar{C_p}$	Layer 1	Layer 2	Layer 3	Layer 4
Foti and Martinelli 2016a, Eq. 3.142	-0.2229	-0.0690	-0.0529	-0.0166
Coefficients a and b, Eq. 3.126	-0.2229	-0.0690	-0.0529	-0.0166

Generalization

As it is clear from the structure of the equations presented in the previous paragraphs (Eqts. 3.128, 3.130, 3.133, 3.135, 3.137 and 3.139), the expressions of the coefficients a and b may be generalized. In fact, Sliding Conditions 1, 2, 3 and 4 clearly affect just the external friction coefficient. On the other hand, Sliding Conditions 5 and 6 are affecting both the internal and the external friction coefficients.
The generalized form of a and b coefficients can be formulated according to the following equations:

$$a = -\mu^{int}|\sin(\alpha)|\xi_{int} \tag{3.143a}$$

$$b = -\mu^{int}|\sin(\alpha)|\xi_{int}\nu_w - \left(\mu^{int}\xi_{int} + \mu^{ext}\xi_{ext}\right) c^{ext} \cdot \hat{f}_r^{ext}|\sin(\alpha)| \tag{3.143b}$$

where ξ_{ext} and ξ_{int} are two coefficients whose values depend upon the specific sliding condition. It is clear that the determination of the coefficients a and b is based on the equilibrium equation in the tangential direction. So it is possible to make reference to the generalization of such equation, by adopting the same coefficients ξ_{ext} and ξ_{int} previously introduced.
One has:

$$\frac{\partial F_{w1}}{\partial S} - \xi_{ext}\, c^{ext} f_t^{ext} - \xi_{int}\, c^{int} f_t^{int} = 0 \tag{3.144}$$

The values of ξ_{ext} and ξ_{int} for different sliding conditions are conveniently collected in Table 3.12.

Table 3.12. Expressions of ξ_{ext} and ξ_{int} for different Sliding Conditions.

Sliding Condition	ξ_{ext}	ξ_{int}
S.C.1	$+1$	$+1$
S.C.2	-1	$+1$
S.C.3	$+\cos(\beta^{ext})$	$+1$
S.C.4	$-\cos(\beta^{ext})$	$+1$
S.C.5	$+\cos(\beta^{ext})$	$+\cos(\beta^{int})$
S.C.6	$-\cos(\beta^{ext})$	$+\cos(\beta^{int})$

It is worth noticing that a big advantage of this formulation is that can be applied to whatever sliding condition one would like to enforce.

3.5.4 Moment – Curvature Law

In this section, an analytical formulation of the moment-curvature ($M-\chi$) relationship is presented. One can write such law in the form:

$$M(\chi) = EI_{min}\chi + M^{add}(\chi) \tag{3.145}$$

where:

- the linear term $EI_{min}\chi$ can be regarded as the theoretical response of the strand under the full-slip assumption (perfectly lubricated internal contact surfaces);
- the term $M^{add}(\chi)$ is non-linear and non-holonomic and accounts for the additional contribution to the bending moment of the strand coming from the axial force of each wire.

Figure 3.61 shows the typical moment-curvature diagram for a generic conductor subject to monotonic loading.
As it can be seen, the first loading branch is characterized by the initial stiffness EI_{max} , corresponding to the full-stick state. The tangent stiffness, then, gradually decreases as a consequence of the evolution of the interwire sliding phenomena. It is assumed that $\pm\chi_{max}$ is sufficiently large to achieve the limit value EI_{min} , which can be attained only if all wires of the cross section are in the slipping state.
Then, to quantitatively characterize the shape of the first loading branch, the parameters χ_0 and M_0 are introduced as shown in Figure 3.61. They define the coordinates of the yielding point of an "ideal" bi-linear elastic-plastic moment-curvature relation.
If a cyclic curvature is applied, then a typical hysteresis loop is obtained in the plane $M-\chi$. The ratio between the maximum moment reached and the associated curvature χ_{max} is used to define the secant stiffness of the cycle: EI_{sec}. In order to compare different hysteresis loops, the area enclosed within a full loop is denoted as A_{cycle}. This is a very important physical parameter, related to the energy dissipated in bending per unit of length during vibrations of the cable.

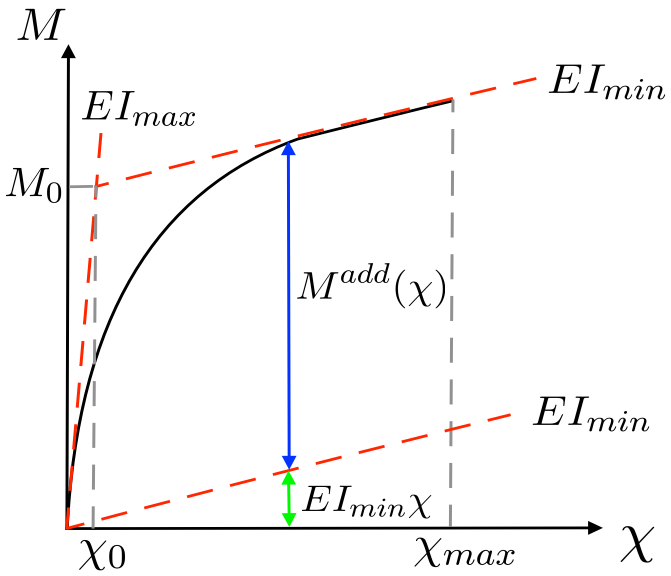

Figure 3.61. Cross-sectional bending response for a generic conductor, in case of monotonic loading.

The energy dissipated per unit of length of a stranded cable subject to cyclic bending can be calculated as the area E_{ds} of the hysteresis loop enclosed by the moment-curvature diagram, in the plane (M, χ), according to the following equation:

$$E_{ds} = \oint M(\chi) d\chi = EI_{max,ef}\, \chi_0^2 \oint \overline{M}(\overline{\chi}) d\overline{\chi} \tag{3.146}$$

Foti and Martinelli (2016b, 2018a, 2018b) have proposed an unified moment-curvature diagram for ACSR conductors in the non-dimensional plane $\overline{M} - \overline{\chi}$, with:

$$\overline{M} = \frac{M}{M_0} \qquad \overline{\chi} = \frac{\chi}{\chi_0} \tag{3.147}$$

The non-dimensional dissipated energy per unit of length ω_{ds} (see Equation 3.148) turns out to be practically independent of the internal geometry, for common ACSR conductors, and can be computed as:

$$\omega_{ds} = \oint \overline{M}(\overline{\chi}) d\overline{\chi} = \frac{\overline{\chi}_{max}^2}{2} \tag{3.148}$$

with:

$$\overline{\chi}_{max} = \frac{\chi_{max}}{\chi_0} \tag{3.149}$$

According to the theoretical developments presented by Foti and Martinelli (2018a, 2018b), the "first yielding" curvature χ_0 can be conveniently computed with the following equation:

$$\chi_0 = c_0\, \mu\, \eta \tag{3.150}$$

where μ is the friction coefficient between the wires of the stranded cable, η is the ratio between the tensile force in the cable and its Rated Tensile Strength (RTS) and c_0 is a construction parameter depending only on the internal geometry of the strand, that generally ranges between 0.050-0.450 m^{-1}. A specific Section (3.6) is dedicated to the computation of the model coefficient c_0 for different conductor cross-sections and different assumption on both the radial pressure models and the sliding conditions.
Equation 3.148 turns out to be valid to model dissipation in the large curvature regime, since it is related to the activation of gross-sliding mechanism at the interwire contact interfaces. Conversely, where dissipation is mainly due to micro-slip phenomena, i.e. in the small curvature regime, it can be shown (Foti and Martinelli, 2018b) that the non-dimensional dissipated power can be computed according to equation 3.151.

$$\omega_{ds} = \oint \overline{M}(\overline{\chi}) d\overline{\chi} = \frac{\overline{\chi}_{max}^3}{2} \tag{3.151}$$

In the enhanced unified model proposed by (Foti and Martinelli, 2018b), the transition between the micro-slip and the gross-sliding dissipation mechanisms, has been postulated to take place for $\chi_{max} = \chi_0$, i.e. when $\overline{\chi}_{max} = 1$. This means that once the "first yielding" curvature is reached, the interwire sliding phenomenon is activated.
Summarizing, the non-dimensional dissipated energy per unit length is postulated to be defined for any conductor as follows:

$$\omega_{ds}(\overline{\chi}_{max}) = \begin{cases} \omega_{ds}^{ms} & = \frac{1}{2}\,\overline{\chi}_{max}^3 \quad \forall \overline{\chi}_{max} \leq 1 \\ \omega_{ds}^{gs} & = \frac{1}{2}\,\overline{\chi}_{max}^2 \quad \forall \overline{\chi}_{max} > 1 \end{cases} \tag{3.152}$$

More specific considerations about the dissipation mechanisms of overhead electrical line conductors will be addressed in Chapter 4.

3.6 Computation of the model coefficient c_0

In this section, the procedures developed for the computation of the model coefficient c_0 are assessed. In particular, the user-coded programs in Matlab environment are presented with reference to the main steps. It is worth noticing that the two implemented procedures are equivalent in terms of final results.
As already mentioned in subsection 3.5.4, the geometric coefficient c_0 permits to fully describe the bi-linear approximated form of the moment-curvature relationship for each conductor cross-section. This is a great advantage because a full range of c_0 coefficients can be determined by exploiting different combinations between radial pressure transmission models and stick-slip mechanical models. This will be useful also for the assessment of the self-damping properties of each conductor cross-sections.

3.6.1 Numerical Evaluation

A user-coded Matlab program has been implemented, as a part of this research work, in order to numerically evaluate the coefficient c_0. The program is articulated as follows.
First of all, a variable `section` is decleared for each conductor cross-sections, which has a number of rows equal to the number of layers of wires of the conductor and 7 columns. These contain, for each layer: the number of wires (n_w), the wire diameter (d), the preferred pitch with sign (P_p), the Young Modulus (E), the Poisson coefficient (ν), the friction coefficient (μ) and the initial swept angle (θ_0). The solution procedure is articulated as follows:

1. some preliminary geometrical calculation are performed, by the user-coded function `prel_calc`: `[core, layer, NL] = prel_calc(section);`
2. the linear stiffness coefficients are computed thorough the user-coded function `lin_stiff` `[stiffness] = lin_stiff(core, layer, NL);`
3. a `for` cycle over different level of tension on the conductor is performed, i.e. $\forall \eta \in [0.1, 0.6]$, with $\eta = T/RTS$ (loading ratio parameter).
4. the linear axial-torsional problem is solved for each value of η, through the user-coded function `axial_problem`, the solution is stored in the data structure `axtor_solution`: `[axtor_solution] = axial_problem(options, input_data);`
5. the nonlinear bending problem is solved for each value of η, through the user-coded function `bending_problem`, the solution is stored in the data structure `bending_solution`: `[bending_solution] = bending_problem(NL, layer, stiffness, axtor_solution , options, core);`

From the solution of the direct monotonic bending test, one can then obtain the values of the maximum bending moment M_{max} and the maximum curvature χ_{max}.
Let us make reference to Figure 3.61.
By expressing the difference between maximum and minimum values of the bending stiffness as:

$$\Delta EI = EI_{max} - EI_{min} \tag{3.153}$$

one can obtain the "first-yielding" curvature χ_0 in the following way:

$$\chi_0 = \frac{M_{max} - EI_{min}\,\chi_{max}}{\Delta EI} = \frac{M_{max}^{add} + EI_{min}\chi_{max} - EI_{min}\chi_{max}}{\Delta EI} = \frac{M_{max}^{add}}{\Delta EI} \tag{3.154}$$

So that the moment associated to χ_0 will be computed as:

$$M_0 = EI_{max}\,\chi_0 \tag{3.155}$$

At this stage, the coefficient c_0 can be derived from the linear interpolation of the relation $\chi_0 - \eta$, with fixed-end condition, so that:

$$\chi_0 = z_0 + z_1 \cdot \eta \tag{3.156}$$

with:

$$z_0 \cong 0 \tag{3.157}$$

Comparing Equations 3.150 and 3.156 one obtains:

$$c_0 = \frac{z_1}{\mu} \tag{3.158}$$

For convenience, $\mu = 0.3$ was used (that is supposed to describe the condition of a new conductor).
It is worth underlining that the friction coefficient only slightly affects the values of c_0 depending on the assumed sliding condition and radial pressures model.

The user-coded program for the numerical evaluation of c_0 allows to select different options:

- `switch` between direct and inverse bending problems;
- `switch` between time history and single step time grid;
- `switch` between closed-form expressions and solution of the axial-torsional problem for the computation of the non-dimensional partition coefficient of axial force in each wire;
- `switch` between fixed ends and free ends, only for the case in which the axial force in the wire is computed according to closed-form expressions. In fact, when the solution of the axial-torsional problem is used, the real boundary conditions are enforced (e.g. a rotational spring);
- `switch` between different radial contact pressure models, namely the Radial Pressure Models A, B and C;
- `switch` between different sliding conditions, namely the Sliding Conditions 1, 2, 3 ,4, 5 and 6;

Such code was extensively used for the computations of c_0 parameters which will be reported and discussed in the next section.

3.6.2 Closed-Form Solution

The coefficient c_0 can also be obtained through a closed form solution. Another user-coded Matlab program is adopted for such computations. Both the case with conductor fixed-end and the one with free-end case are considered.
The important difference with respect to the numerical solution is that in this case, the additional bending moment due to the nonlinear axial force contribution is computed in a closed form. In fact, according to what was discussed in Section 3.5 one has:

$$M_s^{add}(x_1,t) = \sum_{j=0}^{m} \left[\cos(\alpha_j)\, R_j \sum_{i=1}^{n_j} \sin(\theta_i)\, F_{w,i}^{NL}(x_1,t) \right] \tag{3.159}$$

and its non-dimensional counterpart can be computed by substituting $F_{w,i}^{NL}(x_1,t)$ with the respective value of the non-dimensional limit function (see Eq. 3.122) and dividing by the conductor diameter. The non-dimensional additional bending moment due to the nonlinear axial force contribution is then given by:

$$M_s^{add,ND}(x_1,t) = \sum_{j=0}^{m} \left[\cos(\alpha_j)\, R_j \sum_{i=1}^{n_j} \sin(\theta_i)\, N^{lim}(\theta) \right] \cdot \frac{1}{D} \tag{3.160}$$

The additional bending moment M^{add} is then computed as follows, for the sake of convenience:

$$M^{add} = M_s^{add,ND}\, \eta\, RTS\, D \tag{3.161}$$

Then the first-yielding curvature χ_0 can be finally computed as:

$$\chi_0 = \frac{M^{add}}{EI_{max} - EI_{min}} = \frac{M^{add}}{\Delta EI} \tag{3.162}$$

At this stage, the coefficient c_0 can be derived from the linear interpolation of the relation $\chi_0 - \eta$. Equations 3.156, 3.157 and 3.158 apply.
The difference between the free-ends or fixed-ends boundary conditions is limited to the different admissible domain of the wire axial force. The latter is influenced by the coefficients a and b that specialize for the two different cases:

1. fixed ends, where the non-dimensional radial contact forces per unit of length are computed by using the partition coefficients expressed into Eq. 3.83, here recalled for the sake of clarity:
$$\nu_{w,l}^{fix} = \frac{\cos^2(\alpha_l) EA_{wl}}{\sum_{k=1}^{n_w} EA_{wk} \cdot \cos^3(\alpha_k)} \tag{3.163}$$
2. free ends, where the non-dimensional radial contact forces per unit of length are computed by using the partition coefficients expressed by the following equation:
$$\nu_{w,l}^{free} = \frac{\left[\cos^2(\alpha_l) - C_{AT} \sin(\alpha_l) \cos(\alpha_l) \right] EA_{wl}}{\sum_{k=1}^{n_w} EA_{wk} \cdot \cos^3(\alpha_k)} \tag{3.164}$$

The user-coded program for the closed-form solution of c_0 allows to select different options:

- `switch` between different radial contact pressure models, namely the Radial Pressure Models A, B and C;
- `switch` between different sliding conditions, namely the Sliding Conditions 1, 2, 3, 4, 5 and 6;

3.6.3 Preliminary analysis for ACSR conductors

In this Section, some preliminary analysis regarding the dependence of some mechanical parameters on the strand diameter are performed.
The following mechanical properties (Young's modulus and Poisson's ratio) for steel and aluminium wires have been adopted for all the analysis:

$$E_{st} = 200\,\text{GPa} \qquad \nu_{st} = 0.3$$

$$E_{al} = 69\,\text{GPa} \qquad \nu_{al} = 0.3$$

The geometric characteristics of ACSR conductors are collected in Appendix A for convenience.
Let us now define the parameter γ as the square root of the ratio between the minimum and maximum bending stiffness of the cable, or equivalently, parameter γ^2 as:

$$\gamma^2 = \frac{EI_{min}}{EI_{max}} \cdot 100 \quad (\%) \tag{3.165}$$

Let us also recall the definition of the proportionality coefficient k of the empirical self-damping power law (Eq. 2.17), typical of each conductor, here reported for the sake of convenience:

$$k = \frac{D}{\sqrt{m \cdot RTS}}$$

where D is the conductor diameter expressed in mm, RTS is the Rated Tensile Strength, expressed in kN and m is the mass per unit of length of the cable, expressed in kg/m. This unities of measure lead the proportionality coefficient k to be dimensional.
Table 3.13 collects such parameters for each type of ACSR conductor treated in this work.

Table 3.13. Geometric and mechanical characteristics of commercial ACSR conductors.

Code Word	Stranding	$D\,(mm)$	$RTS\,(kN)$	$m\,(kg/m)$	$\gamma^2\,(\%)$	k
Sparrow	6/1	8.01	12.4	0.136	16.01	6.168
Pigeon	6/1	12.75	29.6	0.344	16.01	3.996
Penguin	6/1	14.31	37.3	0.434	16.01	3.557
Partridge	26/7	16.28	50.0	0.546	2.89	3.116
Hawk	26/7	21.80	86.1	0.977	2.89	2.377
Drake	26/7	28.11	138	1.626	2.89	1.877
Carillon	48/7	30.48	136	1.745	1.62	1.979
Gatineau	48/7	33.00	155	2.042	1.62	1.852
Bersfort	48/7	35.58	180	2.375	1.62	1.720
Duck	54/7	24.21	101	1.160	1.58	2.237
Crow	54/7	26.28	117	1.371	1.58	2.075
Curlew	54/7	31.59	163	1.980	1.58	1.758
Falcon	72/7	37.69	172	2.501	1.11	1.817
Nelson I	72/7	40.61	200	2.902	1.11	1.687
Nelson II	72/7	43.20	226	3.277	1.11	1.587

As it can be clearly assessed:

- γ^2 parameter is constant for conductors having the same stranding, i.e. it does not depend upon the different mechanical and/or geometrical characteristics of different conductors belonging to the same stranding class (Figure 3.62);
- the proportionality coefficient k decreases as the diameter of the conductor increases, within the different stranding classes (Figure 3.63).

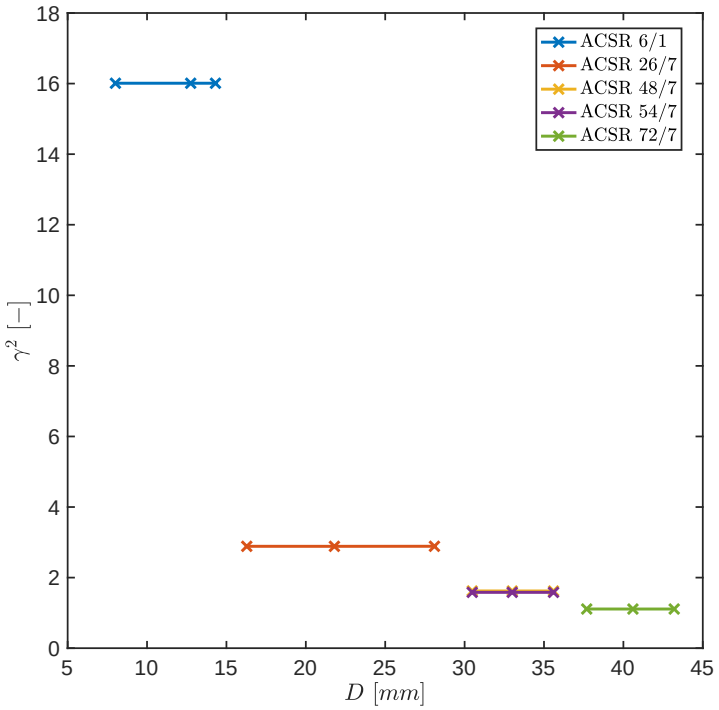

Figure 3.62. Plot of the non-dimensional parameter γ^2 versus conductor diameter D.

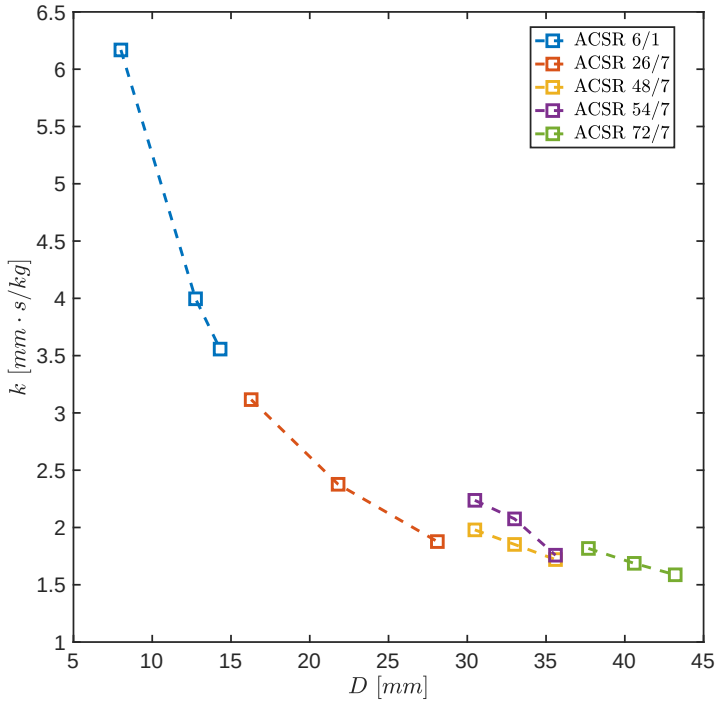

Figure 3.63. Plot of the proportionality coefficient k versus conductor diameter D.

In the following Figures, the plots of $M_0 - \eta$ and $\chi_0 - \eta$ relationships are reported for some of the ACSR conductors listed in Table A.1, with $\eta \in [0, 1/2]$, for the sake of completeness and to exemplify the procedures explained Subsections 3.6.1 and 3.6.2.

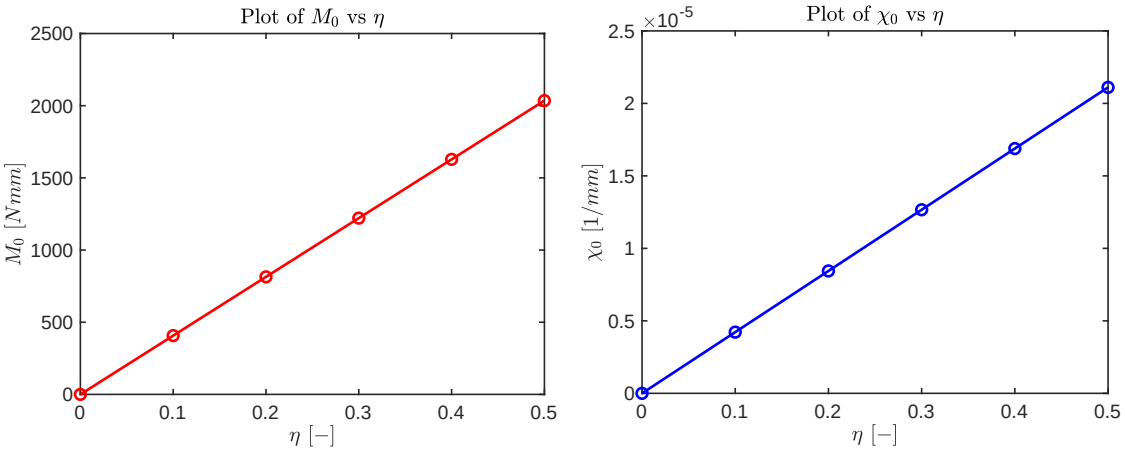

Figure 3.64. Penguin conductor: plots of the relationships $M_0 - \eta$ and $\chi_0 - \eta$, P.M.C and S.C.1.

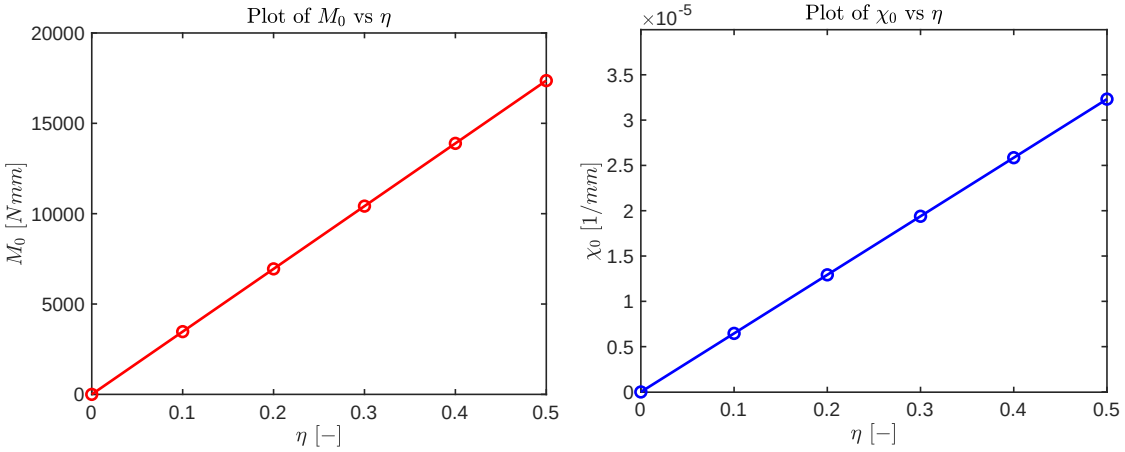

Figure 3.65. Hawk conductor: plots of the relationships $M_0 - \eta$ and $\chi_0 - \eta$, P.M.C and S.C.1.

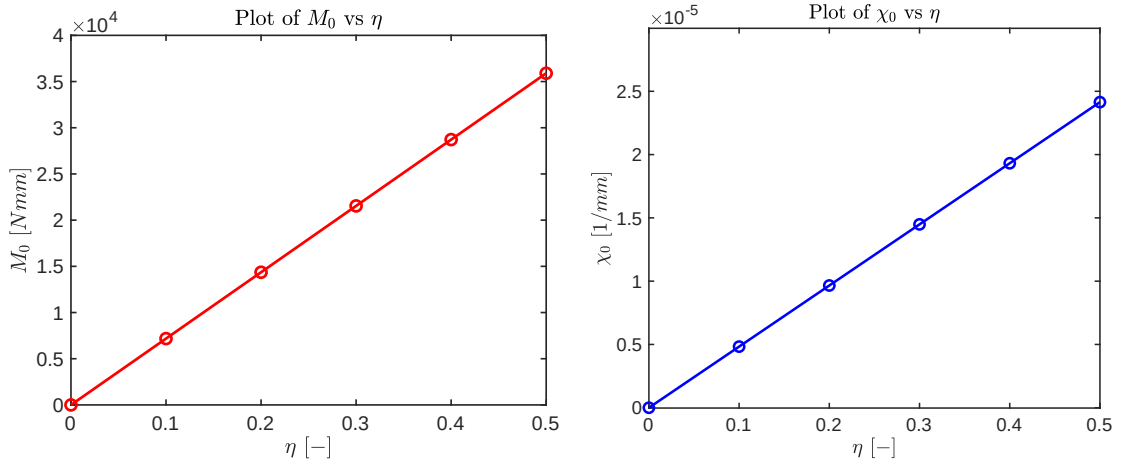

Figure 3.66. Drake conductor: plots of the relationships $M_0 - \eta$ and $\chi_0 - \eta$, P.M.C and S.C.1.

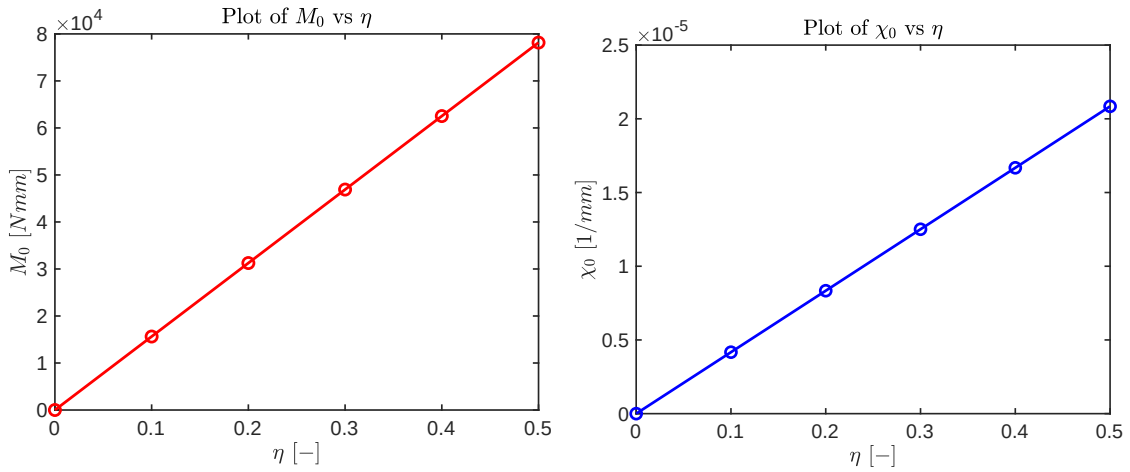

Figure 3.67. Bersfort conductor: plots of the relationships $M_0 - \eta$ and $\chi_0 - \eta$, P.M.C and S.C.1.

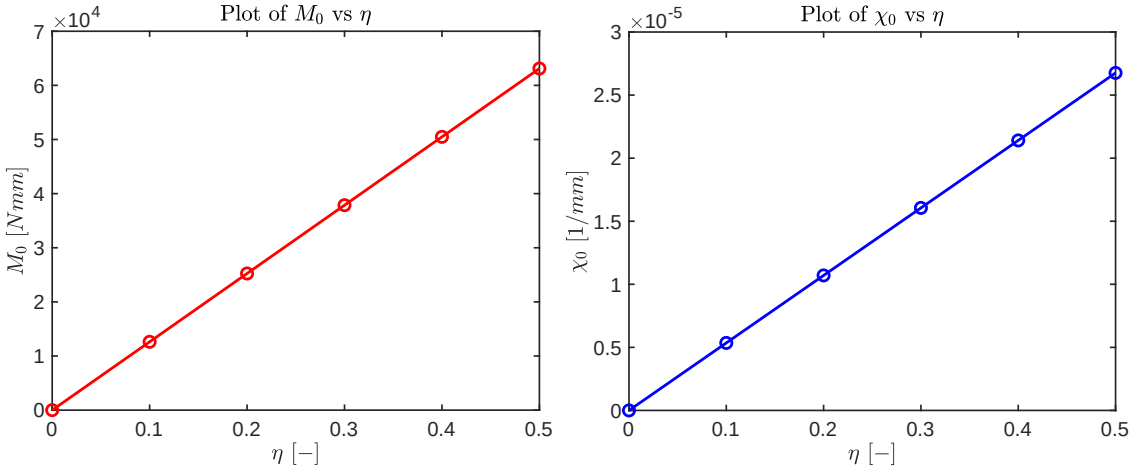

Figure 3.68. Curlew conductor: plots of the relationships $M_0 - \eta$ and $\chi_0 - \eta$, P.M.C and S.C.1.

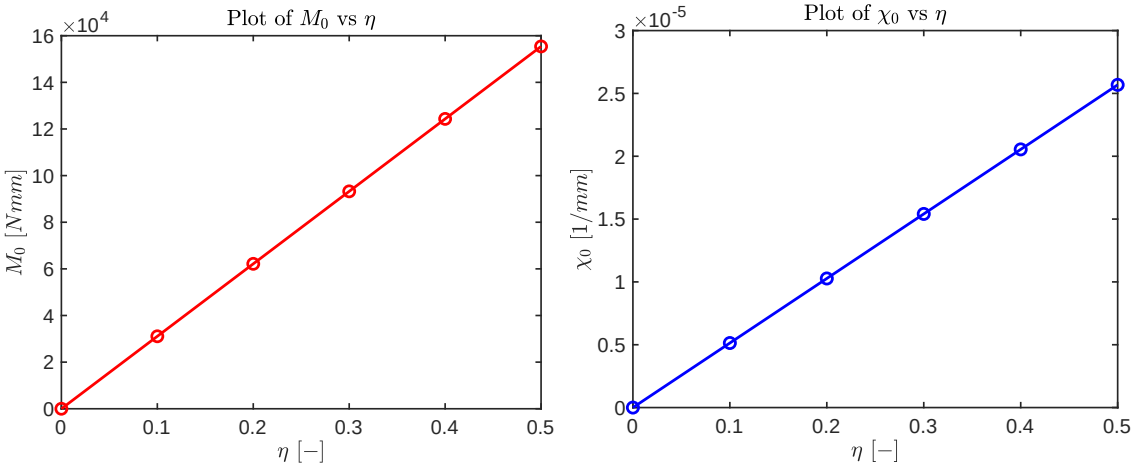

Figure 3.69. Nelson I conductor: plots of the relationships $M_0 - \eta$ and $\chi_0 - \eta$, P.M.C and S.C.1.

3.7 Construction parameter c_0: Results

In this section, the values of the construction parameter c_0 obtained for the different radial pressure models and sliding conditions are reported and discussed.
Such values of c_0 have been obtained by applying the numerical procedure implemented in a user-coded Matlab program, which have been addressed in Subsection 3.6.1.
The mechanical and geometrical properties of the considered sample of 15 ACSR conductors are listed in Appendix A, whereas their cross-sections schemes are conveniently reported in Appendix B.
In particular, a total of 18 combinations of c_0 values for each conductor cross-sections are possible, coming from the product of total number of sliding conditions implemented and the total number of radial pressures models considered, i.e. $6 \times 3 = 18$.
In order to allow for an easier assessment of the various results, the full tables are collected in Appendix F.
In this section, some considerations are done and the more relevant results are reported.
First of all, after the considerations made in Subsection 3.4.2, it is possible to observe that the Radial Pressure Model B is slightly different from the Radial Pressure Model A, just because it neglects the correction coefficients c^{int} and c^{ext}. So in this section, only the P.M A and C will be considered, for the sake of simplicity, being the most different ones.
For what concerns the sliding conditions, it is possible to recognize a very little difference between sliding condition 1 and 3 and between sliding condition 2 and 4 (being radial pressures model fixed). For this reason, only sliding conditions 5 and 6 will be reported here and will be compared with the reference situation given by sliding conditions 1 and 2.
In fact, as a general comment, the angles β^{ext} and β^{int} considered in Sliding Conditions 3-4-5-6 are small, so that their cosine won't be far from 1, leading to a slight difference in term of results with respect to the reference situations in which tangential contact forces are horizontal (S.C.1 and S.C.2).
See subsection 3.5.3 for further details about the various slip conditions and their closed-form expressions for the characterization of the differential equation describing the wire axial force admissible domain.
At the and, a total of 8 combinations are here considered, i.e. 4 S.C.s $\times$ 2 P.M.s $= 8$.

3.7.1 ACSR 6/1 Conductors

The values of c_0 coefficient for 3 ACSR 6/1 are reported in Table 3.14, 3.15 and 3.16.

Table 3.14. ACSR 6/1 Sparrow: coefficient c_0 $(1/m)$.

	P.M. A	P.M. C
S.C. 1	0.267	0.267
S.C. 2	0.267	0.267
S.C. 5	0.263	0.267
S.C. 6	0.263	0.267

Table 3.15. ACSR 6/1 Pigeon: coefficient c_0 $(1/m)$.

	P.M. A	P.M. C
S.C. 1	0.158	0.158
S.C. 2	0.158	0.158
S.C. 5	0.156	0.158
S.C. 6	0.156	0.158

Table 3.16. ACSR 6/1 Penguin: coefficient c_0 $(1/m)$.

	P.M. A	P.M. C
S.C. 1	0.141	0.141
S.C. 2	0.141	0.141
S.C. 5	0.139	0.141
S.C. 6	0.139	0.141

As it can be clearly assessed, for S.C.1 and S.C.2 there is no difference in the prediction of c_0 by applying the Radial Pressure Models (as well as for S.C.3 and S.C.4). The difference arises in the case of Sliding Conditions 5 and 6, where the angle β^{int} on the internal side of the conductor slightly influences the result of c_0.
This was of course expected, since the Radial Pressures Model has no influence at all on single-layer conductors. The difference in the results between the P.M.A and P.M.C (for fixed S.C.s 5 or 6) is only due to the coefficient c^{ext}.

3.7.2 ACSR Multilayer Conductors

As in can be assess from Tabl. 3.17 to Tab. 3.28, the situation drastically changes in the case of multilayer conductors.
Different values of construction parameter c_0 are attained for the different cases.
It is interesting to notice that the value of c_0 for Slip Condition 2 is not influenced by the Radial Pressures Model. This is a direct consequence of the fact that, in all the analysis performed, the internal friction coefficient coincides with the external one, i.e: $\mu^{int} = \mu^{ext}$. This leads the second term into Eq. 3.143b to vanish, so that the dependence upon the non-dimensional radial contact forces per unit of length $\hat{f}_r^{ext}$ is lost.
This is a general comment that is valid also for all the other conductors, with different stranding, provided that the external friction coefficient is equal to the internal one.
Another general comment is about the obtainment of the maximum and minimum values of the construction parameter c_0. In particular, the maximum value is attained for the case of P.M.A, with S.C.1, while the minimum for the case of P.M.A, with S.C.6.

Table 3.17. ACSR 26/7 Partridge: coefficient c_0 $(1/m)$.

	P.M. A	P.M. C
S.C. 1	0.404	0.300
S.C. 2	0.177	0.177
S.C. 5	0.400	0.300
S.C. 6	0.173	0.177

Table 3.18. ACSR 26/7 Hawk: coefficient c_0 $(1/m)$.

	P.M. A	P.M. C
S.C. 1	0.290	0.215
S.C.2	0.127	0.127
S.C. 5	0.287	0.215
S.C. 6	0.124	0.127

Table 3.19. ACSR 26/7 Drake: coefficient c_0 $(1/m)$.

	P.M. A	P.M. C
S.C. 1	0.217	0.161
S.C. 2	0.095	0.095
S.C. 5	0.214	0.161
S.C. 6	0.093	0.095

Table 3.20. ACSR 48/7 Bersfort: coefficient c_0 $(1/m)$.

	P.M. A	P.M. C
S.C. 1	0.190	0.139
S.C. 2	0.069	0.069
S.C. 5	0.189	0.139
S.C. 6	0.068	0.069

Table 3.21. ACSR 48/7 Carillon: coefficient c_0 $(1/m)$.

	P.M. A	P.M. C
S.C. 1	0.228	0.167
S.C. 2	0.083	0.083
S.C. 5	0.227	0.167
S.C. 6	0.081	0.083

Table 3.22. ACSR 48/8 Gatineau: coefficient c_0 $(1/m)$.

	P.M. A	P.M. C
S.C. 1	0.205	0.150
S.C. 2	0.074	0.074
S.C. 5	0.204	0.150
S.C. 6	0.073	0.074

Table 3.23. ACSR 54/7 Duck: coefficient c_0 $(1/m)$.

	P.M. A	P.M. C
S.C. 1	0.412	0.295
S.C. 2	0.138	0.138
S.C. 5	0.409	0.295
S.C. 6	0.135	0.138

Table 3.24. ACSR 54/7 Crow: coefficient c_0 $(1/m)$.

	P.M. A	P.M. C
S.C. 1	0.373	0.267
S.C. 2	0.125	0.125
S.C. 5	0.370	0.267
S.C. 6	0.122	0.125

Table 3.25. ACSR 54/7 Curlew: coefficient c_0 $(1/m)$.

	P.M. A	P.M. C
S.C. 1	0.248	0.178
S.C. 2	0.084	0.084
S.C. 5	0.246	0.178
S.C. 6	0.083	0.084

Table 3.26. ACSR 72/7 Falcon: coefficient c_0 $(1/m)$.

	P.M. A	P.M. C
S.C. 1	0.261	0.184
S.C. 2	0.075	0.075
S.C. 5	0.259	0.184
S.C. 6	0.073	0.075

Table 3.27. ACSR 72/7 Nelson I: coefficient c_0 $(1/m)$.

	P.M. A	P.M. C
S.C. 1	0.243	0.171
S.C. 2	0.070	0.070
S.C. 5	0.241	0.171
S.C. 6	0.068	0.070

Table 3.28. ACSR 72/7 Nelson II: coefficient c_0 $(1/m)$.

	P.M. A	P.M. C
S.C. 1	0.228	0.161
S.C. 2	0.066	0.066
S.C. 5	0.226	0.161
S.C. 6	0.064	0.066

It is now convenient to plot the construction parameters c_0 against the conductor diameters D, subdivided by stranding. Since four slip conditions were reported in the previous tables, then four graphs (one for each imposed sliding condition) are realized (Figures 3.70, 3.71, 3.72 and 3.73). In this way, it is possible to appreciate both the trend of c_0 versus D for different stranding classes and the difference in terms of results caused by the Radial Contact Pressures Models A and C.
Moreover, other four graphs are realized for the case of multilayer conductors, in which the Radial Contact Pressures Model is fixed, and the difference in the results of c_0 within the various sliding conditions can be appreciated (Figures 3.74, 3.75, 3.76 and 3.77).

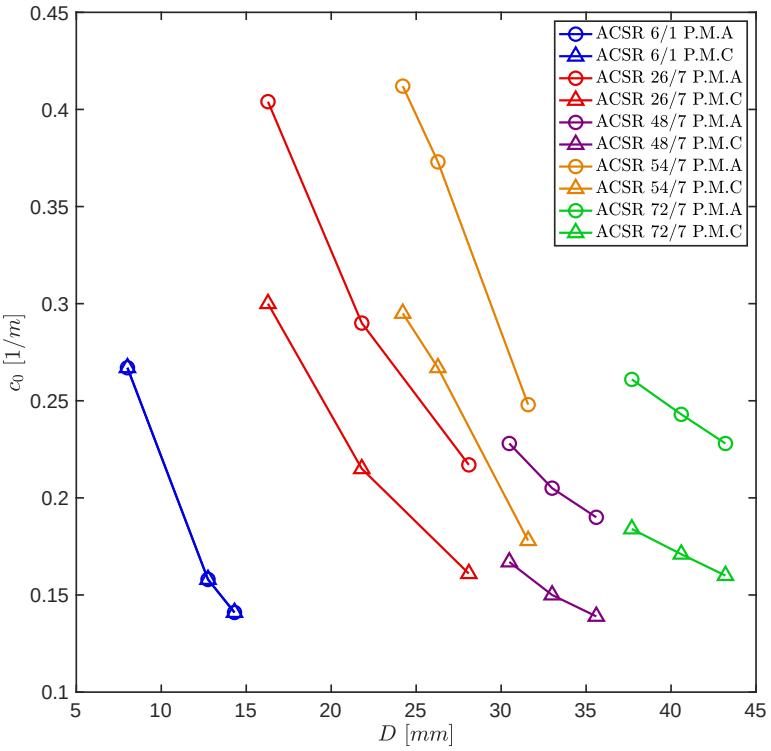

Figure 3.70. Plot of construction parameters c_0 vs strand diameters D for Slip Condition 1.

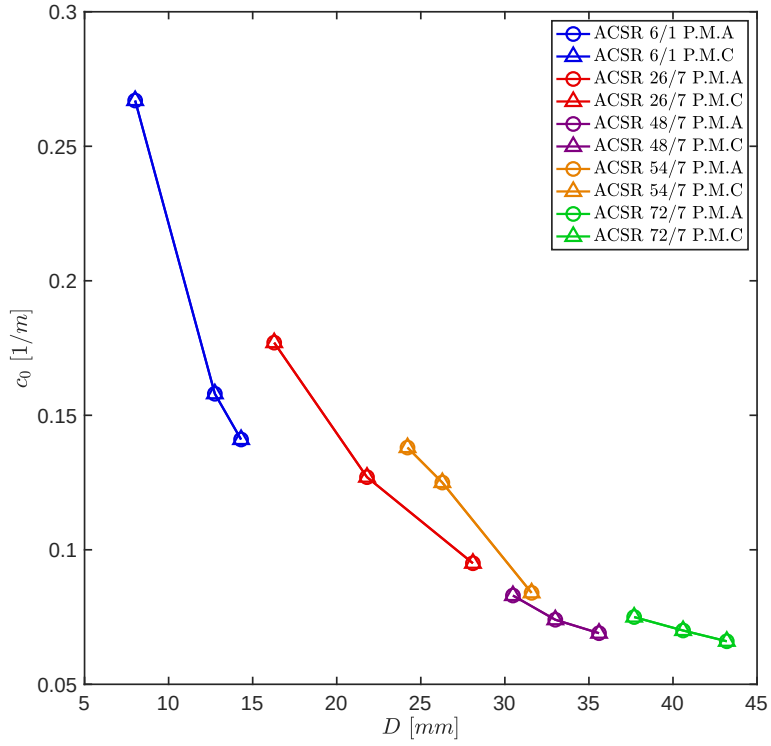

Figure 3.71. Plot of construction parameters c_0 vs strand diameters D for Slip Condition 2.

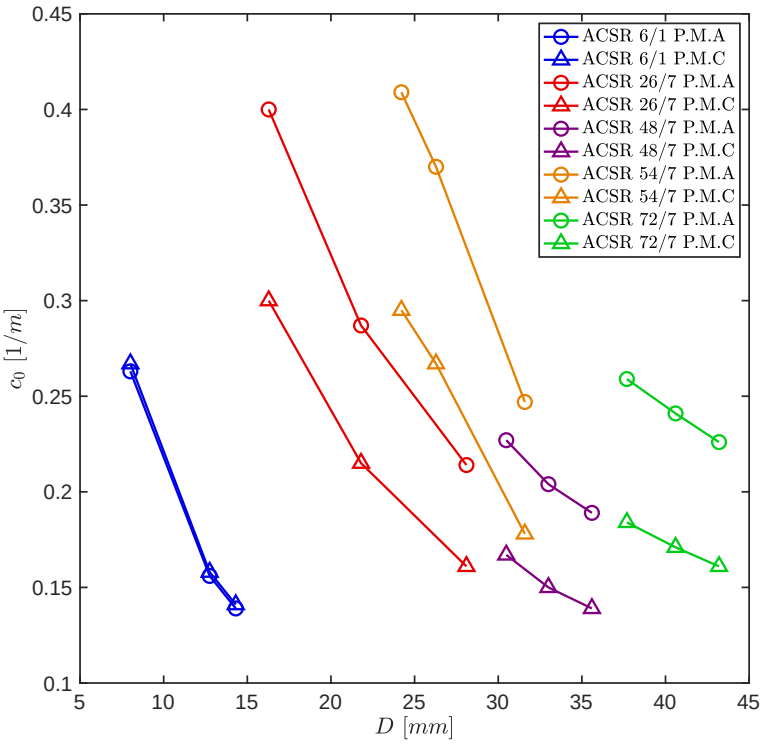

Figure 3.72. Plot of construction parameters c_0 vs strand diameters D for Slip Condition 5.

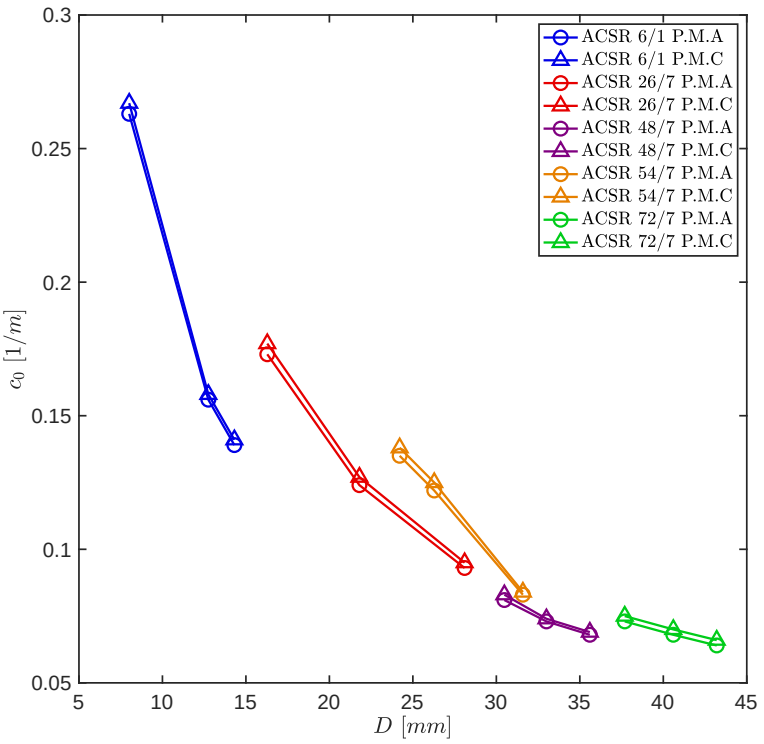

Figure 3.73. Plot of construction parameters c_0 vs strand diameters D for Slip Condition 6.

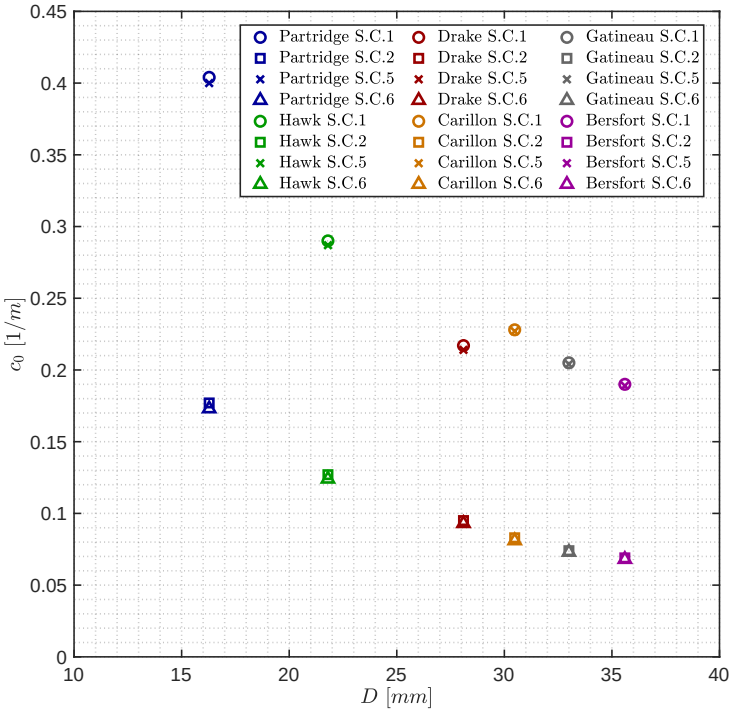

Figure 3.74. Plot of construction parameters c_0 vs strand diameters D for Pressure Model A. ACSR 26/7 and ACSR 48/7 conductors.

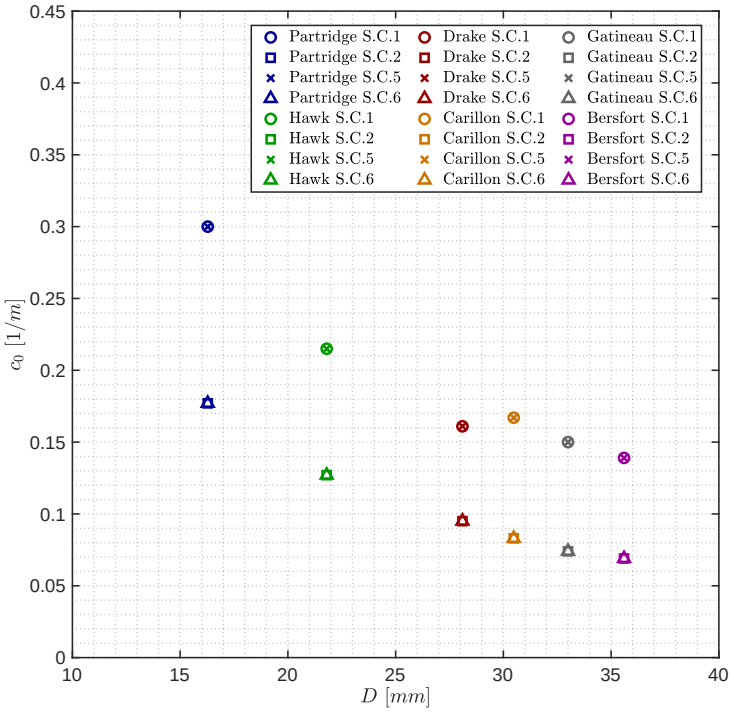

Figure 3.75. Plot of construction parameters c_0 vs strand diameters D for Pressure Model C. ACSR 26/7 and ACSR 48/7 conductors.

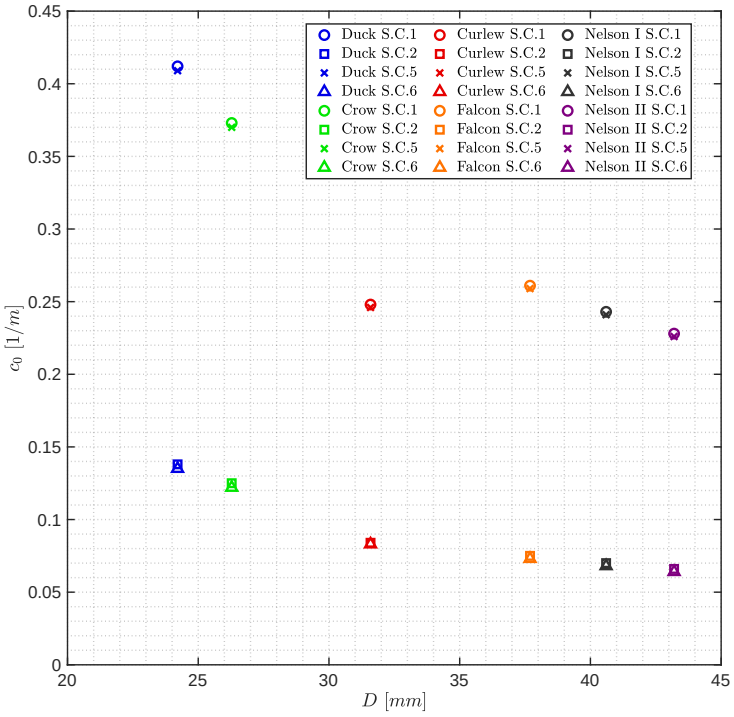

Figure 3.76. Plot of construction parameters c_0 vs strand diameters D for Pressure Model A. ACSR 54/7 and ACSR 72/7 conductors.

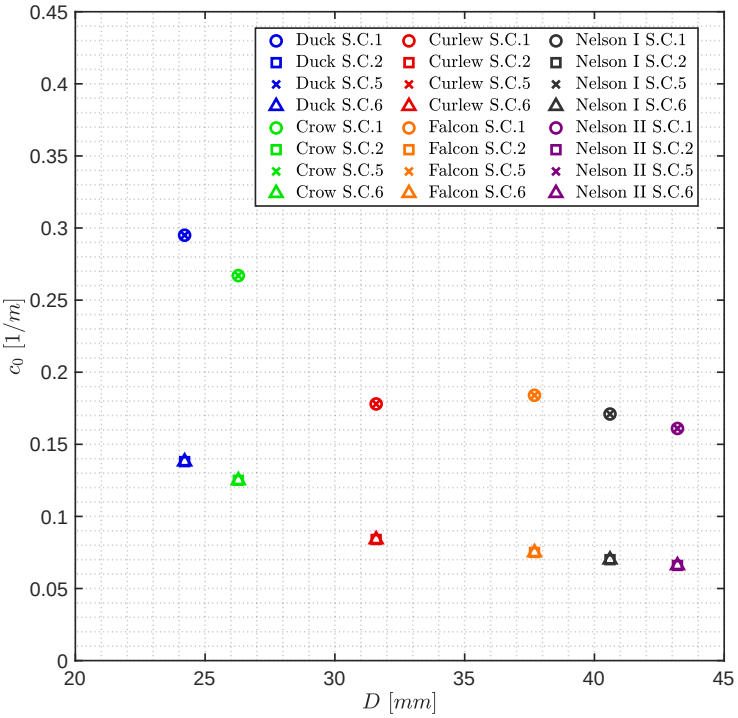

Figure 3.77. Plot of construction parameters c_0 vs strand diameters D for Pressure Model C. ACSR 54/7 and ACSR 72/7 conductors.

Conclusions

From the previous graphs, some interesting conclusion can be drawn:

1. In general terms, the construction parameter c_0 decreases as the conductor diameter D increases, within the same stranding class;

2. Radial Pressures Models A and C do not affect results of c_0 for 6/1 conductors both for Slip conditions 1 and 2, while for Slip Conditions 5 and 6 they have a very little influence;

3. Results of c_0 obtained with Slip Conditions 2 are not influenced by the Radial Pressures Transmission Models, because in general, for a generic layer of wires j, it holds: $\mu_j^{int} = \mu_j^{ext}$ and the dependence upon $\hat{f}_r^{ext}$ is lost, as already recalled;

4. Radial Pressure Models A and C slightly affect results of c_0 for all the different stranding classes, in the case of Slip Condition 6 (Fig. 3.73);

5. The biggest differences in the results of c_0 (by changing the Radial Pressures Model) are obtained for Slip Conditions 1 and 5: here the Radial Pressures Models play a big role, and in general, a vertical translation of the curves for different stranding classes is observed, passing from P.M.C to P.M.A. (Fig.s 3.70 and 3.72);

6. The maximum values of the construction parameter c_0 are attained by applying the Radial Pressures Model A and enforcing Slip Condition 1, within the same conductor cross-section;

7. The minimum values of the construction parameter c_0 are attained by applying the Radial Pressures Model A and enforcing Slip Condition 6, within the same conductor cross-section;

8. The "median" values of the construction parameter c_0 are attained by applying the Radial Pressures Model C and enforcing Slip Condition 1, within the same conductor cross-section;

9. By fixing one radial pressure model (either P.M.A or P.M.C.), the difference of results of c_0 obtained with S.C.1 and S.C.5 is negligible (Fig.s 3.74-3.77);

10. By fixing one radial pressure model (either P.M.A or P.M.C.), the difference of results of c_0 obtained with S.C.2 and S.C.6 is negligible (Fig.s 3.74-3.77).

11. At the end, what plays a big role in the variation of c_0 due to the sliding conditions, is the direction of tangential forces, because angles β^{ext} and β^{int} are obviously small, so that their effect is limited.

12. As a final conclusion of this part of the work, the linear interpolations of the construction parameter c_0 as a function of the strand diameter D are provided for different stranding classes and for the most three significant combinations of Radial Pressure Models and Sliding Conditions (namely, the one declared at points 6, 7 and 8 of this list). See the next paragraph for the obtainment of the linear regression coefficients.

Linear Interpolation

In this paragraph, the linear interpolation of the construction parameter c_0 as a function of the strand diameter D is performed.
The regression coefficients of the linear fitting will be useful for the application of theoretical self-damping models for ACSR conductors (see Chapter 4).
The case of single-layer conductors is distinguished from the case of multi-layer conductors. This is an obvious consequence of the results obtained in this section, being the construction parameter c_0 of 6/1 conductors slightly affected by the sliding conditions 5 and 6 only (see Subsection 3.7.1).
Figure 3.78 shows the linear interpolation of the construction parameter for the case of ACSR 6/1 conductors, P.M.s A or C and S.C.s 1 or 6.

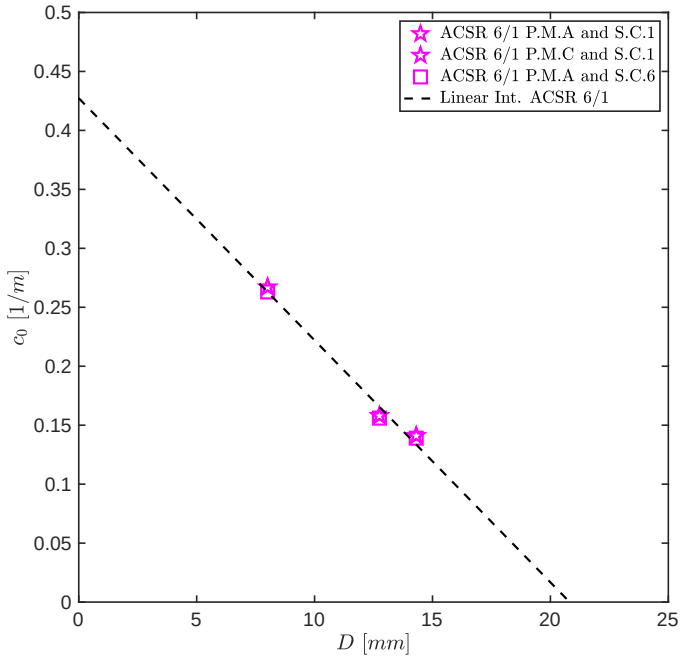

Figure 3.78. Linear interpolation of c_0 vs D for single-layer conductors.

The interpolating line has the following equation:

$$c_0 = 0.4273 - 0.0205D \tag{3.166}$$

Figures 3.79, 3.80 and 3.81 show the plots of c_0 as a function of the strand diameters D and its linear interpolation for the case of multi-layer conductors, distinguishing on the basis of the stranding classes. Tables 3.31, 3.30 and 3.29 collects the equations of the linear fitting for the various stranding classes. Three situations are considered:

- Plot of the minimum values of c_0, attained for the combination of Radial Pressures Model A and Sliding Condition 6 (see Fig. 3.79 and Tab. 3.29).
- Plot of the median values of c_0, attained for the combination of Radial Pressures Model C and Sliding Condition 1 (see Fig. 3.80 and Tab. 3.30).
- Plot of the maximum values of c_0, attained for the combination of Radial Pressures Model A and Sliding Condition 1 (see Fig. 3.81 and Tab. 3.31).

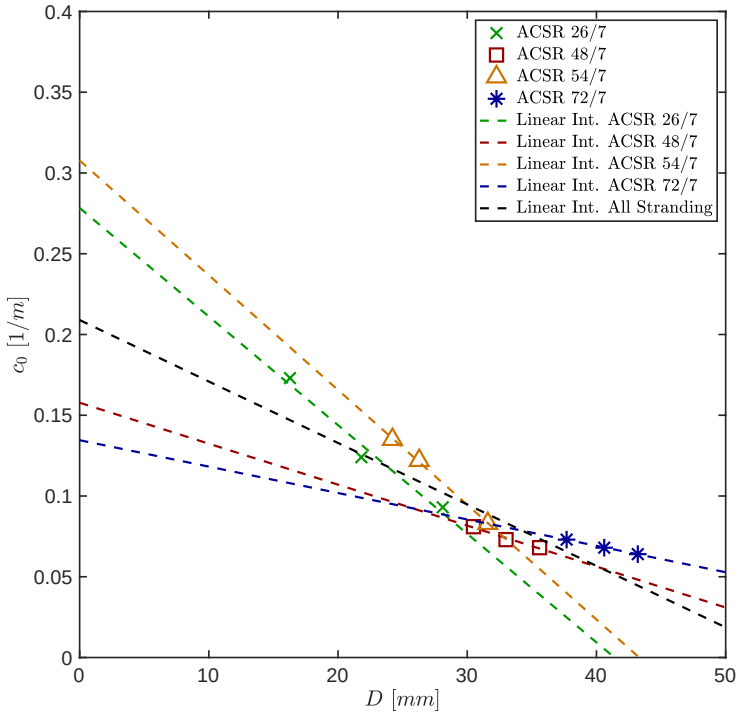

Figure 3.79. Linear interpolation of c_0 vs D for Pressure Model A and S.C.6. Multi-layer conductors.

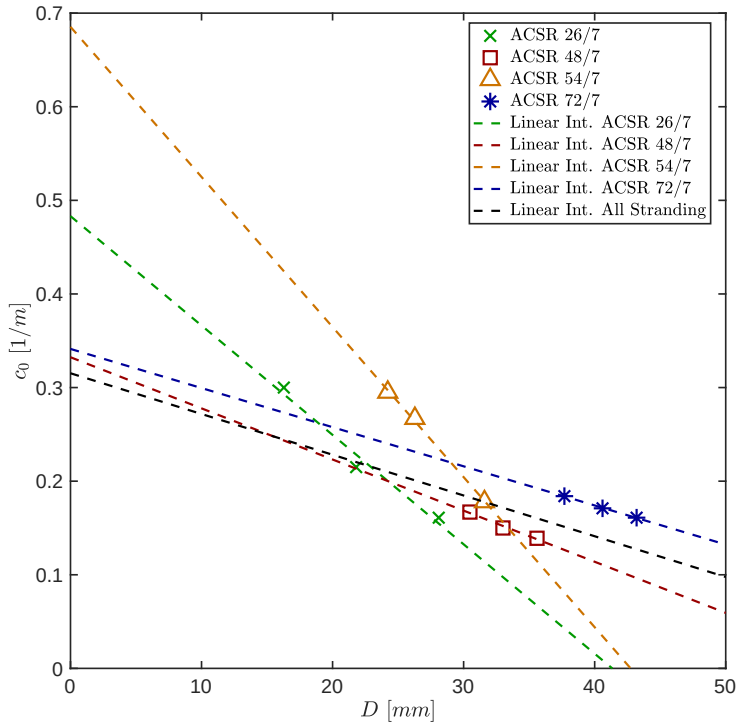

Figure 3.80. Linear interpolation of c_0 vs D for Pressure Model C and S.C.1. Multi-layer conductors.

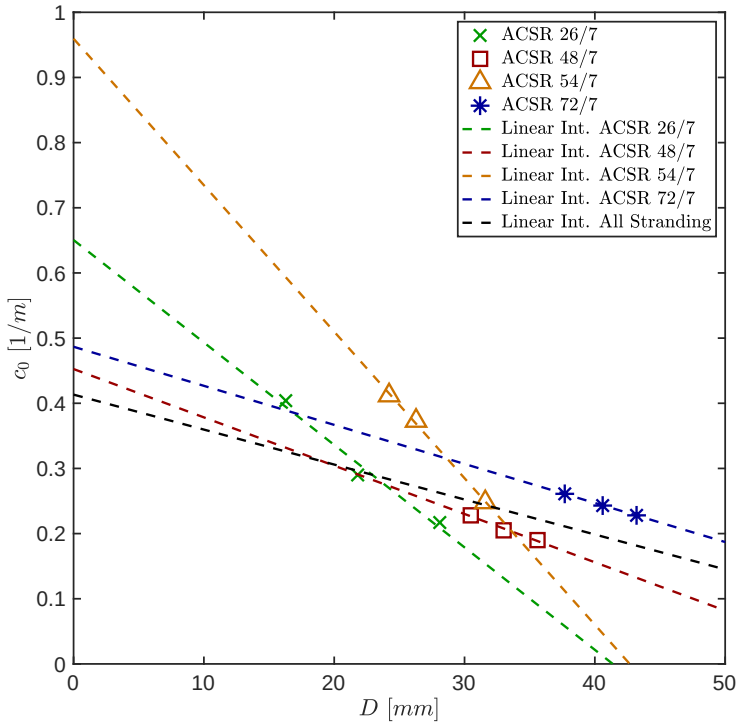

Figure 3.81. Linear interpolation of c_0 vs D for Pressure Model A and S.C.1. Multi-layer conductors.

Table 3.29. Linear Interpolations of c_0 vs D for different stranding in the case of P.M.A and S.C.6.

Stranding	Linear Interpolation
ACSR 26/7	$c_0 = 0.2784 - 0.0067\,D$
ACSR 48/7	$c_0 = 0.1577 - 0.0025\,D$
ACSR 54/7	$c_0 = 0.3077 - 0.0071\,D$
ACSR 72/7	$c_0 = 0.1345 - 0.0016\,D$
All	$c_0 = 0.2089 - 0.0038\,D$

Table 3.30. Linear Interpolations of c_0 vs D for different stranding in the case of P.M.C and S.C.1.

Stranding	Linear Interpolation
ACSR 26/7	$c_0 = 0.4831 - 0.1170\,D$
ACSR 48/7	$c_0 = 0.3324 - 0.0055\,D$
ACSR 54/7	$c_0 = 0.6853 - 0.0160\,D$
ACSR 72/7	$c_0 = 0.3413 - 0.0042\,D$
All	$c_0 = 0.3153 - 0.0044\,D$

Table 3.31. Linear Interpolations of c_0 vs D for different stranding in the case of P.M.A and S.C.1.

Stranding	Linear Interpolation
ACSR 26/7	$c_0 = 0.6505 - 0.0157\,D$
ACSR 48/7	$c_0 = 0.4525 - 0.0074\,D$
ACSR 54/7	$c_0 = 0.9595 - 0.0225\,D$
ACSR 72/7	$c_0 = 0.4867 - 0.0060\,D$
All	$c_0 = 0.4133 - 0.0054\,D$

3.8 Application: description of the strand static response

In this Section, the impact of the different values obtained for the coefficient c_0 (see Section 3.7) is assessed with reference to a well-documented bending test (Baumann and Novak, 2017) performed on a short stretch of 2 m length of an ACSR Drake conductor.
The cable was first subjected to an horizontal force $H = 0.2\,RTS$ and then loaded with a transverse force F applied at midspan.
The force F was growing from zero up to the maximum value $0.05\,H$.
Geometric and mechanical parameters $(D, RTS, EI_{max}, EI_{min}, m)$ of the ACSR Drake are reported in Appendix A, whereas its cross-section is depicted in Appendix B (see Fig. B.2c).
By assuming a unitary stiffness reduction parameter (i.e. $\beta = 1$), the ratio of the bending stiffness results:

$$\gamma^2 = \frac{EI_{min}}{EI_{max,ef}} = \frac{EI_{min}}{\beta EI_{max}} = \frac{EI_{min}}{EI_{max}} = 2.89\% \tag{3.167}$$

Furthermore, an interwire friction coefficient $\mu = 0.5$ was selected, coherently with the consideration reported in (3).
The scheme of the tested ACSR Drake conductor, as well as a photo of the test bench are reported in Figures 3.82 and 3.83.
The aim of the simulations is to verify the sensitivity of the cable response to the parameter c_0, by means of a user-coded Matlab program which solves the boundary value problem formulated in (Foti et al., 2021).
In particular, the cable response can be studied by solving the following non-linear second order differential equation:

$$EI_{max,ef}\Big[\gamma^2 + (1-\gamma^2)\exp\Big(-\frac{|d\theta/ds|}{\chi_0}\Big)\Big]\frac{d^2\theta}{ds^2} = H\sin(\theta) - (V - ws)\cos(\theta) \tag{3.168}$$

with the boundary conditions accounting for the symmetry of the problem:

$$\theta(s=0) = \theta(s=l/2) = 0 \tag{3.169}$$

where s is an arc-length coordinate running over the cable span, $\theta(s)$ is the inclination angle of the cable centerline to the horizontal direction, and V is the vertical reaction arising at the supports, which is calculated by considering simultaneously two loading conditions:

1. the suspended cable subject to a constant load per unit of length $w = m\,g$;
2. the suspended weightless ($w = 0$) cable subject to the concentrated force F applied at midspan.

Then, the vertical reaction is simply:

$$V = \frac{wl + F}{2} \tag{3.170}$$

It is worth noting that the dependence of the cable response to the parameter c_0 is hidden into the evaluation of the first-yielding curvature χ_0:

$$\chi_0 = c_0\,\mu\,\eta \tag{3.171}$$

where η is the ratio between the axial force in the cable and its Rated Tensile Strength RTS:

$$\eta(s) = \frac{N(s)}{RTS} \tag{3.172}$$

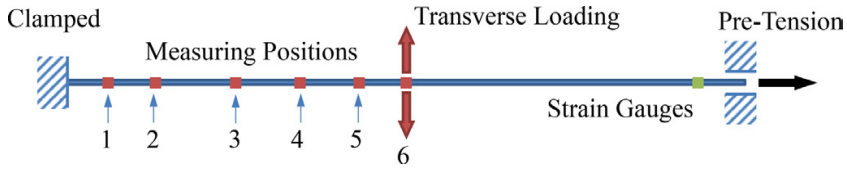

Figure 3.82. Schematic of the test bench, from (Bauman and Novak, 2017).

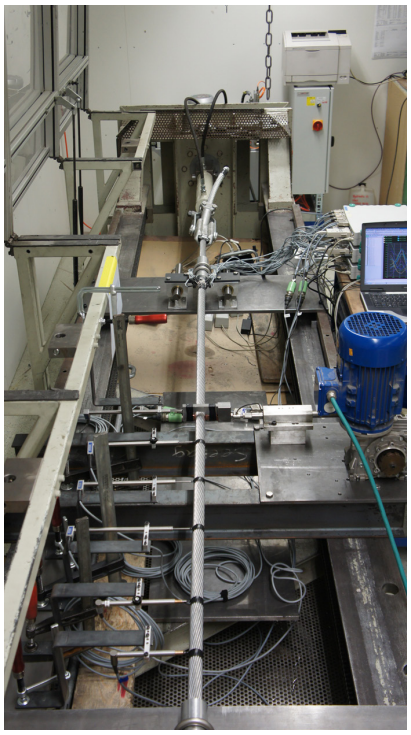

Figure 3.83. Photo of the test bench with the ACSR Drake conductor, from (Bauman and Novak, 2017).

It is also possible to rely on the non-dimensional formulation of the problem, that will conveniently adopted for the following developments (see (29) for further details).
One can introduce the non-dimensional arc-length coordinate:

$$\xi = s/l, \ \xi \in [0, 1/2] \tag{3.173}$$

leading to the obtainment of the following differential equation:

$$\varepsilon^2 \Big[\gamma^2 + (1-\gamma^2)\exp\Big(-\frac{|\Theta'|}{X_0}\Big)\Big]\Theta'' = \sin(\Theta) - \Big[(\omega+\psi)/2 - \omega\xi\Big]\cos(\Theta) \tag{3.174}$$

where $\Theta = \theta(s(\xi))$ and:

$$\varepsilon^2 = EI_{max,ef}/(Hl^2), \qquad X_0 = \chi_0\, l, \qquad \omega = wl/H, \qquad \psi = F/H \tag{3.175}$$

The boundary conditions naturally translate to:

$$\Theta(\xi = 0) = \Theta(\xi = 1/2) = 0 \tag{3.176}$$

3.8.1 Cable Deflection

The following plot shows the prediction of the non-dimensional transverse displacement $v^* = v(s(\xi))/l$ of the cable for different values of the construction parameter c_0.
Such values have been computed and collected in Section 3.7 according to the numerical procedure explained in Subsection 3.6.1.
The full range of values of c_0 for the ACSR Drake conductor can be conveniently read in Appendix F (see Tab. F.6).
Due to the symmetry of the cable, quantities are plotted for the non-dimensional abscissa $\xi \in [0, 1/2]$. The two curves obtained from the application of the model by Foti et al. (2021) under the simplifying assumption of linearly elasticity and constant bending stiffness equal to EI_{min} and EI_{max} are also shown.
The experimental results and the results obtained with a Finite Element Model developed with beam elements by Baumann and Novak are reported as well.

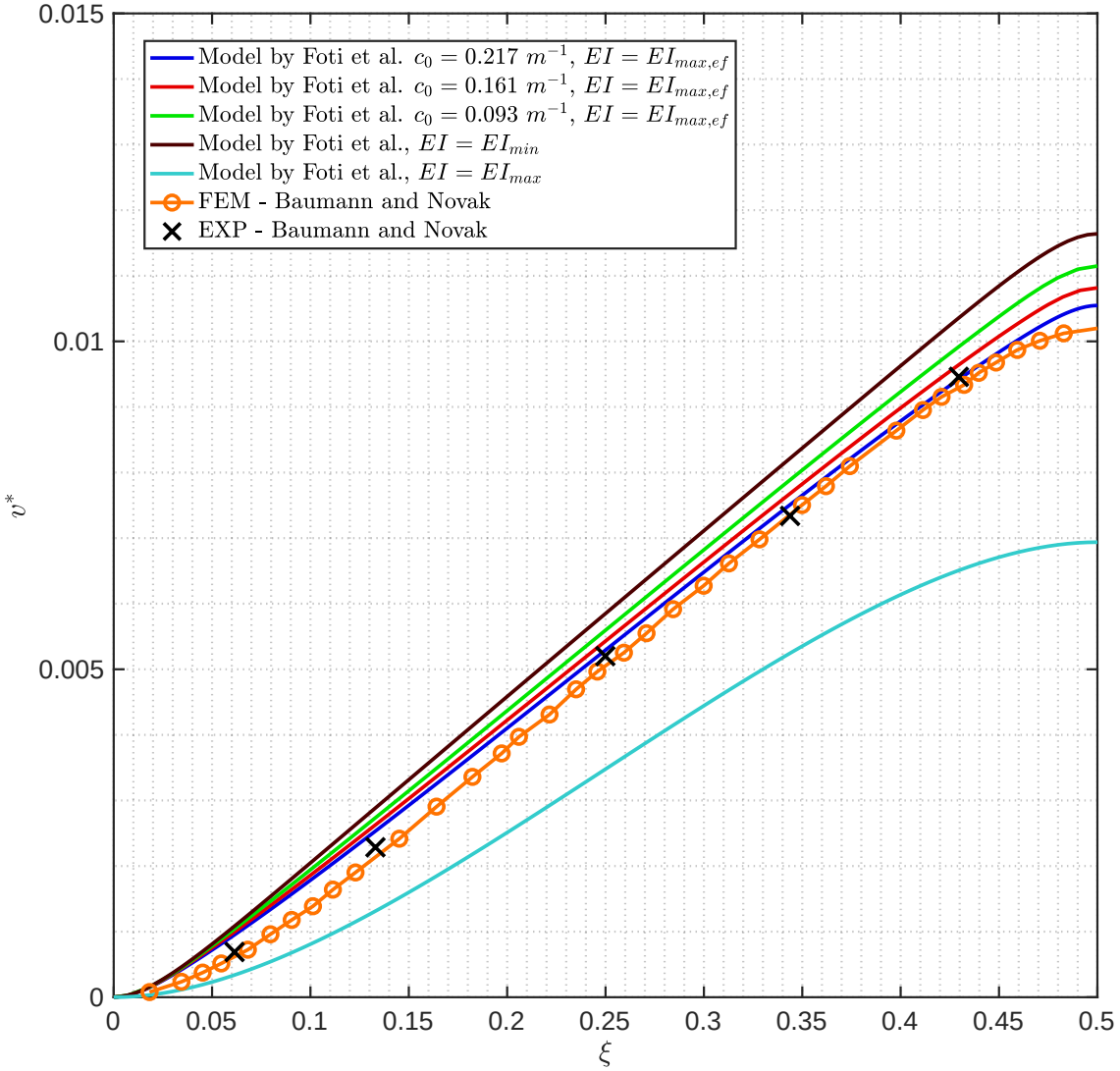

Figure 3.84. Plot of the non-dimensional transverse displacement $v^*(\xi)$ over the interval $\xi \in [0, 1/2]$ for different values of construction parameter c_0.

It can be observed that, as c_0 decreases, the predicted non-dimensional deflection is increasing. The FEM solution by Baumann and Novak is a little bit stiffer with respect to the experimental results; this is consistent with the intrinsic nature of the solution procedure, which lead to the converge of displacements from below.
On the other hand, the model proposed by Foti et al. in (29) leads to a slight overestimation of v^*, which is on the safe side. However, the predicted non-dimensional deflection with construction parameter $c_0 = 0.217\ m^{-1}$ is giving very accurate results, especially for $\xi \in [1/4, 1/2]$.
In the first branch of the curves, for $\xi < 0.25$ the overestimation of the non-dimensional deflection is bigger and the difference between different values of c_0 is not so important. The latter, is indeed important at the midspan of the cable.
It is worth noticing that the non-dimensional deflection predicted by the simplified model with constant bending stiffness $EI = EI_{max}$ is dangerously underestimating the real response of the cable. The relative difference of the non-dimensional deflections at midspan is about 32.3%. On the contrary, the non-dimensional deflection predicted by the simplified model with constant bending stiffness $EI = EI_{min}$ is overestimating the real response of the cable of about 13.5% (at midspan).
At the end, it is possible to say that, in the need of a precise ad reliable estimation of the cable response under a generic loading condition, the correct choice of the construction parameter c_0 is indeed an important aspect, in order to retrieve a representative and appropriate modeling of its real behavior.

3.8.2 Cable Bending Stiffness

Figure 3.85 shows the variation of the non-dimensional bending stiffness $EI^* = EI/(Hl^2)$ predicted by the model for different values of the construction parameter c_0.
Such values were determined in Section 3.7 according to the numerical procedure explained in Subsection 3.6.1.
The non-dimensional bending stiffness EI^* is normalized by the parameter ε^2. One has:

$$\frac{EI^*(\xi)}{\varepsilon^2} = \frac{EI(\xi)}{Hl^2} \cdot \frac{Hl^2}{EI_{max,ef}} = \frac{EI(\xi)}{\beta EI_{max}} = \frac{EI(\xi)}{EI_{max}} \tag{3.177}$$

Eq. 3.177 has the following meaning: once EI^*/ε^2 reaches the unitary value, the maximum bending stiffness is attained. Conversely, if the straight line representing γ^2 is touched, then the bending stiffness is at its minimum value. As it can be seen from Fig. 3.85, the models with different values of construction parameters substantially differ in the interval $\xi \in [0.05, 0.20]$ and, symmetrically for $\xi \in [0.3, 0.45]$.
The γ^2 parameter is constant and equal to the ratio of the minimum bending stiffness EI_{min} and the maximum bending stiffness EI_{max}, having considered a unitary stiffness reduction coefficient $\beta = 1$.
For the sake of convenience, the curves obtained under the simplifying assumption of linearly elasticity and constant bending stiffness equal to EI_{min} and EI_{max} are also shown in Fig. 3.85.

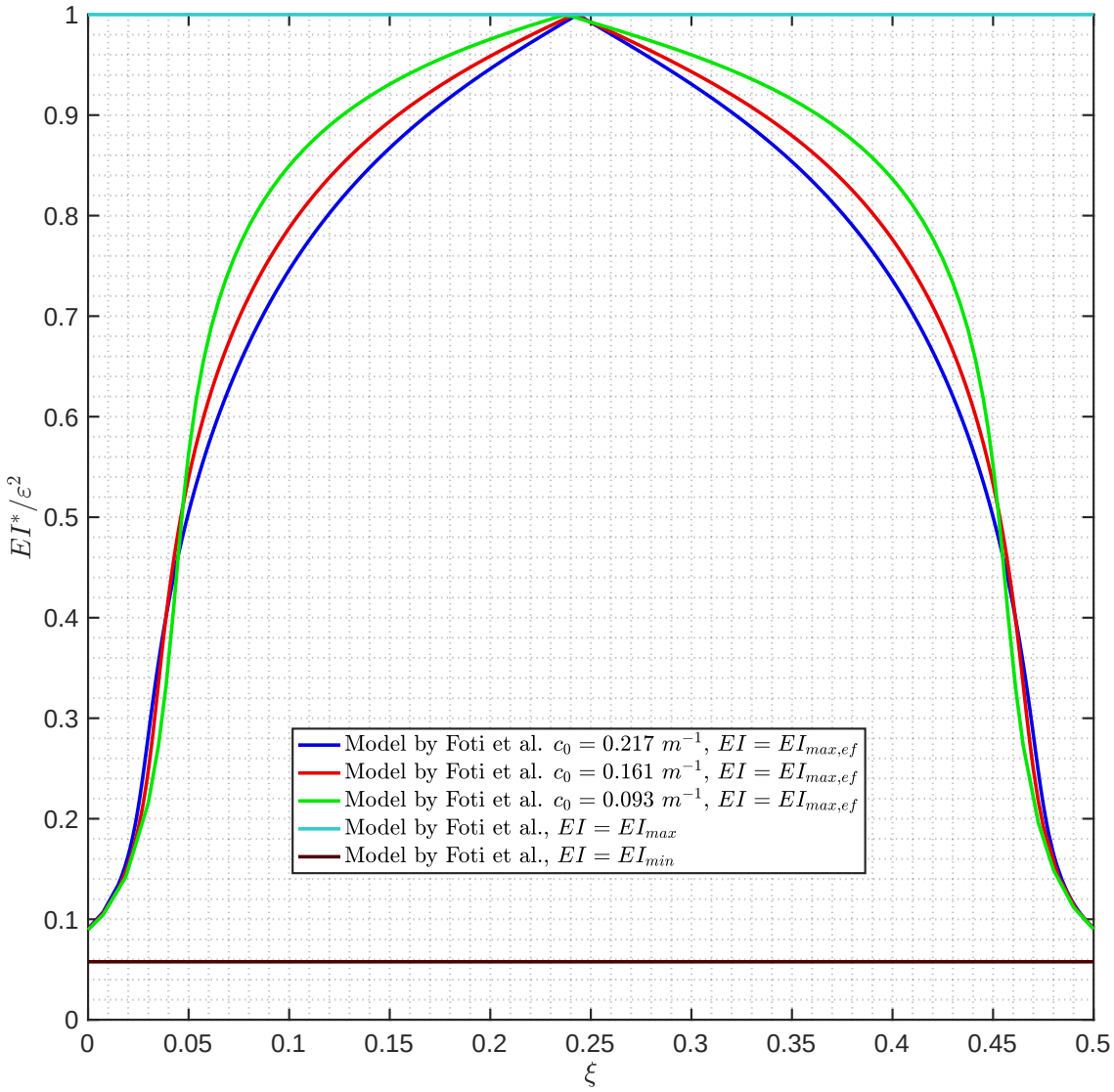

Figure 3.85. Plot of the non-dimensional bending stiffness EI^* over the interval $\xi \in [0, 1/2]$ for different values of construction parameter c_0.

It is hence shown that parameter c_0 plays a significant role in the bending stiffness variation along the cable and can be used to predict such variation inside the boundary layers in cables, i.e. zones where stress and strain fields are markedly different with respect to the one predicted by the perfectly flexible structural models (that is the catenary solution).
In the context of comparing experimental results of an ACSR Drake conductor, it has been shown that the maximum of the construction parameters c_0 was the one better representing the real response of the cable. As it is clear from Table F.6, this value was computed according to Pressure Model A and considering equivalently Slip Condition 1 or 3. Such a physical interpretation of the sliding mechanism might be due to the experimental set-up, such as the support conditions and the cable span length.

3.9 Conclusions

In this last Section, some interesting conclusions about the topics presented in this Chapter are drawn.

- Radial Contact condition has been proven to be the most diffused condition in the external layers of ACSR conductors;
- Radial Transmission Model A appears to be the most accurate among the three considered in this work, since it takes into account the difference between dS and the length of the infinitesimal segments of the contact helices, through the coefficients c^{int} and c^{ext}, especially for the predictions of internal radial contact forces per unit of length acting on the inner layers of wires, as it has been shown through the comparison with numerical (FEM) results;
- Radial Pressure Model C is strongly and systematically underestimating both internal and external radial forces per unit of length, especially at inner layers of multilayer conductors;
- The effects of different Sliding Conditions on the wires can be conveniently taken into account throughout a and b coefficients, which uniquely identify the differential equation in the non-linear component of the wire axial force F_{w1}^{NL};
- A generalization is possible by considering two additional coefficients ξ^{int} and ξ^{ext} that account for the direction and inclination of the tangential forces of the infinitesimal wire dS;
- Both the different radial transmission models and the various sliding conditions clearly affect the computation of the parameter c_0;
- The parameter c_0 can be evaluated by means both of a numerical procedure and a closed-from expression, involving the determination of the admissible wire axial force domain. Both procedures give equivalent results;
- A range of values of c_0 is provided for 15 conductors cross-sections, for the description of their moment-curvature relationship as an equivalent ideal bi-linear law defined by c_0 itself;
- As a general result, c_0 decreases as the diameter of the strand increases within the same stranding class. Linear interpolations relationship have also been provided;
- The maximum of c_0 is always attained for Radial Pressure Model A and Sliding Condition 1, whereas the minimum is attained in the case of Sliding Condition 6, for the same radial pressure transmission model;
- The first yielding curvature is affecting the static response of the strand, i.e. the parameter c_0 affects the prediction of the cable deflections and contributes to the determination of the bending stiffness variation;
- Due to the description of the moment-curvature law, c_0 will surely affect the dissipation characteristics of stranded cables, and more particularly the Self-Damping properties of ACSR conductors, as it will be assessed in Chapter 4.

Chapter 4

Self-damping of Stranded Cables

In this chapter, the Self-Damping properties of stranded cables are investigated, with direct applications to ACSR conductors.
In Section 4.1 the enhanced unified analytical model proposed by (Foti and Martinelli, 2018a, 2018b) for the theoretical predictions of the cable self-damping is presented.
Afterwords, a new parametric form for a convenient application of such model is proposed in Subsection 4.1.1, according to the developments presented by (Foti et al., 2021).
Section 4.2 deals with the comparison between the experimental results obtained through different testing campaigns ((EPRI, 2006), (Southwire, 1996), (Paradis, 2022)) and the theoretical predictions of the self-damping obtained by direct application of the analytical model.
The influence of the different values of the construction parameter c_0 (which were obtained in Section 3.7) on the theoretical predictions of the dissipation models is also investigated. To this aim, different graphical representations are introduced, and both cartesian and bi-logarithmic planes are used in order to facilitate the identification of possible transitions between two dissipation mechanisms and also to assess the capability of the theoretical models in the predictions of experimental results.
Finally, in Section 4.3, some interesting conclusions are drawn.

4.1 The adopted enhanced unified analytical model

Foti and Martinelli (2018b) have proposed an analytical model for the self-damping of stranded cables that accounts for both the gross-sliding and micro-slip dissipation mechanisms (see Subsection 2.4.2).
Let us recall the moment-curvature law of stranded cables that was treated in Subsection 3.5.4 and in particular, let's focus on Eq. 3.152, which expresses the non-dimensional dissipated energy per unit of length in the cases of Gross-Sliding and Micro-Slip mechanisms.
Let us assume that the natural modes of the conductor can be described by means of the sinusoidal function (according to the taut-string model):

$$y = A \sin\Big(\frac{2\pi x}{\lambda}\Big) \tag{4.1}$$

By deriving the previous equation two times, one can easily obtain the modal curvatures as:

$$\chi_{mod} = |\frac{d^2y}{dx^2}| = \frac{4\pi^2}{\lambda^2} A |\sin\Big(\frac{2\pi x}{\lambda}\Big)| \tag{4.2}$$

The latter can be used to evaluate the position of the transition point x_0, which corresponds to the transition from the "low" curvature zone (where the dissipation is mainly due to the Micro-Slip phenomenon), to the "high" curvature zone, i.e. $\chi_{max} = \chi_0$ (where the dissipation is assumed to be mainly related to the Gross-Sliding of wires).
Due to the symmetries of the modal shape, point x_0 will be located at $\lambda/4$ from a modal shape node (see Foti and Martinelli 2018a, 2018b).
One has then:

$$0 \leq \frac{x_0}{\lambda} = \frac{1}{2\pi} \arcsin\Big(\frac{\lambda^2\,\chi_0}{4\pi^2\,A}\Big) \leq \frac{1}{4} \tag{4.3}$$

By taking 4.3, it is possible to express the dissipated energy per unit of length as:

$$E_d = \frac{M_0\,\chi_0}{\lambda}\int_0^{\lambda} \omega_{ds}(x)dx = \frac{4M_0\chi_0}{\lambda}\Big(\int_0^{x_0} \omega_{ds}^{ms}(x)dx + \int_{x_0}^{\frac{\lambda}{4}} \omega_{ds}^{gs}(x)dx\Big) \tag{4.4}$$

and the following results are obtained:

$$\frac{4M_0\chi_0}{\lambda}\int_0^{x_0} \omega_{ds}^{ms}(x)dx = \frac{128\,\pi^5\,m^3\,RTS\,EI_{max,ef}}{c_0\,\mu}\,G_1\Big(\frac{x_0}{\lambda}\Big)\,\frac{A^3 f^7}{T^4} \tag{4.5}$$

$$\frac{4M_0\chi_0}{\lambda}\int_0^{x_0} \omega_{ds}^{gs}(x)dx = 4\,\pi^3 m^2\,EI_{max,ef}\,G_2\Big(\frac{x_0}{\lambda}\Big)\frac{A^2 f^5}{T^2} \tag{4.6}$$

The dissipated power per unit of length P_d can then be expressed as the sum between the two contributions, weighted through the functions G_1 and G_2, according to the following equation:

$$P_d = \frac{128\,\pi^5\,m^3\,RTS\,EI_{max,ef}}{c_0\,\mu}\,G_1\Big(\frac{x_0}{\lambda}\Big)\,\frac{A^3 f^7}{T^4} + 4\,\pi^3 m^2\,EI_{max,ef}\,G_2\Big(\frac{x_0}{\lambda}\Big)\frac{A^2 f^5}{T^2} \tag{4.7}$$

where:

$$G_1\left(\frac{x_0}{\lambda}\right) = \frac{1}{3} - \frac{3}{8}\cos\left(2\pi\frac{x_0}{\lambda}\right) + \frac{1}{24}\cos\left(6\pi\frac{x_0}{\lambda}\right) \tag{4.8}$$

$$G_2\left(\frac{x_0}{\lambda}\right) = \pi - 4\pi\frac{x_0}{\lambda} + \sin\left(4\pi\frac{x_0}{\lambda}\right) \tag{4.9}$$

The two conceptual limit cases reported in table 4.1 can be obtained by imposing different values of x_0/λ. In case of no sliding, one has the condition $x_0/\lambda = 1/4$, so that $G_1(1/4) = 1/3$ and $G_2(1/4) = 0$. The dissipated power per unit of length is entirely due the micro-slip phenomenon:

$$P_d = P_d^{ms} = \frac{128\,\pi^5\,m^3\,RTS\,EI_{max,ef}}{3\,c_0\,\mu}\frac{A^3 f^7}{T^4} \tag{4.10}$$

If the cable is completely in gross-sliding, one has the condition $x_0/\lambda = 0$, so that $G_1(1/4) = 0$ and $G_2(1/4) = \pi$. The dissipated power per unit of length becomes:

$$P_d = P_d^{gs} = 4\,\pi^4 m^2 EI_{max,ef}\frac{A^2 f^5}{T^2} \tag{4.11}$$

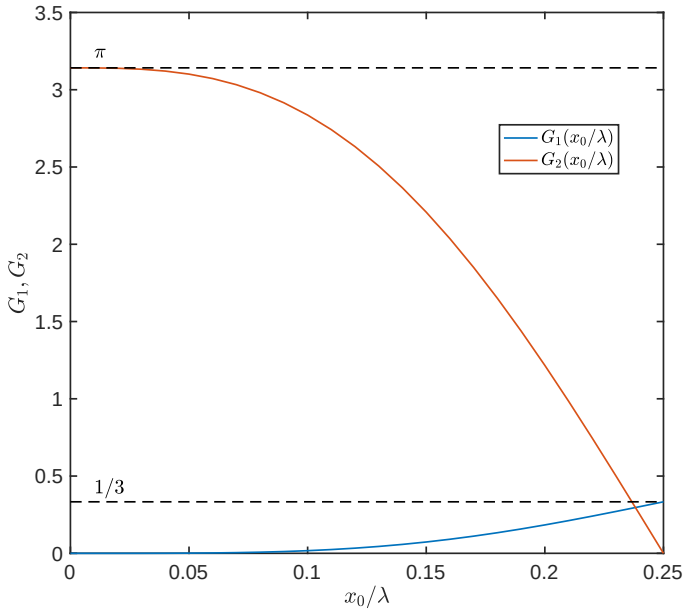

Figure 4.1. Plot of the non-dimensional weight functions G_1 and G_2, according to the model proposed by (Foti and Martinelli, 2018b).

Such analytical model can be cast in the form expressed by the empirical power law, with different set of exponents and different proportionality coefficients. The latter are conveniently collected in Table 4.1.
The formulation proposed by Foti and Martinelli (2018b) has the following advantages:

- it is derived from mechanical considerations;
- it is dimensionally homogeneous;
- it leads to a proportionality coefficient physically justified, for both the dissipation mechanisms.

Table 4.1. Exponents an proportionality coefficient of the empirical power law obtained through an analytical formulation.

Reference	l	m	n	k	Dissipation Mechanism
Foti and Martinelli 2018a	2	5	2	$4\,\pi^4 m^2 EI_{max,ef}$	Gross-Sliding (GS)
Foti and Martinelli 2018b	3	7	4	$\frac{128\,\pi^5\,m^3\,RTS\,EI_{max,ef}}{3\,c_0\,\mu}$	Micro-Slip (MS)

4.1.1 Formulation of the analytical model in a new parametrisation

In this section, the analytical model proposed by (Foti and Martinelli, 2018a, 2018b) is casted in a new form that accounts for a new convenient parametrisation, that allows for a more effective comparison of the theoretical predictions with available experimental data of the literature.
Let's start again with the hypothesis previously introduced. Let us assume, according to the taut-string model, that the natural vibration modes of the cable can be described by means of sinusoidal functions.

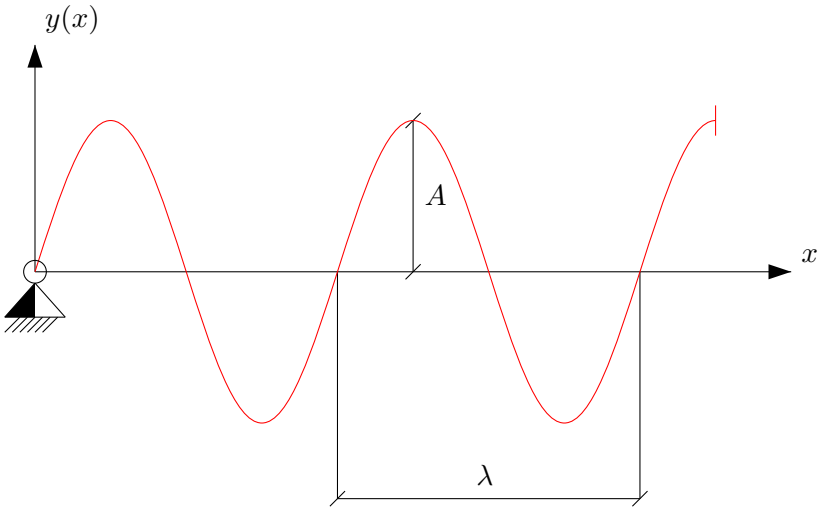

Figure 4.2. Natural modes of the suspended cable. Definition of the modal amplitude A and of the wavelength λ.

Defining with $y = y(x, \lambda)$ the modal displacement of the cable centerline, one has:

$$y = A \sin\left(\frac{2\pi x}{\lambda}\right) \tag{4.12}$$

where A is the single-peak antinode vibration amplitude, x is a spacial coordinate running over the span of the cable ($x \in [0, l]$) and λ is the wavelength of the mode, defined as follows:

$$\lambda = \frac{1}{f}\sqrt{\frac{T}{m}} \tag{4.13}$$

where f is the vibration frequency, T is the axial force in the cable and m is the mass per unit length of the conductor.
By deriving with respect to the coordinate x one and two times, the modal rotations and

curvatures can be respectively obtained, as shown in Equation 4.14 and 4.15.

$$\varphi_{mod} = \frac{dy}{dx} = \frac{2\pi}{\lambda} A \cos\left(\frac{2\pi x}{\lambda}\right) = \Phi \cos\left(\frac{2\pi x}{\lambda}\right) \tag{4.14}$$

$$\chi_{mod} = \frac{d^2y}{dx^2} = -\frac{4\pi^2}{\lambda^2} A \sin\left(\frac{2\pi x}{\lambda}\right) = -K \sin\left(\frac{2\pi x}{\lambda}\right) \tag{4.15}$$

In the previous equations, the following parameters have been introduced:

$$\Phi = \frac{2\pi A}{\lambda} \qquad K = \frac{4\pi^2 A}{\lambda^2} \tag{4.16}$$

Both of them have a clear physical meaning: Φ is the absolute value of the angle of rotation of a node of the mode shape, and K is the maximum absolute value of the modal curvature. The energy per unit of length dissipated through the Gross-Sliding or Micro-Slip dissipation mechanisms (E_{ds}^{gs}, E_{ds}^{ms}) and its non-dimensional counterpart (ω_{ds}^{gs}, ω_{ds}^{ms}) can be computed substituting $\chi_{max} = |\chi_{mod}|$ into Equations 3.146, 3.148, 3.151.
The dissipated power per unit of length can be obtained averaging over the wavelength λ and multiplying by the vibration frequency f:

$$P_d^{gs} = \frac{C}{\lambda^*} \cdot \int_0^1 \omega_{ds}^{gs}(\xi) d\xi \tag{4.17}$$

$$P_d^{ms} = \frac{C}{\lambda^*} \cdot \int_0^1 \omega_{ds}^{ms}(\xi) d\xi \tag{4.18}$$

where λ^* is the non-dimensional wavelength and ξ is a non-dimensional abscissa.

$$\xi = \frac{x}{\lambda} \qquad \lambda^* = \frac{\lambda}{2l} \tag{4.19}$$

C is a coefficient having the same units of a power per unit of length, defined as:

$$C = \frac{1}{2} EI_{max,ef} \chi_0^2 \sqrt{\frac{T}{ml^2}} \tag{4.20}$$

The Non-dimensional power per unit of length dissipated through the Gross-Sliding and Micro-Slip mechanisms can be computed with equation 4.21 and 4.22 respectively.

$$\Pi^{gs} = \frac{P_d^{gs}}{C} = \frac{1}{\lambda^*} \cdot \int_0^1 \omega_{ds}^{gs}(\xi) d\xi \tag{4.21}$$

$$\Pi^{ms} = \frac{P_d^{ms}}{C} = \frac{1}{\lambda^*} \cdot \int_0^1 \omega_{ds}^{ms}(\xi) d\xi \tag{4.22}$$

Solving the previous integrals, one gets:

$$\Pi^{gs} = \frac{J}{4} \cdot \frac{1}{(\chi_0 l)^2} \tag{4.23}$$

$$\Pi^{ms} = \frac{2\pi^2}{3} \cdot J \cdot \frac{\Phi}{\lambda^*} \cdot \frac{1}{(\chi_0 l)^3} \tag{4.24}$$

where the parameter J is defined as follows:

$$J = \frac{\Phi^2}{(\lambda^*)^3} \tag{4.25}$$

and represents a sort of "mean curvature" of the conductor.
As already pointed out, this new parametrisation proposed in (Foti et al., 2021) allows for a more effective comparison with available experimental data of the literature, and will be largely adopted in Section 4.2.
In particular, transition between different dissipation mechanisms in the tests may be graphically identified, as it will be later on assessed.
A preliminary theoretical prediction threshold between the different dissipation mechanisms can be obtained by equating the maximum absolute value of the modal curvature K (Eq. 4.16) to the "first yielding" curvature χ_0 (Eq 3.150).
One has:

$$K = \frac{4\pi^2 A}{\lambda^2} = c_0\,\mu\,\eta = \chi_0 \tag{4.26}$$

so that:

$$\frac{\Phi}{\lambda^*} = \frac{2\pi A}{\lambda} \cdot \frac{2l}{\lambda} = \frac{Kl}{\pi} = \frac{c_0\,\mu\,\eta\,l}{\pi}$$

The theoretical value of the threshold can be evaluated as follows:

$$\frac{\Phi}{\lambda^*} = \frac{c_0\,\mu\,\eta\,l}{\pi} \tag{4.27}$$

4.2 Comparison between experimental and theoretical results

In this section, the available experimental results of the dissipated power for the commercial ACSR conductors listed in Table A.2 are compared with the theoretical predictions of the analytical model described in Subsection 4.1.1.
For the different ACSR conductors, the following procedure is adopted:

1. Plot of the experimental dissipated power per unit of length P_d versus the non-dimensional antinode amplitude A/D;

2. Plot of the non-dimensional dissipated power $(2\chi_0\, l)^2\Pi$ vs. J parameter. The theoretical predictions of the gross-sliding ("GS") and micro-slip ("MS") damping models for different values of the construction parameter c_0 (see also Section 3.7 and Appendix F) are compared with the experimental data;

3. Plot of the non-dimensional dissipated power $(2\chi_0\, l)^2\Pi$ vs. Φ/λ^*. The theoretical predictions of the gross-sliding ("GS") and micro-slip ("MS") damping models for different values of the construction parameter c_0 (see also Section 3.7 and Appendix F) are compared with the experimental data. This graph will be useful for the evaluation at point 5;

4. A linear interpolation of the experimental non-dimensional dissipated power vs J parameter is performed: $(2\chi_0\, l)^2\Pi = p_0 + p_1\, J$. The same interpolation is also performed for the logarithm of the previous quantities: $\log\left((2\chi_0\, l)^2\Pi\right) = q_0 + q_1\, \log(J)$. The linear regression coefficients p_0, q_0 and p_1, q_1 are then collected, as well as the coefficient of determination R^2;

5. Assessment of the experimental threshold value Φ/λ^* related to a possible transition from a region controlled by the Micro-Slip and the Gross-Sliding dissipation mechanism, if it can be identified (see also subsection 4.1.1);

6. Comparison between the experimental and theoretical threshold values. The latter can be computed by means of Equation 4.27;

7. Plot of the non-dimensional dissipated power predicted with the theoretical models for different values of c_0 (see also Section 3.7 and Appendix F) versus the experimental non-dimensional dissipated power. That is, plot of both theoretical and experimental results in the plane Π_{exp} - Π_{th}.
   Such plane is conveniently introduced to assess the capability of the theoretical models to predict the experimental results;

8. A linear interpolation of the non-dimensional dissipated power in the plane introduced at point 7 is performed, i.e $\Pi_{th} = s_0 + s_1\Pi_{exp}$. The linear regression coefficients s_0 and s_1 for each theoretical model are then collected, as well as the coefficient of determination R^2. The more s_1 tends to 1 (i.e. the slope of the bisector), the more the theoretical models are correctly predicting experimental results;

9. Plot of the moment-curvature diagram under cyclic loading conditions.

Useful information regarding the tested ACSR conductors considered in this work are reported in Table 4.2.

Table 4.2. Parameters of the tested ACSR conductors.

Code Word	Condition	$\beta\,(-)$	$\mu\,(-)$	$l\,(m)$	$\eta\ (\%)$	Subsec.	Ref.
Bersfort	New	0.5	0.3	63	15, 20, 25, 30	4.2.1	E
Bersfort	New	0.5	0.3	450	15, 25, 35	4.2.2	P
Curlew	New	0.5	0.3	92	22	4.2.3	E
Nelson I	New	0.5	0.3	24	20	4.2.4	E
Hawk	New Greased	0.5	0.15	28	10, 20, 30	4.2.5	E
Hawk	Old Greased	0.5	0.45	28	10, 20, 30	4.2.6	E
Penguin	New	0.5	0.3	36	16	4.2.7	E
Drake	New, Initial State	0.5	0.3	33	15, 20, 25	4.2.8	S
Drake	New, Final State	0.5	0.3	33	15, 20, 25	4.2.9	S

S: (Southwire, 1996), Laboratory Report
E: (EPRI, 2006), Appendix-A, "The Orange Book"
P: (Paradis, 2022), PhD Thesis

For the sake of clarity, an example of linear interpolation of the experimental results is reported as follows.
In particular, a linear interpolation of the experimental data $(2\chi_0\, l)^2\Pi$-J is performed, as well as a linear interpolation of the quantities $\log((2\chi_0\, l)^2\Pi)$-$\log(J)$.
Both straight lines are reported in Figure 4.3 along with experimental results obtained through the ISWR method by Paradis (2022).

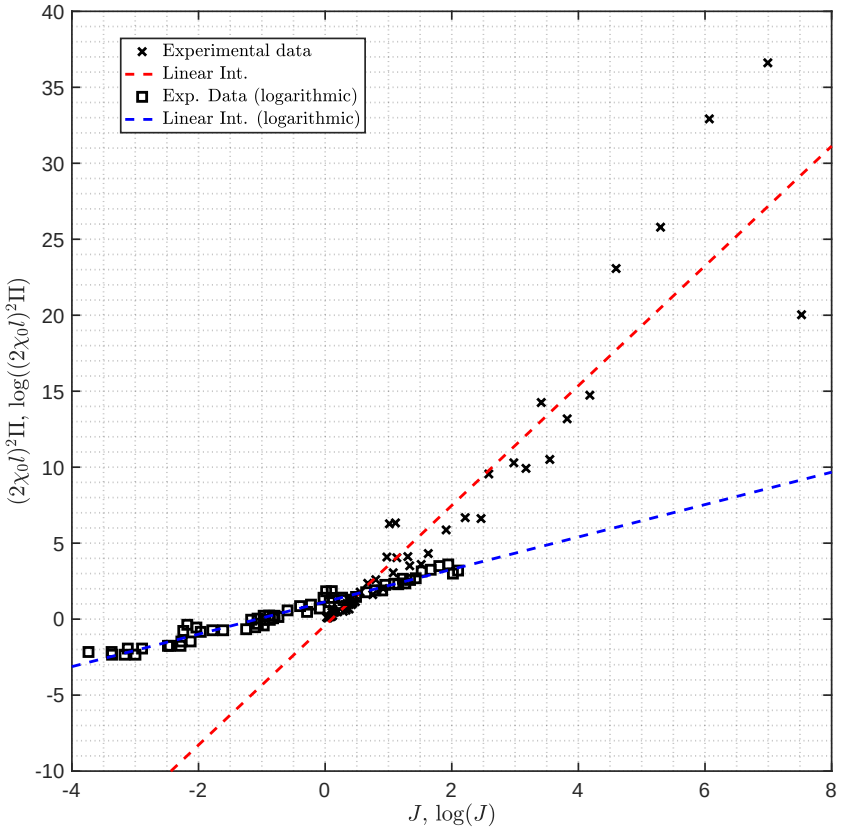

Figure 4.3. Example of linear interpolation of the experimental data in the plane $(2\chi_0\, l)^2\Pi$-J.

4.2.1 ACSR 48/7 Bersfort

In this subsection, the ACSR 48/7 Bersfort conductor is considered. Its mechanical and geometrical properties are collected in Appendix A, whereas its cross-section is depicted in Fig. B.3c (see Appendix B). The power per unit of length (P_d) dissipated during forced vibration tests, performed at different values of frequency f and antinode vibration amplitude A and for different values of the tension T, was measured through the Inverse Standing Wave Ratio (ISWR) technique and corrected to subtract the aerodynamic damping.

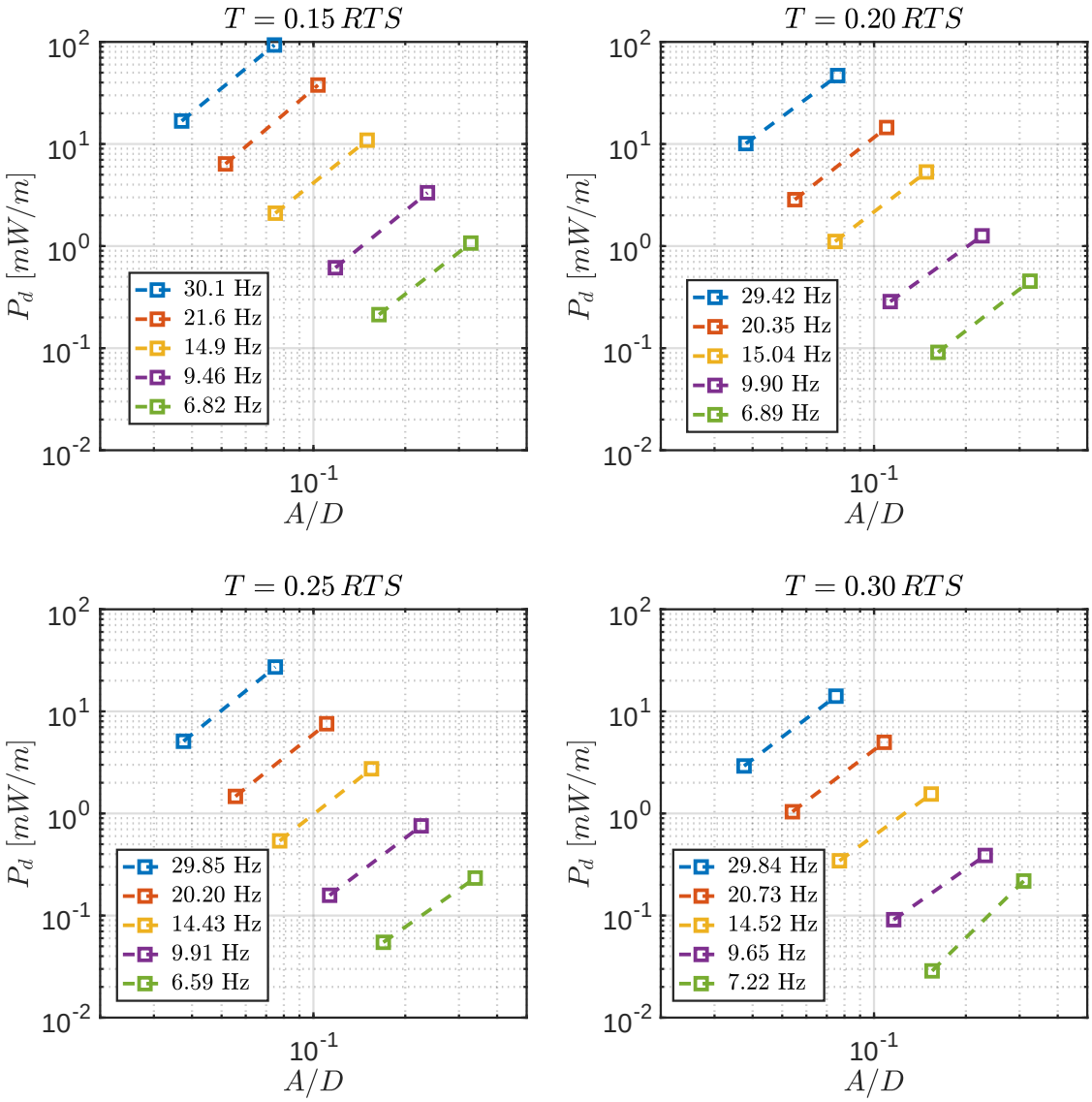

Figure 4.4. Dissipated power per unit of length vs. non-dimensional antinode amplitude. Data from (EPRI, 2006), Appendix-A. Bersfort conductor.

Figure 4.5 and 4.6 show the non-dimensional dissipated power predictions with the theoretical damping models for different values of the construction parameter c_0 (see sections 3.6 and 3.7), and the comparison with the experimental data, in both $(2\chi_0\, l)^2\Pi$ - J and $(2\chi_0\, l)^2\Pi$ - Φ/λ^* planes.

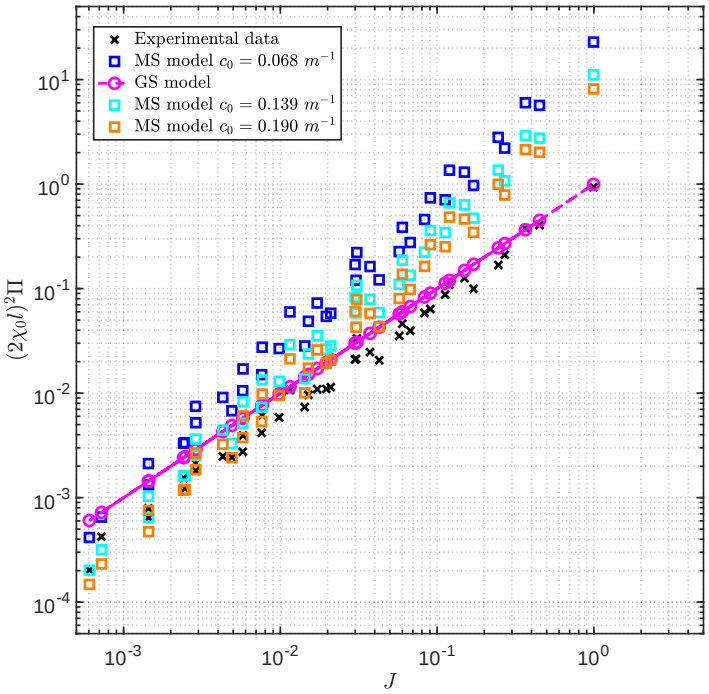

Figure 4.5. Non-dimensional Dissipated power vs. J parameter. Comparison between experimental data and theoretical predictions of the gross-sliding ("GS") and micro-slip ("MS") damping models, for different values of c_0. Bersfort conductor.

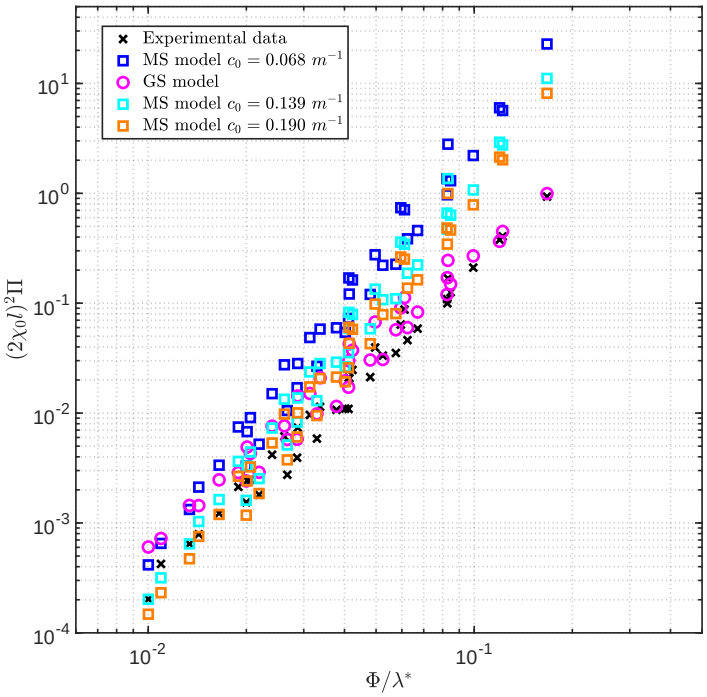

Figure 4.6. Non-dimensional Dissipated power vs. Φ/λ^*. Comparison between experimental data and theoretical predictions of the gross-sliding ("GS") and micro-slip ("MS") damping models, for different values of c_0. Bersfort conductor.

In this case, two different slopes of the predicted dissipated power values according to the Gross-Sliding and Micro-Slip dissipation mechanisms theoretical models, can be observed. According to Figure 4.5 and 4.6, it is possible to recognize that, for small values of J, the line interpolating experimental data has a similar slope to the one predicted by the Micro-Slip model. On the contrary, for large values of J (over the recognized experimental threshold), the data are in closer agreement with the theoretical predictions of the Gross-Sliding dissipation mechanism.
Table 4.3 collects the linear regression coefficients for the experimental data.

Table 4.3. ACSR Bersfort: Regression Coefficients of experimental data.

$(2\chi_0\, l)^2\Pi = p_0 + p_1\, J$	p_0	p_1	R^2
	-0.0083	0.9287	0.9903
$\log((2\chi_0\, l)^2\Pi) = q_0 + q_1\, \log(J)$	q_0	q_1	R^2
	-0.104	1.084	0.9912

From Fig. 4.6 an experimental threshold $(\Phi/\lambda^*)_{exp} = 0.02$ could be identified, as reported in Tab. 4.4.

Table 4.4. ACSR Bersfort: Experimental Threshold.

Identifiable	$(\Phi/\lambda^*)_{exp}$
Yes	0.02

The predictions of the theoretical thresholds are computed and reported in Table 4.5.

Table 4.5. ACSR Bersfort: Theoretical thresholds for different values of c_0.

	Theoretical Thresholds $(\Phi/\lambda^*)_{th}$			
c_0 (m^{-1})	$\eta = 0.15$	$\eta = 0.20$	$\eta = 0.25$	$\eta = 0.30$
0.068	0.039	0.052	0.065	0.078
0.139	0.080	0.106	0.133	0.159
0.190	0.109	0.145	0.181	0.218

The closest prediction of the theoretical threshold is the one obtained for $c_0 = 0.068\ m^{-1}$ and $\eta = 0.15$, corresponding to $\Phi/\lambda^* = 0.039$. As a matter of fact, by adopting different sliding conditions, and having computed various construction parameters, the theoretical predictions of such threshold values have improved with respect to the open research question evidenced in (Foti et al, 2021).

Figure 4.7 shows the plot of Π_{th} vs. Π_{exp}. An enlargement of the previous plot is also included in Fig. 4.8 for convenience.

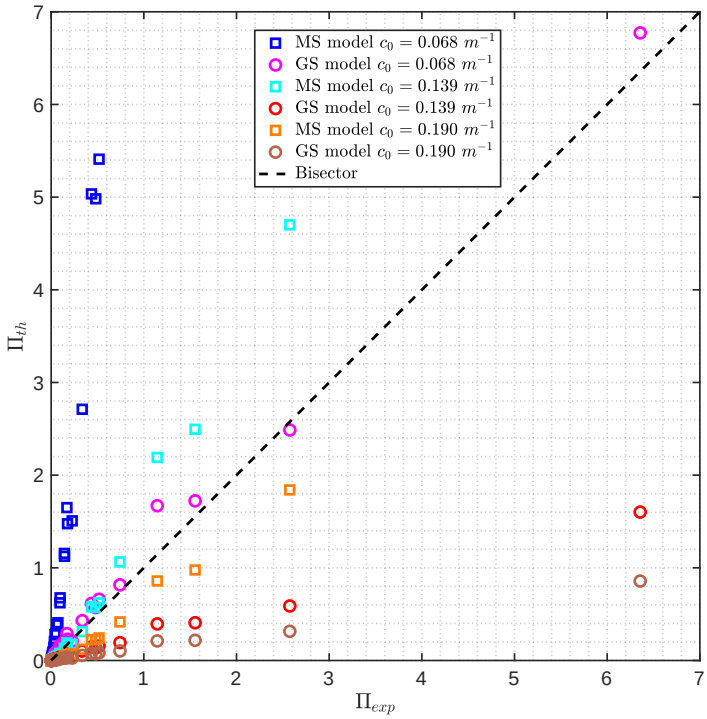

Figure 4.7. Theoretical predictions of the non-dimensional dissipated power Π_{th} vs. non-dimensional dissipated power computed from experimental data Π_{exp}. Bersfort conductor.

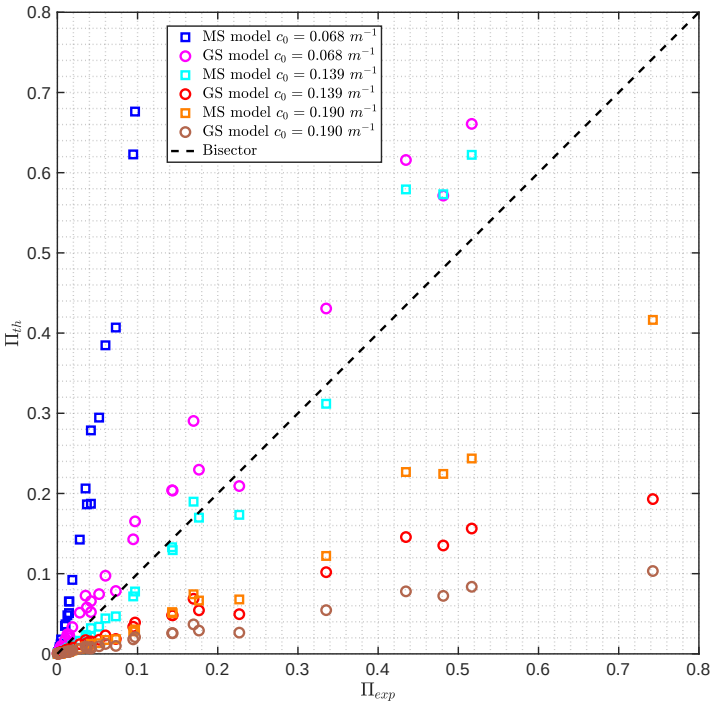

Figure 4.8. Theoretical predictions of the non-dimensional dissipated power Π_{th} vs. non-dimensional dissipated power computed from experimental data Π_{exp}. Enlargement. Bersfort conductor.

As it can be assess from the linear regression coefficients of the theoretical dissipated power predictions (see Table 4.6), the Gross-Sliding dissipation model is the one which better represent experimental results, because the slope of its linear interpolation is the closest to 1 (i.e. the slope of the bisector, that is the locus of the points which are in perfect agreement with experimental results).
And among the different Gross-Sliding models, the one with $c_0 = 0.068\ m^{-1}$ appears to be in good agreement with the experimental results, as is can be graphically assessed in Fig. 4.7.

Table 4.6. ACSR Bersfort: Regression Coefficients of theoretical predictions.

Model	$c_0\ (m^{-1})$	s_0	s_1	R^2
Gross-Sliding	0.068	0.033	1.059	0.994
Gross-Sliding	0.139	0.008	1.059	0.994
Gross-Sliding	0.190	0.004	1.059	0.994
Micro-Slip	0.068	-2.104	22.926	0.971
Micro-Slip	0.139	-0.242	11.149	0.971
Micro-Slip	0.190	-0.095	8.157	0.971

Some others considerations are here proposed:

- the determination coefficient R^2 do not vary for varying c_0 parameter, within the same dissipation model. This is because c_0 is affecting only the slope and/or the intercept of the linear interpolation and not the data dispersion;
- the construction parameter c_0 for the case of Gross-Sliding dissipation mechanism affects just the regression coefficient s_0 i.e., the intercept of the interpolation line. That is, the slope of the interpolating line remains the same and data are just affected by a vertical translation in the plane Π_{exp} - Π_{th};
- the construction parameter c_0 for the case of Micro-Slip dissipation mechanism affects both coefficients s_0 and s_1 i.e., both the intercept and the slope of the interpolating line.

These are general conclusions that hold also for analysis that will be addressed in the next subsections.

Finally, the moment-curvature diagrams for different loading ratios η are reported in Figure 4.9.

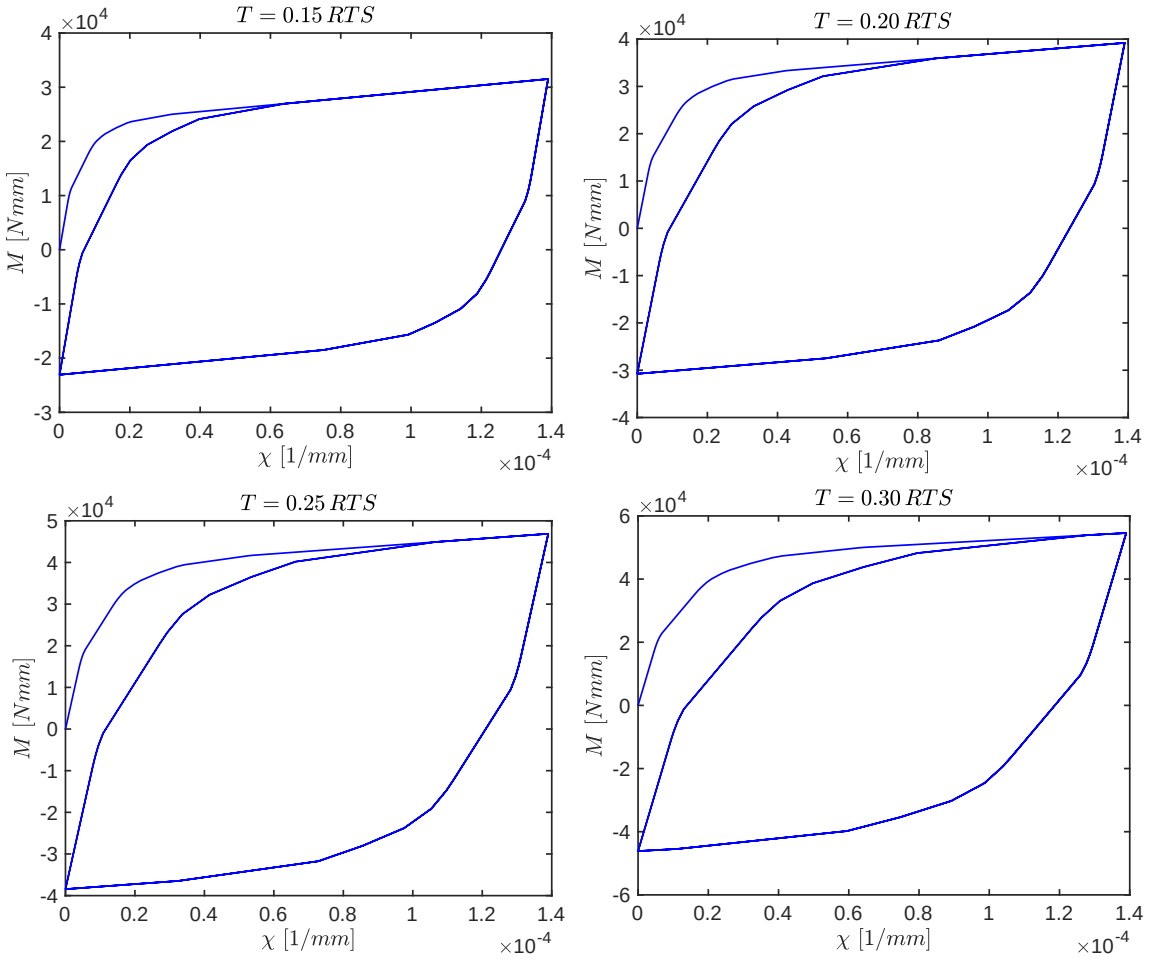

Figure 4.9. Bersfort conductor ($\mu = 0.3$): plot of the Moment-Curvature diagrams in the case of cyclic loading, for different values of the tension T.

4.2.2 ACSR 48/7 Bersfort (New Results)

In this section, the available experimental results of the dissipated power for an ACSR Bersfort conductor from Paradis (2022) are compared with the analytical model described in Subsection 4.1.1.
The experimental results are collected in Annex G of her PhD thesis (see Ref. (58)).
Such results that have been obtained with multi-frequencies measurements technique.
However, for the application of the analytical model, we are just interested to the single frequency excitation of the strand.
The properties of the ACSR Bersfort that was tested are listed in Table 4.7 for convenience, being slightly different from the one reported in Appendix A.

Table 4.7. ACSR Bersfort: geometrical and mechanical properties.

Quantity	Value	UoM
Diameter D	35.56	mm
Mass per unit length m	2.369	kg/m
Rated Tensile Strength RTS	180.1	kN
Max. Bending Stiffness EI_{max}	4130	Nm^2
Min. Bending Stiffness EI_{min}	60.8	Nm^2

Contact conditions of the ACSR 48/7 Bersfort are related to a new state and such conductor span was tested for three different tension levels ($\eta = 15, 25, 35\%$).
Self-Damping measurements were performed on the experimental line of Varennes (Québec) according to two different methods, namely the Power Method and the Inverse Standing Wave Ratio (ISWR) Method. The differences between such methods and the experimental procedures have been assessed in Section 2.3.
Results obtained with the Power Method are analyzed in Paragraph 4.2.2, while the ones obtained with the ISWR Method are analyzed in Paragraph 4.2.2.
As an additional comment, the slightly different mechanical and geometrical properties of the testes ACSR Bersfort (reported in Tab. 4.7) would lead in principle to the obtainment od different values of c_0 coefficients with respect to the ones found in Section 3.7.
However, since the difference is practically negligible, the values already determined (see Tab. 3.20) will be adopted for the next developments.

Results from Power Method

Figures 4.10 and 4.11 show the non-dimensional dissipated power predictions with the theoretical damping models for different values of the construction parameter c_0 (see sections 3.6 and 3.7), and the comparison with the experimental data, in both $(2\chi_0\, l)^2\Pi$ - J and $(2\chi_0\, l)^2\Pi$ - Φ/λ^* planes.

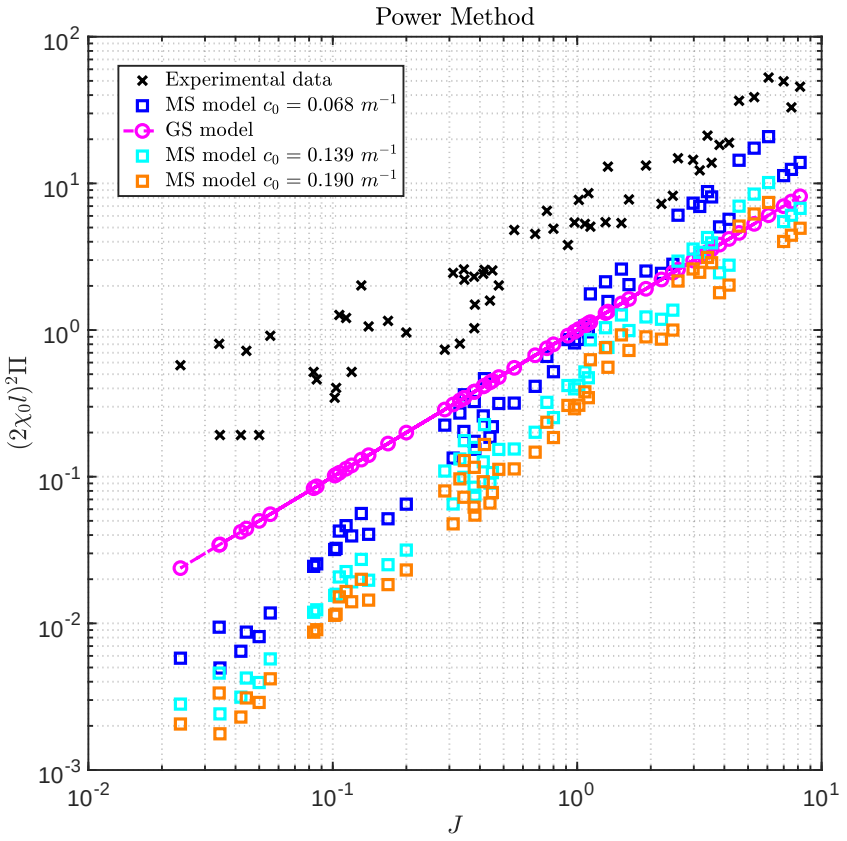

Figure 4.10. Non-dimensional Dissipated power vs. J parameter. Comparison between experimental data and theoretical predictions of the gross-sliding ("GS") and micro-slip ("MS") damping models, for different values of c_0. Bersfort conductor.

It is worth noticing that different values of the construction parameter c_0 lead to different predictions of both Micro-Slip and Gross-Sliding dissipation mechanisms. However, in both planes $(2\chi_0\, l)^2\,\Pi$ - J and $(2\chi_0\, l)^2\,\Pi$ - Φ/λ^*, the points associated to the GS model prediction do not vary. The same consideration obviously holds for the experimental data.
On the contrary, the difference for the Micro-Slip predictions can be appreciated. The non-dimensional dissipated power Π, multiplied by $(2\chi_0\, l)^2$ is increasing as the construction parameter c_0 decreases.
Table 4.8 collects the linear regression coefficients for the experimental data.

Table 4.8. ACSR Bersfort: Regression coefficients of experimental data, Power Method results.

$(2\chi_0\, l)^2\Pi = p_0 + p_1\, J$	p_0	p_1	R^2
	-0.296	6.02	0.902
$\log((2\chi_0\, l)^2\Pi) = q_0 + q_1\, \log(J)$	q_0	q_1	R^2
	1.721	0.899	0.903

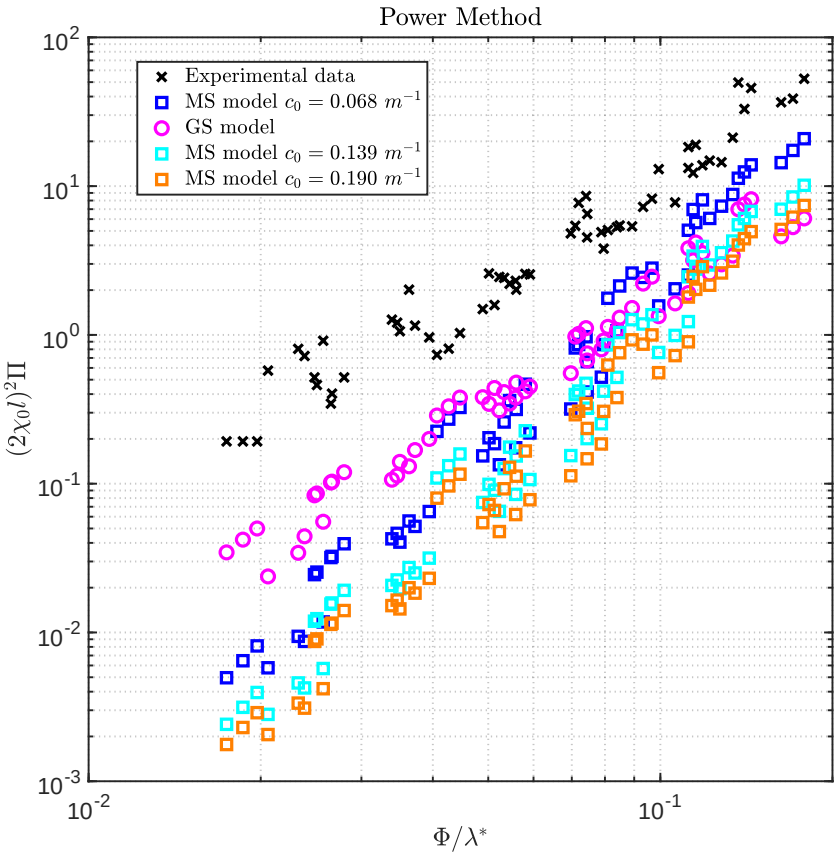

Figure 4.11. Non-dimensional Dissipated power vs. Φ/λ^*. Comparison between experimental data and theoretical predictions of the gross-sliding ("GS") and micro-slip ("MS") damping models, for different values of c_0. Bersfort conductor.

In this case, the experimental threshold couldn't be identified, as it can be seen from Tab. 4.9. However, the predictions of the theoretical thresholds are computed and reported in Table 4.10.

Table 4.9. ACSR Bersfort: Experimental Threshold, Power Method.

Identifiable	$(\Phi/\lambda^*)_{exp}$
No	-

Table 4.10. ACSR Bersfort: Theoretical thresholds for different values of c_0.

	Theoretical Thresholds $(\Phi/\lambda^*)_{th}$		
$c_0\ (m^{-1})$	$\eta = 0.15$	$\eta = 0.24$	$\eta = 0.30$
0.068	0.436	0.710	1.061
0.139	0.896	1.459	2.089
0.190	1.224	1.995	2.856

Figure 4.12 shows the plot of Π_{th} vs. Π_{exp}. An enlargement of the previous plot is also included in Fig. 4.13 for convenience.
As it can be assess from the linear regression coefficients of the theoretical dissipated power predictions (see Table 4.11), the Micro-Slip dissipation model with $c_0 = 0.068\ m^{-1}$ is the one which better represent experimental results, because the slope of its linear interpolation is the closest to 1 (i.e. the slope of the bisector, that is the locus of the points which are in perfect agreement with experimental results).

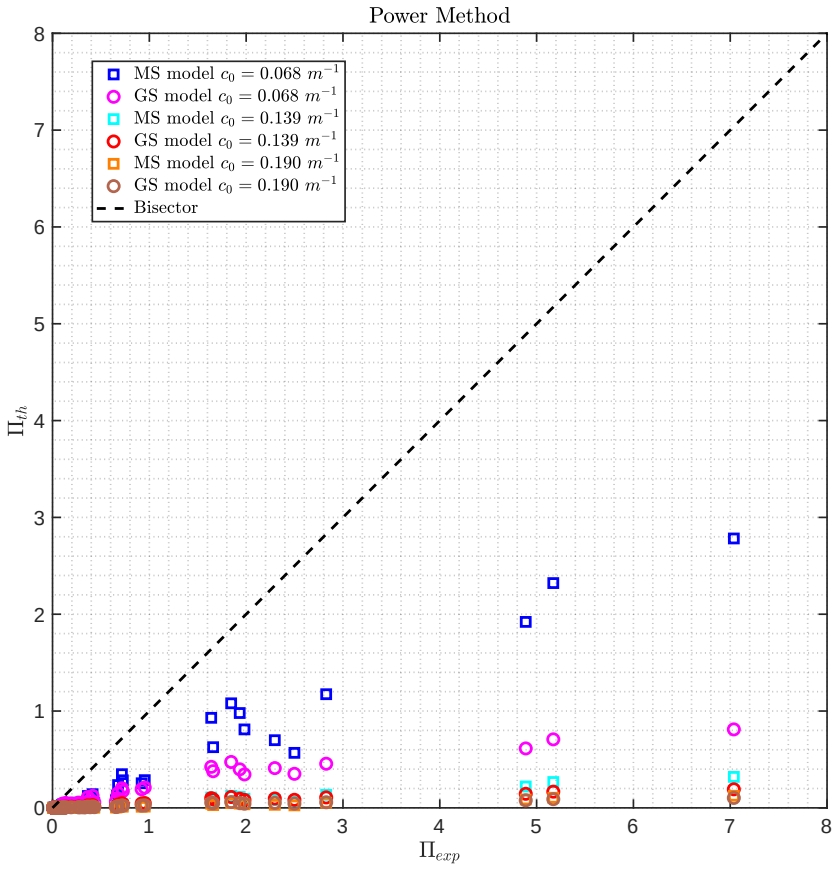

Figure 4.12. Theoretical predictions of the non-dimensional dissipated power Π_{th} vs. non-dimensional dissipated power computed from experimental data Π_{exp}.

Table 4.11. ACSR Bersfort: Regression Coefficients of theoretical predictions, Power Method results.

Model	c_0 (m^{-1})	s_0	s_1	R^2
Gross-Sliding	0.068	0.025	0.135	0.915
Gross-Sliding	0.139	0.006	0.135	0.915
Gross-Sliding	0.190	0.003	0.135	0.915
Micro-Slip	0.068	-0.031	0.411	0.966
Micro-Slip	0.139	-0.004	0.200	0.966
Micro-Slip	0.190	-0.001	0.146	0.966

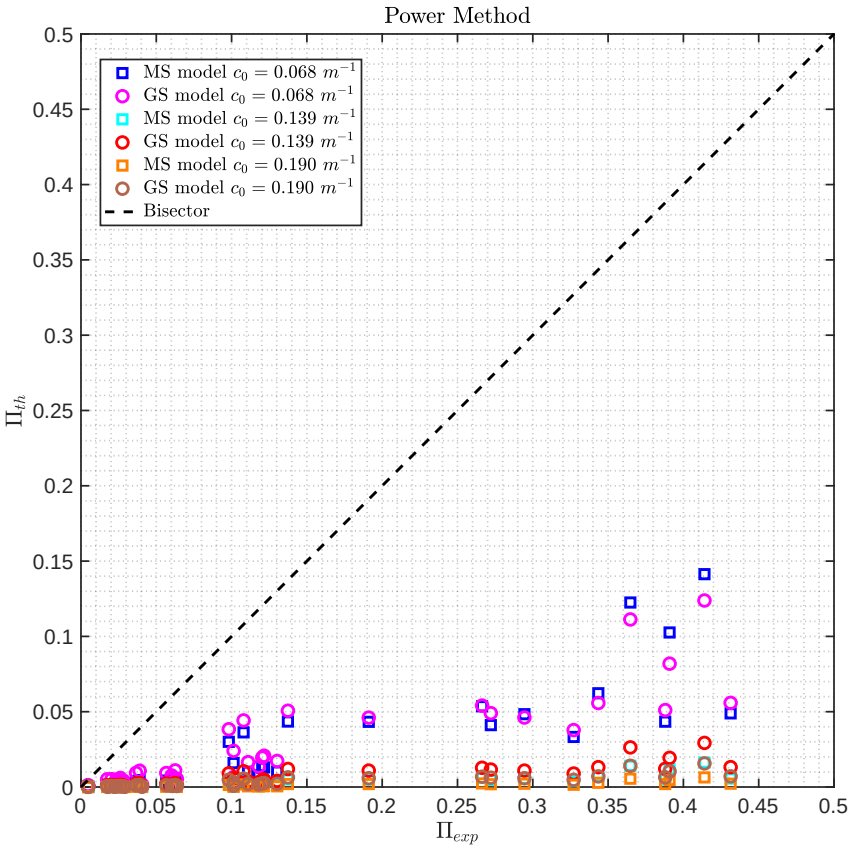

Figure 4.13. Theoretical predictions of the non-dimensional dissipated power Π_{th} vs. non-dimensional dissipated power computed from experimental data Π_{exp}. Enlargement.

Results from ISWR Method

Figures 4.14 and 4.15 show the non-dimensional dissipated power predictions with the theoretical damping models for different values of the construction parameter c_0 (see sections 3.6 and 3.7), and the comparison with the experimental data, in both $(2\chi_0\, l)^2\Pi$ - J and $(2\chi_0\, l)^2\Pi$ - Φ/λ^* planes.

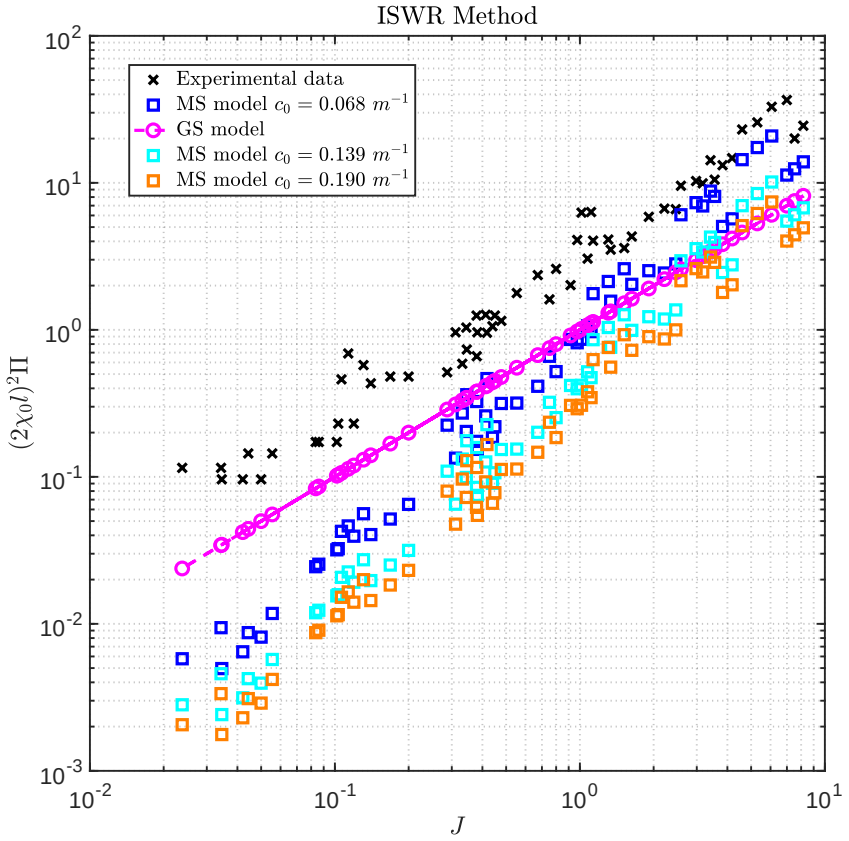

Figure 4.14. Non-dimensional Dissipated power vs. J parameter. Comparison between experimental data and theoretical predictions of the gross-sliding ("GS") and micro-slip ("MS") damping models, for different values of c_0. Bersfort conductor.

Table 4.12 collects the linear regression coefficients for the experimental data.

Table 4.12. ACSR Bersfort: Regression coefficients of experimental data, ISWR Method results.

$(2\chi_0\, l)^2\Pi = p_0 + p_1\, J$	p_0	p_1	R^2
	-0.4005	3.941	0.896
$\log((2\chi_0\, l)^2\Pi) = q_0 + q_1\, \log(J)$	q_0	q_1	R^2
	1.1408	1.0663	0.968

By comparing the R^2 coefficient computed in the case of linear interpolation in the bi-logarithmic plane for both the Power Method and the ISWR Method (Tables 4.12 and 4.12), one can assess that results obtained through the ISWR Method are more accurate, in the sense that the ordinary least squares better fits experimental values, as expected.

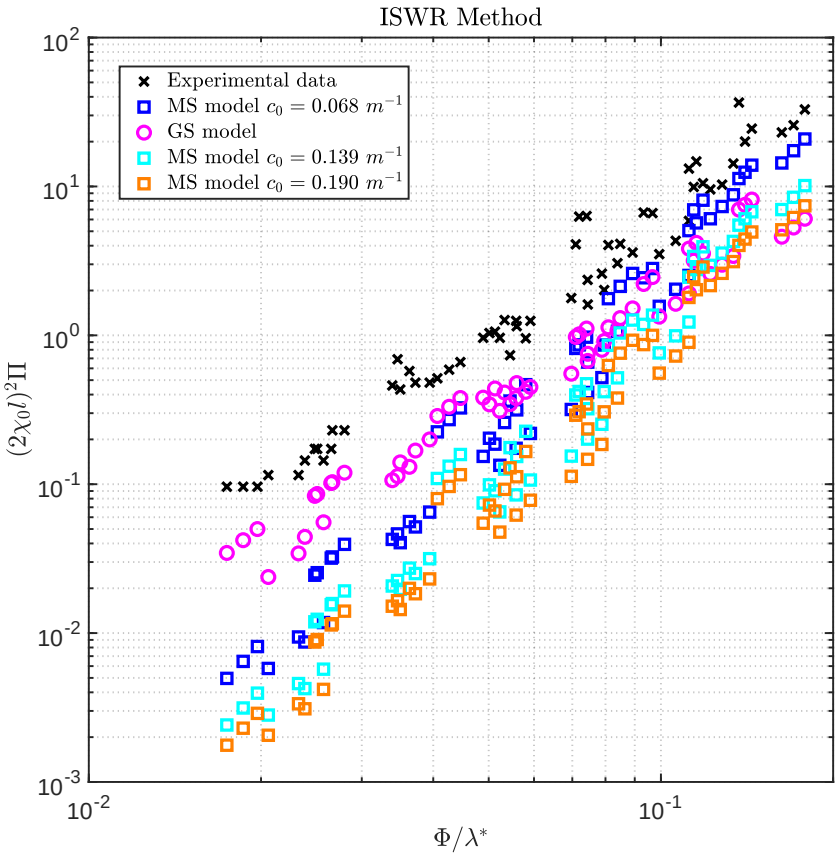

Figure 4.15. Non-dimensional Dissipated power vs. Φ/λ^*. Comparison between experimental data and theoretical predictions of the gross-sliding ("GS") and micro-slip ("MS") damping models, for different values of c_0. Bersfort conductor.

Also in this case, the experimental threshold couldn't be identified (see Tab. 4.13). However, the predictions of the theoretical thresholds are computed and reported in Table 4.14.

Table 4.13. ACSR Bersfort: Experimental Threshold, ISWR Method.

Identifiable	$(\Phi/\lambda^*)_{exp}$
No	-

Table 4.14. ACSR Bersfort: Theoretical thresholds for different values of c_0.

	Theoretical Thresholds $(\Phi/\lambda^*)_{th}$		
$c_0\ (m^{-1})$	$\eta = 0.15$	$\eta = 0.24$	$\eta = 0.30$
0.068	0.436	0.710	1.061
0.139	0.896	1.459	2.089
0.190	1.224	1.995	2.856

Figure 4.16 shows the plot of Π_{th} vs. Π_{exp}. An enlargement of the previous plot is also included in Fig. 4.17 for convenience.
As it can be assess from the linear regression coefficients of the theoretical dissipated power predictions (see Table 4.11), the Micro-Slip dissipation model with $c_0 = 0.068\ m^{-1}$ is the one which better represent experimental results, because the slope of its linear interpolation is the closest to 1 (i.e. the slope of the bisector, that is the locus of the points which are in perfect agreement with experimental results).

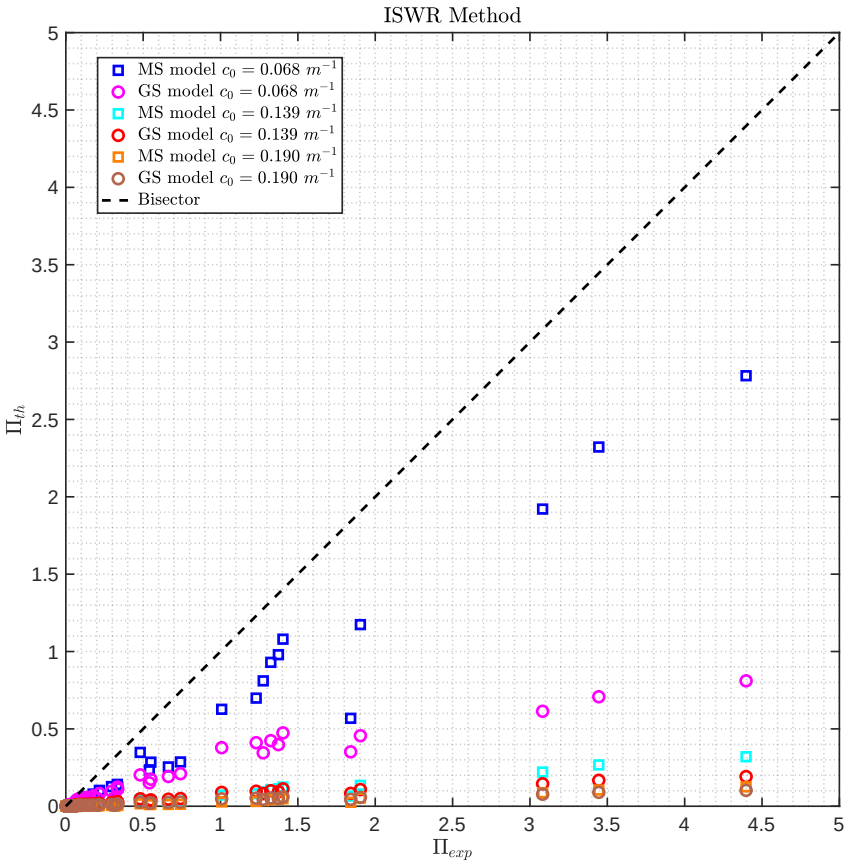

Figure 4.16. Theoretical predictions of the non-dimensional dissipated power Π_{th} vs. non-dimensional dissipated power computed from experimental data Π_{exp}.

Table 4.15. ACSR Bersfort: Regression Coefficients of theoretical predictions, ISWR Method results.

Model	$c_0\ (m^{-1})$	s_0	s_1	R^2
Gross-Sliding	0.068	0.024	0.210	0.935
Gross-Sliding	0.139	0.006	0.210	0.935
Gross-Sliding	0.190	0.003	0.210	0.935
Micro-Slip	0.068	-0.030	0.633	0.971
Micro-Slip	0.139	-0.004	0.308	0.971
Micro-Slip	0.190	-0.001	0.225	0.971

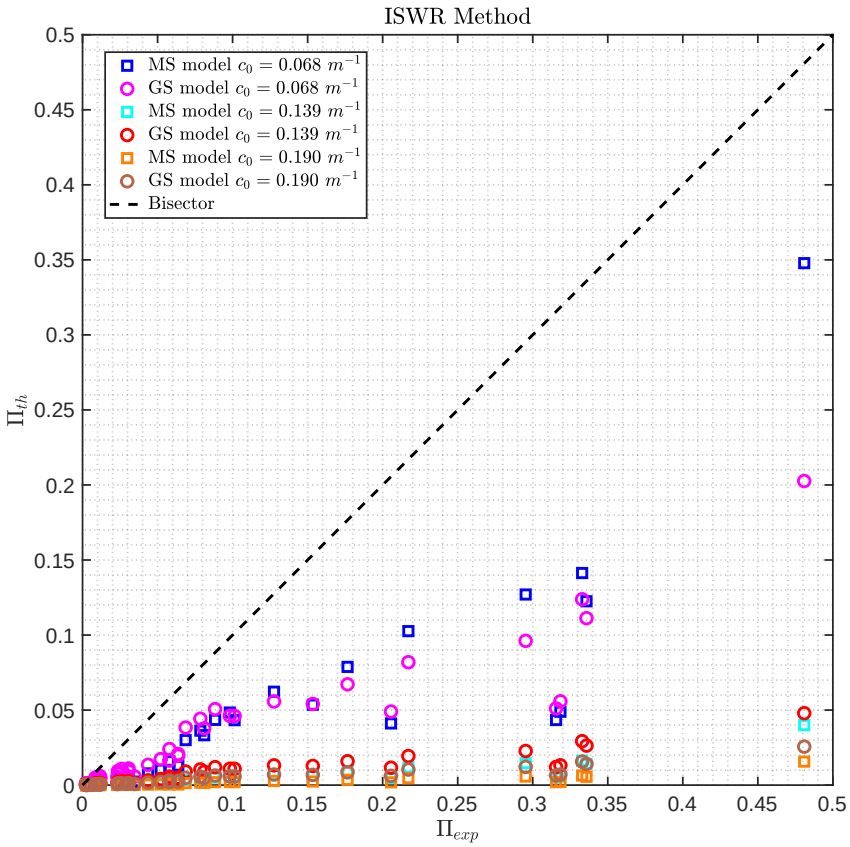

Figure 4.17. Theoretical predictions of the non-dimensional dissipated power Π_{th} vs. non-dimensional dissipated power computed from experimental data Π_{exp}. Enlargement.

Results Summary

In this paragraph, results of experimental campaigns by E = (EPRI, 2006) and P = (Paradis, 2022) obtained through the Inverse Standing Wave Ratio (ISWR) technique for the ACSR 48/7 Bersfort conductor are presented in an aggregate form.
Figure 4.18 and 4.19 show the non-dimensional dissipated power predictions with the theoretical damping models (for different values of the construction parameter c_0) and the comparison with the experimental data, in both $(2\chi_0\, l)^2\Pi$ - J and $(2\chi_0\, l)^2\Pi$ - Φ/λ^* planes. Both sets of results are plotted.
It is worth recalling that the two tested ACSR Bersfort conductors are characterized by slightly different mechanical and geometrical parameters. A summary of the main parameters for both conductors is collected in Tab. 4.2.
Detailed information about the mechanical and geometrical properties of the ACSR 48/7 Bersfort conductor tested in E = (EPRI, 2006) can be found in Appendix A. Its cross-section is depicted in Fig. B.3c.
Mechanical and geometrical properties of the ACSR 48/7 Bersfort conductor tested in P = (Paradis, 2022) which differ from the previous ones, are reported in Tab. 4.7.
The difference in between such parameters is therefore not permitting a direct comparison between the two set of results.

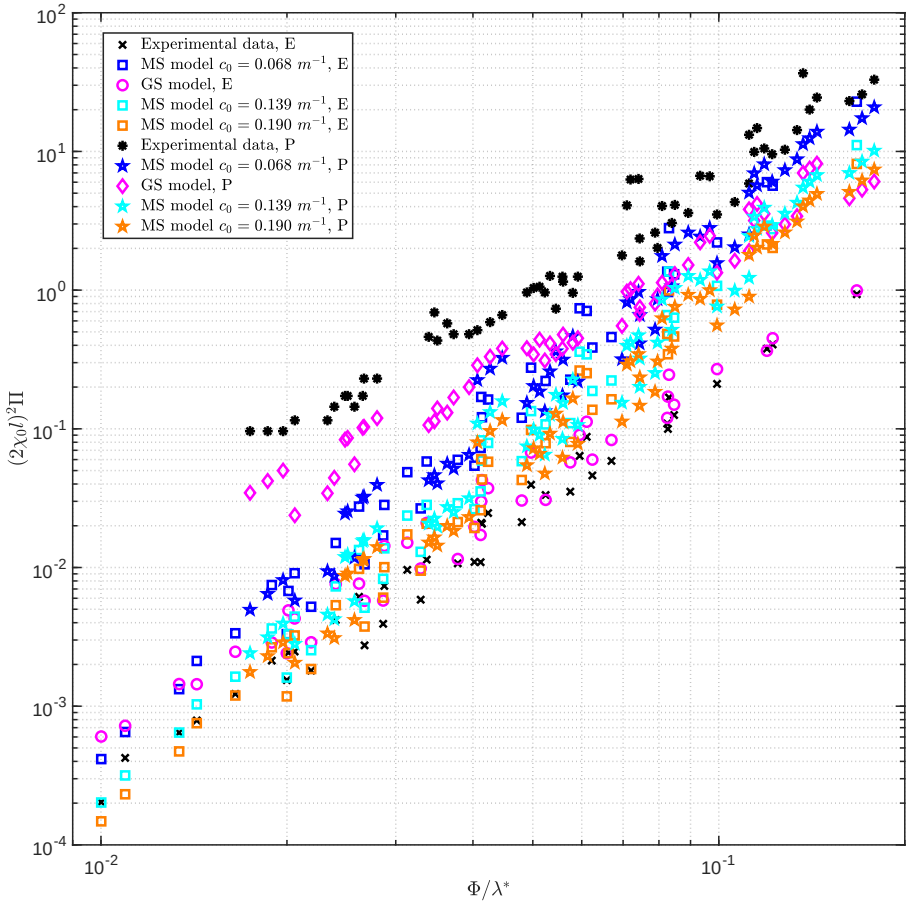

Figure 4.18. Non-dimensional Dissipated power vs. J parameter. Comparison between experimental data and theoretical predictions of the gross-sliding ("GS") and micro-slip ("MS") damping models, for different values of c_0. Bersfort conductors by E and P.

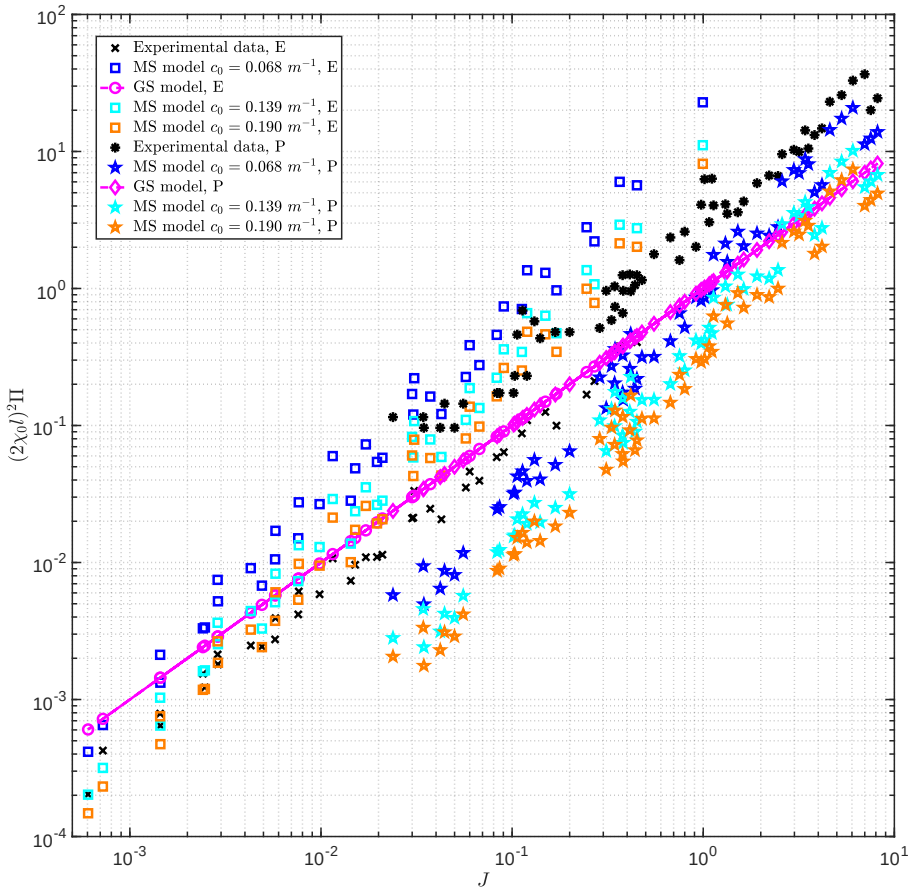

Figure 4.19. Non-dimensional Dissipated power vs. J parameter. Comparison between experimental data and theoretical predictions of the gross-sliding ("GS") and micro-slip ("MS") damping models, for different values of c_0. Bersfort conductors by E and P.

Some considerations are still interesting to do.
Fig 4.18 clearly shows how the theoretical predictions obtained through the Gross-Sliding dissipation mechanism for both conductors, lie on the same straight line. This is a direct consequence of the choice of the quantity that has been used on the y axis, i.e. $(2\chi_0\, l)^2\Pi$. In such way, the dependence upon the span length and the first yielding curvature is lost. Conversely, the predictions obtained through the Micro-Slip dissipation mechanism diversify both for the conductor geometrical characteristics and for its hysteretic behavior, described by the construction parameter c_0.
Gross-Sliding theoretical predictions appear to be the most suitable to describe the set of experimental data by (EPRI, 2006) and with minor accuracy, the one by (Paradis, 2022).

4.2.3 ACSR 54/7 Curlew

In this subsection, the ACSR 54/7 Curlew conductor is considered. Its mechanical and geometrical properties are collected in Appendix A, whereas its cross-section is depicted in Fig. B.4c (see Appendix B). Its contact conditions are related to a new state ($\mu = 0.3$ is adopted). The power per unit of length (P_d) dissipated during forced vibration tests, performed at different values of frequency f and antinode vibration amplitude A and for different values of the tension T, was measured through the Power Method technique.
It is worth notice that during this test, the end-point damping (dead end losses) was not minimized. In fact, in such case, the power method provides high uncertainty limits, because the dead end losses may be quite relevant. As it can be seen in Figure 4.20, the quality of the measured dissipated power per unit of length is clearly affected by this phenomenon.

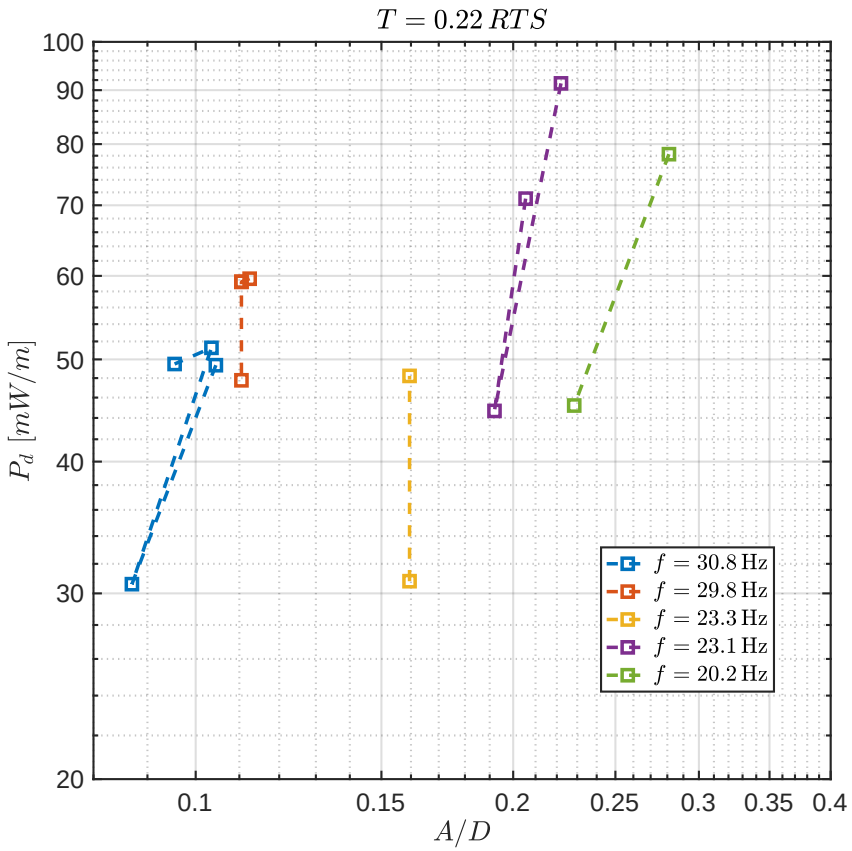

Figure 4.20. Dissipated power per unit of length vs. non-dimensional antinode amplitude. Data from (EPRI, 2006), Appendix-A. Curlew conductor.

Figures 4.21 and 4.22 show the non-dimensional dissipated power predictions with the theoretical damping models for different values of the construction parameter c_0 (see sections 3.6 and 3.7), and the comparison with the experimental data, in both $(2\chi_0\, l)^2\Pi$ - J and $(2\chi_0\, l)^2\Pi$ - Φ/λ^* planes.

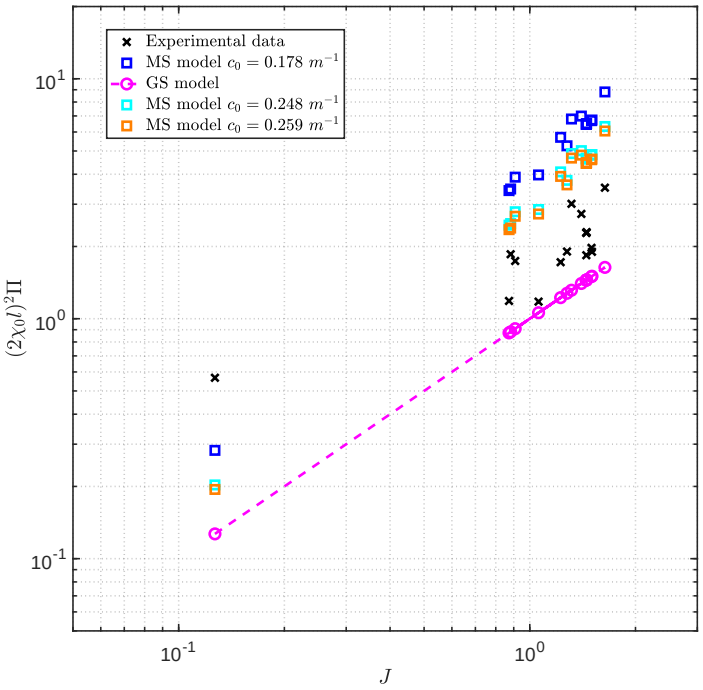

Figure 4.21. Non-dimensional Dissipated power vs. J parameter. Comparison between experimental data and theoretical predictions of the gross-sliding ("GS") and micro-slip ("MS") damping models, for different values of c_0. Curlew conductor.

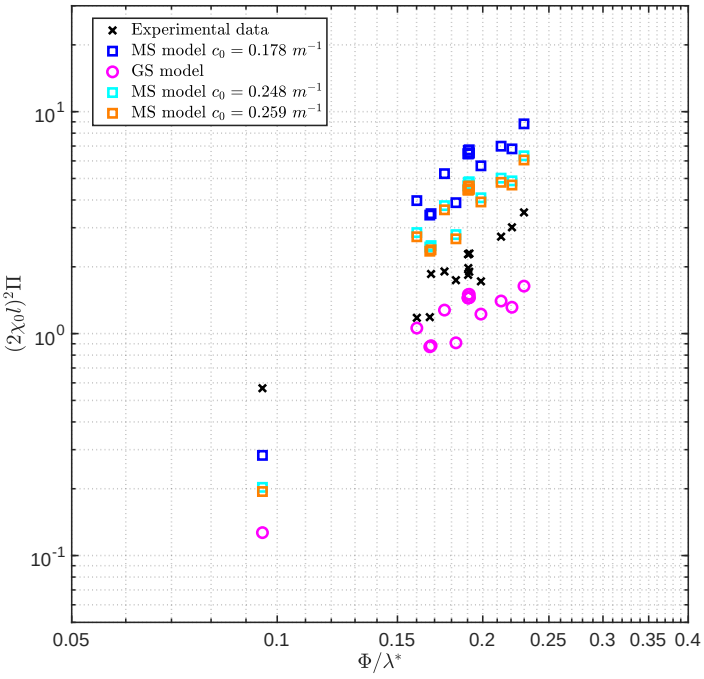

Figure 4.22. Non-dimensional Dissipated power vs. Φ/λ^*. Comparison between experimental data and theoretical predictions of the gross-sliding ("GS") and micro-slip ("MS") damping models, for different values of c_0. Curlew conductor.

Table 4.16 collects the linear regression coefficients for the experimental data.

Table 4.16. ACSR Curlew: Regression Coefficients of experimental data.

$(2\chi_0\, l)^2\Pi = p_0 + p_1\, J$	p_0 0.2399	p_1 1.4432	R^2 0.578
$\log((2\chi_0\, l)^2\Pi) = q_0 + q_1\, \log(J)$	q_0 0.5640	q_1 0.5942	R^2 0.7174

In this case, the experimental threshold couldn't be identified (see Tab. 4.17) and experimental results appear to be better represented by the predictions obtained through the Micro-Slip dissipation model with $c_0 = 0.259\ m^{-1}$. However, the predictions of the theoretical thresholds are computed and reported in Table 4.18.
As an additional comment, from Fig. 4.22 it is possible to recognize that for low values of the parameter Φ/λ^*, experimental data are in closer agreement with the predictions of the MS dissipation model, whereas, for high values of Φ/λ^*, the trend is inverted and GS dissipation model predictions are better representing the experimental results.

Table 4.17. ACSR Curlew: Experimental Threshold.

Identifiable	$(\Phi/\lambda^*)_{exp}$
No	-

Table 4.18. ACSR Curlew: Theoretical thresholds for different values of c_0.

$c_0\ (m^{-1})$	$(\Phi/\lambda^*)_{th}$
0.178	0.062
0.248	0.087
0.259	0.091

Figure 4.23 shows the moment-curvature diagram for the conductor subject to a tension level equal to $\eta = 0.22$.

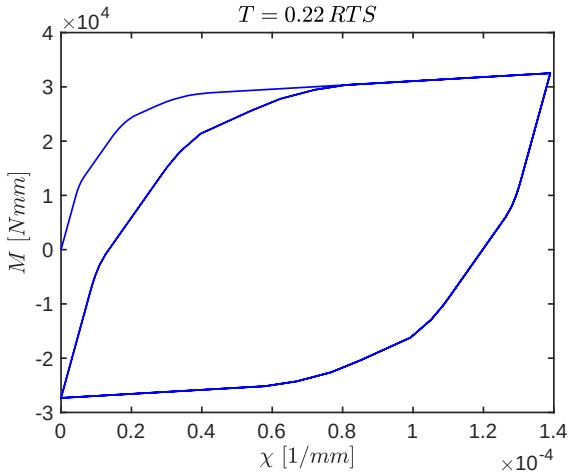

Figure 4.23. Curlew conductor ($\mu = 0.30$): plot of the Moment-Curvature diagram in the case of cyclic loading.

4.2.4 ACSR 72/7 Nelson I

In this subsection, the ACSR 72/7 Nelson I conductor is considered. Its mechanical and geometrical properties are collected in Appendix A, whereas its cross-section is depicted in Fig. B.5b (see Appendix B). Its contact conditions are related to a new state ($\mu = 0.3$ is adopted). The power per unit of length (P_d) dissipated during forced vibration tests, performed at different values of frequency f and antinode vibration amplitude A and for different values of the tension T, was measured through the Power Method technique.

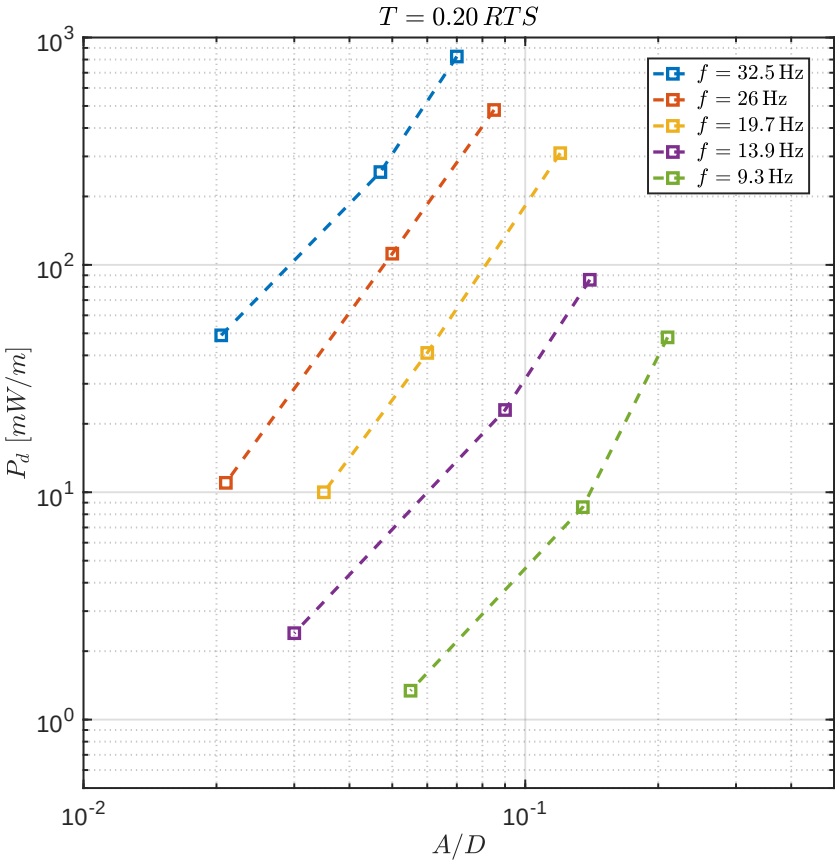

Figure 4.24. Dissipated power per unit of length vs. non-dimensional antinode amplitude. Data from (EPRI, 2006), Appendix-A. Nelson I conductor.

Figures 4.25 and 4.26 show the non-dimensional dissipated power predictions with the theoretical damping models for different values of the construction parameter c_0 (see sections 3.6 and 3.7), and the comparison with the experimental data, in both $(2\chi_0\, l)^2\Pi$ - J and $(2\chi_0\, l)^2\Pi$ - Φ/λ^* planes.

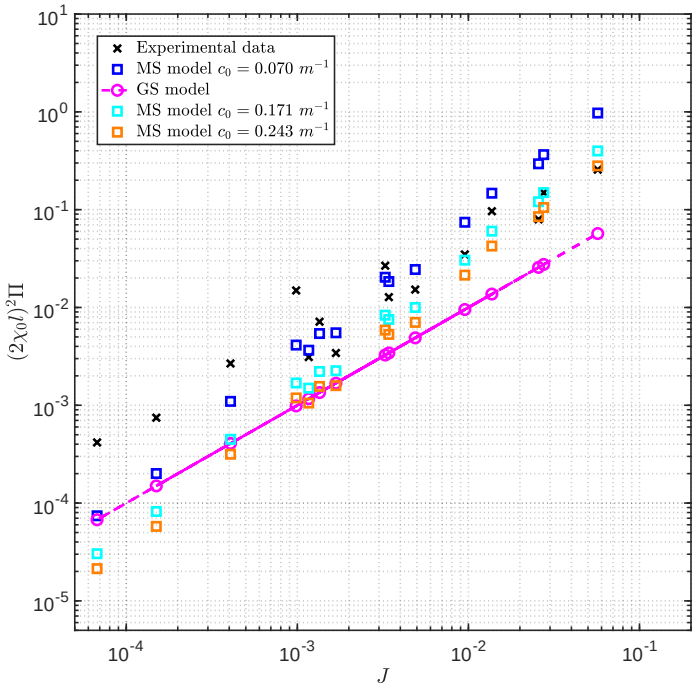

Figure 4.25. Non-dimensional Dissipated power vs. J parameter. Comparison between experimental data and theoretical predictions of the gross-sliding ("GS") and micro-slip ("MS") damping models, for different values of c_0. Nelson I conductor.

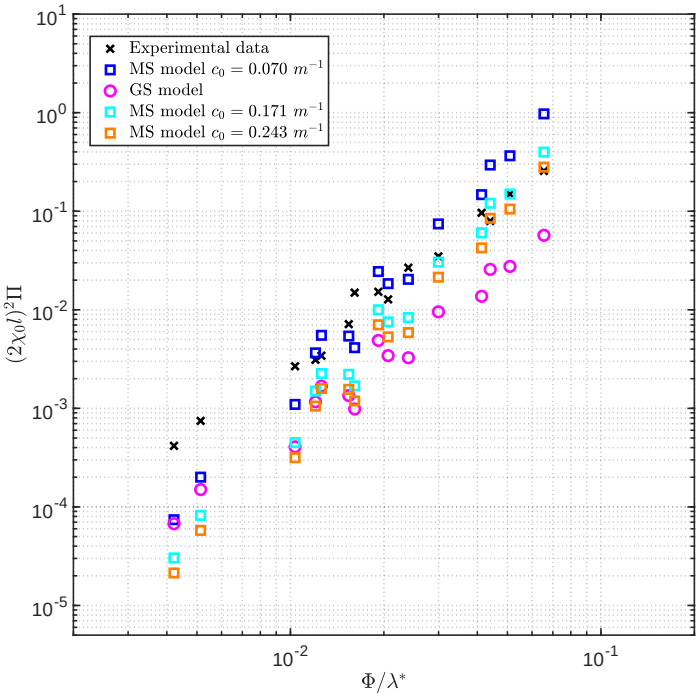

Figure 4.26. Non-dimensional Dissipated power vs. Φ/λ^*. Comparison between experimental data and theoretical predictions of the gross-sliding ("GS") and micro-slip ("MS") damping models, for different values of c_0. Nelson I conductor.

Table 4.19 collects the linear regression coefficients for the experimental data.

Table 4.19. ACSR Nelson I: Regression Coefficients of experimental data.

$(2\chi_0\, l)^2\Pi = p_0 + p_1\, J$	p_0 0.0019	p_1 4.4779	R^2 0.952
$\log((2\chi_0\, l)^2\Pi) = q_0 + q_1\, \log(J)$	q_0 1.2519	q_1 0.9466	R^2 0.933

From Fig. 4.26 an experimental threshold $(\Phi/\lambda^*)_{exp} = 0.01$ could be tentatively identified (see also Tab. 4.20). The closest prediction of the theoretical threshold is the one computed with $c_0 = 0.070\ m^{-1}$ (see Tab. 4.21) and is equal to the double of the experimental one.

Table 4.20. ACSR Nelson I: Experimental Threshold.

Identifiable	$(\Phi/\lambda^*)_{exp}$
Yes	0.01

Table 4.21. ACSR Nelson I: Theoretical thresholds for different values of c_0.

$c_0\ (m^{-1})$	$(\Phi/\lambda^*)_{th}$
0.070	0.020
0.171	0.049
0.243	0.070

Figure 4.27 shows the moment-curvature diagram for the conductor subject to a tension level equal to $\eta = 0.20$.

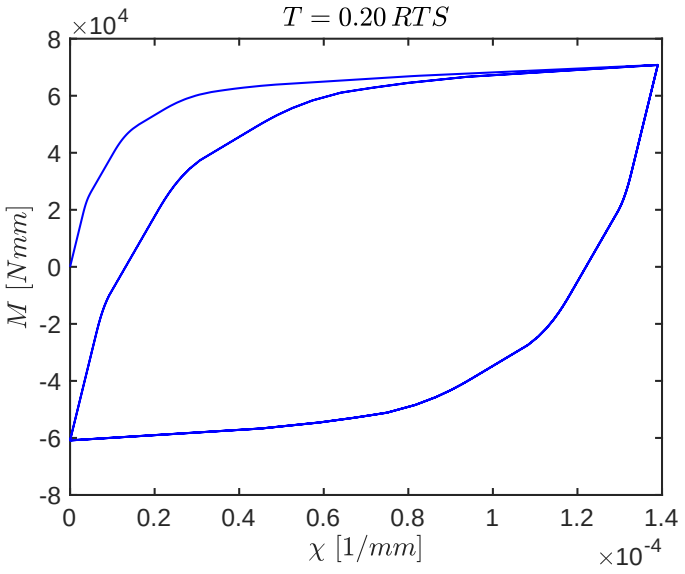

Figure 4.27. Nelson I conductor ($\mu = 0.30$): plot of the Moment-Curvature diagram in the case of cyclic loading.

4.2.5 ACSR 26/7 Hawk (New Greased)

In this subsection, the ACSR 26/7 Hawk conductor is considered. Its mechanical and geometrical properties are collected in Appendix A, whereas its cross-section is depicted in Fig. B.2b (see Appendix B). Its contact conditions are related to a greased new state ($\mu = 0.15$ is adopted). The power per unit of length (P_d) dissipated during forced vibration tests, performed at different values of frequency f and antinode vibration amplitude A and for different values of the tension T, was measured through the Power Method technique. The end-point damping (dead end losses) was minimized, in order to reduce the uncertainty limits.

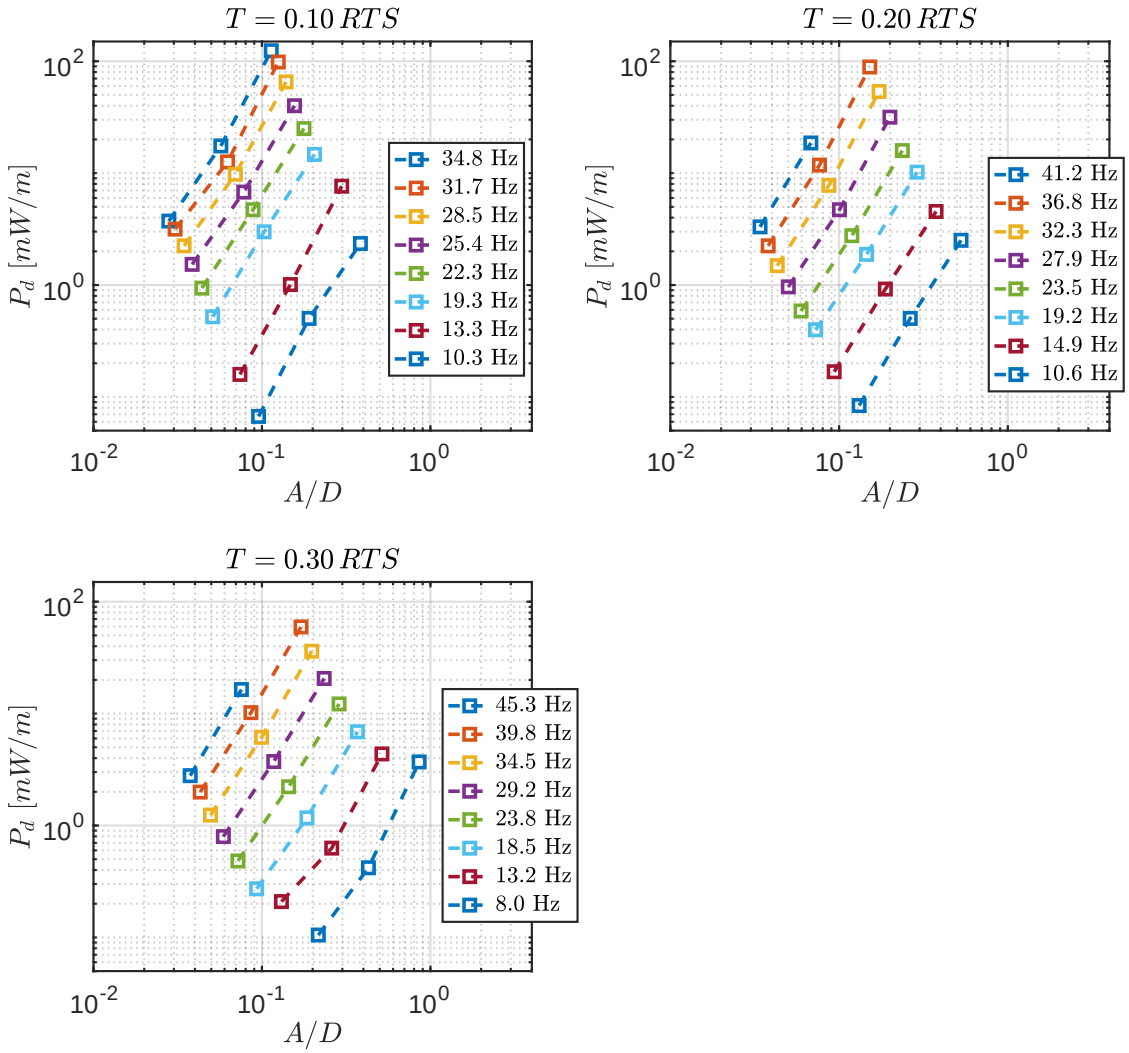

Figure 4.28. Dissipated power per unit of length vs. non-dimensional antinode amplitude. Data from (EPRI, 2006), Appendix-A. Hawk conductor.

Figures 4.29 and 4.30 show the non-dimensional dissipated power predictions with the theoretical damping models for different values of the construction parameter c_0 (see sections 3.6 and 3.7), and the comparison with the experimental data, in both $(2\chi_0\, l)^2\Pi$ - J and $(2\chi_0\, l)^2\Pi$ - Φ/λ^* planes.

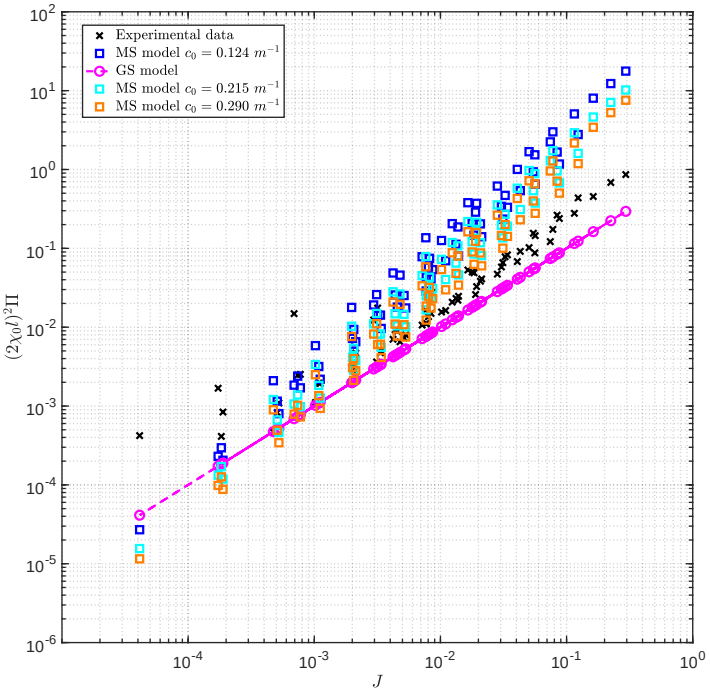

Figure 4.29. Non-dimensional Dissipated power vs. J parameter. Comparison between experimental data and theoretical predictions of the gross-sliding ("GS") and micro-slip ("MS") damping models, for different values of c_0. Hawk (New) conductor.

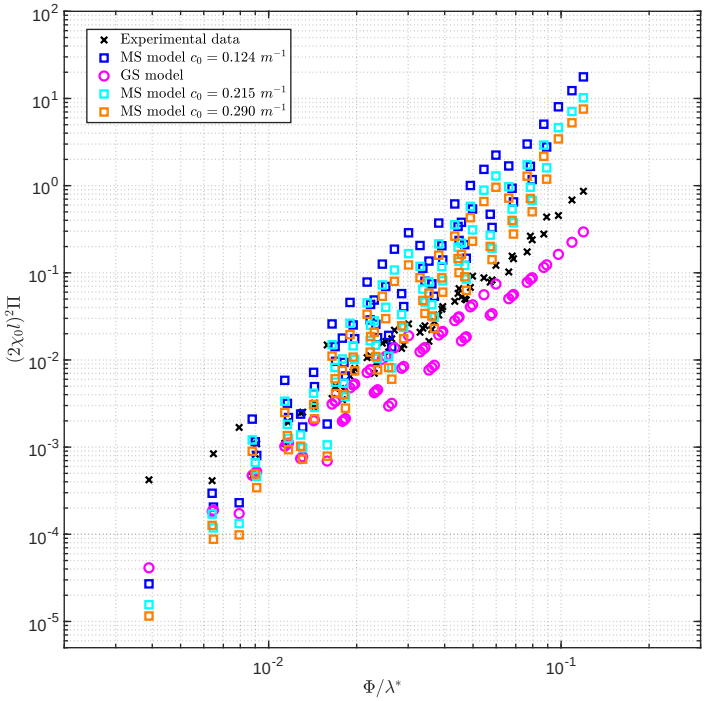

Figure 4.30. Non-dimensional Dissipated power vs. Φ/λ^*. Comparison between experimental data and theoretical predictions of the gross-sliding ("GS") and micro-slip ("MS") damping models, for different values of c_0. Hawk (New) conductor.

Table 4.22 collects the linear regression coefficients for the experimental data.

Table 4.22. ACSR Hawk (New Greased) Regression Coefficients of experimental data.

$(2\chi_0\, l)^2\Pi = p_0 + p_1\, J$	p_0	p_1	R^2
	-0.0107	2.9129	0.978
$\log((2\chi_0\, l)^2\Pi) = q_0 + q_1\, \log(J)$	q_0	q_1	R^2
	0.5255	0.9464	0.926

In this case, the experimental threshold couldn't be identified (see Tab. 4.24). However, the predictions of the theoretical thresholds are computed and reported in Table 4.24.

Table 4.23. ACSR Hawk (New Greased): Experimental Threshold.

Identifiable	$(\Phi/\lambda^*)_{exp}$
No	-

Table 4.24. ACSR Hawk (New Greased): Theoretical thresholds for different values of c_0.

	Theoretical Thresholds $(\Phi/\lambda^*)_{th}$		
c_0 (m^{-1})	$\eta = 0.10$	$\eta = 0.20$	$\eta = 0.30$
0.124	0.042	0.083	0.125
0.215	0.072	0.144	0.216
0.290	0.097	0.195	0.292

Figure 4.31 shows the plot of Π_{th} vs. Π_{exp}. An enlargement of the previous plot is also included in Fig. 4.32 for convenience.
As it can be assessed from the linear regression coefficients of the theoretical dissipated power predictions (see Table 4.25), the Micro-Slip dissipation model with $c_0 = 0.215\ m^{-1}$ is the one which better represent experimental results, especially for small values of the non-dimensional dissipated power, as can be assessed in Fig. 4.32.

Table 4.25. ACSR Hawk (New Greased): Regression Coefficients of theoretical predictions.

Model	c_0 (m^{-1})	s_0	s_1	R^2
Gross-Sliding	0.124	0.244	0.346	0.982
Gross-Sliding	0.215	0.081	0.346	0.982
Gross-Sliding	0.290	0.045	0.346	0.982
Micro-Slip	0.124	-13.32	19.22	0.989
Micro-Slip	0.215	-2.56	11.09	0.989
Micro-Slip	0.290	-1.04	8.22	0.989

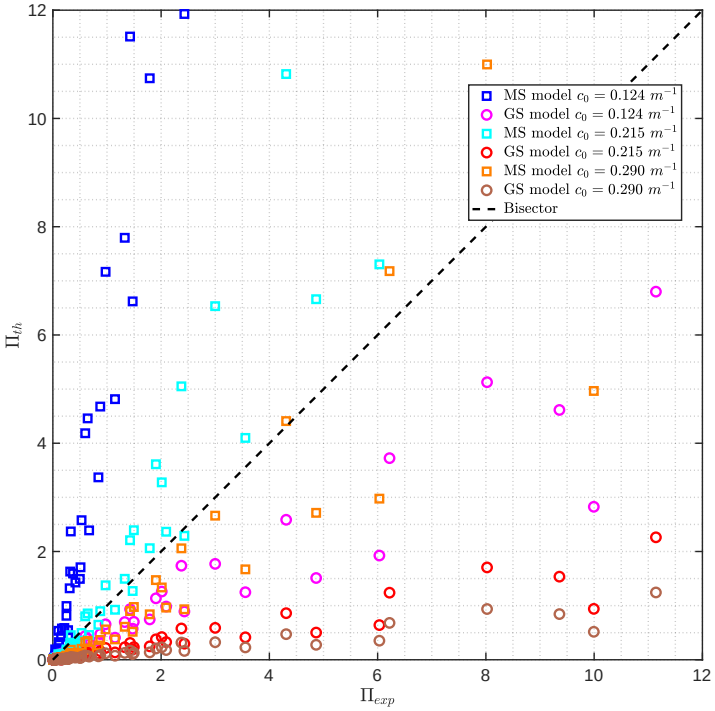

Figure 4.31. Theoretical predictions of the non-dimensional dissipated power Π_{th} vs. non-dimensional dissipated power computed from experimental data Π_{exp}. Hawk (New) conductor.

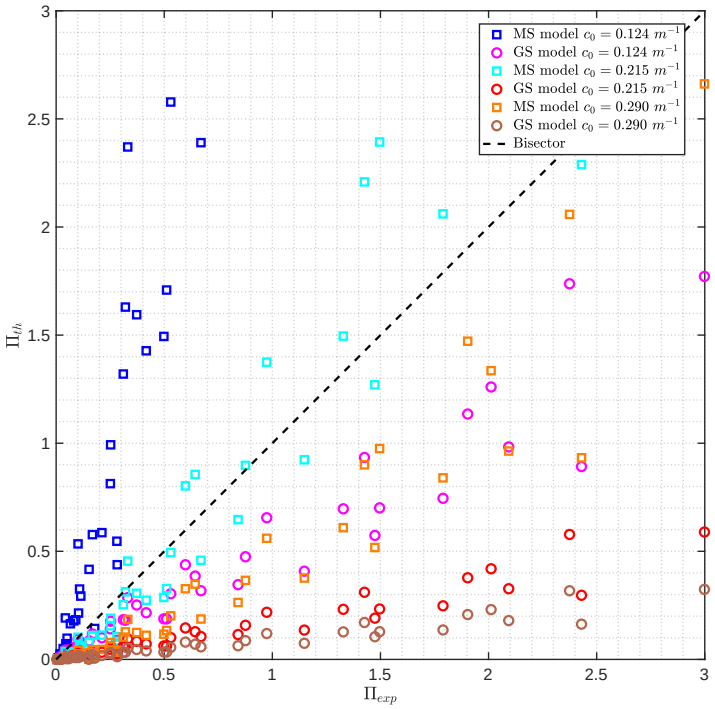

Figure 4.32. Theoretical predictions of the non-dimensional dissipated power Π_{th} vs. non-dimensional dissipated power computed from experimental data Π_{exp}. Enlargement. Hawk (New) conductor.

Finally, the moment-curvature diagrams for different loading ratios η are reported in Figure 4.33

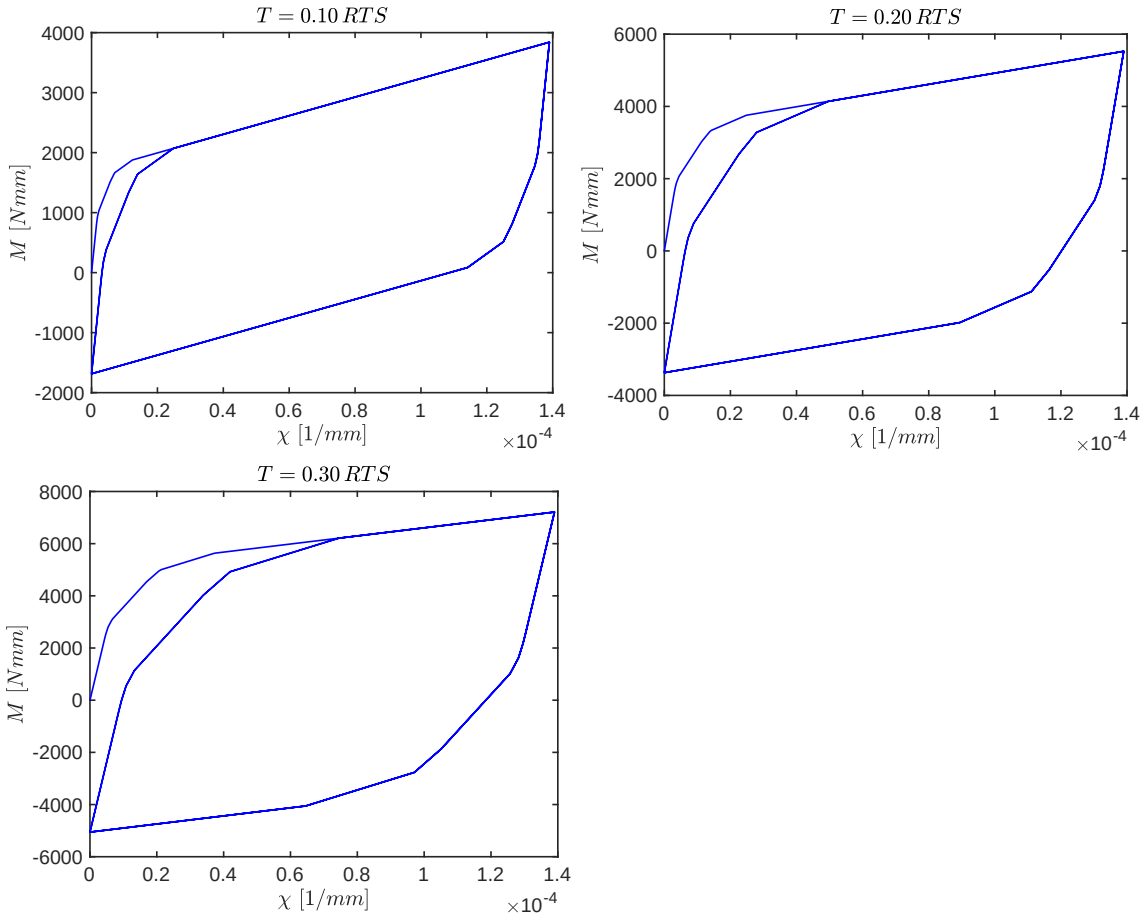

Figure 4.33. Hawk conductor ($\mu = 0.15$): plot of the Moment-Curvature diagrams in the case of cyclic loading, for different values of the tension T.

4.2.6 ACSR 26/7 Hawk (Old Greased)

In this subsection, the ACSR 26/7 Hawk conductor is considered. Its mechanical and geometrical properties are collected in Appendix A, whereas its cross-section is depicted in Fig. B.2b (see Appendix B). Its contact conditions are related to a greased old state ($\mu = 0.45$ is adopted). The power per unit of length (P_d) dissipated during forced vibration tests, performed at different values of frequency f and antinode vibration amplitude A and for different values of the tension T, was measured through the Power Method technique. The end-point damping (dead end losses) was minimized, in order to reduce the uncertainty limits.

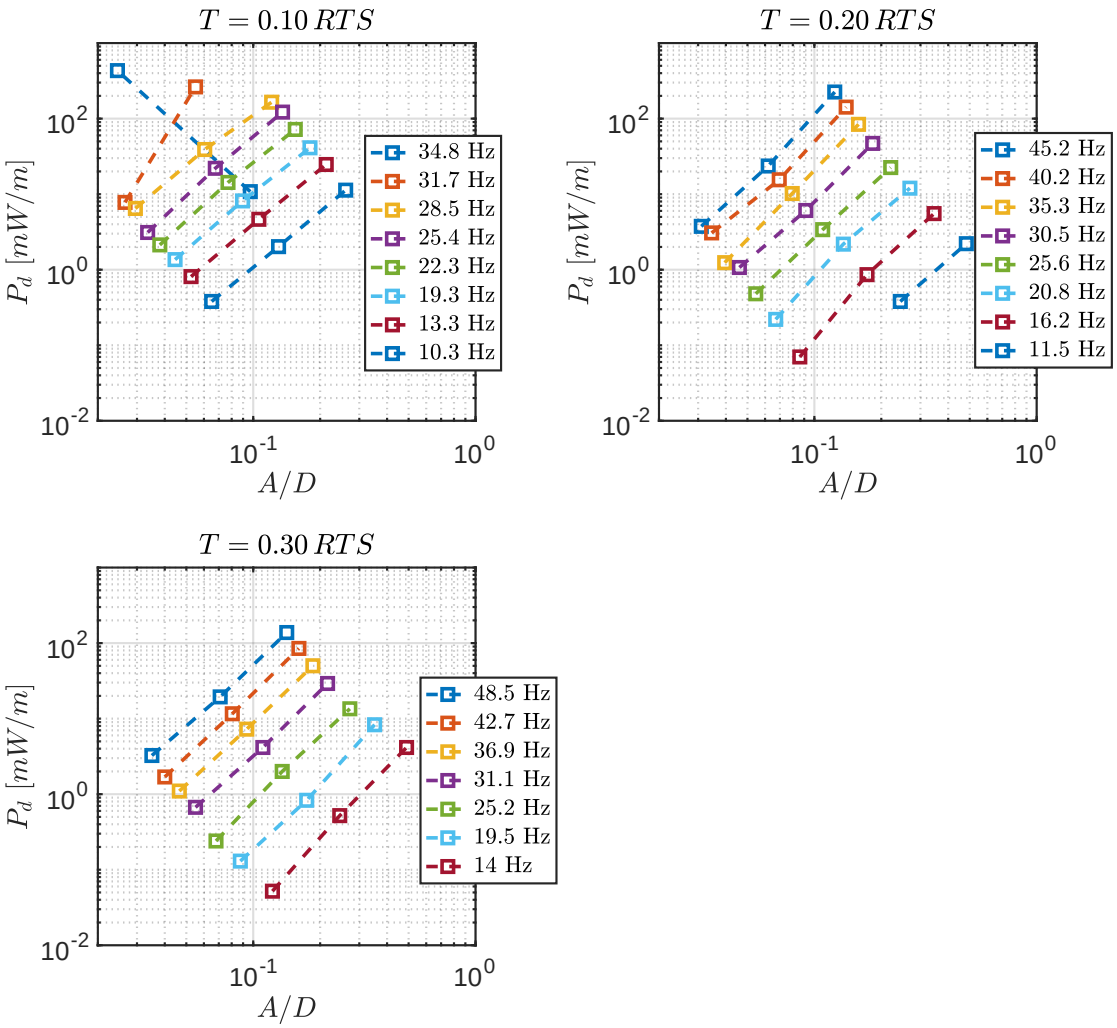

Figure 4.34. Dissipated power per unit of length vs. non-dimensional antinode amplitude. Data from (EPRI, 2006), Appendix-A. Hawk conductor.

Figures 4.35 and 4.36 show the non-dimensional dissipated power predictions with the theoretical damping models for different values of the construction parameter c_0 (see sections 3.6 and 3.7), and the comparison with the experimental data, in both $(2\chi_0\, l)^2\Pi$ - J and $(2\chi_0\, l)^2\Pi$ - Φ/λ^* planes.

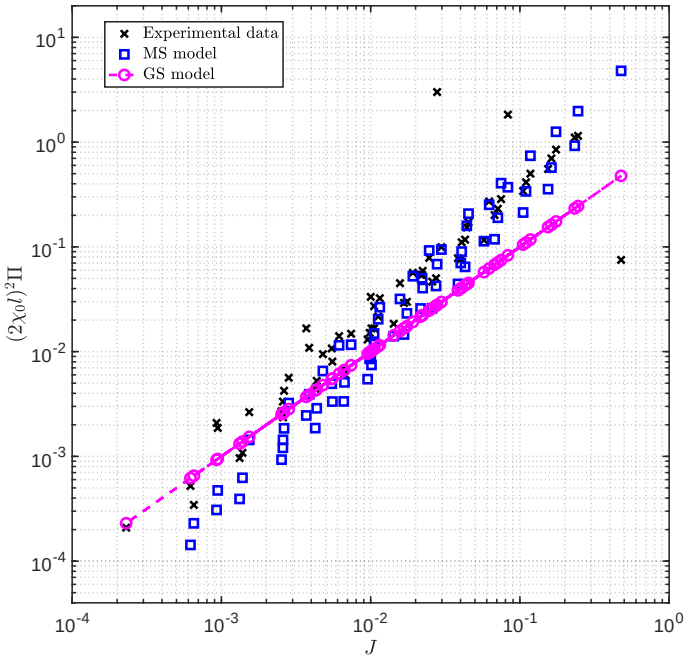

Figure 4.35. Non-dimensional Dissipated power vs. J parameter. Comparison between experimental data and theoretical predictions of the gross-sliding ("GS") and micro-slip ("MS") damping models. Hawk (Old) conductor.

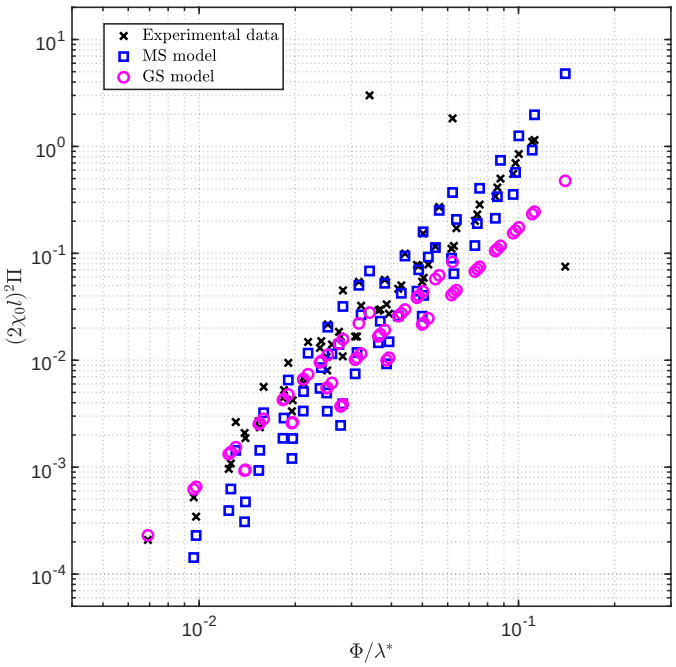

Figure 4.36. Non-dimensional Dissipated power vs. Φ/λ^*. Comparison between experimental data and theoretical predictions of the gross-sliding ("GS") and micro-slip ("MS") damping models. Hawk (Old) conductor.

Table 4.26 collects the linear regression coefficients for the experimental data.

Table 4.26. ACSR Hawk (Old Greased) Regression Coefficients of experimental data.

$(2\chi_0\, l)^2\Pi = p_0 + p_1\, J$	p_0 0.1042	p_1 2.2060	R^2 0.126
$\log((2\chi_0\, l)^2\Pi) = q_0 + q_1\, \log(J)$	q_0 1.7122	q_1 1.2158	R^2 0.876

As it appears clear from table 4.26, the coefficient of determination R^2 of the experimental data linear interpolation indicates that the fitting is non representative of the whole set of data. This is due to the presence of few outliers, that are clearly visible in the previous figures. It is onsequently convenient to remove the outliers and re-work the same plots.

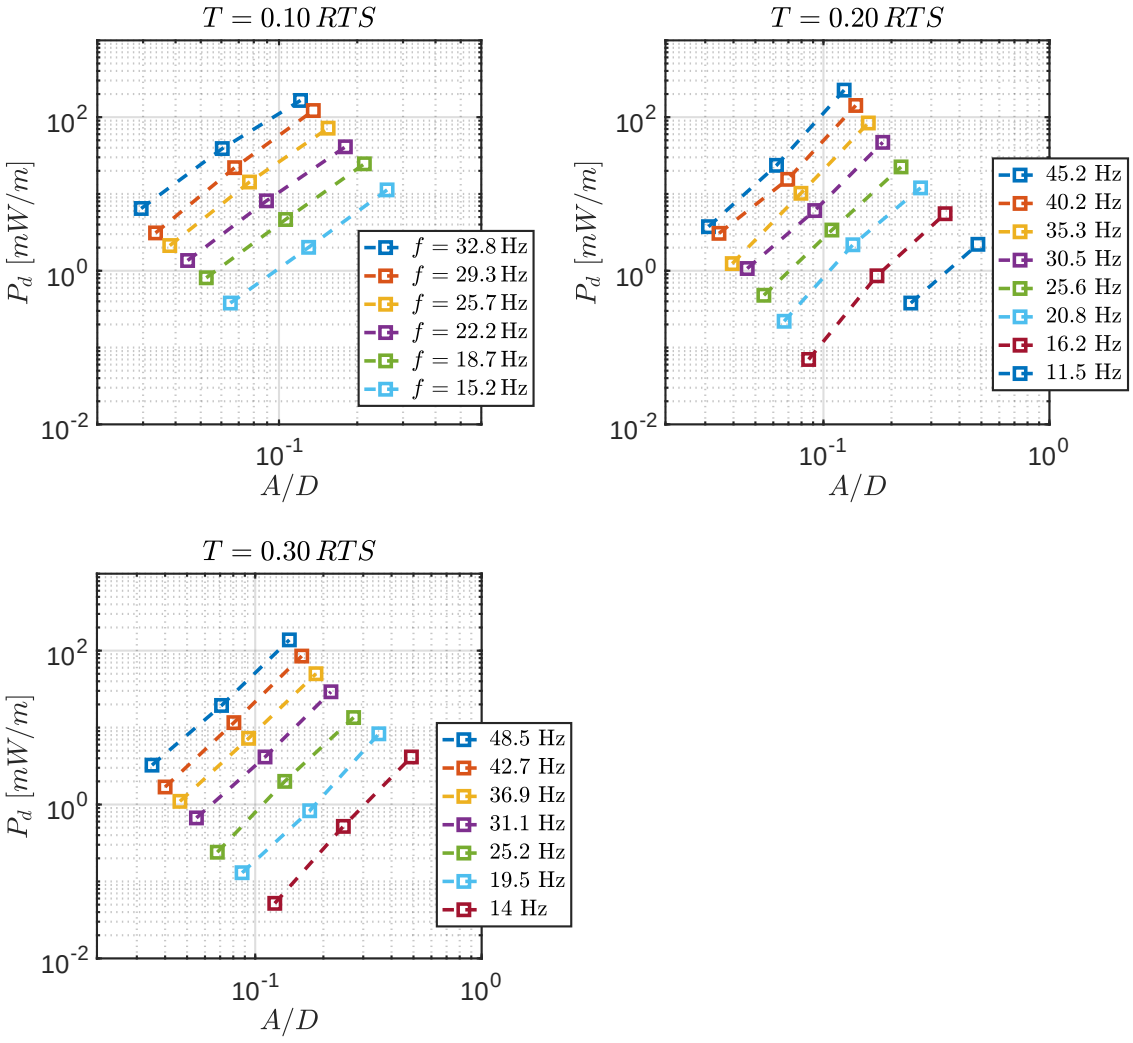

Figure 4.37. Dissipated power per unit of length vs. non-dimensional antinode amplitude. Data from EPRI 2006, Appendix-A. Hawk conductor (Outliers removed).

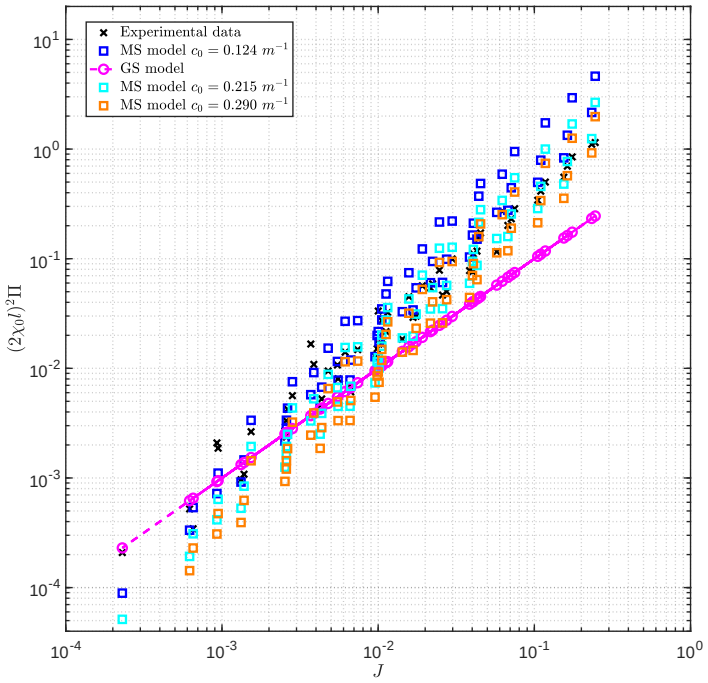

Figure 4.38. Non-dimensional Dissipated power vs. J parameter. Comparison between experimental data and theoretical predictions of the gross-sliding ("GS") and micro-slip ("MS") damping models, for different values of c_0. Hawk (Old) conductor (Outliers removed).

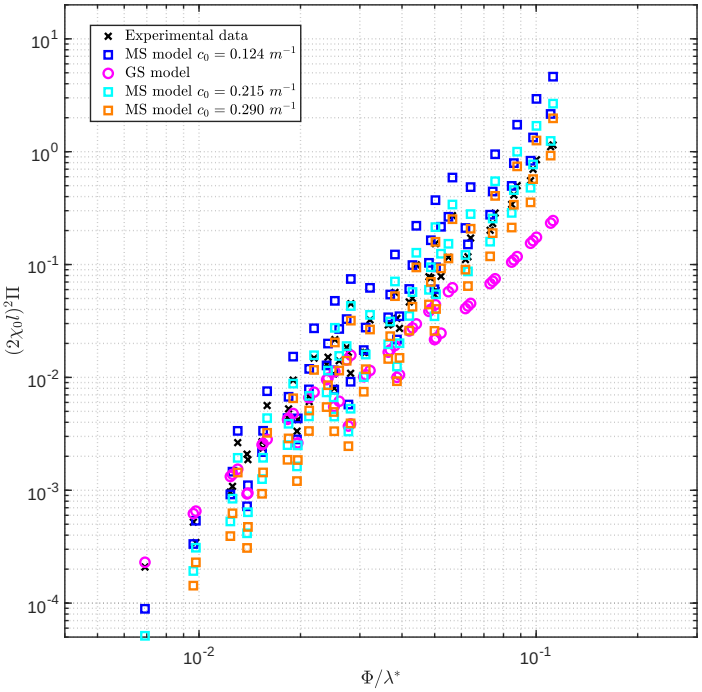

Figure 4.39. Non-dimensional Dissipated power vs. Φ/λ^*. Comparison between experimental data and theoretical predictions of the gross-sliding ("GS") and micro-slip ("MS") damping models, for different values of c_0. Hawk (Old) conductor (Outliers removed).

Table 4.26 collects the linear regression coefficients for the experimental data after the outliers removal.

Table 4.27. ACSR Hawk (Old Greased) Regression Coefficients of experimental data (Outliers removed).

$(2\chi_0\, l)^2\Pi = p_0 + p_1\, J$	p_0	p_1	R^2
	-0.032	4.488	0.974
$\log((2\chi_0\, l)^2\Pi) = q_0 + q_1\, \log(J)$	q_0	q_1	R^2
	1.833	1.252	0.972

From Fig. 4.36 an experimental threshold $(\Phi/\lambda^*)_{exp} = 0.03$ could be tentatively identified (see Tab. 4.28). The closest prediction of the theoretical threshold is the one computed with $c_0 = 0.124\ m^{-1}$ and $\eta = 0.10$ is equal to 0.111, as can be seen from Tab. 4.29.

Table 4.28. ACSR Hawk (Old Greased): Experimental Threshold.

Identifiable	$(\Phi/\lambda^*)_{exp}$
Yes	0.03

Table 4.29. ACSR Hawk (Old Greased): Theoretical thresholds for different values of c_0.

	Theoretical Thresholds $(\Phi/\lambda^*)_{th}$		
$c_0\ (m^{-1})$	$\eta = 0.10$	$\eta = 0.20$	$\eta = 0.30$
0.124	0.111	0.221	0.332
0.215	0.192	0.383	0.575
0.290	0.258	0.517	0.775

Figure 4.40 shows the plot of Π_{th} vs. Π_{exp}. An enlargement of the previous plot is also included in Fig. 4.41 for convenience.
As it can be assessed from the linear regression coefficients of the theoretical dissipated power predictions (see Table 4.25), the Micro-Slip dissipation model with $c_0 = 0.215\ m^{-1}$ is the one which better represent experimental results, especially for small values of the non-dimensional dissipated power, as can be assessed in Fig. 4.41.

Table 4.30. ACSR Hawk (Old Greased): Regression Coefficients of theoretical predictions.

Model	$c_0\ (m^{-1})$	s_0	s_1	R^2
Gross-Sliding	0.124	0.028	0.214	0.993
Gross-Sliding	0.215	0.009	0.214	0.993
Gross-Sliding	0.290	0.005	0.214	0.993
Micro-Slip	0.124	-0.504	3.688	0.977
Micro-Slip	0.215	-0.097	2.127	0.977
Micro-Slip	0.290	-0.039	1.577	0.977

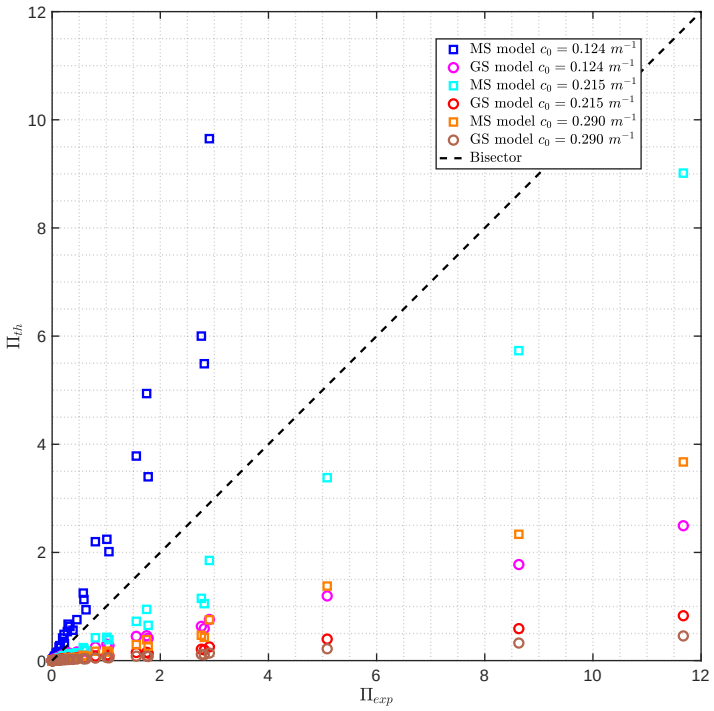

Figure 4.40. Theoretical predictions of the non-dimensional dissipated power Π_{th} vs. non-dimensional dissipated power computed from experimental data Π_{exp}. Hawk (Old) conductor.

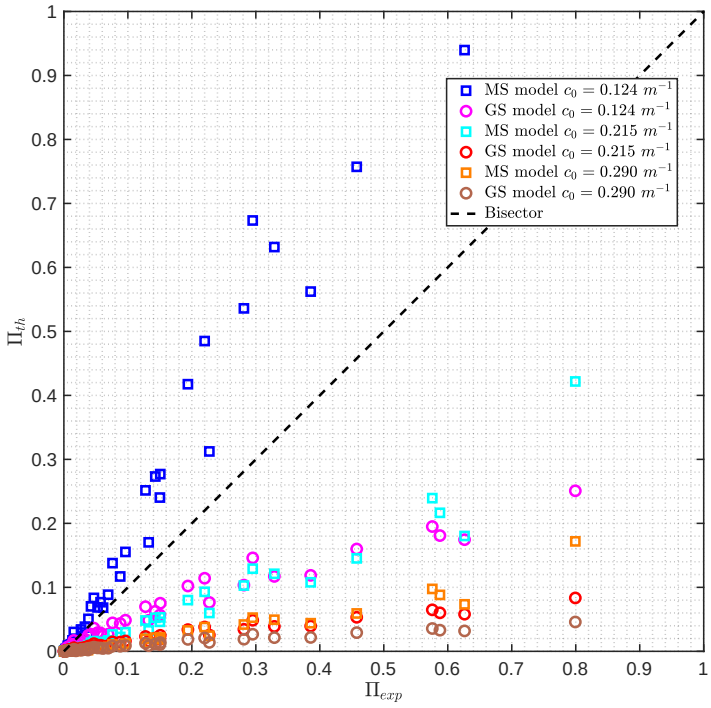

Figure 4.41. Theoretical predictions of the non-dimensional dissipated power Π_{th} vs. non-dimensional dissipated power computed from experimental data Π_{exp}. Enlargement. Hawk (Old) conductor.

Finally, the moment-curvature diagrams for different loading ratios η are reported in Figure 4.42.

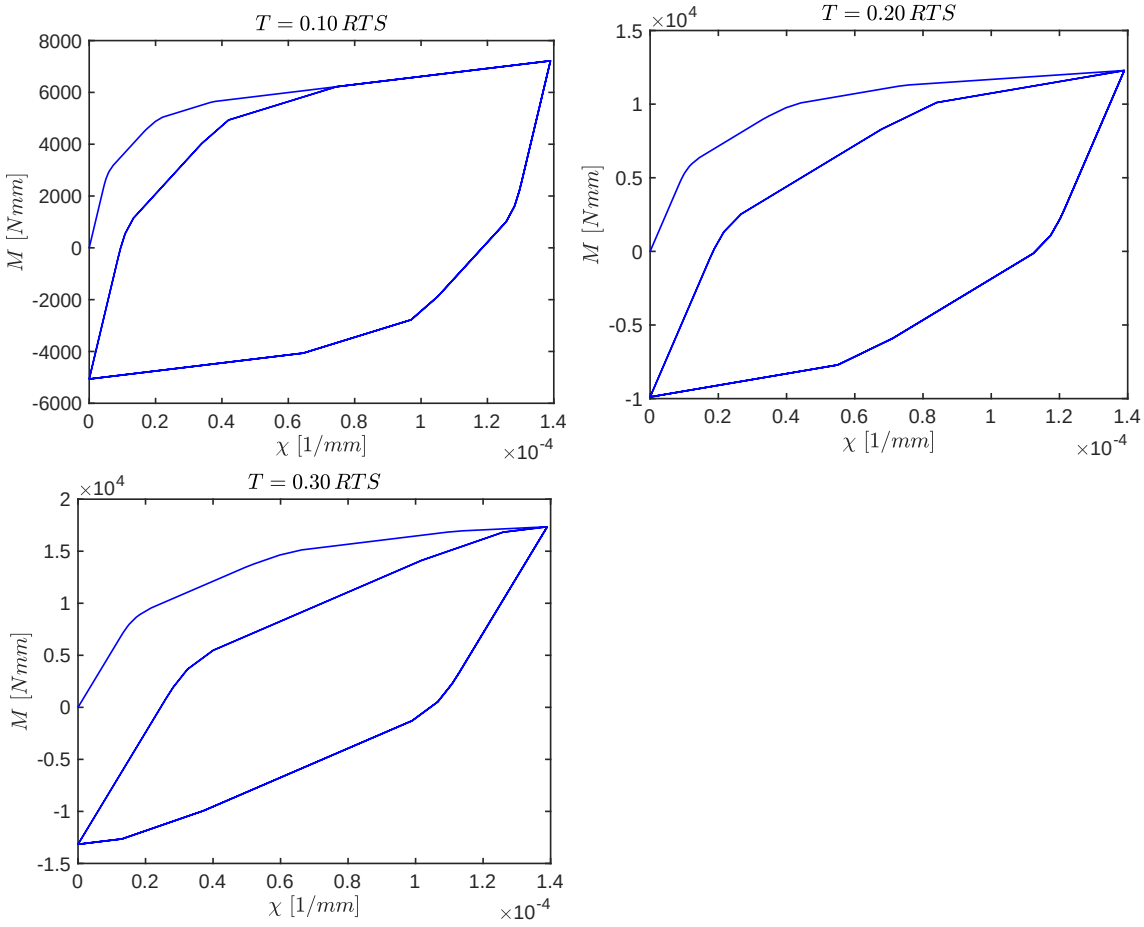

Figure 4.42. Hawk conductor ($\mu = 0.45$): plot of the Moment-Curvature diagrams in the case of cyclic loading, for different values of the tension T.

4.2.7 ACSR 6/1 Penguin

In this subsection, the ACSR 6/1 Penguin conductor is considered. Its mechanical and geometrical properties are collected in Appendix A, whereas its cross-section is depicted in Fig. B.1c (see Appendix B).
The EPRI results indicate this conductor typology as a 6/1 Pigeon, but the outer diamater $D = 14.31$ mm corresponds to the one of a Penguin conductor, as well as other mechanical properties, with the exception of the Rated Tensile Stength RTS. For this reasons, in the following, this data will be associated to the test of a commercial ACSR "Penguin" conductor, and not to a commercial ACSR "Pigeon" conductor.
The power per unit of length (P_d) dissipated during forced vibration tests, performed at different values of frequency f and antinode vibration amplitude A and for different values of the tension T, was measured through the Inverse Standing Wave Ratio (ISWR) technique and corrected to subtract the aerodynamic damping.

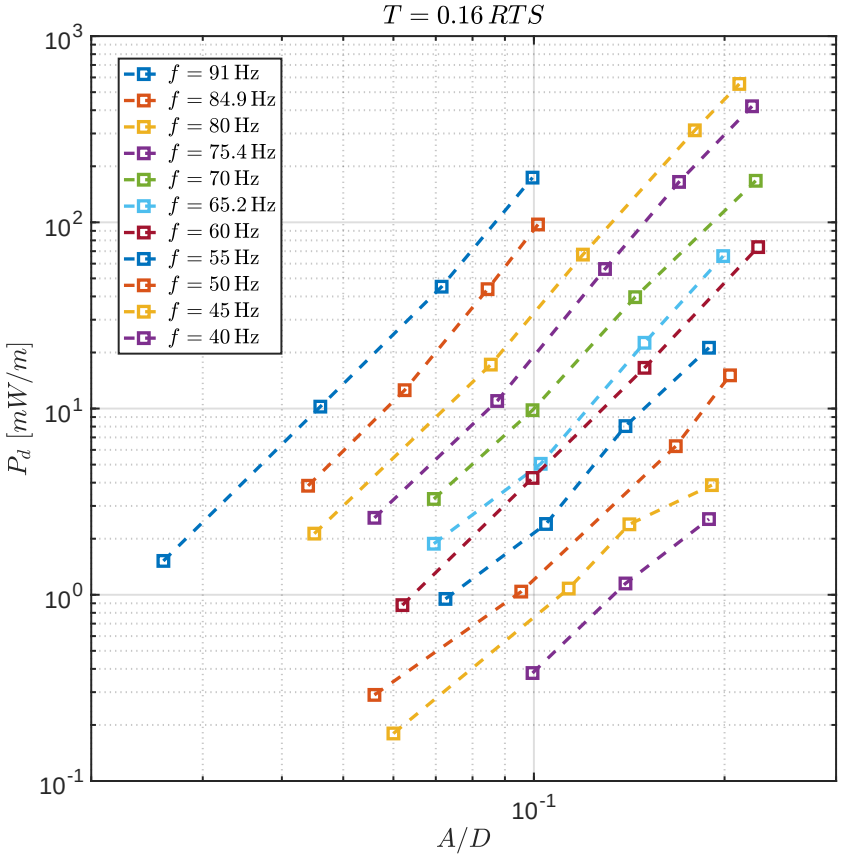

Figure 4.43. Dissipated power per unit of length vs. non-dimensional antinode amplitude. Data from (EPRI, 2006), Appendix-A. Penguin conductor.

Figures 4.44 and 4.45 show the non-dimensional dissipated power predictions with the theoretical damping models for different values of the construction parameter c_0 (see sections 3.6 and 3.7), and the comparison with the experimental data, in both $(2\chi_0\, l)^2\Pi$ - J and $(2\chi_0\, l)^2\Pi$ - Φ/λ^* planes.
As it can be seen, since the two values of the construction parameters are approximately equal, the Micro-Slip dissipation predictions are almost equivalent.

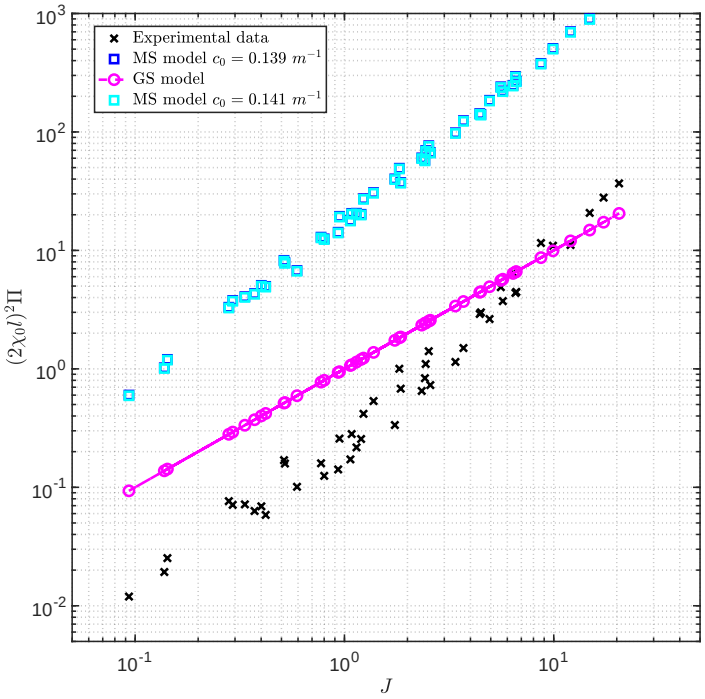

Figure 4.44. Non-dimensional Dissipated power vs. J parameter. Comparison between experimental data and theoretical predictions of the gross-sliding ("GS") and micro-slip ("MS") damping models, for different values of c_0. Penguin conductor.

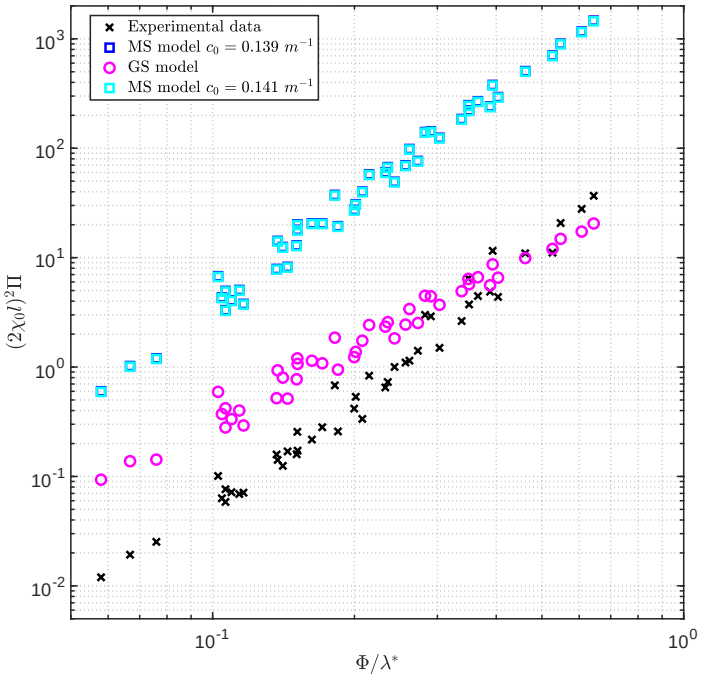

Figure 4.45. Non-dimensional Dissipated power vs. Φ/λ^*. Comparison between experimental data and theoretical predictions of the gross-sliding ("GS") and micro-slip ("MS") damping models, for different values of c_0. Penguin conductor.

Table 4.31 collects the linear regression coefficients for the experimental data.

Table 4.31. ACSR Penguin: Regression Coefficients of experimental data.

$(2\chi_0\, l)^2\Pi = p_0 + p_1\, J$	p_0	p_1	R^2
	-1.9997	1.5303	0.919
$\log((2\chi_0\, l)^2\Pi) = q_0 + q_1\, \log(J)$	q_0	q_1	R^2
	-1.2485	1.4817	0.972

In this case, the slope of the line interpolating experimental data is approximately equal to one predicted by the MS damping model, for all values of J. This fact may be related to the influence of the tangential contact compliance mechanism between the external wires and the core. Further studies are needed to correctly understand the dissipation mechanisms of 6/1 conductors accounting for the tangential contact compliance mechanism (Foti and Martinelli, 2019). As a matter of fact, the transition curvature between micro-slip and gross-sliding dissipation mechanisms cannot be identified (see Tab. 4.32).

Table 4.32. ACSR Penguin: Experimental Threshold.

Identifiable	$(\Phi/\lambda^*)_{exp}$
No	-

The predictions of the theoretical thresholds for different values of c_0 are computed for the sake of completeness and are reported in Tab. 4.33.

Table 4.33. ACSR Penguin: Theoretical thresholds for different values of c_0.

$c_0\ (m^{-1})$	$(\Phi/\lambda^*)_{th}$
0.139	0.096
0.141	0.098

Figure 4.46 shows the moment-curvature diagram for the conductor subject to a tension level equal to $\eta = 0.16$.

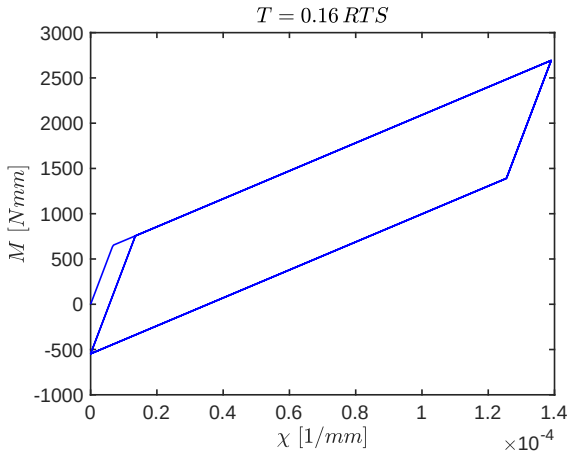

Figure 4.46. Penguin conductor ($\mu = 0.30$): plot of the Moment-Curvature diagram in the case of cyclic loading.

4.2.8 ACSR 26/7 Drake (Initial State)

In this subsection, the ACSR 26/7 Drake conductor is considered. Its mechanical and geometrical properties are collected in Appendix A, whereas its cross-section is depicted in Fig. B.2c (see Appendix B). According to the self-damping tests performed by Southwire, the conductor was tested at 15%, 20% and 30% of its Rated Tensile Strength (RTS). In the following, reference will be made to this three levels of the test tension as "Initial State". Upon completion of the 30% level, the conductor was stretched by raising the tension to 50% RTS and then this level of tension was held for one hour. This stretching is necessary to help facilitate the final loading/unloading conditions of the conductors.
At the end, reversing the order, the conductor was tested again at 30%, 20%, and 15% of its RTS. In the following, reference will be made to this other three levels of the test tension as "Final State" (see Subsection 4.2.9).
The power per unit of length (P_d) dissipated during forced vibration tests, performed at different values of frequency f and antinode vibration amplitude A and for different values of the tension T, was measured through the Inverse Standing Wave Ratio (ISWR) technique.

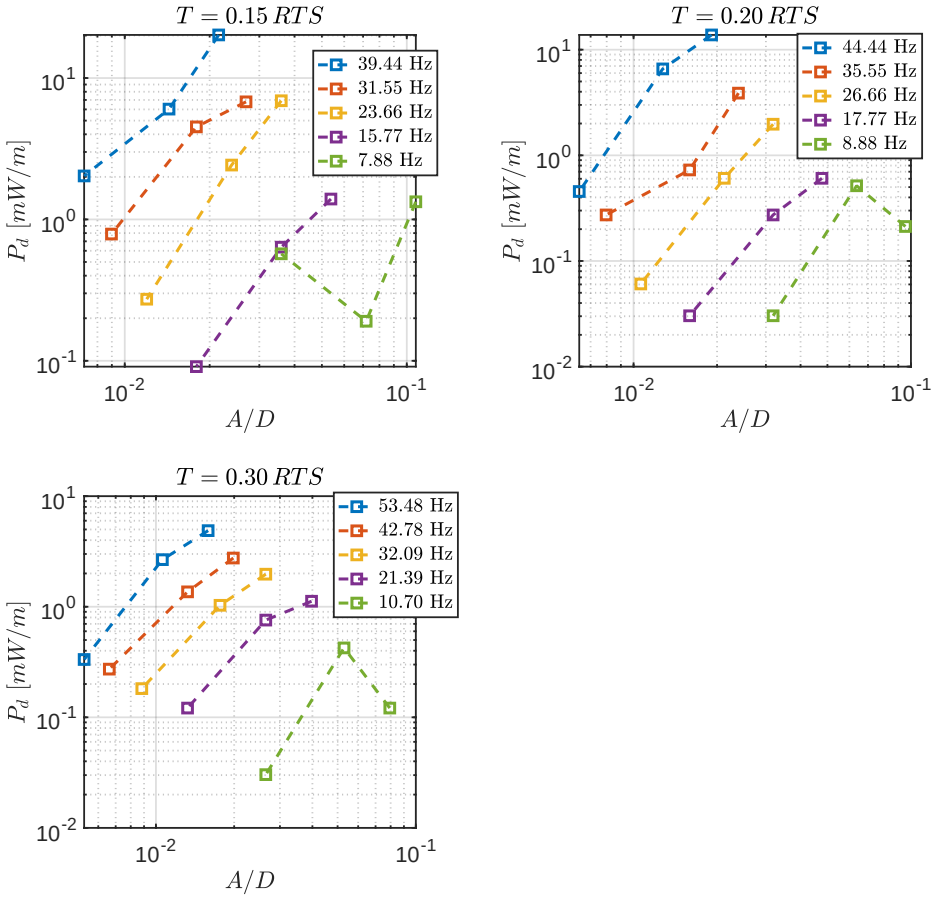

Figure 4.47. Dissipated power per unit of length vs. non-dimensional antinode amplitude. Data from (Southwire, 1996).

Figures 4.48 and 4.49 show the non-dimensional dissipated power predictions with the theoretical damping models for different values of the construction parameter c_0 (see sections 3.6 and 3.7), and the comparison with the experimental data, in both $(2\chi_0\, l)^2\Pi$ - J and $(2\chi_0\, l)^2\Pi$ - Φ/λ^* planes.

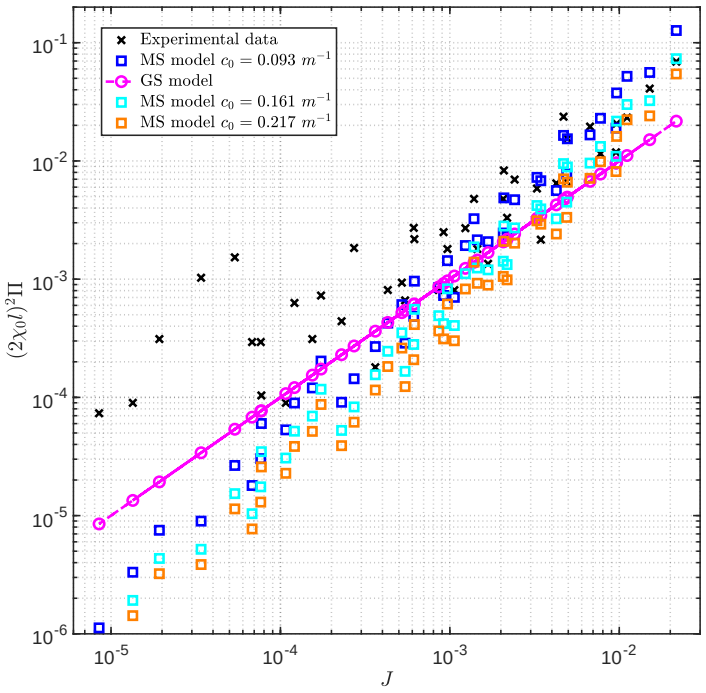

Figure 4.48. Non-dimensional Dissipated power vs. J parameter. Comparison between experimental data and theoretical predictions of the gross-sliding ("GS") and micro-slip ("MS") damping models, for different values of c_0. Drake conductor, Initial State.

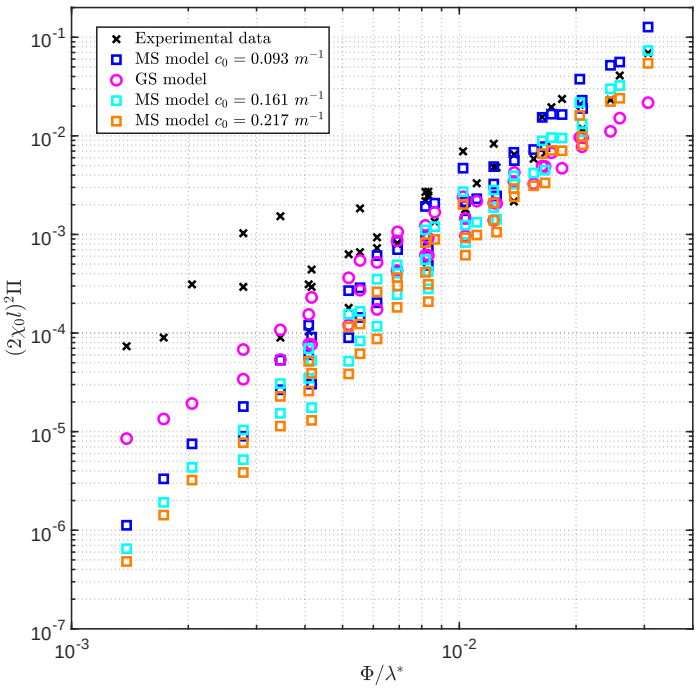

Figure 4.49. Non-dimensional Dissipated power vs. Φ/λ^*. Comparison between experimental data and theoretical predictions of the gross-sliding ("GS") and micro-slip ("MS") damping models, for different values of c_0. Drake conductor, Initial State.

Table 4.34 collects the linear regression coefficients for the experimental data.

Table 4.34. ACSR Drake (Initial State): Regression Coefficients of experimental data.

$(2\chi_0\, l)^2\Pi = p_0 + p_1\, J$	p_0	p_1	R^2
	-0.0008	2.6769	0.895
$\log((2\chi_0\, l)^2\Pi) = q_0 + q_1\, \log(J)$	q_0	q_1	R^2
	-0.6132	0.7839	0.799

In this case, the experimental threshold couldn't be identified (see Tab. 4.35). However, the predictions of the theoretical thresholds are computed and reported in Table 4.36.

Table 4.35. ACSR Drake (Initial State): Experimental Threshold.

Identifiable	$(\Phi/\lambda^*)_{exp}$
No	-

Table 4.36. ACSR Drake (Initial State): Theoretical thresholds for different values of c_0.

	Theoretical Thresholds $(\Phi/\lambda^*)_{th}$		
c_0 (m^{-1})	$\eta = 0.15$	$\eta = 0.20$	$\eta = 0.30$
0.093	0.060	0.080	0.120
0.161	0.104	0.138	0.208
0.217	0.140	0.186	0.279

Figure 4.50 shows the plot of Π_{th} vs. Π_{exp}. An enlargement of the previous plot is also included in Fig. 4.51 for convenience.
As it can be assessed from the linear regression coefficients of the theoretical dissipated power predictions (see Table 4.37), the Micro-Slip dissipation model with $c_0 = 0.093\ m^{-1}$ is the one which better represent experimental results.

Table 4.37. ACSR Drake (Initial State): Regression Coefficients of theoretical predictions.

Model	c_0 (m^{-1})	s_0	s_1	R^2
Gross-Sliding	0.093	0.004	0.324	0.941
Gross-Sliding	0.161	0.001	0.324	0.941
Gross-Sliding	0.217	0.001	0.324	0.941
Micro-Slip	0.093	-0.022	1.73	0.940
Micro-Slip	0.161	-0.004	1.00	0.940
Micro-Slip	0.217	-0.002	0.74	0.940

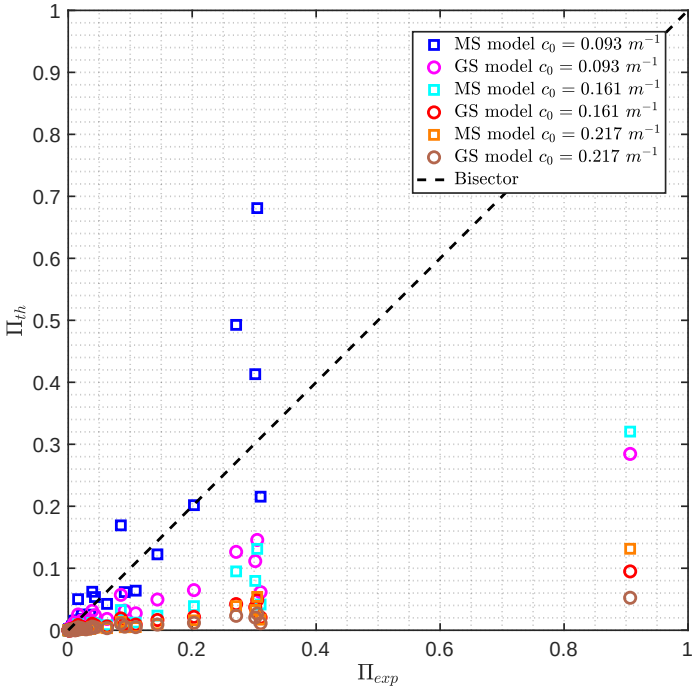

Figure 4.50. Theoretical predictions of the non-dimensional dissipated power Π_{th} vs. non-dimensional dissipated power computed from experimental data Π_{exp}. Drake conductor, Initial State.

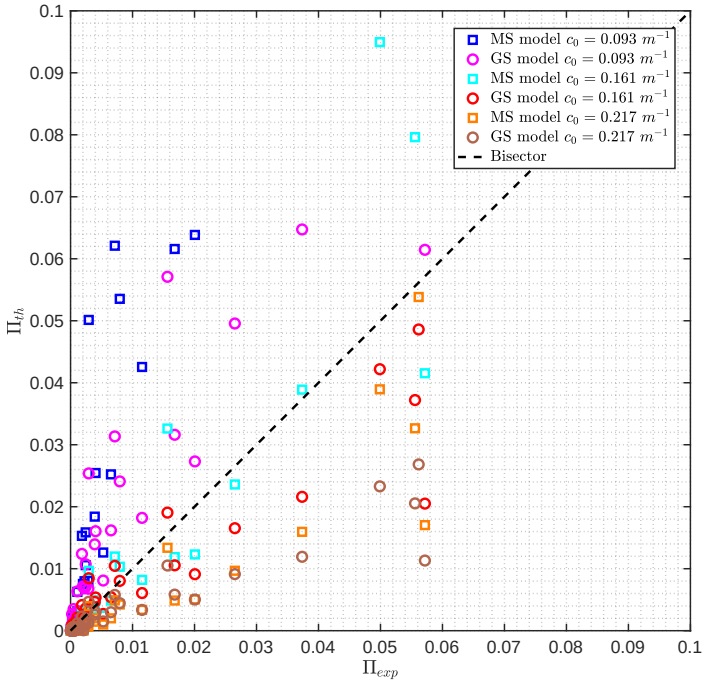

Figure 4.51. Theoretical predictions of the non-dimensional dissipated power Π_{th} vs. non-dimensional dissipated power computed from experimental data Π_{exp}. Enlargement. Drake conductor, Initial State.

Finally, the moment-curvature diagrams for different loading ratios η are reported in Figure 4.52.

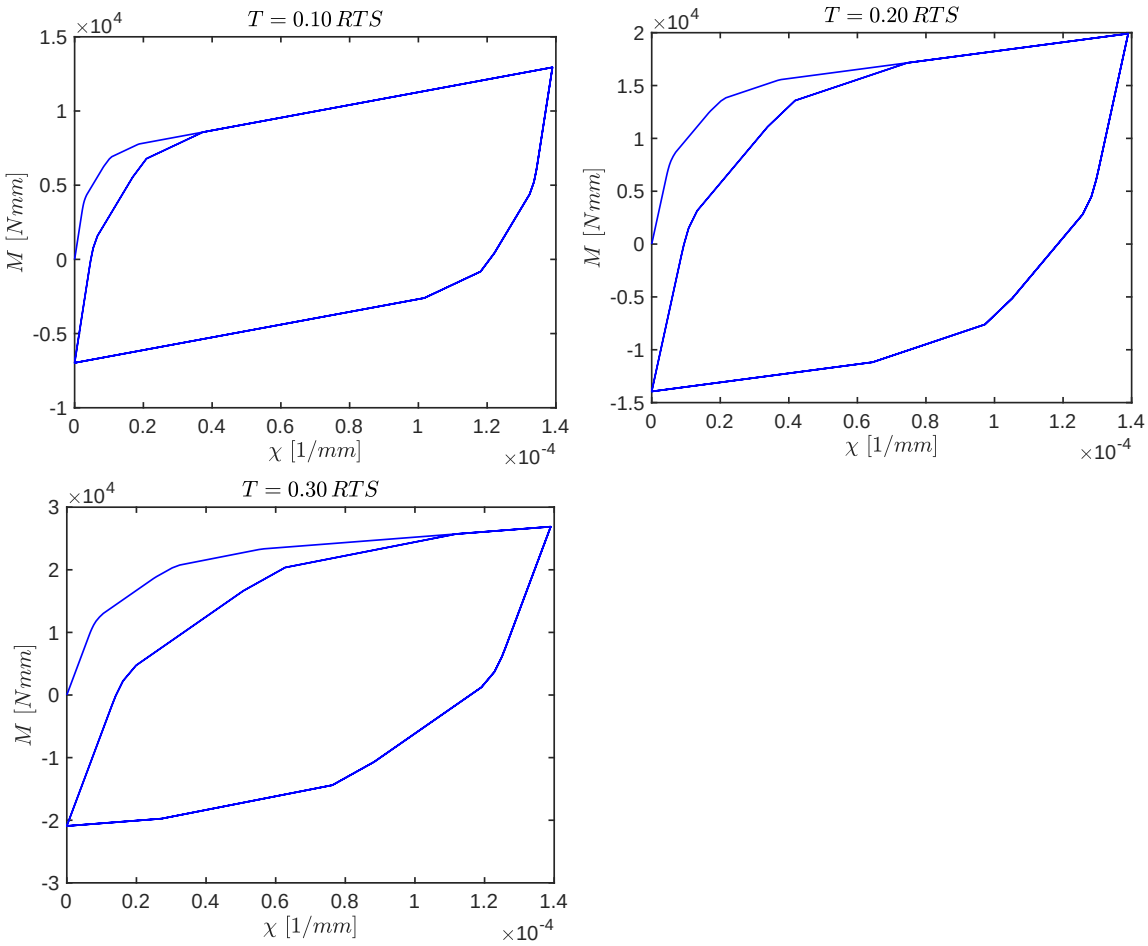

Figure 4.52. Drake conductor ($\mu = 0.3$): plot of the Moment-Curvature diagrams in the case of cyclic loading, for different values of the tension T.

4.2.9 ACSR 26/7 Drake (Final State)

As already anticipated, in this section the ACSR 26/7 Drake conductor is considered. ts mechanical and geometrical properties are collected in Appendix A, whereas its cross-section is depicted in Fig. B.2c (see Appendix B). According to the self-damping tests performed by Southwire, the conductor was stretched by raising the tension to 50% RTS and then this level of tension was held for one hour.
After this stretching, the conductor was tested again at 30%, 20%, and 15% of its RTS. In this section, reference is made to this three levels of the test tension as "Final State". The power per unit of length (P_d) dissipated during forced vibration tests, performed at different values of frequency f and antinode vibration amplitude A and for different values of the tension T, was measured through the Inverse Standing Wave Ratio (ISWR) technique.

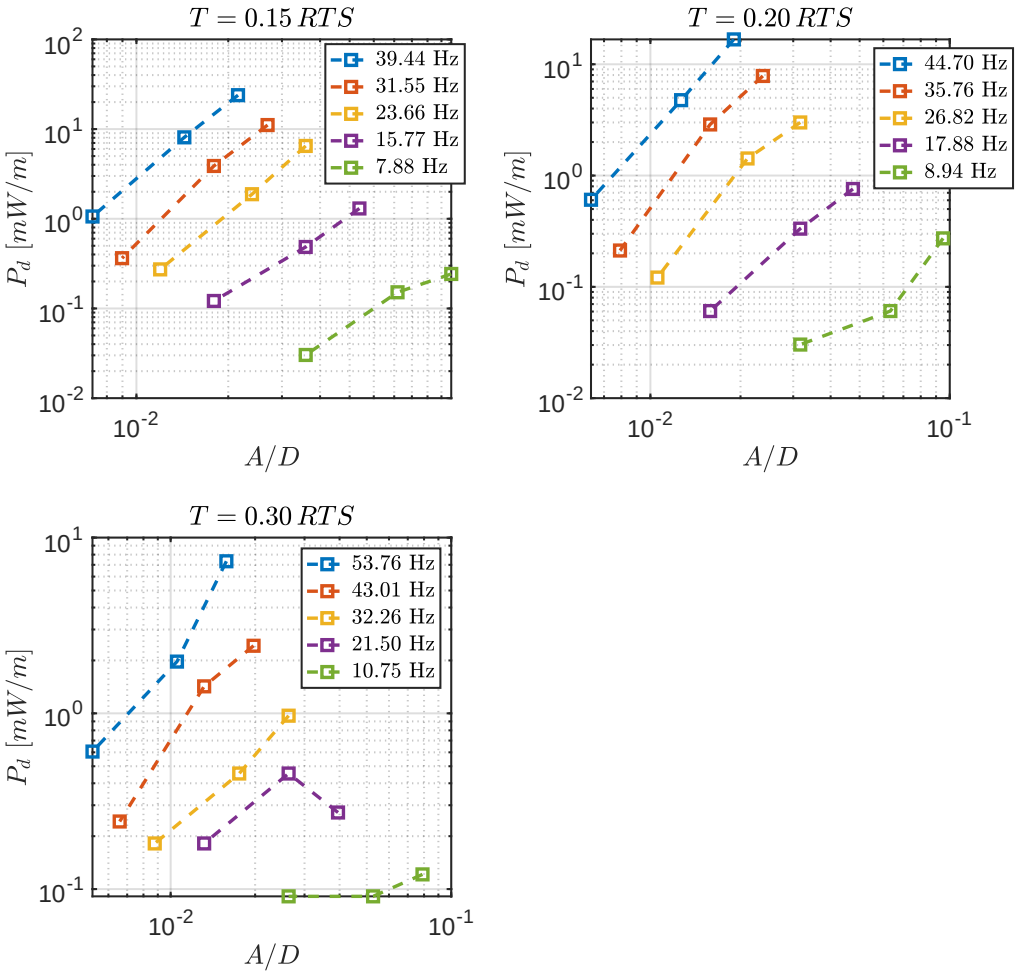

Figure 4.53. Dissipated power per unit of length vs. non-dimensional antinode amplitude. Data from (Southwire, 1996).

Figures 4.54 and 4.55 show the non-dimensional dissipated power predictions with the theoretical damping models for different values of the construction parameter c_0 (see sections 3.6 and 3.7), and the comparison with the experimental data, in both $(2\chi_0\, l)^2\Pi$ - J and $(2\chi_0\, l)^2\Pi$ - Φ/λ^* planes.

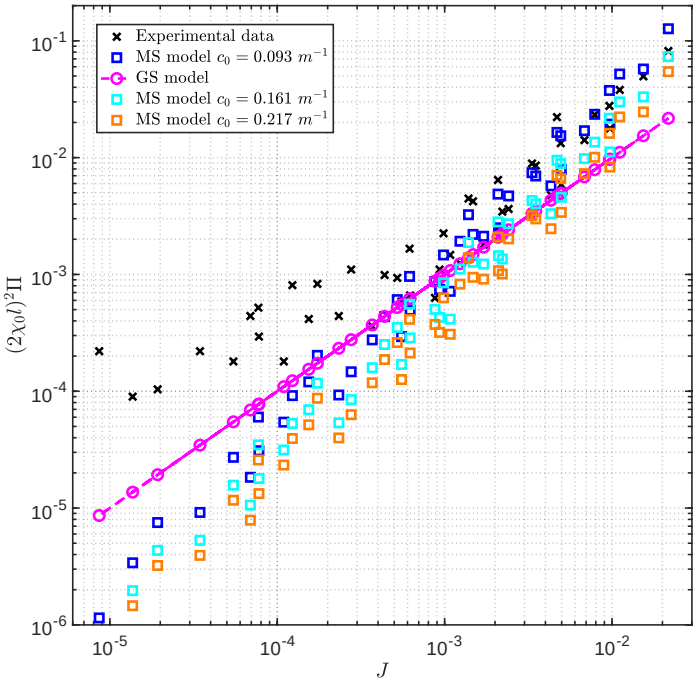

Figure 4.54. Non-dimensional Dissipated power vs. J parameter. Comparison between experimental data and theoretical predictions of the gross-sliding ("GS") and micro-slip ("MS") damping models, for different values of c_0. Drake conductor, Final State.

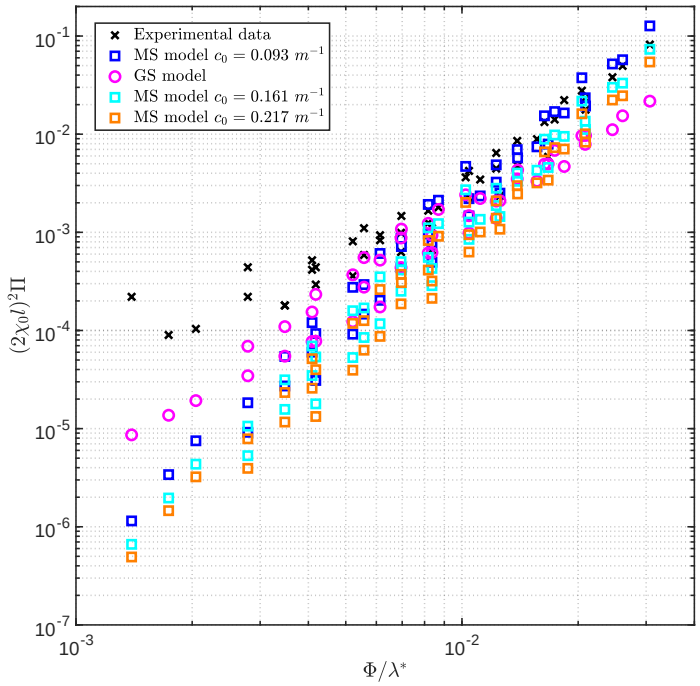

Figure 4.55. Non-dimensional Dissipated power vs. Φ/λ^*. Comparison between experimental data and theoretical predictions of the gross-sliding ("GS") and micro-slip ("MS") damping models, for different values of c_0. Drake conductor, Final State.

Table 4.38 collects the linear regression coefficients for the experimental data.

Table 4.38. ACSR Drake (Final State): Regression Coefficients of experimental data.

$(2\chi_0\, l)^2\Pi = p_0 + p_1\, J$	p_0	p_1	R^2
	-0.0017	3.3314	0.938
$\log((2\chi_0\, l)^2\Pi) = q_0 + q_1\, \log(J)$	q_0	q_1	R^2
	-0.2853	0.8313	0.877

In this case, the experimental threshold couldn't be identified (see Tab. 4.39). However, the predictions of the theoretical thresholds are computed and reported in Table 4.40.

Table 4.39. ACSR Drake (Final State): Experimental Threshold.

Identifiable	$(\Phi/\lambda^*)_{exp}$
No	-

Table 4.40. ACSR Drake (Final State): Theoretical thresholds for different values of c_0.

	Theoretical Thresholds $(\Phi/\lambda^*)_{th}$		
c_0 (m^{-1})	$\eta = 0.15$	$\eta = 0.20$	$\eta = 0.30$
0.093	0.060	0.080	0.120
0.161	0.104	0.138	0.208
0.217	0.140	0.186	0.279

Figure 4.56 shows the plot of Π_{th} vs. Π_{exp}. An enlargement of the previous plot is also included in Fig. 4.57 for convenience.
As it can be assessed from the linear regression coefficients of the theoretical dissipated power predictions (see Table 4.41), the Micro-Slip dissipation model with $c_0 = 0.093\ m^{-1}$ is the one which better represent experimental results.

Table 4.41. ACSR Drake (Final State): Regression Coefficients of theoretical predictions.

Model	c_0 (m^{-1})	s_0	s_1	R^2
Gross-Sliding	0.093	0.005	0.273	0.977
Gross-Sliding	0.161	0.002	0.273	0.977
Gross-Sliding	0.217	0.001	0.273	0.977
Micro-Slip	0.093	-0.018	1.45	0.978
Micro-Slip	0.161	-0.004	0.84	0.978
Micro-Slip	0.217	-0.002	0.62	0.978

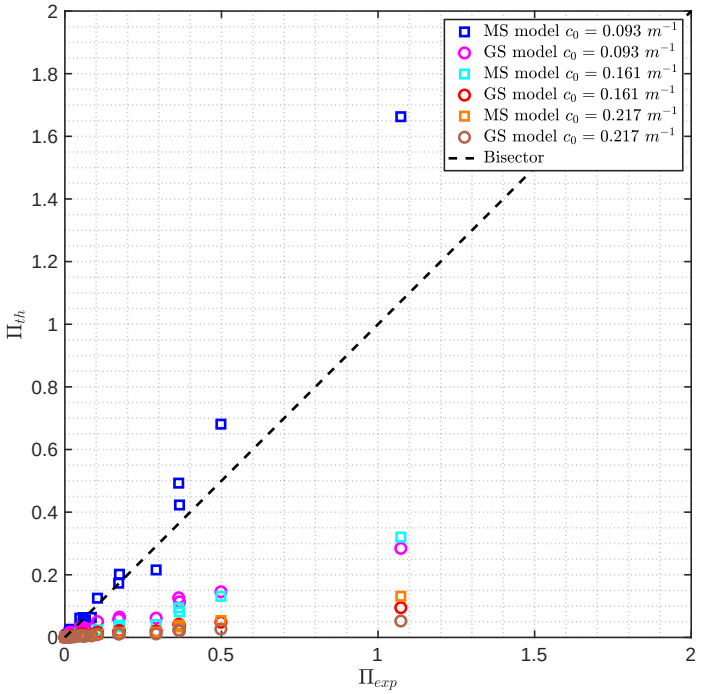

Figure 4.56. Theoretical predictions of the non-dimensional dissipated power Π_{th} vs. non-dimensional dissipated power computed from experimental data Π_{exp}. Drake conductor, Final State.

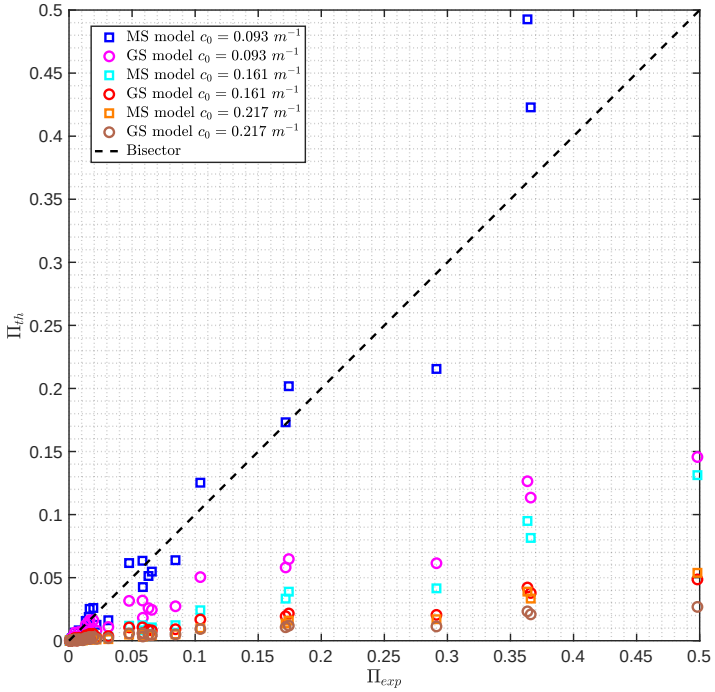

Figure 4.57. Theoretical predictions of the non-dimensional dissipated power Π_{th} vs. non-dimensional dissipated power computed from experimental data Π_{exp}. Enlargement. Drake conductor, Final State.

Finally, the moment-curvature diagrams for different loading ratios η are reported in Figure 4.58.

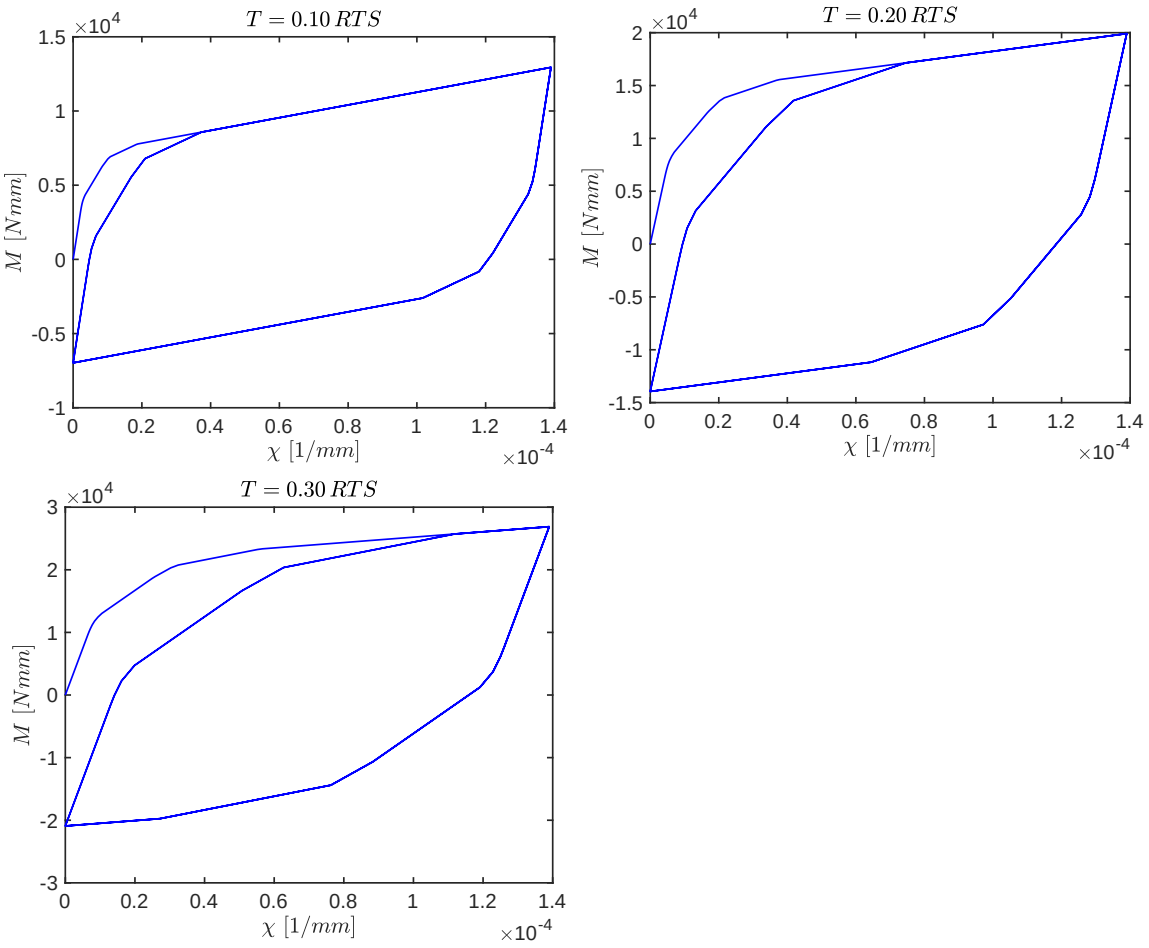

Figure 4.58. Drake conductor ($\mu = 0.3$): plot of the Moment-Curvature diagrams in the case of cyclic loading, for different values of the tension T.

4.3 Conclusions

In this Chapter, the Self-Damping properties of overhead electrical conductors have been studied, with particular emphasis on the Aluminium Conductors Steel Reinforced typology. The enhanced unified analytical model proposed by Foti and Martinelli (2018a, 2018b) was applied and compared to various experimental results coming from EPRI (2006), Southwire (1996) and Paradis (2022).
The experimental threshold between the region of curvatures controlled by the Micro-Slip dissipation mechanism and the one controlled by the Gross-Sliding dissipation mechanism couldn't be always identified.
The theoretical threshold (corresponding to the enforcement of the transition curvature between the two dissipation mechanisms, see Eq. 4.27) was computed for different values of the construction parameter c_0 and compared with the experimental one, when identified.
Conclusions of this part of the work are herein collected:

- Experimental results largely influence the possibility to observe a transition between the Micro-Slip and Gross-Sliding dissipation mechanisms;
- Self-Damping measurements are a quite delicate issue and the choice of most suitable measurement method is of paramount importance to obtain accurate results;
- Gross-Sliding dissipation mechanism appears to be the most suitable to describe the Self-Damping results of conductors, both for the low and high curvature regions;
- The parameter c_0 significantly influences the prediction of the Micro-Slip dissipation mechanism, in both plane $(2\chi_0\, l)^2\, \Pi$ - J and $(2\chi_0\, l)^2\, \Pi$ - Φ/λ^*;
- The plane Π_{exp} - Π_{th} can be effectively used to assess the capability of the theoretical models for experimental results predictions. In some cases, it has been shown that the Micro-Slip dissipation model with the minimum or median value of the construction parameter c_0 was providing the best estimation of the experimental results;
- The parameter c_0 significantly influences the prediction of the Gross-Sliding dissipation mechanism, in the plane Π_{exp} - Π_{th};
- The transition between the Micro-Slip and Gross-Sliding dissipation mechanisms could be observed in few cases only. In such cases, the minimum value of c_0 appeared to be the most suitable to reproduce the experimental results and to obtain a closer theoretical threshold to the experimental one;
- Such values of theoretical thresholds have considerably improved the preliminary predictions obtained by (Foti et al., 2021, 2022). However, a difference with respect to the experimental threshold is still present, highlighting the need for further research;
- As a general conclusion, a full range of construction parameter c_0 for each conductor cross-section see Appendix F can be adopted to correctly describe the dissipation properties of ACSR conductors by applying the enhanced unified analytical model that has been applied in this section (see Section 4.1). An estimation of the proper value of c_0 can also be obtained by means of the linear interpolating laws that have been provided in Sec. 3.7, as functions of the strand diameter D.

Chapter 5

Assessment of Aeolian Vibrations Amplitude

This chapter focuses on the application of the Energy Balance Principle (EBP) for the assessment of aeolian vibrations amplitudes of bare conductors.
In particular, different on-field experimental results for an ACSR 48/7 Bersfort conductor strung at different tension levels are considered. The latter have been collected by Langlois and Legeron (2014) and from Hardy and Van Dyke (1995).
The objective of Section 5.1 is the assessment of the influence of various parameters on the prediction of the non-dimensional amplitude of vibration, such as the friction coefficient μ, the stiffness reduction factor β, the loading ratio η, the turbolence intensity I_v and most importantly, the construction parameter c_0.

5.1 Application of the Energy Balance Principle

In this section, an application of the Energy Balance Principle (EBP) is presented, with reference to the case of an ACSR 48/7 Bersfort conductor.
Under the assumption that the cable vibrates according to one vibration mode only, it is possible to compute the maximum steady-state (single-peak) vibration amplitude A, for each of the excited natural frequencies f. This can be done by imposing the energy balance over one oscillation cycle between the average input wind power P_w and the average power dissipated by the conductor P_d.
The following nonlinear algebraic equation holds:

$$P_w(A, f) - P_d(A, f) = 0 \quad \forall f \tag{5.1}$$

and can be solved for any frequency f, to evaluate the amplitude of vibration A that allows to satisfy the Energy Balance Principle.
The wind power input data can generally be expressed through the following relationship (Lilien, 2013):

$$P_w(A, f) = B_w(I_v) D^4 f^3 \left(-99.73 \left(\frac{A}{D}\right)^3 + 101.62 \left(\frac{A}{D}\right)^2 + 0.1627 \frac{A}{D} + 0.2256 \right) \tag{5.2}$$

where:

$$B_w(I_v) = \left(1 + \left(\frac{I_v}{I_L}\right)^2\right)^{-\frac{1}{2}} \tag{5.3}$$

The parameter I_L present in Equation 5.3 is the "lock-in" index and takes the value of 0.09 (see (Lu, 2015)), whereas I_v is the turbolence intensity. Typical values reported in test settings and in in-situ measurements are in the range $I_v \in [0, 15\%]$.

The aim of this section is to compare the theoretical predictions for the cable Self-Damping obtained through the application of the enhanced unified model proposed by (Foti and Martinelli, 2018b) (Subsection 4.1.1) with available experimental data.
Furthermore, the influence of the different parameters such as the loading ratio η, the stiffness reduction factor β, the turbolence intensity I_v, the friction coefficient μ and most importantly, the construction parameter c_0 (which was largely studied and computed in Chapter 3) is assessed.

5.1.1 ACSR 48/7 Bersfort, $\eta = 20\%$

In this Subsection, the filed experimental data obtained by Langlois and Legeron (2014) are considered. Such data are related to the tests of an ACSR 48/7 Bersfort conductor strung at tension $T = 0.2\ RTS$.
Its geometrical and mechanical properties are collected in Appendix A, while its cross-section is depicted in Fig. B.3c of Appendix B.
Vibration records have been performed in the proximity of the suspension clamps and then processed to derive the value of the antinode vibration amplitude as a function of the vibration frequency.
The following figures show the comparison of the maximum non-dimensional vibration amplitude (A/D) predicted by the analytical self-damping models (full model "FM", micro-slip "MS" and gross-sliding "GS") with the experimental data. Two different turbulence intensities are considered ($I_v = 0\%$ and $I_v = 15\%$). The friction coefficient and the construction parameter are assumed respectively equal to $\mu = 0.3$ and $c_0 = 0.068\ m^{-1}$ for Figure 5.1, $\mu = 0.5$ and $c_0 = 0.139\ m^{-1}$ for Figure 5.2, $\mu = 0.7$ and $c_0 = 0.190\ m^{-1}$ for Figure 5.3.
The reduction stiffness coefficient β varies for each subplot.

Three sets of plots are realized, by considering:

1. the best condition in terms of dissipation capacity, where both μ and c_0 takes their minimum values, i.e. $\mu = 0.3$ and $c_0 = 0.068\ m^{-1}$ (see Fig. 5.1). This simulation can be considered representative of a situation in which the conductor is new and lubricated, with a respective construction parameter computed according to a sophisticated radial pressure model (P.M.A), under a physically-sound sliding condition (S.C.6).

2. a sort of "mean" situation, in which both μ and c_0 takes their median values, i.e. $\mu = 0.5$ and $c_0 = 0.139\ m^{-1}$ (see Fig. 5.2). This simulation can be considered representative of a situation in which the conductor is not new, but is still lubricated, and with respective construction parameter computed according to a simplified radial pressure model (P.M.C), under a relatively simple sliding condition (S.C.1);

3. the worst condition in terms of dissipation capacity, in which both μ and c_0 takes their maximum values, i.e. $\mu = 0.7$ and $c_0 = 0.190\ m^{-1}$ (see Fig. 5.3). This simulation can be considered representative of a situation in which the conductor is weathered and has several decades of service life, with a respective construction parameter computed according to a sophisticated radial pressure model (P.M.A), under a relatively simple sliding condition (S.C.1).

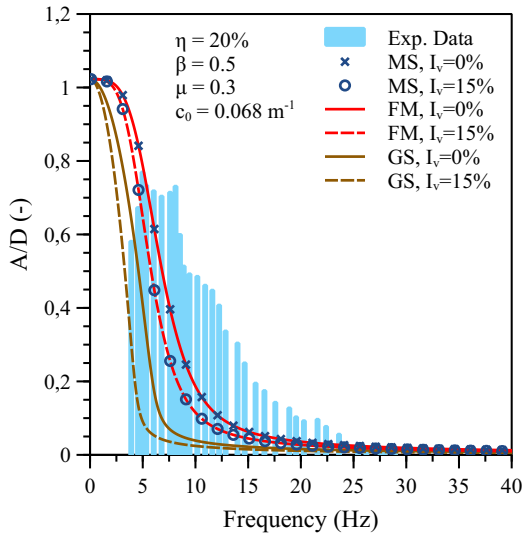

(a) $\beta = 0.5$.

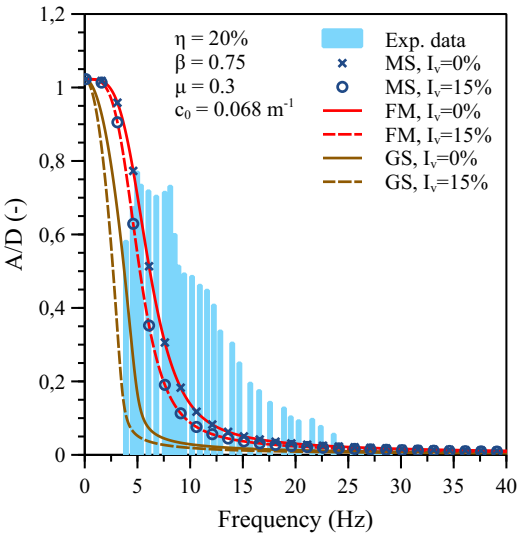

(b) $\beta = 0.75$.

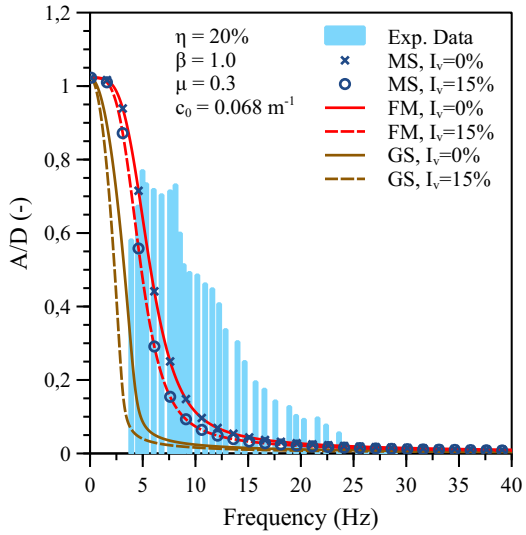

(c) $\beta = 1.0$.

Figure 5.1. Non-dimensional vibration amplitude A/D evaluated through the application of the Energy Balance Principle for an ACSR Bersfort. Parameters: $c_0 = 0.068\ m^{-1}$, $\mu = 0.3$, $\eta = 20\%$ and β varies for each subplot.

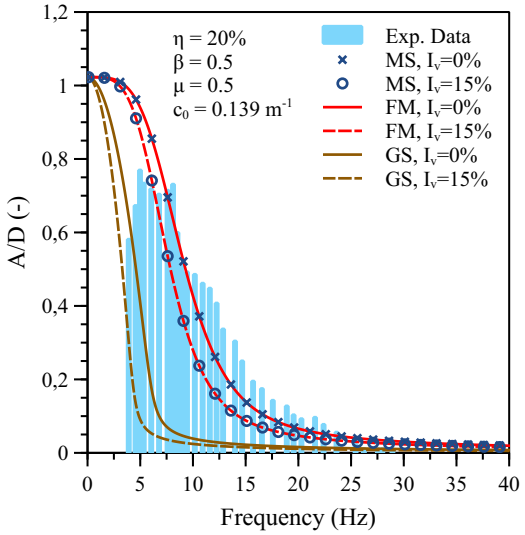

(a) $\beta = 0.5$.

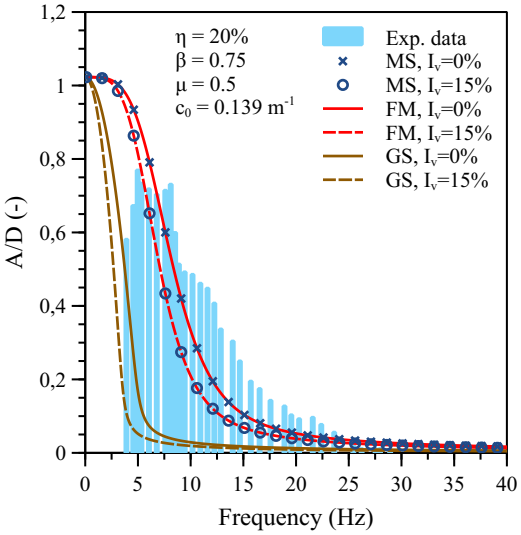

(b) $\beta = 0.75$.

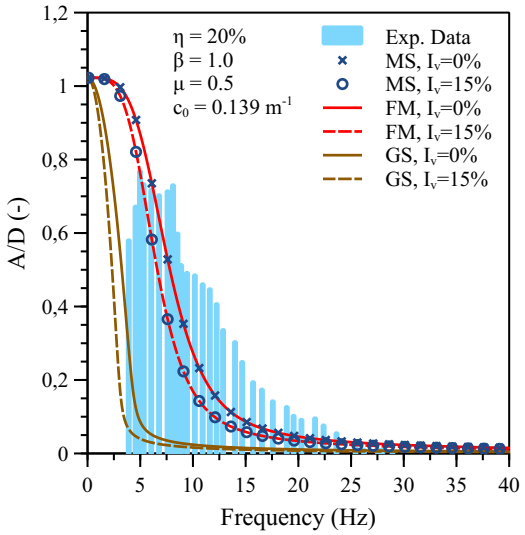

(c) $\beta = 1.0$.

Figure 5.2. Non-dimensional vibration amplitude A/D evaluated through the application of the Energy Balance Principle for an ACSR Bersfort. Parameters: $c_0 = 0.139\ m^{-1}$, $\mu = 0.5$, $\eta = 20\%$ and β varies for each subplot.

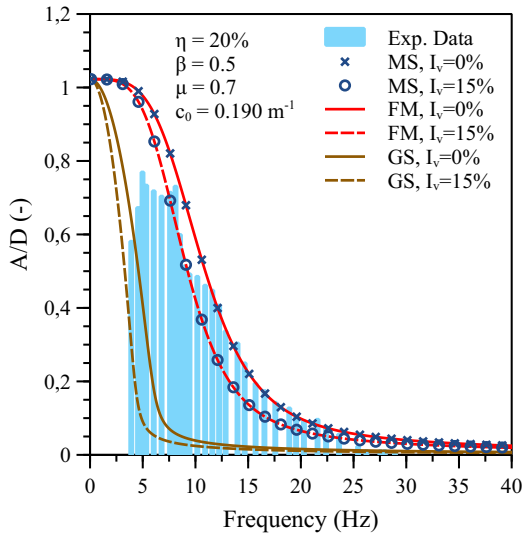

(a) $\beta = 0.5$.

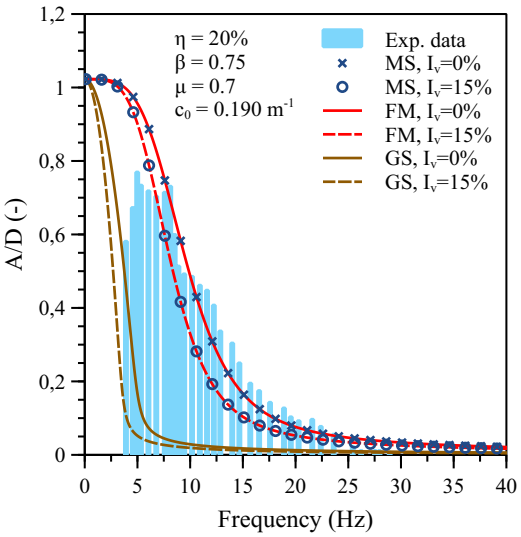

(b) $\beta = 0.75$.

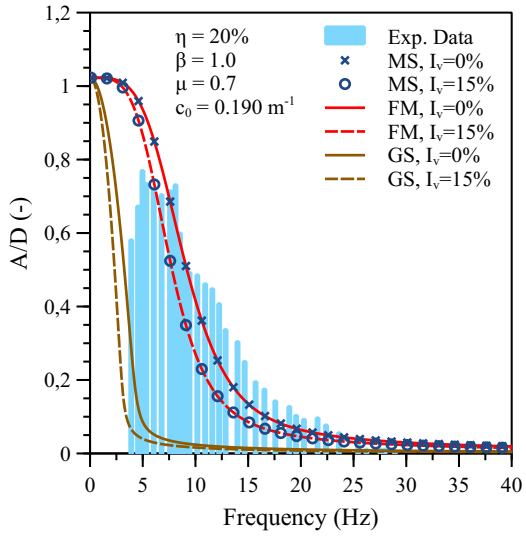

(c) $\beta = 1.0$.

Figure 5.3. Non-dimensional vibration amplitude A/D evaluated through the application of the Energy Balance Principle for an ACSR Bersfort. Parameters: $c_0 = 0.190\ m^{-1}$, $\mu = 0.7$, $\eta = 20\%$ and β varies for each subplot.

The following figures show the comparison of the maximum non-dimensional vibration amplitude predicted by adopting the analytical self-damping models (full model "FM", micro-slip "MS" and gross-sliding "GS") with the experimental data.
Three different values of the construction parameter are considered ($c_0 = 0.068\ m^{-1}$, $c_0 = 0.139\ m^{-1}$ and $c_0 = 0.190\ m^{-1}$) in order to assess its influence on the evaluation of the aeolian vibration amplitude.
Additionally, the empirical power law defined in Equation 2.17 is applied for two sets of exponents (see also Table 2.3): SET A ($l = 2.44$; $m = 5.63$; $n = 2.76$) and SET B ($l = 2.43$; $m = 5.50$; $n = 2.0$).
Figures 5.4 and 5.5 show the comparison of experimental results with the predictions of such empirical damping models.
The friction coefficient is assumed equal to $\mu = 0.3$ in Figures 5.4 and 5.6, $\mu = 0.5$ in Figure 5.7 and $\mu = 0.7$ in Figures 5.5 and 5.8. The turbolence intensity is set to $I_v = 0\%$ and the reduction stiffness coefficient β varies for each subplot.

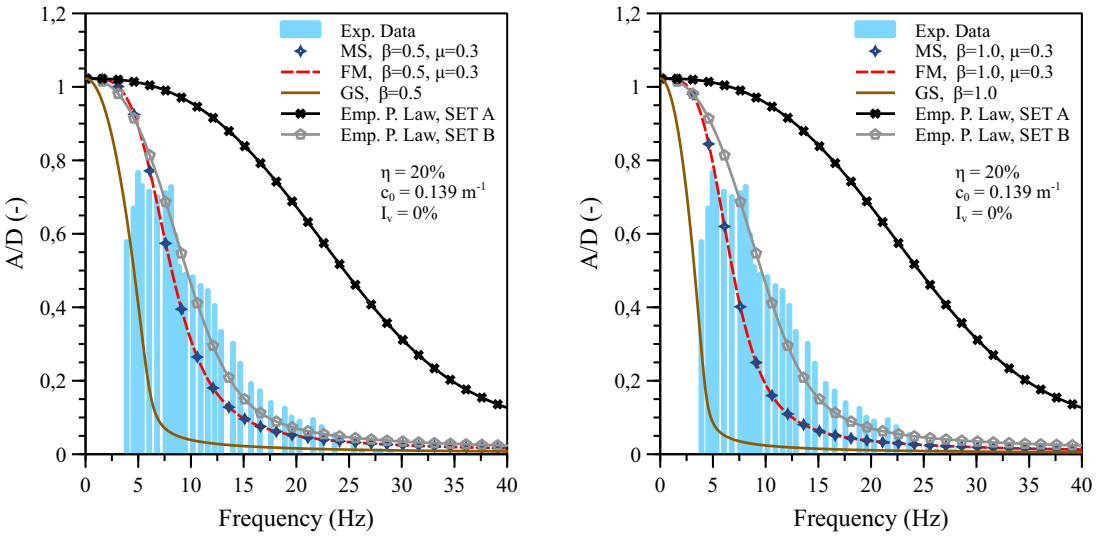

(a) $\beta = 0.5$.

(b) $\beta = 1.0$.

Figure 5.4. Non-dimensional vibration amplitude A/D evaluated through the application of the Energy Balance Principle for an ACSR Bersfort. Parameters: $I_v = 15\%$, $\mu = 0.3$, $\eta = 20\%$, $c_0 = 0.139\ m^{-1}$ and β varies for each subplot. Comparison of the results with the empirical damping model for two sets of exponents.

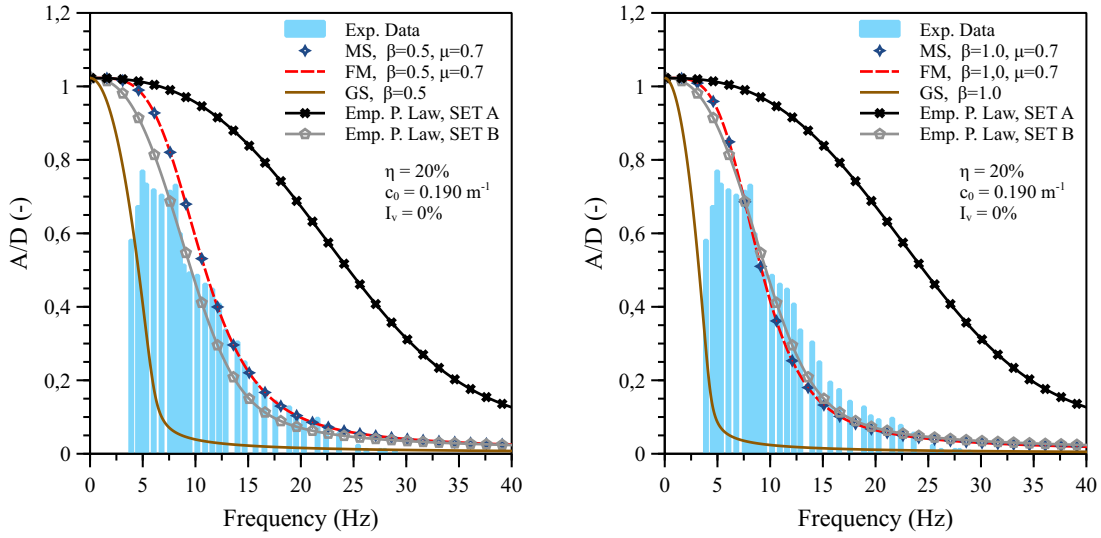

(a) $\beta = 0.5$. (b) $\beta = 1.0$.

Figure 5.5. Non-dimensional vibration amplitude A/D evaluated through the application of the Energy Balance Principle for an ACSR Bersfort. Parameters: $I_v = 15\%$, $\mu = 0.7$, $\eta = 20\%$, $c_0 = 0.190\ m^{-1}$ and β varies for each subplot. Comparison of the results with the empirical damping model for two sets of exponents.

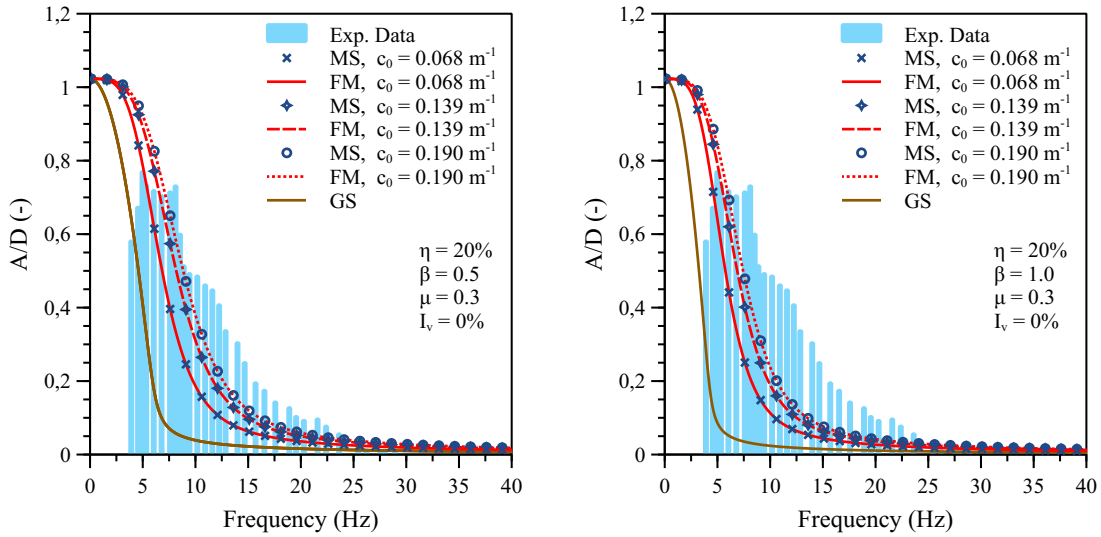

(a) $\beta = 0.5$. (b) $\beta = 1.0$.

Figure 5.6. Non-dimensional vibration amplitude A/D evaluated through the application of the Energy Balance Principle for an ACSR Bersfort. Parameters: $I_v = 0\%$, $\mu = 0.3$, $\eta = 20\%$ and β varies for each subplot.

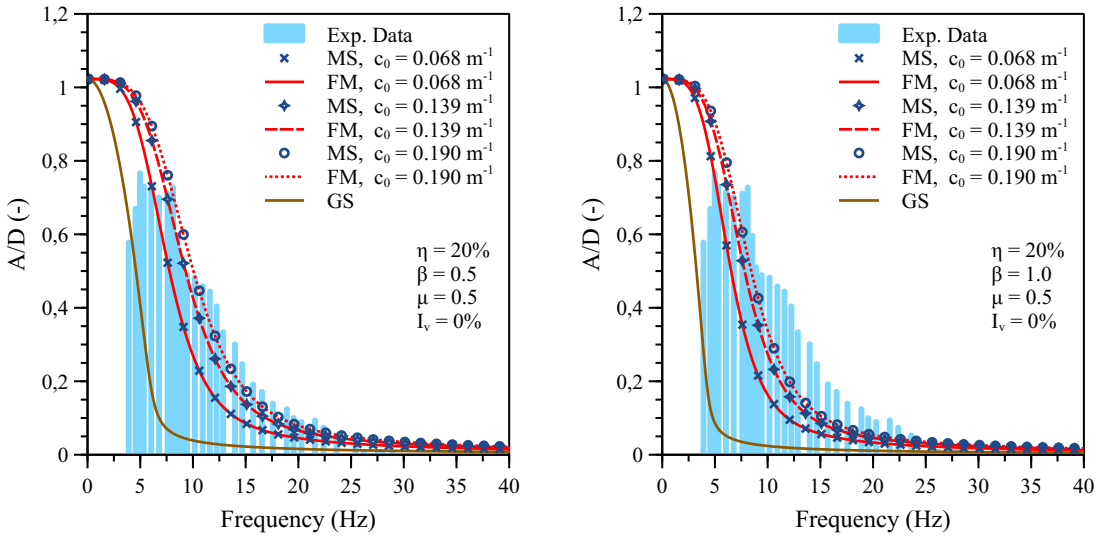

(a) $\beta = 0.5$. (b) $\beta = 1.0$.

Figure 5.7. Non-dimensional vibration amplitude A/D evaluated through the application of the Energy Balance Principle for an ACSR Bersfort. Parameters: $I_v = 0\%$, $\mu = 0.5$, $\eta = 20\%$ and β varies for each subplot.

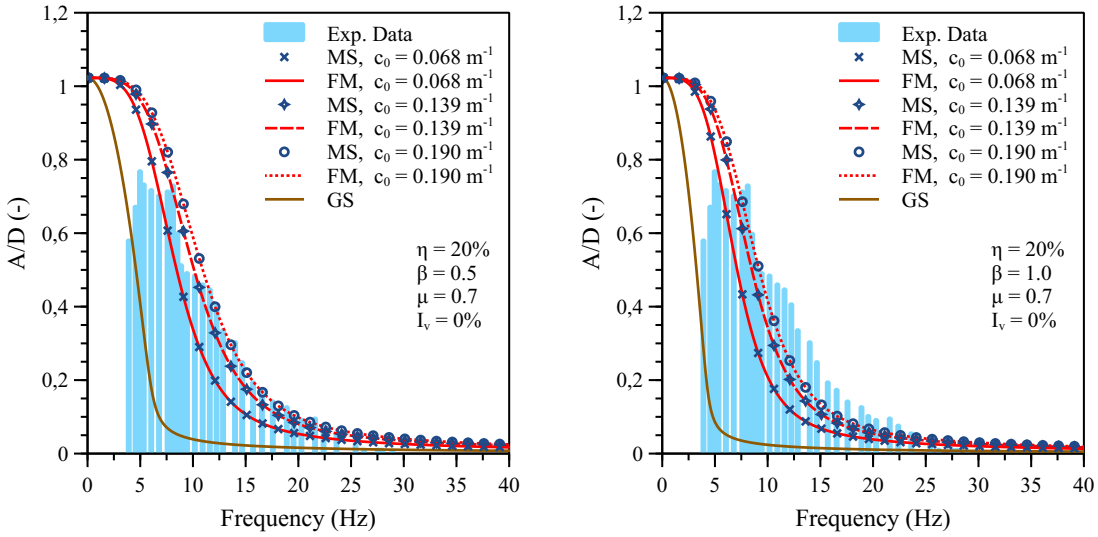

(a) $\beta = 0.5$. (b) $\beta = 1.0$.

Figure 5.8. Non-dimensional vibration amplitude A/D evaluated through the application of the Energy Balance Principle for an ACSR Bersfort. Parameters: $I_v = 0\%$, $\mu = 0.7$, $\eta = 20\%$ and β varies for each subplot.

Conlcusions

From the previous graphs, the following conclusions can be drawn:

- The Gross-Sliding energy dissipation mechanism is practically never activated for the loading conditions herein considered. As a consequence, the Micro-Slip dissipation mechanism is predicting a curve of non-dimensional amplitudes that coincides with the one predicted by the Full model;
- Both the friction coefficient μ and the construction parameter c_0 influence the Micro-Slip dissipation mechanism. In particular, as they decrease, the Micro-Slip term in Equation 4.7 increases, so that the total dissipated power predicted by the analytical model will be larger. This fact is evident in turn of a reduced non-dimensional amplitude of vibration of the cable;
- The experimental data by Langlois and Legeron (2014) are gradually better represented as the friction coefficient μ increases, as well as the construction parameter c_0 increases, i.e. when the dissipated power due to the Micro-Slip dissipation mechanism (and consequently, the total dissipated power) decreases;
- The non-dimensional amplitude predicted by the different models increases as the stiffness reduction factor β decreases. This is obviously clear, because it directly affects the conductor maximum flexural stiffness. In particular, as the maximum bending stiffness increases, the cable response is more stiff and lower non-dimensional vibration amplitudes will be reached;
- Experimental data by Langlois and Legeron (2014) are gradually better represented as the stiffness reduction factor β decreases;
- The increasing of the turbolence intensity positively affects the prediction of the non-dimensional vibration amplitudes. In fact, if the turbolence intensity is higher, the wind dissipated power will be higher too, leading to the obtainment of lower vibration amplitudes (by maintaining constant the conductor dissipated power). On the contrary, if a smooth wind flow acts on the conductor (i.e. $I_v = 0$), vibration amplitudes will be higher;
- Experimental data by Langlois and Legeron (2014) are gradually better represented as the turbolence intensity I_v decreases;
- The curve that is better representing the experimental data is the one obtained with the Full Model ("FM"), with parameters $\beta = 0.5$, $c_0 = 0.190\ m^{-1}$, $\mu = 0.7$ and $I_v = 0$ (see Fig. 5.3a or Fig. 5.8a). One can then compute the first yielding curvature as:

  $$\chi_0 = \mu\,\eta\,c_0 = 0.0266\ m^{-1}$$

  However, as already recalled, the theoretical predictions obtained with the Full-Model coincide with the ones obtained by applying the Micro-Slip dissipation model. As a consequence, the computed value of the first-yielding curvature is practically never reached for vibration levels herein considered.

- The predictions of the non-dimensional vibration amplitude obtained with the empirical self-damping model (i.e. the empirical power law, Eq. 2.17) drastically differ on the basis of the set of exponents that is adopted. In particular, the predictions obtained by adopting SET B exponents ($l = 2.43$; $m = 5.50$; $n = 2.0$) are better representing experimental data of Langlois and Legeron (2014) with respect to the ones obtained by adopting SET A exponents ($l = 2.44$; $m = 5.63$; $n = 2.76$), which lead to a strong overestimation.
  This consideration holds for any value of the reduction stiffness factor β.

- Almost perfect agreement between the predictions of the non-dimensional amplitude obtained with the Full-Model (FM), and the ones obtained with the empirical damping model with SET B exponents is found for the following parameters: $\beta = 1.0$, $c_0 = 0.190\ m^{-1}$, $\mu = 0.7$ and $I_v = 0$ (see Fig. 5.5b).

5.1.2 ACSR 48/7 Bersfort, $\eta = 25\%$

In this Subsection, the filed experimental data obtained by Hardy and Van Dyke (1995) are considered. Such data are related to the tests of an ACSR 48/7 Bersfort conductor, strung at tension $T = 0.25\ RTS$.
Its geometrical and mechanical properties are collected in Appendix A, while its cross-section is depicted in Fig. B.3c of Appendix B.
The following figures show the comparison of the maximum non-dimensional vibration amplitude predicted by adopting the analytical self-damping models (full model "FM", micro-slip "MS" and gross-sliding "GS") with the experimental data.
Three different values of the construction parameter are considered ($c_0 = 0.068\ m^{-1}$, $c_0 = 0.139\ m^{-1}$ and $c_0 = 0.190\ m^{-1}$) in order to assess its influence on the evaluation of the aeolian vibration amplitude.
Additionally, the empirical power law defined in Equation 2.17 is applied for two sets of exponents (see also Table 2.3): SET A ($l = 2.44$; $m = 5.63$; $n = 2.76$) and SET B ($l = 2.43$; $m = 5.50$; $n = 2.0$).
Figure 5.9 shows the comparison of experimental results with the predictions of such empirical damping models.
The friction coefficient is assumed equal to $\mu = 0.3$ in Figures 5.9, 5.10 and in Figure 5.12, while it is assumed equal to $\mu = 0.5$ in Figure 5.11 and in Figure 5.13.
The turbolence intensity is set equal to $I_v = 0\%$ both for Fig. 5.10 and 5.11, while it is equal to $I_v = 15\%$ in Figures 5.9, 5.12 and 5.13.
The reduction stiffness coefficient β varies for each subplot.

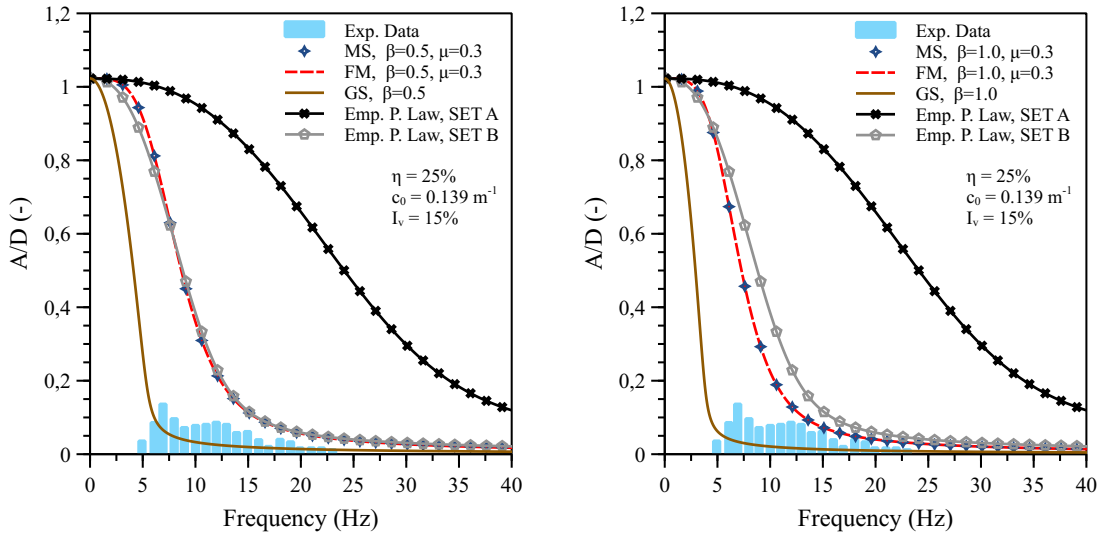

(a) $\beta = 0.5$.

(b) $\beta = 1.0$.

Figure 5.9. Non-dimensional vibration amplitude A/D evaluated through the application of the Energy Balance Principle for an ACSR Bersfort. Parameters: $I_v = 15\%$, $\mu = 0.3$, $\eta = 25\%$, $c_0 = 0.139\ m^{-1}$ and β varies for each subplot. Comparison of the results with the empirical damping model for two sets of exponents.

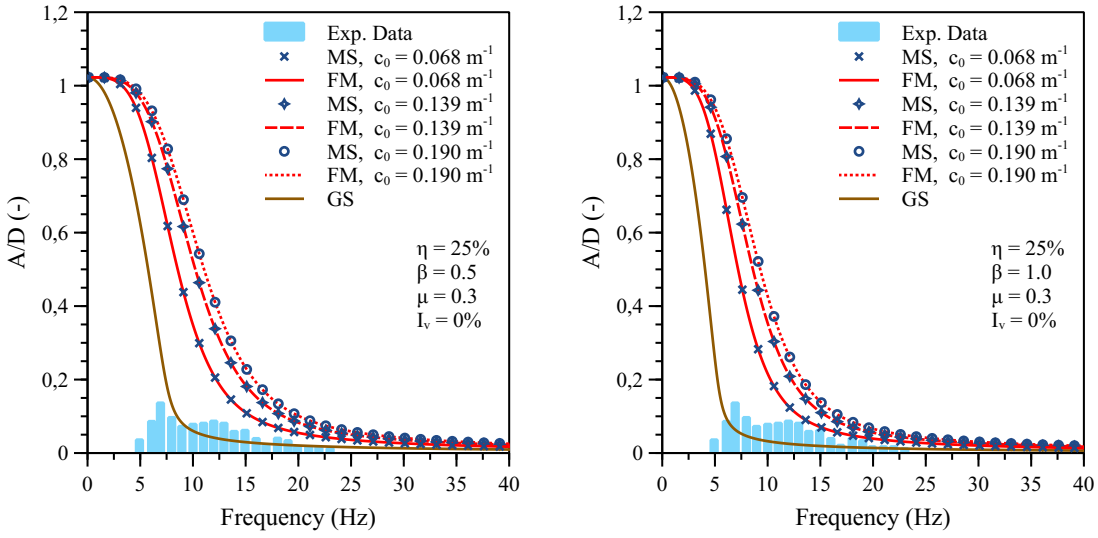

(a) $\beta = 0.5$. (b) $\beta = 1.0$.

Figure 5.10. Non-dimensional vibration amplitude A/D evaluated through the application of the Energy Balance Principle for an ACSR Bersfort. Parameters: $I_v = 0\%$, $\mu = 0.3$, $\eta = 25\%$ and β varies for each subplot.

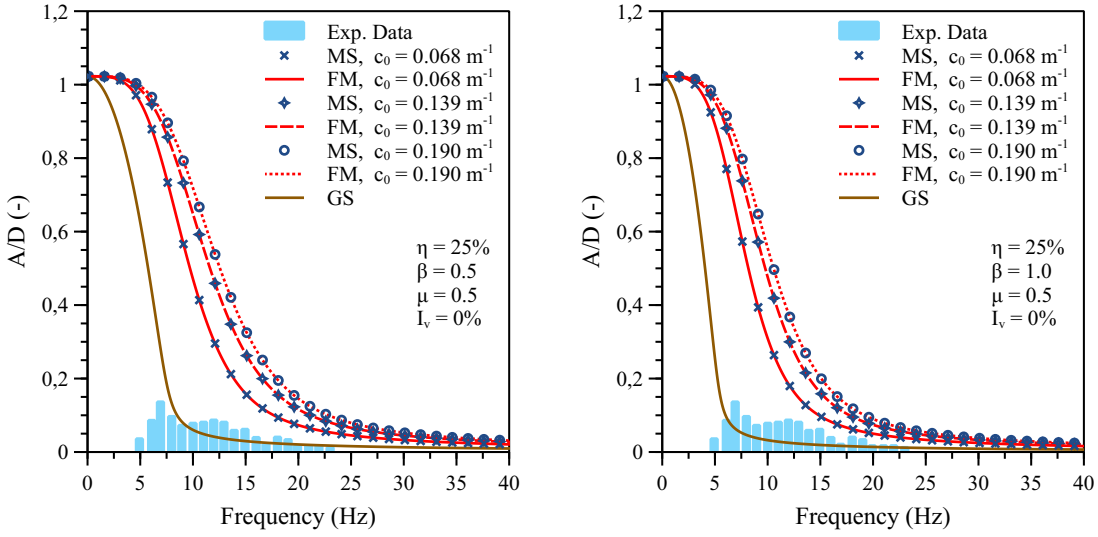

(a) $\beta = 0.5$. (b) $\beta = 1.0$.

Figure 5.11. Non-dimensional vibration amplitude A/D evaluated through the application of the Energy Balance Principle for an ACSR Bersfort. Parameters: $I_v = 0\%$, $\mu = 0.5$, $\eta = 25\%$ and β varies for each subplot.

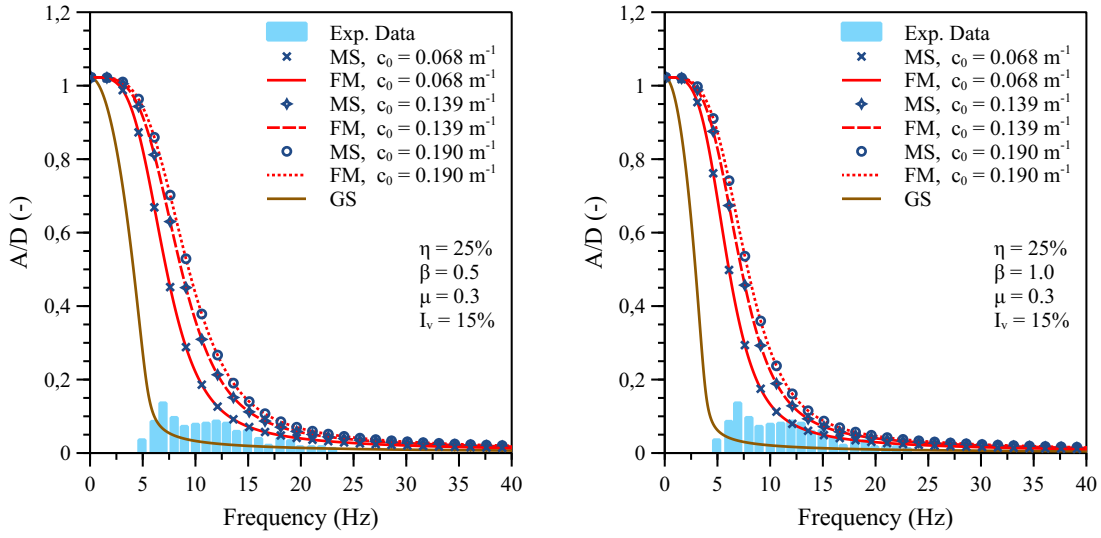

(a) $\beta = 0.5$. (b) $\beta = 1.0$.

Figure 5.12. Non-dimensional vibration amplitude A/D evaluated through the application of the Energy Balance Principle for an ACSR Bersfort. Parameters: $I_v = 15\%$, $\mu = 0.3$, $\eta = 25\%$ and β varies for each subplot.

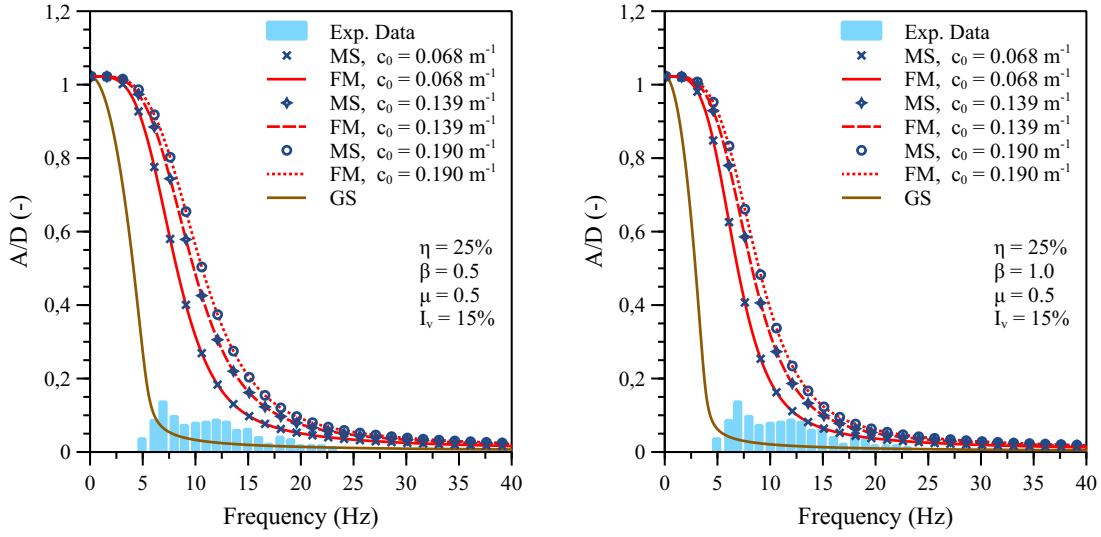

(a) $\beta = 0.5$. (b) $\beta = 1.0$.

Figure 5.13. Non-dimensional vibration amplitude A/D evaluated through the application of the Energy Balance Principle for an ACSR Bersfort. Parameters: $I_v = 15\%$, $\mu = 0.5$, $\eta = 25\%$ and β varies for each subplot.

Conclusions

From the previous graphs, the following conclusions can be drawn:

- The Gross-Sliding energy dissipation mechanism is practically never activated for the loading conditions herein considered. As a consequence, the Micro-Slip dissipation mechanism is predicting a curve of non-dimensional amplitudes that coincides with the one predicted by the Full model;
- As already recalled, both the friction coefficient μ and the construction parameter c_0 influence the Micro-Slip dissipation mechanism. In particular, as they decrease, the Micro-Slip term in Equation 4.7 increases, so that the total dissipated power predicted by the analytical model will be larger. This fact is evident in turn of a reduced non-dimensional amplitude of vibration of the cable;
- The same general considerations previously done about the influence of the stiffness reduction factor β and the turbolence intensity I_v hold (see Subsection 5.1.1);
- The experimental data by Hardy and Van Dyke (1995) are gradually better represented as the friction coefficient μ decreases, as well as the construction parameter c_0 decreases, i.e. when the dissipated power due to the Micro-Slip dissipation mechanism (and consequently, the total dissipated power) increases;
- Experimental data by Hardy and Van Dyke (1995) are gradually better represented as the stiffness reduction factor β increases;
- Experimental data by Hardy and Van Dyke (1995) are gradually better represented as the turbolence intensity I_v increases.
- The predictions of the non-dimensional vibration amplitude obtained with the empirical self-damping model (i.e. the empirical power law, Eq. 2.17) drastically differ on the basis of the set of exponents that is adopted. In particular, the predictions obtained by adopting SET B exponents ($l = 2.43$; $m = 5.50$; $n = 2.0$) are better representing experimental data by Hardy and Van Dyke (1995) with respect to the ones obtained by adopting SET A exponents ($l = 2.44$; $m = 5.63$; $n = 2.76$), which lead to a strong overestimation.
  This consideration holds for any value of the reduction stiffness factor β.
- Almost perfect agreement between the predictions of the non-dimensional amplitude obtained with the Full-Model (FM) and the ones obtained with the empirical damping model with SET B exponents is found for the following parameters: $\beta = 0.5$, $c_0 = 0.139\ m^{-1}$, $\mu = 0.3$ and $I_v = 15\%$ (see Fig. 5.9a).

5.1.3 ACSR 48/7 Bersfort, $\eta = 30\%$

In this Subsection, the filed experimental data obtained by Hardy and Van Dyke (1995) are considered. Such data are related to the tests of an ACSR 48/7 Bersfort conductor, strung at tension $T = 0.30\ RTS$.
Its geometrical and mechanical properties are collected in Appendix A, while its cross-section is depicted in Fig. B.3c of Appendix B.
The following figures show the comparison of the maximum non-dimensional vibration amplitude predicted by adopting the analytical self-damping models (full model "FM", micro-slip "MS" and gross-sliding "GS") with the experimental data.
Three different values of the construction parameter are considered ($c_0 = 0.068\ m^{-1}$, $c_0 = 0.139\ m^{-1}$ and $c_0 = 0.190\ m^{-1}$) in order to assess its influence on the evaluation of the aeolian vibration amplitude.
Additionally, the empirical power law defined in Equation 2.17 is applied for two sets of exponents (see also Table 2.3): SET A ($l = 2.44$; $m = 5.63$; $n = 2.76$) and SET B ($l = 2.43$; $m = 5.50$; $n = 2.0$).
Figure 5.14 shows the comparison of experimental results with the predictions of such empirical damping models.
The friction coefficient is assumed equal to $\mu = 0.3$ in Figures 5.14, 5.15 and in Figure 5.17, while it is assumed equal to $\mu = 0.5$ in Figure 5.16 and in Figure 5.18.
The turbolence intensity is set equal to $I_v = 0\%$ both for Fig. 5.15 and 5.16, while it is equal to $I_v = 15\%$ for Figures 5.14 5.17 and for Fig. 5.18.
The reduction stiffness coefficient β varies for each subplot.

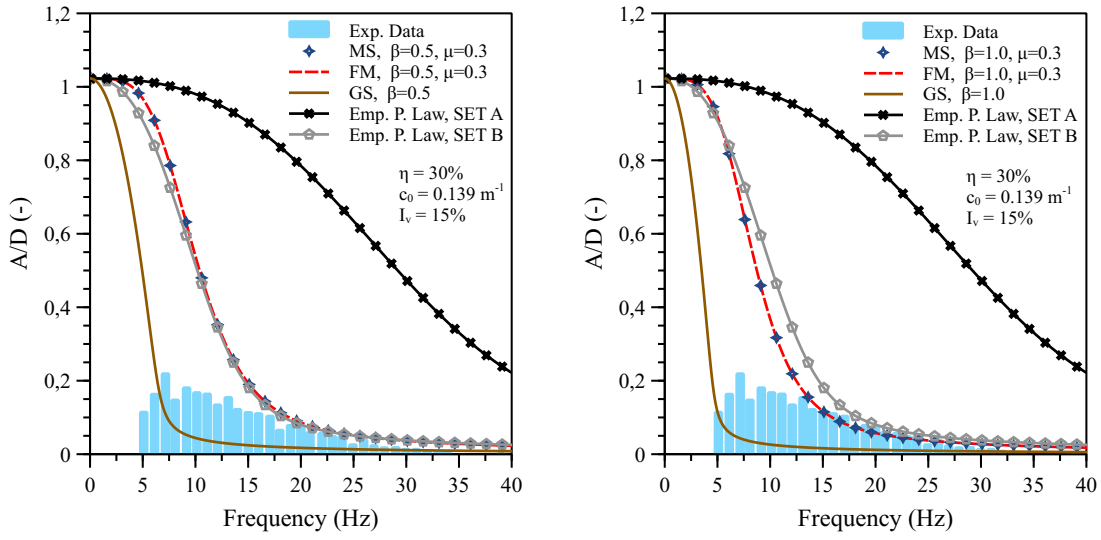

(a) $\beta = 0.5$.

(b) $\beta = 1.0$.

Figure 5.14. Non-dimensional vibration amplitude A/D evaluated through the application of the Energy Balance Principle for an ACSR Bersfort. Parameters: $I_v = 15\%$, $\mu = 0.3$, $\eta = 30\%$, $c_0 = 0.139\ m^{-1}$ and β varies for each subplot. Comparison of the results with the empirical damping model for two sets of exponents.

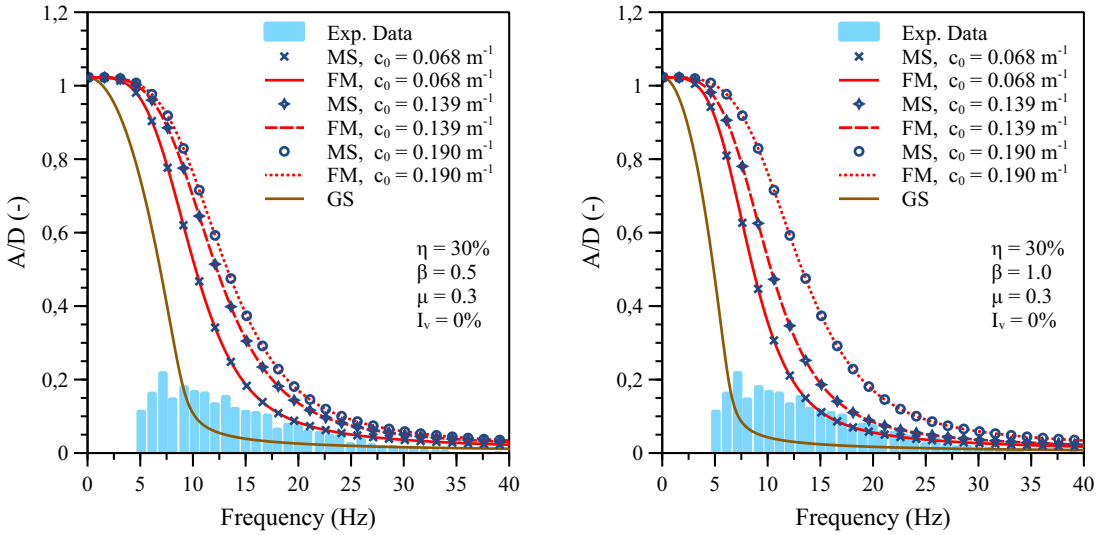

(a) $\beta = 0.5$. (b) $\beta = 1.0$.

Figure 5.15. Non-dimensional vibration amplitude A/D evaluated through the application of the Energy Balance Principle for an ACSR Bersfort. Parameters: $I_v = 0\%$, $\mu = 0.3$, $\eta = 30\%$ and β varies for each subplot.

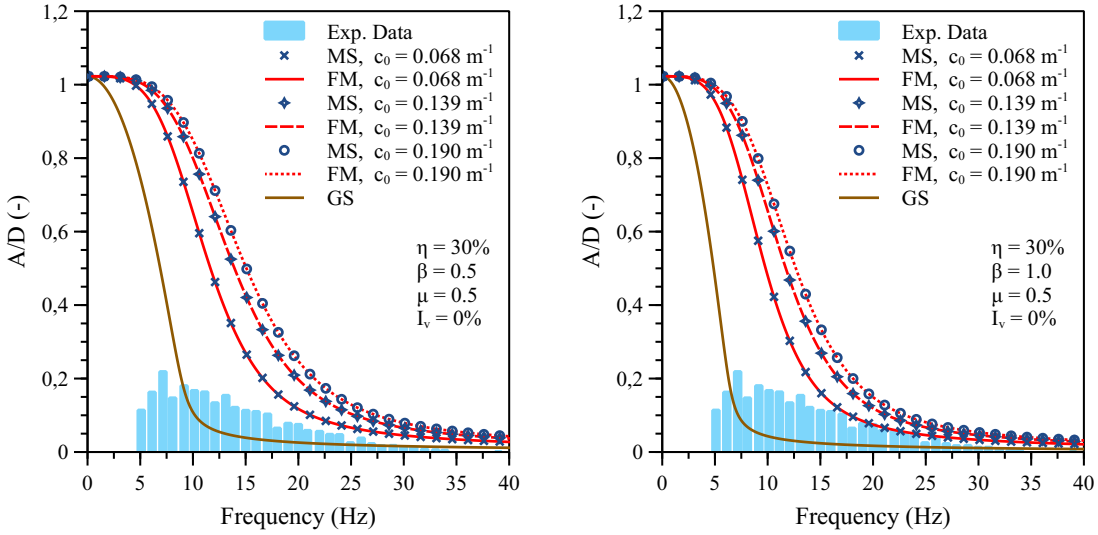

(a) $\beta = 0.5$. (b) $\beta = 1.0$.

Figure 5.16. Non-dimensional vibration amplitude A/D evaluated through the application of the Energy Balance Principle for an ACSR Bersfort. Parameters: $I_v = 0\%$, $\mu = 0.5$, $\eta = 30\%$ and β varies for each subplot.

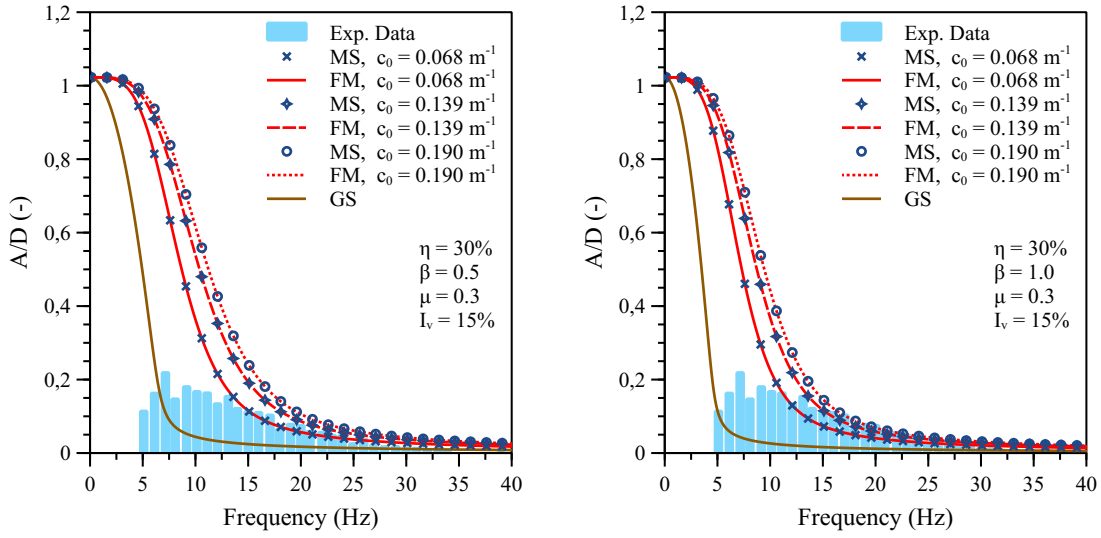

(a) $\beta = 0.5$. (b) $\beta = 1.0$.

Figure 5.17. Non-dimensional vibration amplitude A/D evaluated through the application of the Energy Balance Principle for an ACSR Bersfort. Parameters: $I_v = 15\%$, $\mu = 0.3$, $\eta = 30\%$ and β varies for each subplot.

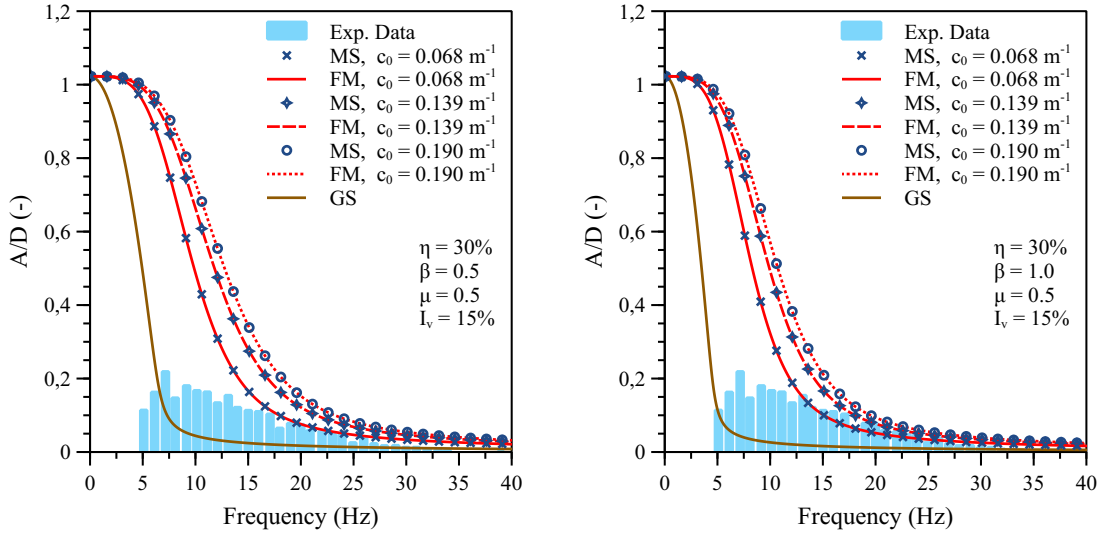

(a) $\beta = 0.5$. (b) $\beta = 1.0$.

Figure 5.18. Non-dimensional vibration amplitude A/D evaluated through the application of the Energy Balance Principle for an ACSR Bersfort. Parameters: $I_v = 15\%$, $\mu = 0.5$, $\eta = 30\%$ and β varies for each subplot.

Conclusions

From the previous graphs, the following conclusions can be drawn:

- The Gross-Sliding energy dissipation mechanism is practically never activated for the loading conditions herein considered. As a consequence, the Micro-Slip dissipation mechanism is predicting a curve of non-dimensional amplitudes that coincides with the one predicted by the Full model;
- As already recalled, both the friction coefficient μ and the construction parameter c_0 influence the Micro-Slip dissipation mechanism. In particular, as they decrease, the Micro-Slip term in Equation 4.7 increases, so that the total dissipated power predicted by the analytical model will be larger. This fact is evident in turn of a reduced non-dimensional amplitude of vibration of the cable;
- The same general considerations previously done about the influence of the stiffness reduction factor β and the turbolence intensity I_v hold;
- The experimental data by Hardy and Van Dyke (1995) are gradually better represented as the friction coefficient μ decreases, as well as the construction parameter c_0 decreases, i.e. when the dissipated power due to the Micro-Slip dissipation mechanism (and consequently, the total dissipated power) increases;
- Experimental data by Hardy and Van Dyke (1995) are gradually better represented as the stiffness reduction factor β increases;
- Experimental data by Hardy and Van Dyke (1995) are gradually better represented as the turbolence intensity I_v increases.
- However, even if the general trend of the single parameters is the one just exposed, an adequate trade-off between such parameters should be found in order to correclty represent the experimental data. In particular, the prediction of the non-dimensional vibration amplitude through the Full-Model of Fig 5.18a, with $c_0 = 0.068\ m^{-1}$ appears to be the most accurate compared to experimental data.
- The predictions of the non-dimensional vibration amplitude obtained with the empirical self-damping model (i.e. the empirical power law, Eq. 2.17) drastically differ on the basis of the set of exponents that is adopted. In particular, the predictions obtained by adopting SET B exponents ($l = 2.43$; $m = 5.50$; $n = 2.0$) are better representing experimental data by Hardy and Van Dyke (1995) with respect to the ones obtained by adopting SET A exponents ($l = 2.44$; $m = 5.63$; $n = 2.76$), which lead to a strong overestimation.
  This consideration holds for any value of the reduction stiffness factor β.
- Almost perfect agreement between the predictions of the non-dimensional amplitude obtained with the Full-Model (FM) and the ones obtained with the empirical damping model with SET B exponents is found for the following parameters: $\beta = 0.5$, $c_0 = 0.139\ m^{-1}$, $\mu = 0.3$ and $I_v = 15\%$ (see Fig. 5.14a).

Chapter 6

Conclusion

This chapter summarizes the results obtained in this dissertation thesis, regarding the mechanical modeling of stranded cables and the self-damping properties of ACSR conductors for aeolian vibrations applications. The novel approaches proposed as a part of the research work are evidenced, an the consequent practical implications are illustrated. Some disadvantages are also shown. Based on the achieved results, some future developments are finally proposed.

6.1 Conclusions

In the present work, different radial transmission pressures models of the literature for metallic stranded cables under bending have been assessed and implemented. The predicted external and internal radial contact forces per unit of length have been rigorously compared for the first time, to the author's knowledge (Subsection 3.4.2). Results have shown the influence of the assumptions initially introduced for the description of the mechanical behavior of such complex structures.
Moreover, a novel approach for the computation of the construction parameter of stranded cables under different radial transmission pressures models and stick-slip mechanical laws was presented. The differential equation describing the admissible domain of the wire axial force (see Appendix E) was uniquely determined throughout coefficients a and b, which depend only upon the sliding condition that is enforced (Subsection 3.5.3).
Additionally, a generalization of both the expressions of such coefficients, and the equilibrium equation in the tangential direction, was obtained by means of ξ^{int} and ξ^{ext} parameters, influencing the internal and external friction coefficients respectively (Paragraph 3.5.3).
A full range of construction parameters c_0 was then determined for a sample of 15 widespread ACSR conductors (which geometrical-mechanical properties and cross-sections are collected in Appendix A and B respectively), through both a numerical evaluation (Subsection 3.6.1) and a closed-form solution (Subsection 3.6.2).
The latter uses a novel expression involving the maximum additional bending moment due to the non-linear contribution of the wire axial force.
Results of c_0 clearly show the influence of both the radial transmission pressures models and the stick-slip mechanical laws on the bending response of multi-layer strands (Subsection 3.7.2). Conversely, results of c_0 for single-layer strands are only slightly influenced by the most severe sliding conditions enforced (Subsection 3.7.1).
Such coefficient permits to describe the hysteretic behavior of stranded cables in a more accessible and accurate way and synthetically accounts for the geometrical and mechanical properties of conductor cross-section, as was extensively treated in Subsection 3.5.4, where the approximated bi-linear relationship for the moment-curvature law was introduced.

An important conclusion of the work regards the influence of the construction parameter on both the static response of the cable and its dynamic behavior, with particular interest on its self-damping properties.
In fact, in Section 3.8 a well documented bending test of the literature was used to assess the different response of an ACSR 48/7 Bersfort in view of the various values of c_0 previously determined. A not negligible influence on the cable deflection as well as on the bending stiffness transition was found.
Furthermore, in Section 4.2 theoretical predictions of the self-damping of ACSR conductors were analyzed by applying the enhanced unified analytical model derived in Section 4.1. It has been shown that the predicted dissipated power through the Micro-Slip dissipation mechanism is significantly affected by the variation of c_0, in the plane $(2\chi_0\, l)^2\Pi$ - J.
However, as a general conclusion, a better correlation between the experimental results and the predictions obtained through Gross-Sliding dissipation mechanism was generally found. The activation of the Micro-Slip dissipation mechanism was present in few cases only.
Additionally, if the transition between Micro-Slip and Gross-Sliding dissipation mechanisms was observed, the theoretical thresholds predicted by applying the analytical model described in Section 4.1 have been improved, i.e. the introduction of a range of c_0 values have led to the obtainment of closer theoretical thresholds with respect to the experimental ones, if compared to past researchers' results (Foti et al., 2021, 2022).
Moreover, the influence of the construction parameter on the theoretical self-damping predictions obtained through the Gross-Sliding dissipation mechanism was conveniently assessed in the plane Π_{exp}-Π_{th}. It has been shown that c_0 only affects the intercept of the regression lines, being their slope unchanged.
In the last part of the work, the severity of aeolian vibrations was assessed with reference to the bare conductor, through the application of the Energy Balance Principle. The influence of the construction parameter on the non-dimensional vibrations amplitude predictions by means of the theoretical damping models was investigated. Results show that the magnitude of the predicted vibrations amplitude can significantly vary, on par with well-known parameters such as the friction coefficient μ and the stiffness reduction factor β.

A disadvantage of the proposed approach lies in the difficulty of identification of the correct sliding condition that should be enforced for the computation of a construction parameter that is representative of the real cable behavior. This is obviously not an easy task, and requires further experimental campaigns on the real on-field conductors flexural behavior.
Furthermore, additional studies are still required for the complete characterization of self-damping properties of ACSR conductors, especially for their hysteretic behavior at small curvature values, i.e. their dissipation capacities whenever the Micro-Slip phenomenon is activated.
However, as a big advantage of the developed work, a full range of c_0 values was provided for a sample of 15 widespread ACSR conductors, resulting in strong simplification of the proposed applications from the point of view of the common engineering practice.
The results obtained as a conclusion of this work paves the way for a more accurate characterization of the hysteretic behavior of stranded cables. Practical interests of the research work are directly related to the possibility of a more accurate assessment of the Self-Damping of overhead electrical line conductors as well as the evaluation of aeolian vibrations amplitude. Such aspects will permit to predict the remaining life of the conductor more precisely, leading to a predictive and optimized maintenance and supporting the decision-making about the inspection methods for critical regions of the line.

6.2 Future Developments

Based on the achieved results, some future developments are proposed:

- analysis of additional radial transmission pressures models and sliding conditions, and assessment on their influence of the construction parameter, according to the general formulation of the proposed methodology (e.g. analysis of the radial pressures model proposed by Foti and Martinelli (2019), which accounts for the deformability of contact patches);
- computation of the construction parameters for other conductors cross-sections (i.e. creation of a database for ACSR conductors), and validation of the proposed linear interpolations for different conductor diameters;
- extension of the procedure to other conductor typologies, for instance to trapezoidal wires conductors (namely ACSR TW conductors), in order to promote an easier assessment of their self-damping properties;
- comparison of the approximated radial contact forces (normal contact forces acting on contact points between adjacent layers) obtained through different formulas for the computation of the distance between two contact points, with numerical results coming from 2D and 3D Finite Elements Models. This proposal aims to verify the influence of the contact points distance formula on the prediction of the approximated values of the radial contact force with respect to FEM numerical results;
- realization of an accurate experimental campaign for the investigation of the transition between Micro-Slip and Gross-Sliding dissipation mechanisms in ACSR conductors;
- establishment of a link between the cross-sectional response of stranded cables through their hysteretic behavior characterization and the response at the micro-scale, i.e. description of the tribological problem, involving fretting fatigue phenomenon and the development of *bending boundary layers*. Such aspects surely involve the identification of proper indicators concerning the damage assessment due to fretting fatigue. On these regards, estimation of relative displacements between wires through micro-slip and gross-sliding mechanisms could be adopted as a novel proposal;
- correlation of the "meso-scale" cross-sectional parameters for the bending response of stranded cables and assessment of the response at the whole infrastructure level, in the context of wind-structure interaction phenomena. The link between the stochastic characteristics of the excitation and the stochastic characteristics of the structural response can however be easily determined only when the structural model is linear. On the contrary, in this case, the mechanical model describing the bending response is inherently nonlinear and non-holonomic, so that the link to be established will be surely nonlinear.

Appendix A

Mechanical and Geometrical Characteristics of ACSR Conductors

In this appendix, the geometrical and mechanical properties of the ACSR conductors used in the different chapters of this thesis are reported.
The geometric characteristics of ACSR conductors are collected in Table A.1. The involved quantities are: the outer diameter D; the number of layers n_L; the diameter of steel and aluminium wires, indicated respectively by the symbols d_{st} and d_{al}.

Table A.1. Geometric characteristics of commercial ACSR conductors.

Code Word	Stranding	$D\,(mm)$	$n_L\,(-)$	$d_{st}\,(mm)$	$d_{al}\,(mm)$
Sparrow	6/1	8.01	1	2.67	2.67
Pigeon	6/1	12.75	1	4.25	4.25
Penguin	6/1	14.31	1	4.77	4.77
Partridge	26/7	16.28	3	2.00	2.57
Hawk	26/7	21.80	3	2.68	3.44
Drake	26/7	28.10	3	3.45	4.44
Carillon	48/7	30.48	4	2.84	3.66
Gatineau	48/7	33.0	4	3.08	3.96
Bersfort	48/7	35.60	4	3.32	4.27
Duck	54/7	24.21	4	2.69	2.69
Crow	54/7	26.28	4	2.92	2.92
Curlew	54/7	31.59	4	3.51	3.51
Falcon	72/7	37.69	5	2.51	3.77
Nelson I	72/7	40.60	5	2.71	4.06
Nelson II	72/7	43.20	5	2.88	4.32

The mechanical characteristics of the ACSR conductors are reported in Table A.2. The involved quantities are: the outer diameter D; the Rated Tensile Strength RTS; the mass per unit length of the cable m; the maximum and minimum theoretical values of the tangent bending stiffness EI_{max} and EI_{min}.
Such mechanical parameters have been computed according to the ASTM standard (1) and by considering a Young's modulus for steel and aluminium wires of $E_{st} = 200$ GPa and $E_{al} = 69$ GPa respectively. The Poisson's ratio was set equal to $\nu = 0.3$ for both steel and aluminium wires.

Table A.2. Mechanical characteristics of commercial ACSR conductors.

Code Word	Stranding	$RTS\,(kN)$	$m\,(kg/m)$	$EI_{max}\,(Nm^2)$	$EI_{min}\,(Nm^2)$
Sparrow	6/1	12.4	0.136	9.47	1.52
Pigeon	6/1	29.6	0.344	60.8	9.73
Penguin	6/1	37.3	0.434	96.4	15.4
Partridge	26/7	50.0	0.546	167	4.8
Hawk	26/7	86.1	0.977	537	15.5
Drake	26/7	138	1.626	1487	42.9
Carillon	48/7	136	1.745	2021	32.8
Gatineau	48/7	155	2.042	2774	45.0
Bersfort	48/7	180	2.375	3749	60.8
Duck	54/7	101	1.160	814	12.9
Crow	54/7	117	1.371	1130	17.9
Curlew	54/7	163	1.980	2359	37.3
Falcon	72/7	172	2.501	4492	49.9
Nelson I	72/7	200	2.902	6051	67.1
Nelson II	72/7	226	3.277	7751	86.0

The composition of the different stranded cables is reported in Tables A.3-A.17.
For each layer of wires, the following quantities are indicated: number of wires n_w, diameter of wires d_w, preferred helix pitch with sign P_p (a positive sign is conventionally assigned to the pitch of helices which are twisted around the strand axis according to the right-hand rule), Young's modulus E, Poisson's ratio ν and initial swept angle of the wires θ_0 (see Section 3.1).
Each section of this appendix is fully devoted to a stranding typology.

A.1 ACSR 6/1 Conductors

Table A.3. ACSR 6/1 Sparrow: strand composition.

Layer	n_w	d_w (mm)	P_p (mm)	E (GPa)	ν (-)	θ_0 (deg)
0	1	2.67	0	200	0.3	0
1	6	2.67	-104.13	69	0.3	0

Table A.4. ACSR 6/1 Pigeon: strand composition.

Layer	n_w	d_w (mm)	P_p (mm)	E (GPa)	ν (-)	θ_0 (deg)
0	1	4.25	0	200	0.3	0
1	6	4.25	-165.75	69	0.3	0

Table A.5. ACSR 6/1 Penguin: strand composition.

Layer	n_w	d_w (mm)	P_p (mm)	E (GPa)	ν (-)	θ_0 (deg)
0	1	4.77	0	200	0.3	0
1	6	4.77	-186.03	69	0.3	0

A.2 ACSR 26/7 Conductors

Table A.6. ACSR 26/7 Partridge: strand composition.

Layer	n_w	d_w (mm)	P_p (mm)	E (GPa)	ν (-)	θ_0 (deg)
0	1	2.00	0	200	0.3	0
1	6	2.00	-150.00	200	0.3	0
2	10	2.57	144.82	69	0.3	0
3	16	2.57	-179.08	69	0.3	0

Table A.7. ACSR 26/7 Hawk: strand composition.

Layer	n_w	d_w (mm)	P_p (mm)	E (GPa)	ν (-)	θ_0 (deg)
0	1	2.68	0	200	0.3	0
1	6	2.68	-201.00	200	0.3	0
2	10	3.44	193.96	69	0.3	0
3	16	3.44	-239.80	69	0.3	0

Table A.8. ACSR 26/7 Drake: strand composition.

Layer	n_w	d_w (mm)	P_p (mm)	E (GPa)	ν (-)	θ_0 (deg)
0	1	3.45	0	200	0.3	0
1	6	3.45	-258.75	200	0.3	0
2	10	4.44	249.99	69	0.3	0
3	16	4.44	-309.21	69	0.3	0

A.3 ACSR 48/7 Conductors

Table A.9. ACSR 48/7 Carillon: strand composition.

Layer	n_w	d_w (mm)	P_p (mm)	E (GPa)	ν (-)	θ_0 (deg)
0	1	2.84	0	200	0.3	0
1	6	2.84	-213.00	200	0.3	0
2	10	3.66	205.92	69	0.3	0
3	16	3.66	-301.08	69	0.3	0
4	22	3.66	355.28	69	0.3	0

Table A.10. ACSR 48/7 Gatineau: strand composition.

Layer	n_w	d_w (mm)	P_p (mm)	E (GPa)	ν (-)	θ_0 (deg)
0	1	3.08	0	200	0.3	0
1	6	3.08	-231.00	200	0.3	0
2	10	3.96	223.08	69	0.3	0
3	16	3.96	-326.04	69	0.3	0
4	22	3.96	363.00	69	0.3	0

Table A.11. ACSR 48/7 Bersfort: strand composition.

Layer	n_w	d_w (mm)	P_p (mm)	E (GPa)	ν (-)	θ_0 (deg)
0	1	3.32	0	200	0.3	0
1	6	3.32	-249.00	200	0.3	0
2	10	4.27	240.50	69	0.3	0
3	16	4.27	-351.52	69	0.3	0
4	22	4.27	391.38	69	0.3	0

A.4 ACSR 54/7 Conductors

Table A.12. ACSR 54/7 Duck: strand composition.

Layer	n_w	d_w (mm)	P_p (mm)	E (GPa)	ν (-)	θ_0 (deg)
0	1	2.69	0	200	0.3	0
1	6	2.69	-201.75	200	0.3	0
2	12	2.69	174.85	69	0.3	0
3	18	2.69	-244.79	69	0.3	0
4	24	2.69	266.31	69	0.3	0

Table A.13. ACSR 54/7 Crow: strand composition.

Layer	n_w	d_w (mm)	P_p (mm)	E (GPa)	ν (-)	θ_0 (deg)
0	1	2.92	0	200	0.3	0
1	6	2.92	-219.00	200	0.3	0
2	12	2.92	189.80	69	0.3	0
3	18	2.92	-265.72	69	0.3	0
4	24	2.92	289.08	69	0.3	0

Table A.14. ACSR 54/7 Curlew: strand composition.

Layer	n_w	d_w (mm)	P_p (mm)	E (GPa)	ν (-)	θ_0 (deg)
0	1	3.51	0	200	0.3	0
1	6	3.51	-263.25	200	0.3	0
2	12	3.51	228.15	69	0.3	0
3	18	3.51	-319.41	69	0.3	0
4	24	3.51	347.49	69	0.3	0

A.5 ACSR 72/7 Conductors

Table A.15. ACSR 72/7 Falcon: strand composition.

Layer	n_w	d_w (mm)	P_p (mm)	E (GPa)	ν (-)	θ_0 (deg)
0	1	2.51	0	200	0.3	0
1	6	2.51	-188.25	200	0.3	0
2	9	3.77	195.91	69	0.3	0
3	15	3.77	-293.93	69	0.3	0
4	21	3.77	391.95	69	0.3	0
5	27	3.77	-414.59	69	0.3	0

Table A.16. ACSR 72/7 Nelson I: strand composition.

Layer	n_w	d_w (mm)	P_p (mm)	E (GPa)	ν (-)	θ_0 (deg)
0	1	2.71	0	200	0.3	0
1	6	2.71	-203.25	200	0.3	0
2	9	4.06	211.25	69	0.3	0
3	15	4.06	-316.81	69	0.3	0
4	21	4.06	422.37	69	0.3	0
5	27	4.06	-446.71	69	0.3	0

Table A.17. ACSR 72/7 Nelson II: strand composition.

Layer	n_w	d_w (mm)	P_p (mm)	E (GPa)	ν (-)	θ_0 (deg)
0	1	2.88	0	200	0.3	0
1	6	2.88	-216.00	200	0.3	0
2	9	4.32	224.64	69	0.3	0
3	15	4.32	-336.96	69	0.3	0
4	21	4.32	449.28	69	0.3	0
5	27	4.32	-475.20	69	0.3	0

Appendix B

Cross-sections of ACSR conductors

In this Appendix, the cross-section of each ACSR conductor analyzed in this thesis work is reported.
The mechanical and geometrical properties of ACSR conductors are listed in Appendix A.
Each Figure is fully dedicated to a stranding typology, whereas the different subfigures collect the conductor cross-sections belonging to the same stranding class.

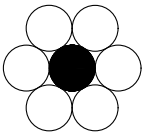

(a) ACSR 6/1 Sparrow.

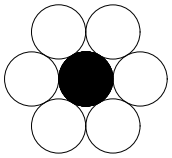

(b) ACSR 6/1 Pigeon.

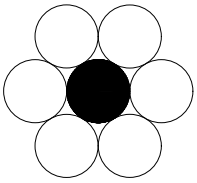

(c) ACSR 6/1 Penguin.

Figure B.1. Cross-sections of ACSR 6/1 conductors.

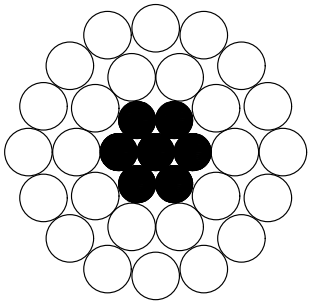

(a) ACSR 26/7 Partridge.

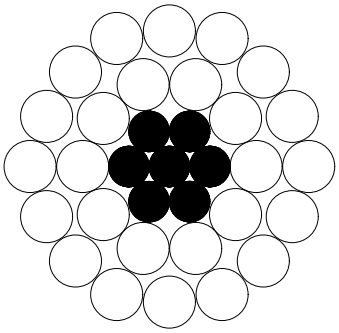

(b) ACSR 26/7 Hawk.

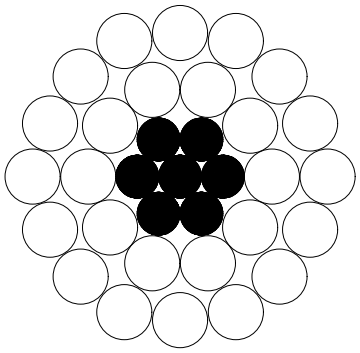

(c) ACSR 26/7 Drake.

Figure B.2. Cross-sections of ACSR 26/7 conductors.

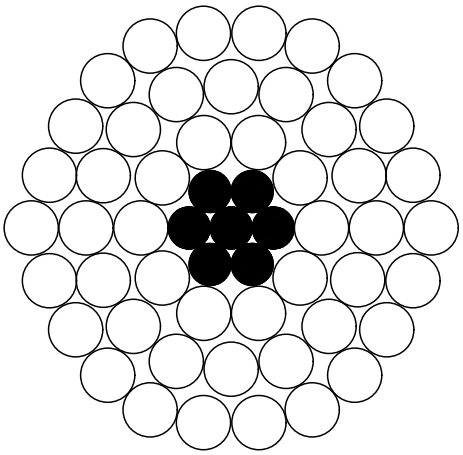

(a) ACSR 48/7 Carillon.

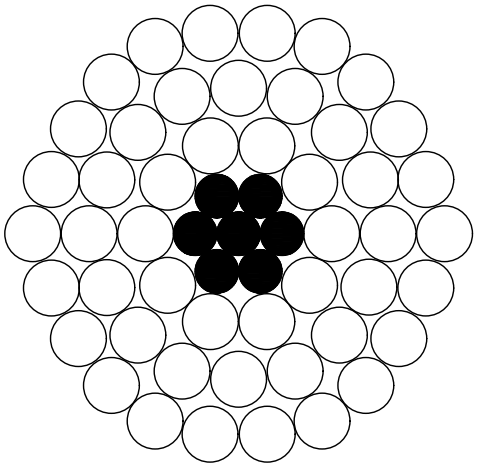

(b) ACSR 48/7 Gatineau.

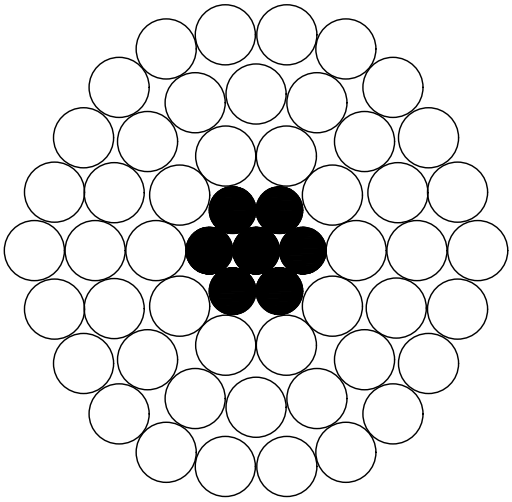

(c) ACSR 48/7 Bersfort.

Figure B.3. Cross-sections of ACSR 48/7 conductors.

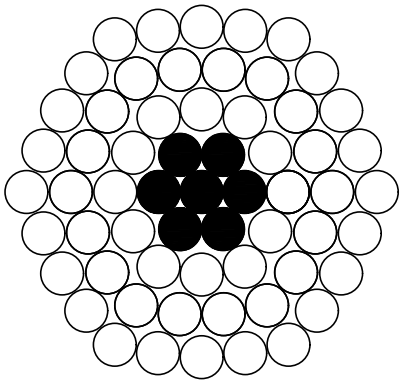

(a) ACSR 54/7 Duck.

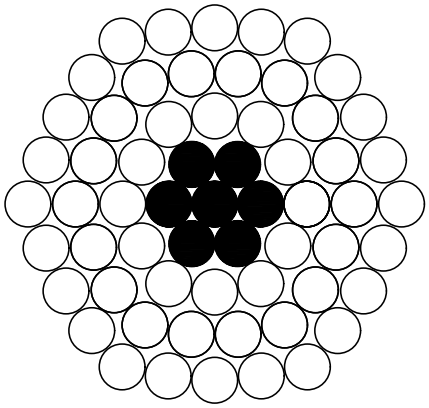

(b) ACSR 54/7 Crow.

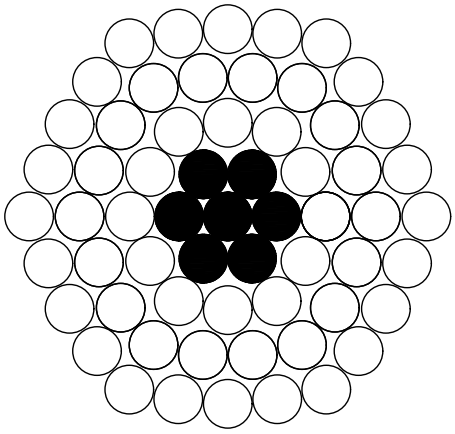

(c) ACSR 54/7 Curlew.

Figure B.4. Cross-sections of ACSR 54/7 conductors.

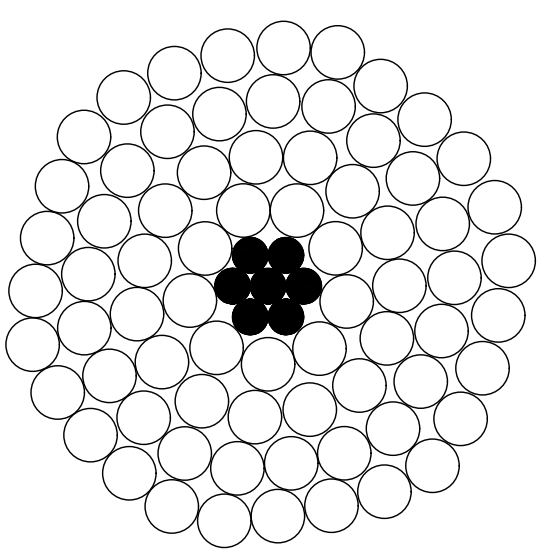

(a) ACSR 72/7 Falcon.

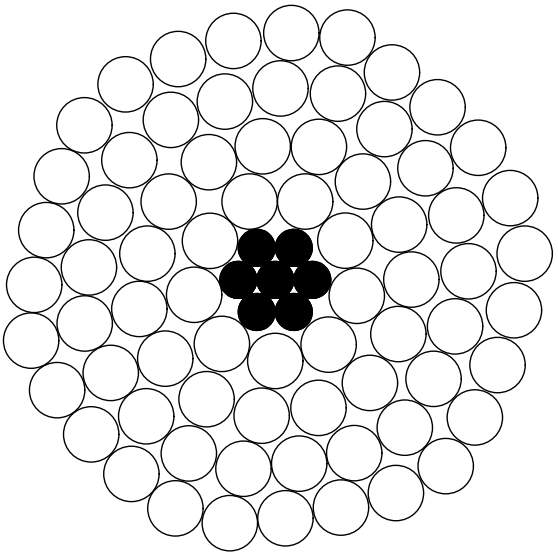

(b) ACSR 72/7 Nelson I.

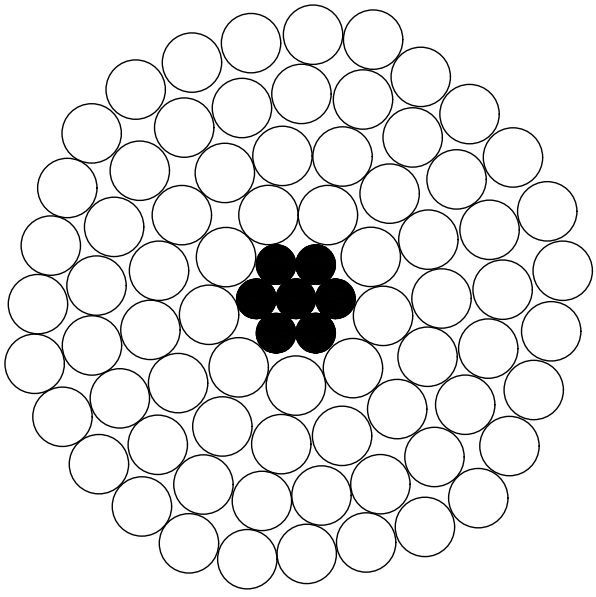

(c) ACSR 72/7 Nelson II.

Figure B.5. Cross-sections of ACSR 72/7 conductors.

Appendix C

Assessment of Lateral Contact Conditions for ACSR Conductors

In this appendix, the lateral contact conditions for ACSR conductors are ssessed, with reference to the different lay angles α, according to ASTM standard (1). The values of the maximum and minimum helix pitch (i.e. P_{max} and P_{min}) are adopted, leading respectively to the minimum and maximum lay angles (i.e. α_{min} and α_{max}).
The latter are obviously compared with the maximum admissible lay angle $\alpha_{max,adm}$ computed according to the procedure explained in Subsection 3.2.1.
Sections C.1 and C.2 deal with the assessment of lateral contact conditions by considering respectively the maximum and minimum lay angle for a sample of 15 ACSR conductors.
The mechanical and geometrical properties of ACSR conductors are listed in Appendix A, whereas their cross-sections schemes are conveniently reported in Appendix B.
As a matter of fact, by considering the minimum lay angle α_{min} computed according to the ASTM standard (1), the lateral contact condition is only present between the core wire and the first layer of wires.

C.1 Maximum Lay Angle

Table C.1. Lateral contact condition for 6/1 conductors. Maximum lay angle.

Code Word	Stranding	$D\,(mm)$	$n_L\,(-)$	$d_{st}\,(mm)$	$d_{al}\,(mm)$	$\alpha_{max,adm}$	α_{max}	Lateral Contact
Innermost Layer $i = 1$.								
Sparrow	6/1	8.01	1	2.67	2.67	0.00	9.90	**Yes**
Pigeon	6/1	12.75	1	4.25	4.25	0.00	9.90	**Yes**
Penguin	6/1	14.31	1	4.77	4.77	0.00	9.90	**Yes**

Table C.2. Lateral contact condition for 26/7 conductors. Maximum lay angle.

Code Word	Stranding	$D\,(mm)$	$n_L\,(-)$	$d_{st}\,(mm)$	$d_{al}\,(mm)$	$\alpha_{max,adm}$	α_{max}	Lateral Contact
Outermost Layer $i = 3$.								
Partridge	26/7	16.28	3	2.00	2.57	16.33	14.82	**No**
Hawk	26/7	21.80	3	2.68	3.44	16.33	14.82	**No**
Drake	26/7	28.10	3	3.45	4.44	16.33	14.82	**No**
Middle Layer $i = 2$.								
Partridge	26/7	16.28	3	2.00	2.57	14.56	13.59	**No**
Hawk	26/7	21.80	3	2.68	3.44	14.56	13.59	**No**
Drake	26/7	28.10	3	3.45	4.44	14.56	13.59	**No**
Innermost Layer $i = 1$.								
Partridge	26/7	16.28	3	2.00	2.57	0.00	6.64	**Yes**
Hawk	26/7	21.80	3	2.68	3.44	0.00	6.64	**Yes**
Drake	26/7	28.10	3	3.45	4.44	0.00	6.64	**Yes**

Table C.3. Lateral contact condition for 48/7 conductors. Maximum lay angle.

Code Word	Stranding	$D\,(mm)$	$n_L\,(-)$	$d_{st}\,(mm)$	$d_{al}\,(mm)$	$\alpha_{max,adm}$	α_{max}	Lateral Contact
Outermost Layer $i = 4$.								
Carillon	48/7	30.48	4	2.84	3.66	16.79	15.45	**No**
Gatineau	48/7	33.00	4	3.08	3.96	16.79	15.45	**No**
Bersfort	48/7	35.60	4	3.32	4.27	16.79	15.45	**No**
Layer $i = 3$.								
Carillon	48/7	30.48	4	2.84	3.66	16.33	14.81	**No**
Gatineau	48/7	33.00	4	3.08	3.96	16.33	14.81	**No**
Bersfort	48/7	35.60	4	3.32	4.27	16.33	14.81	**No**
Layer $i = 2$.								
Carillon	48/7	30.48	4	2.84	3.66	14.55	13.58	**No**
Gatineau	48/7	33.00	4	3.08	3.96	14.55	13.58	**No**
Bersfort	48/7	35.60	4	3.32	4.27	14.55	13.58	**No**
Innermost Layer $i = 1$.								
Carillon	48/7	30.48	4	2.84	3.66	0.00	6.64	**Yes**
Gatineau	48/7	33.00	4	3.08	3.96	0.00	6.64	**Yes**
Bersfort	48/7	35.60	4	3.32	4.27	0.00	6.64	**Yes**

Table C.4. Lateral contact condition for 54/7 conductors. Maximum lay angle.

Code Word	Stranding	$D\,(mm)$	$n_L\,(-)$	$d_{st}\,(mm)$	$d_{al}\,(mm)$	$\alpha_{max,adm}$	α_{max}	Lateral Contact
Outermost Layer $i = 4$.								
Duck	54/7	24.21	4	2.69	2.69	16.87	15.60	**No**
Crow	54/7	26.28	4	2.92	2.92	16.87	15.60	**No**
Curlew	54/7	31.59	4	3.51	3.51	16.87	15.60	**No**
Layer $i = 3$.								
Duck	54/7	24.21	4	2.69	2.69	16.54	15.07	**No**
Crow	54/7	26.28	4	2.92	2.92	16.54	15.07	**No**
Curlew	54/7	31.59	4	3.51	3.51	16.54	15.07	**No**
Layer $i = 2$.								
Duck	54/7	24.21	4	2.69	2.69	15.50	14.11	**No**
Crow	54/7	26.28	4	2.92	2.92	15.50	14.11	**No**
Curlew	54/7	31.59	4	3.51	3.51	15.50	14.11	**No**
Innermost Layer $i = 1$.								
Duck	54/7	24.21	4	2.69	2.69	0.00	6.64	**Yes**
Crow	54/7	26.28	4	2.92	2.92	0.00	6.64	**Yes**
Curlew	54/7	31.59	4	3.51	3.51	0.00	6.64	**Yes**

Table C.5. Lateral contact condition for 72/7 conductors. Maximum lay angle.

Code Word	Stranding	$D\,(mm)$	$n_L\,(-)$	$d_{st}\,(mm)$	$d_{al}\,(mm)$	$\alpha_{max,adm}$	α_{max}	Lateral Contact
Outermost Layer $i = 5$.								
Falcon	72/7	37.69	5	2.51	3.77	16.95	19.46	**Yes**
Nelson I	72/7	40.60	5	2.71	4.06	16.95	19.46	**Yes**
Nelson II	72/7	43.20	5	2.88	4.32	16.95	19.46	**Yes**
Layer $i = 4$.								
Falcon	72/7	37.69	5	2.51	3.77	16.74	20.13	**Yes**
Nelson I	72/7	40.60	5	2.71	4.06	16.74	20.13	**Yes**
Nelson II	72/7	43.20	5	2.88	4.32	16.74	20.13	**Yes**
Layer $i = 3$.								
Falcon	72/7	37.69	5	2.51	3.77	16.19	14.67	**No**
Nelson I	72/7	40.60	5	2.71	4.06	16.19	14.67	**No**
Nelson II	72/7	43.20	5	2.88	4.32	16.19	14.67	**No**
Layer $i = 2$.								
Falcon	72/7	37.69	5	2.51	3.77	13.74	13.26	**No**
Nelson I	72/7	40.60	5	2.71	4.06	13.74	13.26	**No**
Nelson II	72/7	43.20	5	2.88	4.32	13.74	13.26	**No**
Innermost Layer $i = 1$.								
Falcon	72/7	37.69	5	2.51	3.77	0.00	6.64	**Yes**
Nelson I	72/7	40.60	5	2.71	4.06	0.00	6.64	**Yes**
Nelson II	72/7	43.20	5	2.88	4.32	0.00	6.64	**Yes**

C.2 Minimum Lay Angle

Table C.6. Lateral contact condition for 6/1 conductors. Minimum lay angle.

Code Word	Stranding	$D\,(mm)$	$n_L\,(-)$	$d_{st}\,(mm)$	$d_{al}\,(mm)$	$\alpha_{max,adm}$	α_{min}	Lateral Contact
Innermost Layer $i = 1$.								
Sparrow	6/1	8.01	1	2.67	2.67	0.00	8.22	**Yes**
Pigeon	6/1	12.75	1	4.25	4.25	0.00	8.22	**Yes**
Penguin	6/1	14.31	1	4.77	4.77	0.00	8.22	**Yes**

Table C.7. Lateral contact condition for 26/7 conductors. Minimum lay angle.

Code Word	Stranding	$D\,(mm)$	$n_L\,(-)$	$d_{st}\,(mm)$	$d_{al}\,(mm)$	$\alpha_{max,adm}$	α_{min}	Lateral Contact
Outermost Layer $i = 3$.								
Partridge	26/7	16.28	3	2.00	2.57	16.33	11.50	**No**
Hawk	26/7	21.80	3	2.68	3.44	16.33	11.50	**No**
Drake	26/7	28.10	3	3.45	4.44	16.33	11.50	**No**
Middle Layer $i = 2$.								
Partridge	26/7	16.28	3	2.00	2.57	14.56	8.09	**No**
Hawk	26/7	21.80	3	2.68	3.44	14.56	8.09	**No**
Drake	26/7	28.10	3	3.45	4.44	14.56	8.09	**No**
Innermost Layer $i = 1$.								
Partridge	26/7	16.28	3	2.00	2.57	0.00	3.99	**Yes**
Hawk	26/7	21.80	3	2.68	3.44	0.00	3.99	**Yes**
Drake	26/7	28.10	3	3.45	4.44	0.00	3.99	**Yes**

Table C.8. Lateral contact condition for 48/7 conductors. Minimum lay angle.

Code Word	Stranding	$D\,(mm)$	$n_L\,(-)$	$d_{st}\,(mm)$	$d_{al}\,(mm)$	$\alpha_{max,adm}$	α_{min}	Lateral Contact
Outermost Layer $i = 4$.								
Carillon	48/7	30.48	4	2.84	3.66	16.79	12.00	**No**
Gatineau	48/7	33.00	4	3.08	3.96	16.79	12.00	**No**
Bersfort	48/7	35.60	4	3.32	4.27	16.79	12.00	**No**
Layer $i = 3$.								
Carillon	48/7	30.48	4	2.84	3.66	16.33	9.39	**No**
Gatineau	48/7	33.00	4	3.08	3.96	16.33	9.39	**No**
Bersfort	48/7	35.60	4	3.32	4.27	16.33	9.39	**No**
Layer $i = 2$.								
Carillon	48/7	30.48	4	2.84	3.66	14.55	8.09	**No**
Gatineau	48/7	33.00	4	3.08	3.96	14.55	8.09	**No**
Bersfort	48/7	35.60	4	3.32	4.27	14.55	8.09	**No**
Innermost Layer $i = 1$.								
Carillon	48/7	30.48	4	2.84	3.66	0.00	3.99	**Yes**
Gatineau	48/7	33.00	4	3.08	3.96	0.00	3.99	**Yes**
Bersfort	48/7	35.60	4	3.32	4.27	0.00	3.99	**Yes**

Table C.9. Lateral contact condition for 54/7 conductors. Minimum lay angle.

Code Word	Stranding	$D\,(mm)$	$n_L\,(-)$	$d_{st}\,(mm)$	$d_{al}\,(mm)$	$\alpha_{max,adm}$	α_{min}	Lateral Contact
Outermost Layer $i = 4$.								
Duck	54/7	24.21	4	2.69	2.69	16.87	12.12	**No**
Crow	54/7	26.28	4	2.92	2.92	16.87	12.12	**No**
Curlew	54/7	31.59	4	3.51	3.51	16.87	12.12	**No**
Layer $i = 3$.								
Duck	54/7	24.21	4	2.69	2.69	16.54	9.55	**No**
Crow	54/7	26.28	4	2.92	2.92	16.54	9.55	**No**
Curlew	54/7	31.59	4	3.51	3.51	16.54	9.55	**No**
Layer $i = 2$.								
Duck	54/7	24.21	4	2.69	2.69	15.50	8.41	**No**
Crow	54/7	26.28	4	2.92	2.92	15.50	8.41	**No**
Curlew	54/7	31.59	4	3.51	3.51	15.50	8.41	**No**
Innermost Layer $i = 1$.								
Duck	54/7	24.21	4	2.69	2.69	0.00	3.99	**Yes**
Crow	54/7	26.28	4	2.92	2.92	0.00	3.99	**Yes**
Curlew	54/7	31.59	4	3.51	3.51	0.00	3.99	**Yes**

Table C.10. Lateral contact condition for 72/7 conductors. Minimum lay angle.

Code Word	Stranding	$D\,(mm)$	$n_L\,(-)$	$d_{st}\,(mm)$	$d_{al}\,(mm)$	$\alpha_{max,adm}$	α_{min}	Lateral Contact
Outermost Layer $i = 5$.								
Falcon	72/7	37.69	5	2.51	3.77	16.95	15.21	**No**
Nelson I	72/7	40.60	5	2.71	4.06	16.95	15.21	**No**
Nelson II	72/7	43.20	5	2.88	4.32	16.95	15.21	**No**
Layer $i = 4$.								
Falcon	72/7	37.69	5	2.51	3.77	16.74	12.90	**No**
Nelson I	72/7	40.60	5	2.71	4.06	16.74	12.90	**No**
Nelson II	72/7	43.20	5	2.88	4.32	16.74	12.90	**No**
Layer $i = 3$.								
Falcon	72/7	37.69	5	2.51	3.77	16.19	9.29	**No**
Nelson I	72/7	40.60	5	2.71	4.06	16.19	9.29	**No**
Nelson II	72/7	43.20	5	2.88	4.32	16.19	9.29	**No**
Layer $i = 2$.								
Falcon	72/7	37.69	5	2.51	3.77	13.74	7.89	**No**
Nelson I	72/7	40.60	5	2.71	4.06	13.74	7.89	**No**
Nelson II	72/7	43.20	5	2.88	4.32	13.74	7.89	**No**
Innermost Layer $i = 1$.								
Falcon	72/7	37.69	5	2.51	3.77	0.00	3.99	**Yes**
Nelson I	72/7	40.60	5	2.71	4.06	0.00	3.99	**Yes**
Nelson II	72/7	43.20	5	2.88	4.32	0.00	3.99	**Yes**

Appendix D

Approximated Radial Forces for ACSR Conductors

In this Appendix, the approximated radial forces computed in Subsection 3.4.3 are reported in tabular form for the sake of convenience. Results are distinguished for each layer of the various conductor cross-sections. The mechanical and geometrical properties of ACSR conductors are listed in Appendix A, whereas their cross-sections schemes are conveniently reported in Appendix B.
It is worth noticing that:

- distances between contact points are not computed for the case of 6/1 conductors and for the first layer (i.e $i = 1$) of multilayer strands. This is due to the fact that contact patches between the core and the first layer of wires are assumed to be continuous and not pointwise distributed (see Subsection 3.2.2 for further details). As a consequence, approximated radial contact forces are not computed for such cases;

- radial contact forces per unit of length that are adopted for the computation of such approximated radial forces, have been computed in Paragraph 3.4.2 with reference to an axial load of 1 kN acting on the strand. Due to the linearity property of the axial-torsional problem, the following results can be easily scaled up in order to obtain the corresponding values of the approximated radial contact forces for any magnitude of the axial load N_s acting on the strand.

Each section of this Appendix is fully dedicated to a stranding typology.
Tables D.1-D.12 collect the approximated radial contact forces P^{int} and P^{ext} computed at each layer of the considered conductor for three radial pressures models (P.M A, B and C) and for three different distances between contact points, computed according to the equations proposed by Cardou (2013) (Eq. 3.20), Chouinard (1994) (Eq. 3.21) and Papailiou (1995) (Eq. 3.22).
See Subsection 3.4.2 for the description of the three radial pressures transmission models and Subsection 3.2.2 for further details on the computation of the distances between contact points through the application of the three different equations of the literature.

D.1 ACSR 26/7 Conductors

Table D.1. Approximated Radial Contact Forces, ACSR 26/7 Partridge.

Distance	Pressure Model A		Pressure Model B		Pressure Model C	
Formula	$P_r^{int}(N)$	$P_r^{ext}(N)$	$P_r^{int}(N)$	$P_r^{ext}(N)$	$P_r^{int}(N)$	$P_r^{ext}(N)$
Layer $i = 3$.						
Cardou	2,95	0,00	2,92	0,00	2,92	0,00
Chouinard	3,05	0,00	3,02	0,00	3,02	0,00
Papailiou	2,98	0,00	2,95	0,00	2,95	0,00
Layer $i = 2$.						
Cardou	6,82	4,72	6,67	4,67	5,13	2,92
Chouinard	6,53	4,88	6,38	4,83	4,91	3,02
Papailiou	6,36	4,76	6,22	4,72	4,79	2,95
Layer $i = 1$						
Cardou	-	11,37	-	11,12	-	5,13
Chouinard	-	10,88	-	10,64	-	4,91
Papailiou	-	10,61	-	10,37	-	4,79

Table D.2. Approximated Radial Contact Forces, ACSR 26/7 Hawk.

Distance	Pressure Model A		Pressure Model B		Pressure Model C	
Formula	$P_r^{int}(N)$	$P_r^{ext}(N)$	$P_r^{int}(N)$	$P_r^{ext}(N)$	$P_r^{int}(N)$	$P_r^{ext}(N)$
Layer $i = 3$.						
Cardou	1,71	0,00	1,69	0,00	1,69	0,00
Chouinard	1,77	0,00	1,75	0,00	1,75	0,00
Papailiou	1,72	0,00	1,71	0,00	1,71	0,00
Layer $i = 2$.						
Cardou	6,82	2,73	6,67	2,70	5,13	1,69
Chouinard	6,53	2,83	6,38	2,80	4,91	1,75
Papailiou	6,37	2,76	6,22	2,73	4,79	1,71
Layer $i = 1$						
Cardou	-	11,37	-	11,12	-	5,13
Chouinard	-	10,88	-	10,64	-	4,91
Papailiou	-	10,61	-	10,37	-	4,79

Table D.3. Approximated Radial Contact Forces, ACSR 26/7 Drake.

Distance	Pressure Model A		Pressure Model B		Pressure Model C	
Formula	$P_r^{int}(N)$	$P_r^{ext}(N)$	$P_r^{int}(N)$	$P_r^{ext}(N)$	$P_r^{int}(N)$	$P_r^{ext}(N)$
Layer $i = 3$.						
Cardou	1,71	0,00	1,69	0,00	1,69	0,00
Chouinard	1,77	0,00	1,75	0,00	1,75	0,00
Papailiou	1,73	0,00	1,71	0,00	1,71	0,00
Layer $i = 2$.						
Cardou	6,83	2,74	6,67	2,71	5,13	1,69
Chouinard	6,53	2,83	6,38	2,80	4,91	1,75
Papailiou	6,36	2,76	6,22	2,73	4,79	1,71
Layer $i = 1$						
Cardou	-	11,38	-	11,12	-	5,13
Chouinard	-	10,88	-	10,64	-	4,91
Papailiou	-	10,61	-	10,37	-	4,79

D.2 ACSR 48/7 Conductors

Table D.4. Approximated Radial Contact Forces, ACSR 48/7 Bersfort.

Distance	Pressure Model A		Pressure Model B		Pressure Model C	
Formula	$P_r^{int}(N)$	$P_r^{ext}(N)$	$P_r^{int}(N)$	$P_r^{ext}(N)$	$P_r^{int}(N)$	$P_r^{ext}(N)$
Layer $i = 4$.						
Cardou	0,75	0,00	0,74	0,00	0,74	0,00
Chouinard	0,76	0,00	0,76	0,00	0,76	0,00
Papailiou	0,76	0,00	0,75	0,00	0,75	0,00
Layer $i = 3$.						
Cardou	2,14	1,03	2,11	1,02	1,76	0,74
Chouinard	2,25	1,05	2,22	1,04	1,86	0,76
Papailiou	2,16	1,04	2,12	1,03	1,78	0,75
Layer $i = 2$.						
Cardou	6,63	3,43	6,43	3,37	4,15	1,76
Chouinard	6,34	3,61	6,15	3,55	3,97	1,86
Papailiou	6,18	3,45	5,99	3,39	3,87	1,78
Layer $i = 1$						
Cardou	-	11,04	-	10,72	-	4,15
Chouinard	-	10,56	-	10,25	-	3,97
Papailiou	-	10,30	-	9,99	-	3,87

Table D.5. Approximated Radial Contact Forces, ACSR 48/7 Carillon.

Distance	Pressure Model A		Pressure Model B		Pressure Model C	
Formula	$P_r^{int}(N)$	$P_r^{ext}(N)$	$P_r^{int}(N)$	$P_r^{ext}(N)$	$P_r^{int}(N)$	$P_r^{ext}(N)$
Layer $i = 4$.						
Cardou	0,72	0,00	0,71	0,00	0,71	0,00
Chouinard	0,73	0,00	0,73	0,00	0,73	0,00
Papailiou	0,73	0,00	0,72	0,00	0,72	0,00
Layer $i = 3$.						
Cardou	2,01	0,99	1,98	0,98	1,66	0,71
Chouinard	2,13	1,01	2,10	1,00	1,76	0,73
Papailiou	2,03	1,00	1,99	0,99	1,67	0,72
Layer $i = 2$.						
Cardou	5,97	3,22	5,79	3,17	3,74	1,66
Chouinard	5,61	3,41	5,45	3,36	3,52	1,76
Papailiou	5,20	3,24	5,05	3,19	3,26	1,67
Layer $i = 1$						
Cardou	-	9,95	-	9,66	-	3,74
Chouinard	-	9,36	-	9,08	-	3,52
Papailiou	-	8,67	-	8,41	-	3,26

Table D.6. Approximated Radial Contact Forces, ACSR 48/7 Gatineau.

Distance	Pressure Model A		Pressure Model B		Pressure Model C	
Formula	$P_r^{int}(N)$	$P_r^{ext}(N)$	$P_r^{int}(N)$	$P_r^{ext}(N)$	$P_r^{int}(N)$	$P_r^{ext}(N)$
Layer $i = 4$.						
Cardou	0,75	0,00	0,74	0,00	0,74	0,00
Chouinard	0,76	0,00	0,76	0,00	0,76	0,00
Papailiou	0,76	0,00	0,75	0,00	0,75	0,00
Layer $i = 3$.						
Cardou	2,14	1,03	2,11	1,02	1,77	0,74
Chouinard	2,25	1,05	2,22	1,04	1,86	0,76
Papailiou	2,16	1,04	2,12	1,03	1,78	0,75
Layer $i = 2$.						
Cardou	6,62	3,43	6,43	3,37	4,15	1,77
Chouinard	6,34	3,61	6,15	3,55	3,97	1,86
Papailiou	6,18	3,45	5,99	3,39	3,87	1,78
Layer $i = 1$						
Cardou	-	11,04	-	10,71	-	4,15
Chouinard	-	10,57	-	10,25	-	3,97
Papailiou	-	10,29	-	9,99	-	3,87

D.3 ACSR 54/7 Conductors

Table D.7. Approximated Radial Contact Forces, ACSR 54/7 Duck.

Distance	Pressure Model A		Pressure Model B		Pressure Model C	
Formula	$P_r^{int}(N)$	$P_r^{ext}(N)$	$P_r^{int}(N)$	$P_r^{ext}(N)$	$P_r^{int}(N)$	$P_r^{ext}(N)$
Layer $i = 4$.						
Cardou	0,66	0,00	0,65	0,00	0,65	0,00
Chouinard	0,67	0,00	0,66	0,00	0,66	0,00
Papailiou	0,66	0,00	0,66	0,00	0,66	0,00
Layer $i = 3$.						
Cardou	1,77	0,87	1,75	0,87	1,49	0,65
Chouinard	1,85	0,89	1,82	0,88	1,55	0,66
Papailiou	1,78	0,88	1,76	0,87	1,50	0,66
Layer $i = 2$.						
Cardou	6,70	2,66	6,52	2,62	4,45	1,49
Chouinard	6,59	2,77	6,42	2,73	4,38	1,55
Papailiou	6,75	2,68	6,57	2,64	4,49	1,50
Layer $i = 1$						
Cardou	-	13,39	-	13,03	-	4,45
Chouinard	-	13,19	-	12,84	-	4,38
Papailiou	-	13,50	-	13,14	-	4,49

Table D.8. Approximated Radial Contact Forces, ACSR 54/7 Crow.

Distance	Pressure Model A		Pressure Model B		Pressure Model C	
Formula	$P_r^{int}(N)$	$P_r^{ext}(N)$	$P_r^{int}(N)$	$P_r^{ext}(N)$	$P_r^{int}(N)$	$P_r^{ext}(N)$
Layer $i = 4$.						
Cardou	0,66	0,00	0,65	0,00	0,65	0,00
Chouinard	0,66	0,00	0,66	0,00	0,66	0,00
Papailiou	0,66	0,00	0,66	0,00	0,66	0,00
Layer $i = 3$.						
Cardou	1,77	0,87	1,75	0,87	1,49	0,65
Chouinard	1,85	0,89	1,82	0,88	1,55	0,66
Papailiou	1,78	0,88	1,76	0,87	1,50	0,66
Layer $i = 2$.						
Cardou	6,70	2,66	6,52	2,62	4,45	1,49
Chouinard	6,59	2,77	6,42	2,73	4,38	1,55
Papailiou	6,75	2,68	6,57	2,64	4,49	1,50
Layer $i = 1$						
Cardou	-	13,39	-	13,04	-	4,45
Chouinard	-	13,19	-	12,84	-	4,38
Papailiou	-	13,50	-	13,14	-	4,49

Table D.9. Approximated Radial Contact Forces, ACSR 54/7 Curlew.

Distance	Pressure Model A		Pressure Model B		Pressure Model C	
Formula	$P_r^{int}(N)$	$P_r^{ext}(N)$	$P_r^{int}(N)$	$P_r^{ext}(N)$	$P_r^{int}(N)$	$P_r^{ext}(N)$
Layer $i = 4$.						
Cardou	0,55	0,00	0,55	0,00	0,55	0,00
Chouinard	0,56	0,00	0,55	0,00	0,55	0,00
Papailiou	0,55	0,00	0,55	0,00	0,55	0,00
Layer $i = 3$.						
Cardou	1,49	0,73	1,47	0,73	1,25	0,55
Chouinard	1,55	0,74	1,53	0,74	1,30	0,55
Papailiou	1,50	0,74	1,48	0,73	1,26	0,55
Layer $i = 2$.						
Cardou	5,62	2,23	5,47	2,20	3,74	1,25
Chouinard	5,54	2,33	5,39	2,29	3,68	1,30
Papailiou	5,67	2,25	5,52	2,21	3,77	1,26
Layer $i = 1$						
Cardou	-	11,24	-	10,94	-	3,74
Chouinard	-	11,07	-	10,78	-	3,68
Papailiou	-	11,34	-	11,03	-	3,77

D.4 ACSR 72/7 Conductors

Table D.10. Approximated Radial Contact Forces, ACSR 72/7 Falcon.

Distance	Pressure Model A		Pressure Model B		Pressure Model C	
Formula	$P_r^{int}(N)$	$P_r^{ext}(N)$	$P_r^{int}(N)$	$P_r^{ext}(N)$	$P_r^{int}(N)$	$P_r^{ext}(N)$
Layer $i = 5$.						
Cardou	0,53	0,00	0,52	0,00	0,52	0,00
Chouinard	0,54	0,00	0,53	0,00	0,53	0,00
Papailiou	0,53	0,00	0,53	0,00	0,53	0,00
Layer $i = 4$.						
Cardou	1,62	0,68	1,59	0,67	1,39	0,52
Chouinard	1,64	0,69	1,60	0,69	1,41	0,53
Papailiou	1,64	0,69	1,60	0,68	1,41	0,53
Layer $i = 3$.						
Cardou	3,75	2,27	3,63	2,22	2,54	1,39
Chouinard	3,98	2,30	3,85	2,25	2,70	1,41
Papailiou	3,94	2,30	3,81	2,25	2,67	1,41
Layer $i = 2$.						
Cardou	8,98	6,25	8,57	6,05	4,29	2,54
Chouinard	8,43	6,63	8,04	6,42	4,02	2,70
Papailiou	7,74	6,56	7,38	6,36	3,70	2,67
Layer $i = 1$						
Cardou	-	13,48	-	12,85	-	4,29
Chouinard	-	12,64	-	12,06	-	4,02
Papailiou	-	11,61	-	11,08	-	3,70

Table D.11. Approximated Radial Contact Forces, ACSR 72/7 Nelson I.

Distance	Pressure Model A		Pressure Model B		Pressure Model C	
Formula	$P_r^{int}(N)$	$P_r^{ext}(N)$	$P_r^{int}(N)$	$P_r^{ext}(N)$	$P_r^{int}(N)$	$P_r^{ext}(N)$
Layer $i = 5$.						
Cardou	0,53	0,00	0,52	0,00	0,52	0,00
Chouinard	0,54	0,00	0,53	0,00	0,53	0,00
Papailiou	0,53	0,00	0,53	0,00	0,53	0,00
Layer $i = 4$.						
Cardou	1,62	0,68	1,59	0,67	1,39	0,52
Chouinard	1,64	0,69	1,60	0,69	1,41	0,53
Papailiou	1,64	0,69	1,60	0,68	1,41	0,53
Layer $i = 3$.						
Cardou	3,75	2,27	3,63	2,22	2,54	1,39
Chouinard	3,97	2,29	3,85	2,24	2,69	1,41
Papailiou	3,77	2,29	3,66	2,24	2,56	1,41
Layer $i = 2$.						
Cardou	8,99	6,25	8,57	6,05	4,29	2,54
Chouinard	8,43	6,62	8,04	6,42	4,03	2,69
Papailiou	7,76	6,29	7,40	6,09	3,70	2,56
Layer $i = 1$						
Cardou	-	13,48	-	12,86	-	4,29
Chouinard	-	12,65	-	12,07	-	4,03
Papailiou	-	11,64	-	11,10	-	3,70

Table D.12. Approximated Radial Contact Forces, ACSR 72/7 Nelson II.

Distance	Pressure Model A		Pressure Model B		Pressure Model C	
Formula	$P_r^{int}(N)$	$P_r^{ext}(N)$	$P_r^{int}(N)$	$P_r^{ext}(N)$	$P_r^{int}(N)$	$P_r^{ext}(N)$
Layer $i = 5$.						
Cardou	0,53	0,00	0,52	0,00	0,52	0,00
Chouinard	0,54	0,00	0,53	0,00	0,53	0,00
Papailiou	0,53	0,00	0,53	0,00	0,53	0,00
Layer $i = 4$.						
Cardou	1,62	0,68	1,59	0,67	1,39	0,52
Chouinard	1,64	0,69	1,60	0,69	1,41	0,53
Papailiou	1,64	0,69	1,60	0,68	1,41	0,53
Layer $i = 3$.						
Cardou	3,75	2,27	3,63	2,22	2,54	1,39
Chouinard	3,98	2,30	3,85	2,24	2,69	1,41
Papailiou	3,78	2,30	3,66	2,24	2,56	1,41
Layer $i = 2$.						
Cardou	8,99	6,25	8,57	6,05	4,29	2,54
Chouinard	8,43	6,63	8,04	6,42	4,03	2,69
Papailiou	7,75	6,30	7,39	6,10	3,70	2,56
Layer $i = 1$						
Cardou	-	13,48	-	12,86	-	4,29
Chouinard	-	12,65	-	12,06	-	4,03
Papailiou	-	11,62	-	11,08	-	3,70

Appendix E

Nondimensional Wire Axial Force Limit Domain for ACSR Conductors

In this appendix, the plots of the non-dimensional limit functions for the nonlinear component of the wire axial force of different ACSR conductors are reported.
The mechanical and geometrical properties of ACSR conductors are listed in Appendix A, whereas their cross-sections schemes are conveniently reported in Appendix B.
The admissible limit domain of the wire axial forces is represented by the envelope of the continuous black lines, whereas the red dots indicate the values of the non-dimensional limit functions at the swept angles θ identifying the wires positions.
Each curve correspond to the limit domain associated to a specific layer of wires and it is indicated with its proper number, according to an ascending numbering starting from the inner layers towards the outer ones (i.e. $i = 1$ denotes the first layer of wires in contact with the core and $\max(i)$ denotes the outermost layer of wires, for the considered strand).
Such admissible domains are determined by considering the Radial Contact Pressure Model A (see Subsection 3.4.2) and Sliding Condition 1 (see Subsection 3.5.3), according to the developments presented in Section 3.5.
Each section of this appendix is fully dedicated to a stranding typology.
Figures E.1-E.15 show the non-dimensional axial force limit domain for the different ACSR conductors.

E.1 ACSR 6/1 Conductors

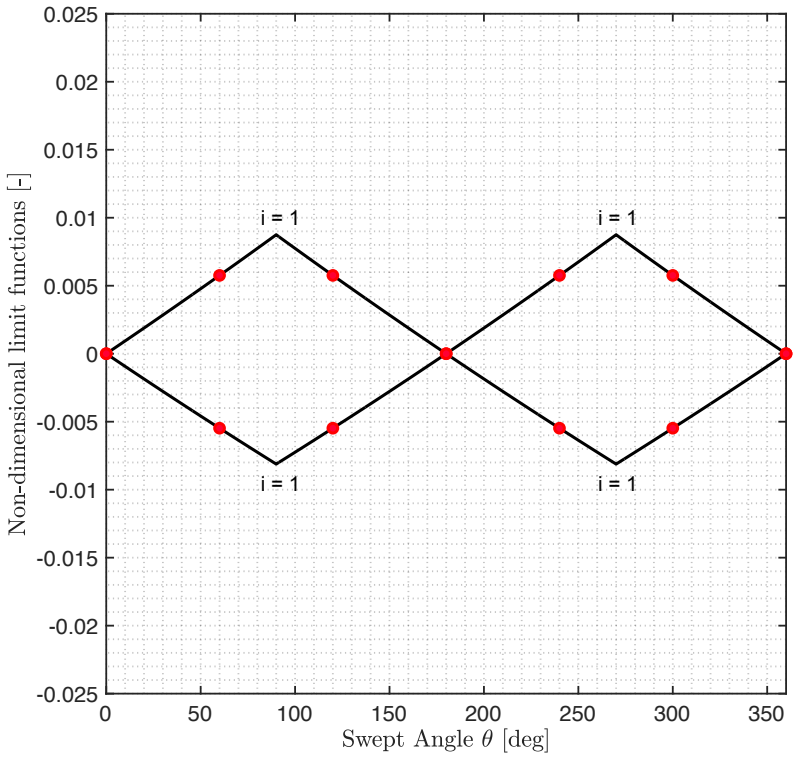

Figure E.1. Limit Domain of F_{w1}^{NL}/N_s for an ACSR 6/1 Sparrow.

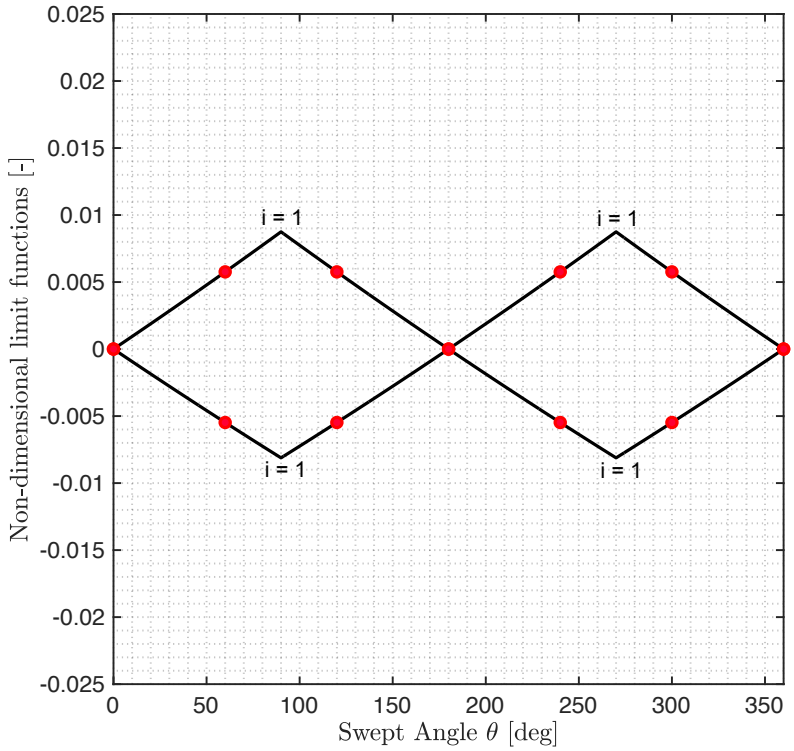

Figure E.2. Limit Domain of F_{w1}^{NL}/N_s for an ACSR 6/1 Pigeon.

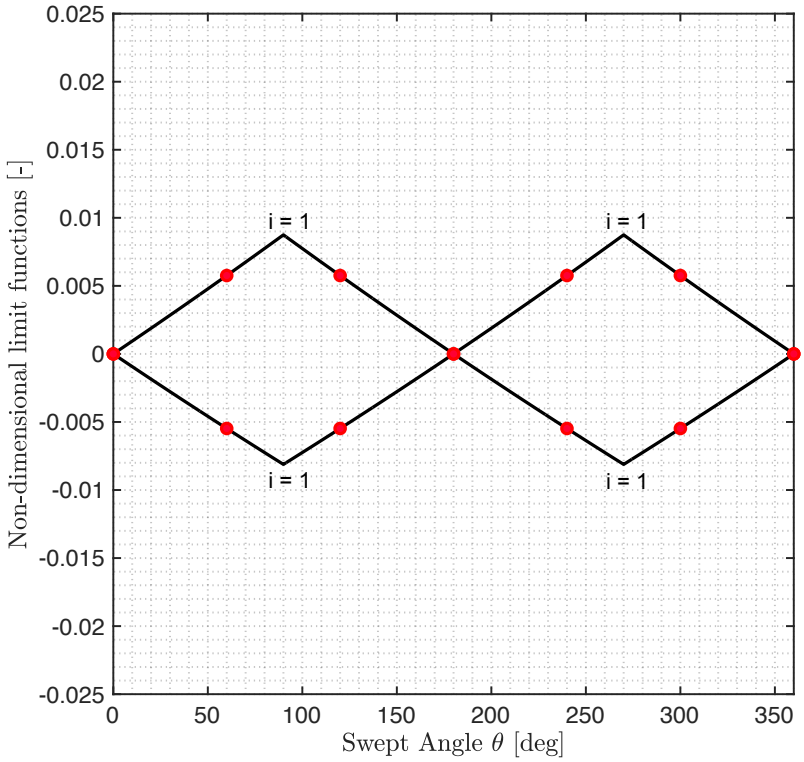

Figure E.3. Limit Domain of F_{w1}^{NL}/N_s for an ACSR 6/1 Penguin.

E.2 ACSR 26/7 Conductors

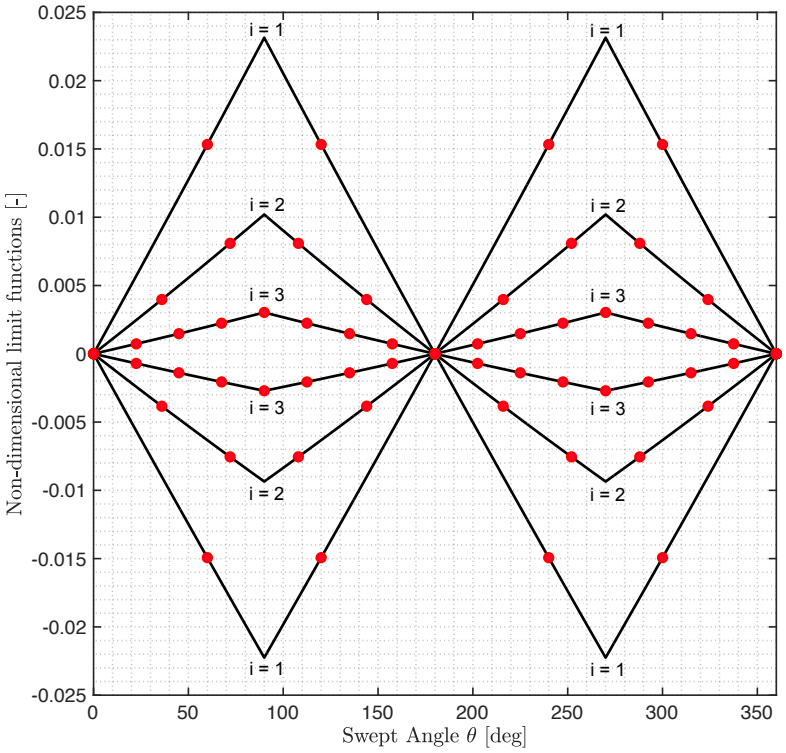

Figure E.4. Limit Domain of F_{w1}^{NL}/N_s for an ACSR 26/7 Partridge.

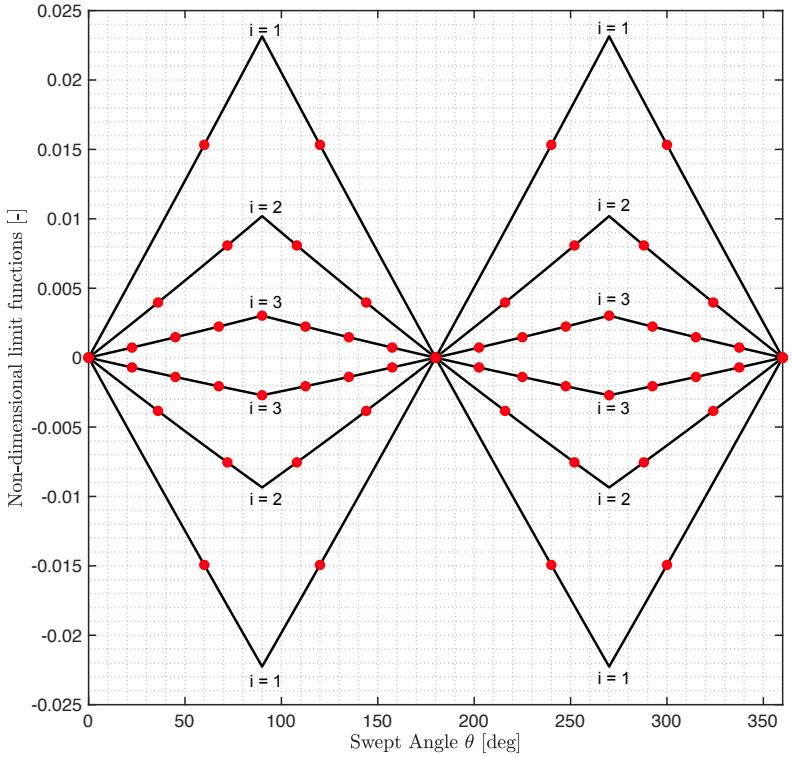

Figure E.5. Limit Domain of F_{w1}^{NL}/N_s for an ACSR 26/7 Hawk.

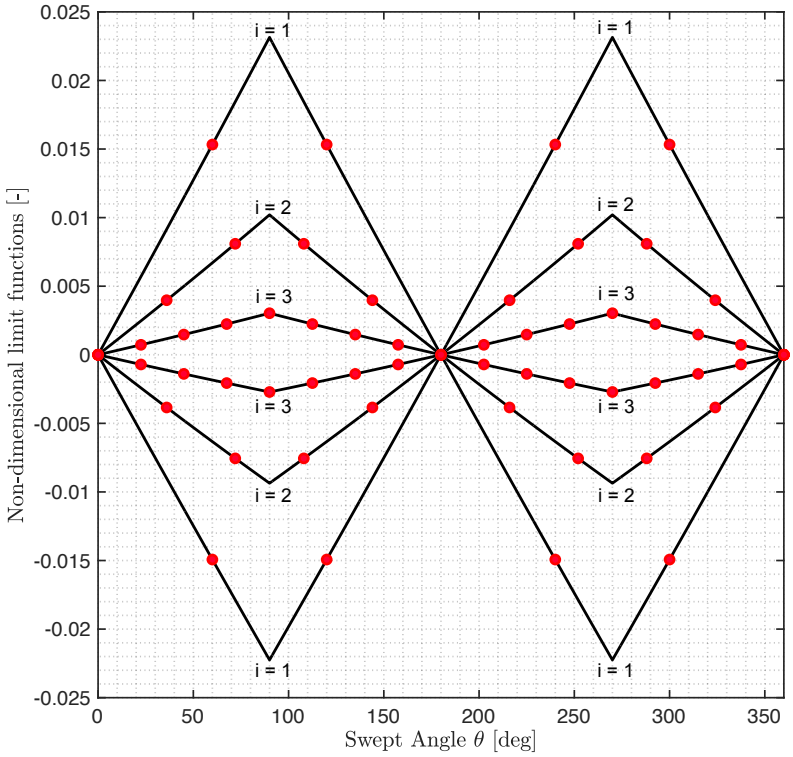

Figure E.6. Limit Domain of F_{w1}^{NL}/N_s for an ACSR 26/7 Drake.

E.3 ACSR 48/7 Conductors

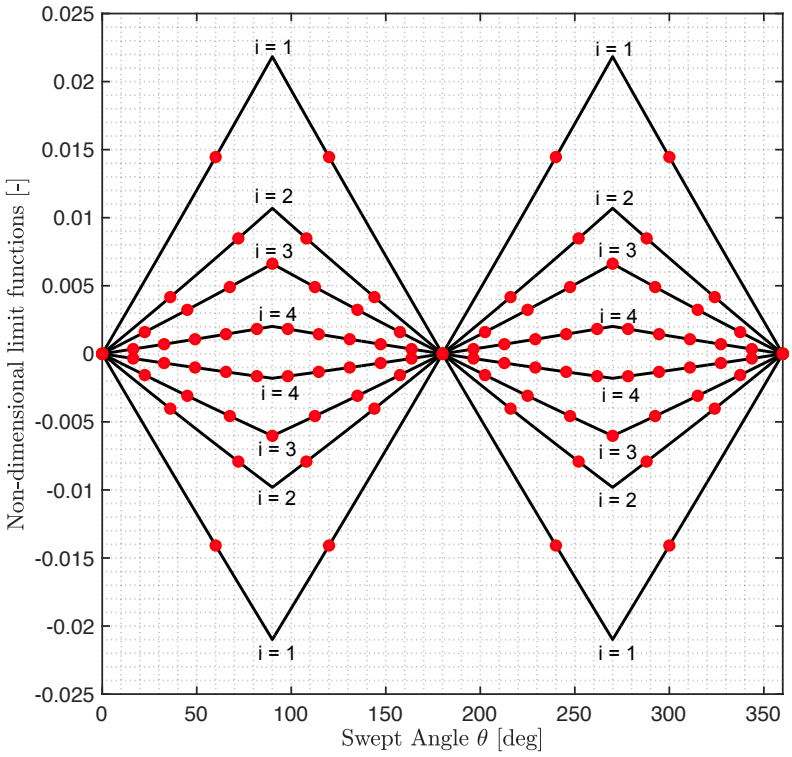

Figure E.7. Limit Domain of F_{w1}^{NL}/N_s for an ACSR 48/7 Bersfort.

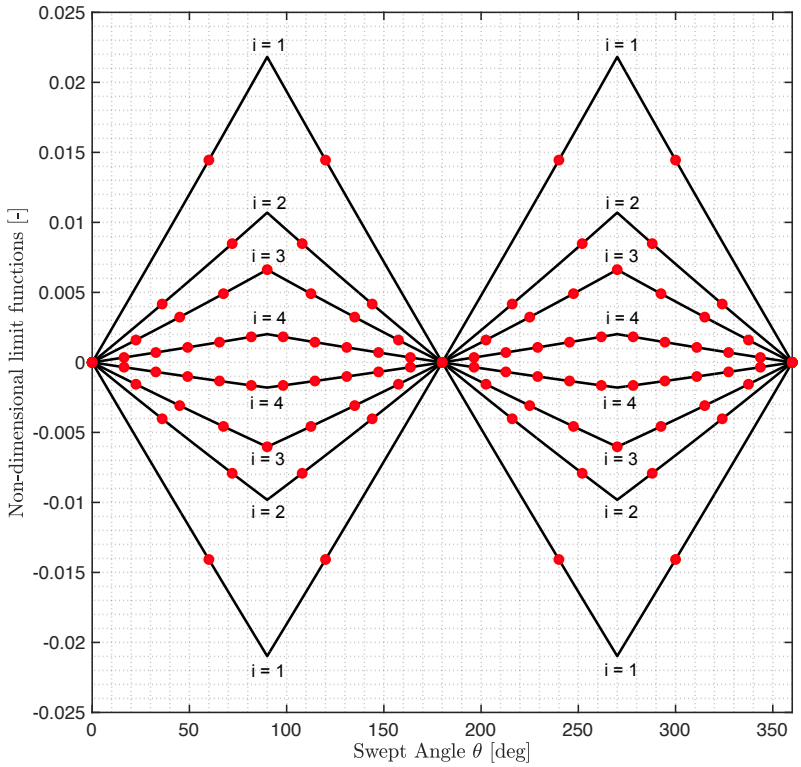

Figure E.8. Limit Domain of F_{w1}^{NL}/N_s for an ACSR 48/7 Carillon.

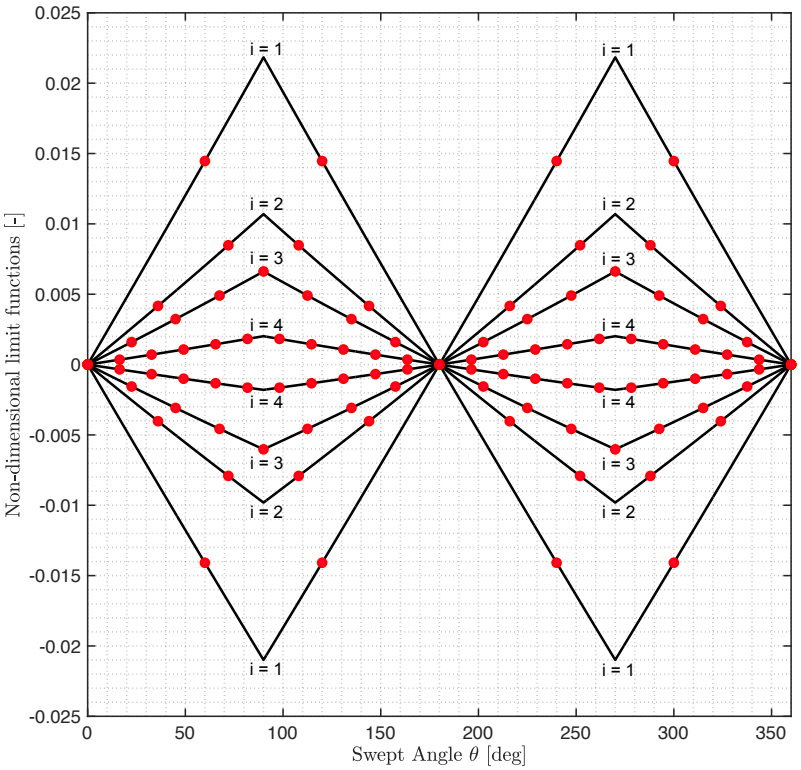

Figure E.9. Limit Domain of F_{w1}^{NL}/N_s for an ACSR 48/7 Gatineau.

E.4 ACSR 54/7 Conductors

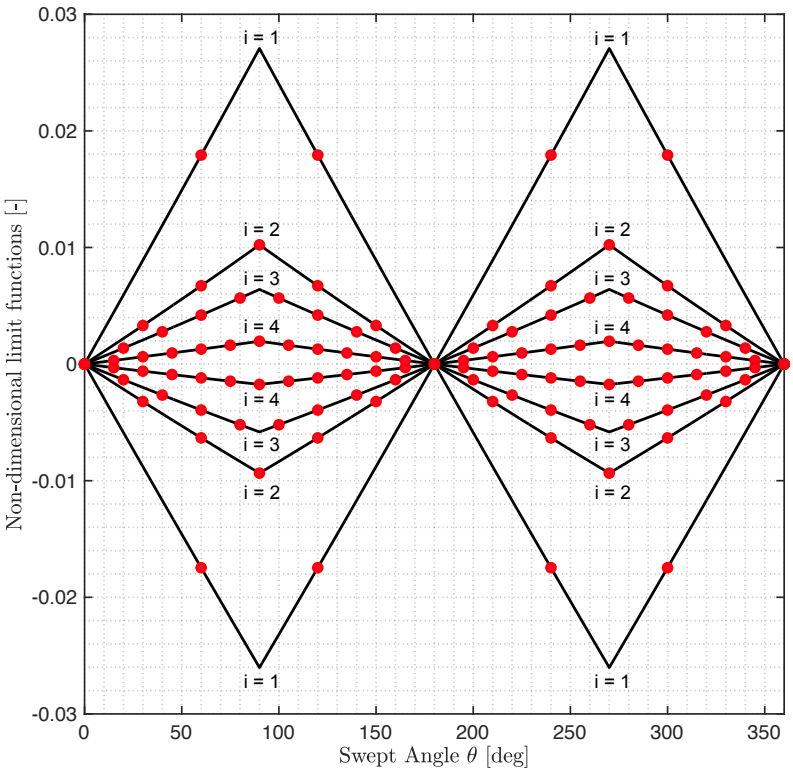

Figure E.10. Limit Domain of F_{w1}^{NL}/N_s for an ACSR 54/7 Duck.

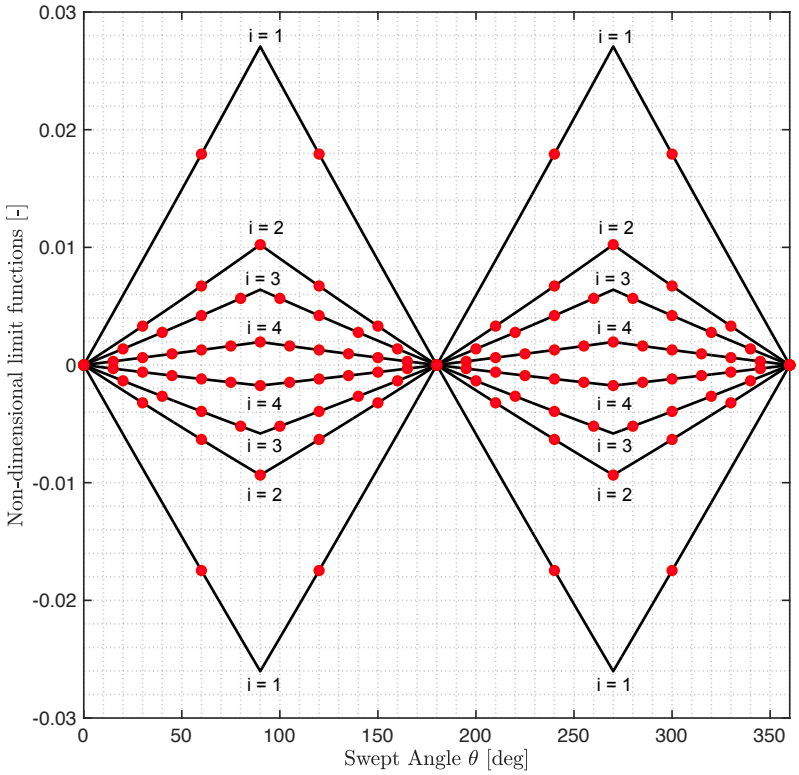

Figure E.11. Limit Domain of F_{w1}^{NL}/N_s for an ACSR 54/7 Crow.

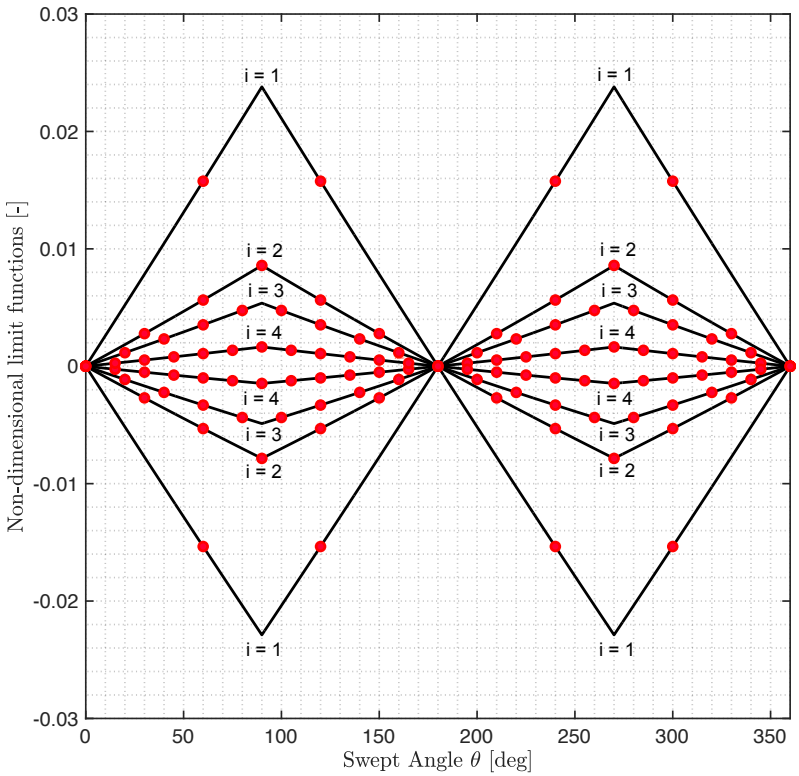

Figure E.12. Limit Domain of F_{w1}^{NL}/N_s for an ACSR 54/7 Curlew.

E.5 ACSR 72/7 Conductors

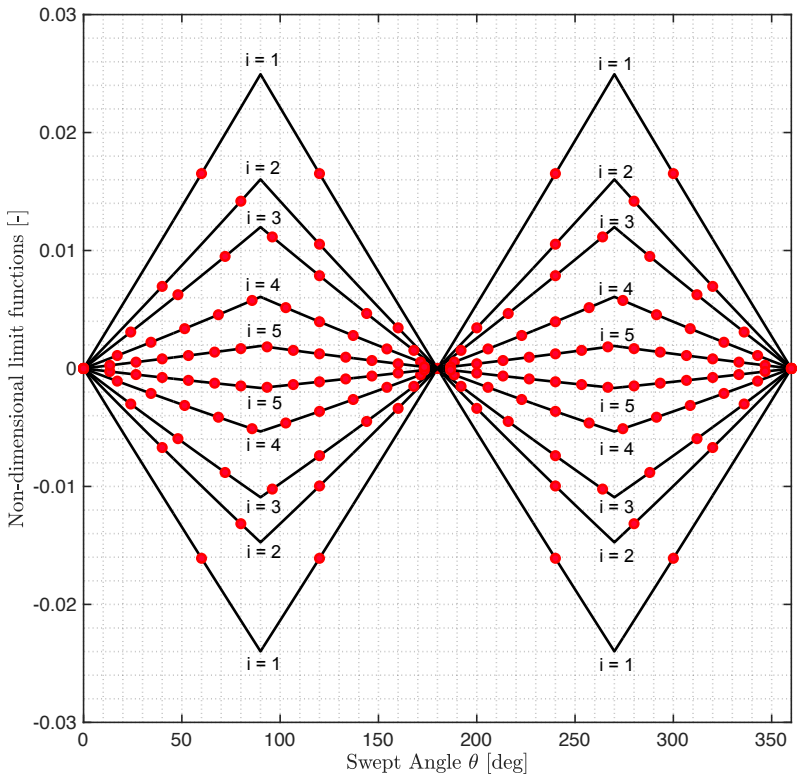

Figure E.13. Limit Domain of F_{w1}^{NL}/N_s for an ACSR 72/7 Falcon.

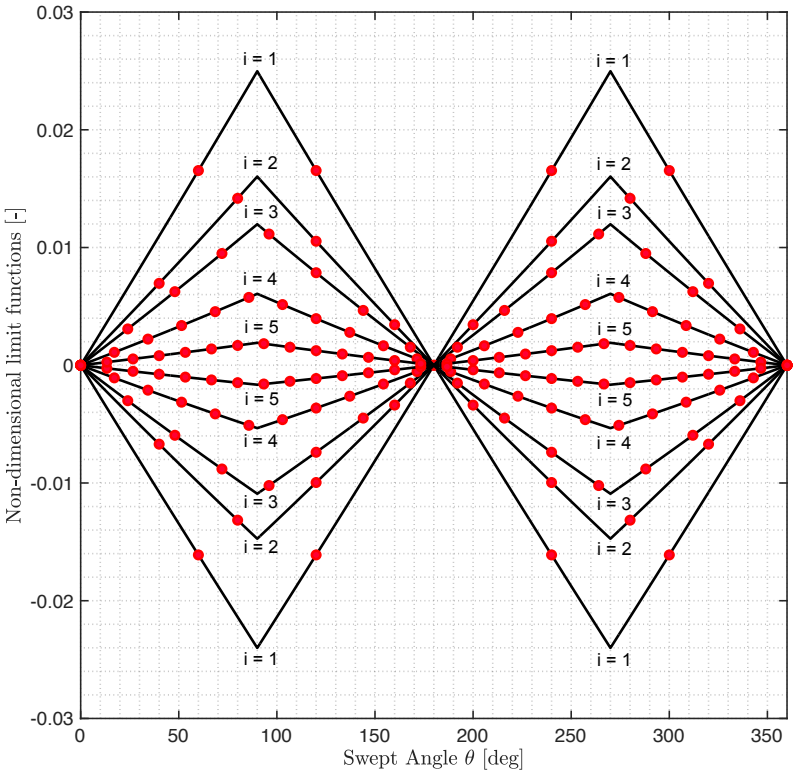

Figure E.14. Limit Domain of F_{w1}^{NL}/N_s for an ACSR 72/7 Nelson I.

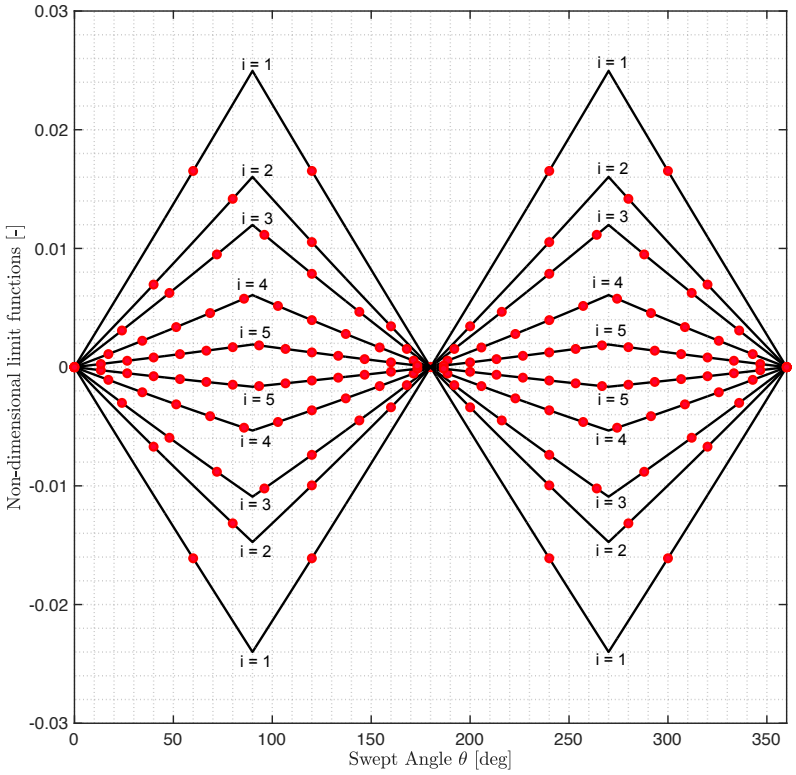

Figure E.15. Limit Domain of F_{w1}^{NL}/N_s for an ACSR 72/7 Nelson II.

Appendix F

Construction Parameter c_0 of ACSR Conductors

In this appendix, the construction parameter c_0 for the description of the bi-linear approximated moment-curvature relationship is reported, for different radial pressures models (P.M., see Subsection 3.4.2) and sliding conditions (S.C., see Subsection 3.5.3).
See Subsection 3.5.4 for further details on the introduction of the construction parameter c_0 for the description of the hysteretic behavior of metallic stranded cables.
The mechanical and geometrical properties of ACSR conductors are listed in Appendix A, whereas their cross-sections schemes are conveniently reported in Appendix B.
Since 6 sliding conditions were enforced and 3 radial pressures models were studied, then 18 combinations for the computation of c_0 arises for each conductor cross-section.
The results obtained for the construction parameter are collected in the following tables (F.1-F.15). Such values were determined according to the numerical procedure presented in Subsection 3.6.1. However, the closed-form expressions provided in Subsection 3.6.2 give equivalent results.
Each section of this Appendix is fully dedicated to a stranding typology.

F.1 ACSR 6/1 Conductors

Table F.1. ACSR 6/1 Sparrow: construction parameter c_0 $(1/m)$.

	P.M. A	P.M. B	P.M. C
S.C. 1	0,267	0,267	0,267
S.C. 2	0,267	0,267	0,267
S.C. 3	0,267	0,267	0,267
S.C. 4	0,267	0,267	0,267
S.C. 5	0,263	0,263	0,267
S.C. 6	0,263	0,263	0,267

Table F.2. ACSR 6/1 Pigeon: construction parameter c_0 $(1/m)$.

	P.M. A	P.M. B	P.M. C
S.C. 1	0,158	0,158	0,158
S.C. 2	0,158	0,158	0,158
S.C. 3	0,158	0,158	0,158
S.C. 4	0,158	0,158	0,158
S.C. 5	0,156	0,156	0,158
S.C. 6	0,156	0,156	0,158

Table F.3. ACSR 6/1 Penguin: construction parameter c_0 $(1/m)$.

	P.M. A	P.M. B	P.M. C
S.C. 1	0,141	0,141	0,141
S.C. 2	0,141	0,141	0,141
S.C. 3	0,141	0,141	0,141
S.C. 4	0,141	0,141	0,141
S.C. 5	0,139	0,139	0,141
S.C. 6	0,139	0,139	0,141

F.2 ACSR 26/7 Conductors

Table F.4. ACSR 26/7 Partridge: construction parameter c_0 $(1/m)$.

	P.M. A	P.M. B	P.M. C
S.C. 1	0,404	0,399	0,300
S.C. 2	0,177	0,177	0,177
S.C. 3	0,404	0,399	0,300
S.C. 4	0,178	0,178	0,177
S.C. 5	0,400	0,395	0,300
S.C. 6	0,173	0,173	0,177

Table F.5. ACSR 26/7 Hawk: construction parameter c_0 $(1/m)$.

	P.M. A	P.M. B	P.M. C
S.C. 1	0,290	0,286	0,215
S.C. 2	0,127	0,127	0,127
S.C. 3	0,290	0,286	0,215
S.C. 4	0,127	0,127	0,127
S.C. 5	0,287	0,283	0,215
S.C. 6	0,124	0,124	0,127

Table F.6. ACSR 26/7 Drake: construction parameter c_0 $(1/m)$.

	P.M. A	P.M. B	P.M. C
S.C. 1	0,217	0,214	0,161
S.C. 2	0,095	0,095	0,095
S.C. 3	0,217	0,214	0,161
S.C. 4	0,095	0,095	0,095
S.C. 5	0,214	0,212	0,161
S.C. 6	0,093	0,093	0,095

F.3 ACSR 48/7 Conductors

Table F.7. ACSR 48/7 Bersfort: construction parameter c_0 $(1/m)$.

	P.M. A	P.M. B	P.M. C
S.C. 1	0,190	0,187	0,139
S.C. 2	0,069	0,069	0,069
S.C. 3	0,190	0,187	0,139
S.C. 4	0,069	0,069	0,069
S.C. 5	0,189	0,186	0,139
S.C. 6	0,068	0,068	0,069

Table F.8. ACSR 48/7 Carillon: construction parameter c_0 $(1/m)$.

	P.M. A	P.M. B	P.M. C
S.C. 1	0,228	0,225	0,167
S.C. 2	0,083	0,083	0,083
S.C. 3	0,228	0,225	0,167
S.C. 4	0,083	0,083	0,083
S.C. 5	0,227	0,223	0,167
S.C. 6	0,081	0,081	0,083

Table F.9. ACSR 48/8 Gatineau: construction parameter c_0 $(1/m)$.

	P.M. A	P.M. B	P.M. C
S.C. 1	0,205	0,202	0,150
S.C. 2	0,074	0,074	0,074
S.C. 3	0,205	0,202	0,150
S.C. 4	0,075	0,075	0,074
S.C. 5	0,204	0,201	0,150
S.C. 6	0,073	0,073	0,074

F.4 ACSR 54/7 Conductors

Table F.10. ACSR 54/7 Duck: construction parameter c_0 $(1/m)$.

	P.M. A	P.M. B	P.M. C
S.C. 1	0,412	0,406	0,295
S.C. 2	0,138	0,138	0,138
S.C. 3	0,412	0,406	0,295
S.C. 4	0,138	0,138	0,138
S.C. 5	0,409	0,403	0,295
S.C. 6	0,135	0,135	0,138

Table F.11. ACSR 54/7 Crow: construction parameter c_0 $(1/m)$.

	P.M. A	P.M. B	P.M. C
S.C. 1	0,373	0,368	0,267
S.C. 2	0,125	0,125	0,125
S.C. 3	0,373	0,368	0,267
S.C. 4	0,125	0,125	0,125
S.C. 5	0,370	0,365	0,267
S.C. 6	0,122	0,122	0,125

Table F.12. ACSR 54/7 Curlew: construction parameter c_0 $(1/m)$.

	P.M. A	P.M. B	P.M. C
S.C. 1	0,248	0,245	0,178
S.C. 2	0,084	0,084	0,084
S.C. 3	0,248	0,245	0,178
S.C. 4	0,084	0,084	0,084
S.C. 5	0,246	0,243	0,178
S.C. 6	0,083	0,083	0,084

F.5 ACSR 72/7 Conductors

Table F.13. ACSR 72/7 Falcon: construction parameter c_0 $(1/m)$.

	P.M. A	P.M. B	P.M. C
S.C. 1	0,261	0,255	0,184
S.C. 2	0,075	0,075	0,075
S.C. 3	0,261	0,255	0,184
S.C. 4	0,075	0,075	0,075
S.C. 5	0,259	0,253	0,184
S.C. 6	0,073	0,073	0,075

Table F.14. ACSR 72/7 Nelson I: construction parameter c_0 $(1/m)$.

	P.M. A	P.M. B	P.M. C
S.C. 1	0,243	0,237	0,171
S.C. 2	0,070	0,070	0,070
S.C. 3	0,243	0,237	0,171
S.C. 4	0,070	0,070	0,070
S.C. 5	0,241	0,235	0,171
S.C. 6	0,068	0,068	0,070

Table F.15. ACSR 72/7 Nelson II: construction parameter c_0 $(1/m)$.

	P.M. A	P.M. B	P.M. C
S.C. 1	0,228	0,223	0,161
S.C.2	0,066	0,066	0,066
S.C. 3	0,228	0,223	0,161
S.C. 4	0,066	0,066	0,066
S.C. 5	0,226	0,220	0,161
S.C. 6	0,064	0,064	0,066

Acronyms

ACSR	Aluminium Conductor Steel Reinforced
VIV	Vortex Induced Vibrations
OHL	Overhead High voltage Lines
EBP	Energy Balance Principle
SRS	Strand-attached Reference System
ISWR	Inverse Standing Wave Ratio
PM	Pressures Model
SC	Sliding Condition
MS	Micro-Slip
GS	Gross-Sliding
FM	Full-Model

Bibliography

[1] ASTM. *ASTM Standards on Metallic Electrical Conductors*. American Society for Testing and Materials, Philadelphia, PA, 1980.

[2] C.R.F. Azevedo, A.M.D. Henriques, A.R. Pulino Filho, J.L.A. Ferreira, and J.A. Arauújo. Fretting fatigue in overhead conductors: Rig design and failure analysis of a grosbeak aluminium cable steel reinforced conductor. *Engineering Failure Analysis*, 16:136–151, 2009.

[3] R. Baumann and P. Novak. Efficient computation and experimental validation of acsr overhead line conductors under tension and bending. *Cigre Science and Engineering*, 9: 5–16, 2017.

[4] IEEE Standards Board. *Guide for Laboratory Measurement of the Power Dissipation Characteristics of Aeolian Vibration Dampers for Single Conductors*. IEEE Power Engineering Society, 1993.

[5] A. Cardou. *Stick-Slip Mechanical Model for Overhead Electrical Conductors in Bending*. Library and Archives Canada, 2013.

[6] A. Cardou and C. Jolicoeur. Mechanical models of helical strands. *Applied Mechanics Reviews*, 50:1–14, 1997.

[7] G. Chouinard. Analyse des caractéristiques de dissipation d'énergie aux points de contact entre les couches 1 et 2 d'un toron 1 x n_1 x n_2. Master's thesis, Université Laval, Québec, Canada, 1994.

[8] CIGRE. Guide on conductor self-damping measurements. *Electra*, 79:79–90, 1979.

[9] CIGRE. *State of the Art for Testing Self-Damping Characteristics of Conductors for Overhead Lines*. Technical Brochure no. 482, 2011.

[10] R. Claren and G. Diana. Mathematical analysis of transmission line vibration. *IEEE Transactions on Power Apparatus and Systems*, 88:1741–1771, 1969.

[11] R. Claren and G. Diana. Dynamic strain distribution on loaded stranded cables. *IEEE Transactions on Power Apparatus and Systems*, 88:1678–1687, 1969.

[12] D. Cooper and K. Nuckles. *Self-Damping Tests of Various "Drake" Conductors*. Southwire, Technology Center, 1996.

[13] G. A. Costello. *Theory of Wire Rope*. Springer, New York, 1990.

[14] G. Diana, M. Falco, A. Cigada, and A. Manenti. On the measurement of over head transmission lines conductor self-dampings. *IEEE Transactions on Power Delivery*, 15: 285–292, January 2000.

[15] G. Diana, M. Falco, A. Cigada, and A. Manenti. Closure to discussion of "on the measurement of overhead transmission lines conductor self-damping". *IEEE Transactions on Power Delivery*, 15:285–292, October 2000.

[16] Electric Research Power Institute EPRI. *Transmission Line Reference Book: Wind-Induced Conductor Motion*. Palo Alto, 2006.

[17] K. Feyrer. *Wire Ropes: Tension, Endurance, Reliability*. Springer-Verlag, Berlin, Heidelberg, 2015.

[18] F. Foti. *A corotational beam element and a refined mechanical model for the nonlinear dynamic analysis of cables*. PhD thesis, Doctoral Programme in Structural, Seismic and Geotechnical Engineering, Politecnico di Milano, February 2013.

[19] F. Foti. A corotational finite element to model bending vibrations of metallic strands. In *Proceedings of the VII European Congress on Computational Methods in Applied Sciences and Engineering*, Crete Island, Greece, June 2016.

[20] F. Foti and A. De Luca di Roseto. Analytical and finite element modelling of the elastic–plastic behaviour of metallic strands under axial–torsional loads. *International Journal of Mechanical Science*, 115-116:202–214, 2016.

[21] F. Foti and L. Martinelli. An analytical approach to model the hysteretic bending behavior of spiral strands. *Applied Mathematical Modelling*, 40:6451–6467, 2016a.

[22] F. Foti and L. Martinelli. Mechanical modeling of metallic strands subjected to tension, torsion and bending. *International Journal of Solids and Structures*, 91:1–17, 2016b.

[23] F. Foti and L. Martinelli. A unified analytical model for the self-damping of stranded cables under aeolian vibrations. *Journal of Wind Engineering and Industrial Aerodynamics*, 176:225–238, 2018a.

[24] F. Foti and L. Martinelli. An enhanced unified model for the self-damping of stranded cables under aeolian vibrations. *Journal of Wind Engineering and Industrial Aerodynamics*, 182:72–86, 2018b.

[25] F. Foti and L. Martinelli. Modeling the axial-torsional response of metallic strands accounting for the deformability of the internal contact surfaces: Derivation of the symmetric stiffness matrix. *International Journal of Solids and Structures*, 171:30–46, 2019.

[26] F. Foti and L. Martinelli. Corrigendum to "an enhanced unified model for the self-damping of stranded cables under aeolian vibrations" [j. wind eng. ind. aerodyn. 182 (2018) 72–86]. *Journal of Wind Engineering and Industrial Aerodynamics*, 214, 2021.

[27] F. Foti, L. Martinelli, and F. Perotti. A parametric study on the structural damping of suspended cables. *Procedia Engineering*, 199:140–145, 2017.

[28] F. Foti, V. Donoël, L Martinelli, and F. Perotti. A stochastic and continuous model of aeolian vibrations of conductors equipped with stockbridge dampers. In *Proceedings of the XI International Conference on Structural Dynamics*, pages 2088–2102, Athens, Greece, November 2020.

[29] F. Foti, L. Martinelli, and V. Donoël. Analytical modelling of the varying bending stiffness inside the boundary layer of cables. In *Proceedings of the second International Symposium on Dynamics and Aerodynamics of Cables*, pages 199–207, Stavanger, Norway, September 2021.

[30] F. Foti, L. Martinelli, and F. Perotti. Hysteretic behavior of stranded cables: recent developments and application to the modeling of self-damping in overhead electrical line conductors. In *Proceedings of the second International Symposium on Dynamics and Aerodynamics of Cables*, Stavanger, Norway, September 2021.

[31] F. Foti, L. Martinelli, S. Corazza, and F. Perotti. On the modeling of self-damping in overhead electrical line conductors subject to vortex-induced vibrations. In *Proceedings of the XVII Conference of the Italian Association for Wind Engineering*, Milan, Italy, 2022.

[32] M. Frigerio, P.B. Buehlmann, J. Buchheim, S.R. Holdsworth, S. Dinser, Ch.M Franck, K. Papailiou, and E. Mazza. Analysis of the tensile response of a stranded conductor using a 3d finite element model. *International Journal of Mechanical Science*, 106: 176–183, 2016.

[33] C. Gazzola. Modelling and assessment of aeolian vibrations of overhead transmission line conductors: theory and implementation. Master's thesis, Master of Science in Civil Engineering - Structures, Politecnico di Milano, Academic Year 2016–2017.

[34] A. Godinas. Experimental measurements of bending and damping properties of conductors for overhead transmission lines. In *Proceeding of the 3rd International Symposium on Cable Dynamics*, Trondheim, Norway, 1999.

[35] S. Goudreau, F. Charette, C. Hardy, and L. Cloutier. Bending energy dissipation of simplified single-layer stranded cable. *Journal of Engineering Mechanics*, 124:811–817, 1998.

[36] S. Guerard and J.L. Lilien. Power line conductor self-damping: a new approach. In *Proceeding of the 9th International Symposium on Cable Dynamics*, pages 217–224, Shangai, China, 2011.

[37] A.R. Hard and R.D. Holben. Applicationof the vibration decay test to transmission line conductors. *IEEE Transactions on Power Apparatus and Systems*, 86:189–199, 1967.

[38] C. Hardy. Analysis of self-damping characteristics of stranded cables in transverse vibrations. In *Proceedings of the CSME Mechanical Engineering Forum*, volume 1, pages 117–122, Ottawa, Canada, 1990.

[39] C. Hardy and P. Van Dyke. Field observations of wind-induced conductor motions. *Journal of Fluid and Structures*, 9:43–60, 1995.

[40] IEC. *Publications 207-210*. International Electrotechnical Commission, Geneva, 1966.

[41] S. Lalonde, B. Guilbault, and F. Légeron. Modeling multilayered wire strands, a strategy based on 3d finite element beam-to-beam contacts - part i: Model formulation and validation. *International Journal of Mechanical Science*, 126:281–296, 2017.

[42] S. Langlois and F. Legeron. Prediction of aeolian vibration on transmission-line conductors using a nonlinear time history model—part ii: Conductor and damper model. *IEEE Transactions on Power Delivery*, 29:1176–1183, June 2014.

[43] J. Lanteigne. Theoretical estimation of the response of helically armored cables to tension, torsion and bending. *ASME Journal of Applied Mehcanics*, 52:423–432, 1985.

[44] J. Lanteigne. Bending behavior of helically wrapped cables. *ASCE Journal of Engineering Mehcanics*, 131:500–511, 2005.

[45] J.H. Lienhard. Synopsis of lift, drag and vortex frequency data for rigid circular cylinders. *Technical Extension Service*, 1966.

[46] J.L. Lilien. *Power Line Aeolian Vibrations*. Department of Electronics, Electricity and Computer Sciences, University of Liege, 2013.

[47] A. E. H. Love. *A Treatise on the Mathematical Theory of Elasticity, fourth ed.* Dover Publications, New York, USA, 1944.

[48] M. L. Lu and J. K. Chan. Rational design equations for the aeolian vibration of overhead power lines. In *Proceedings of IEEE Power and Energy Society General Meeting*, Denver, CO, USA, October 2015.

[49] R. Mendonça and E. Caetanoi. Estimation of the remaining lifetime due to fatigue of a cable conductor using structural health monitoring. In *Proceedings of the second International Symposium on Dynamics and Aerodynamics of Cables*, pages 217–224, Stavanger, Norway, September 2021.

[50] K. Munaswamy and A. Haldar. Self-damping measurements of conductors with circular and trapezoidal wires. *IEEE Transactions on Power Delivery*, 15:604–609, April 2000.

[51] O. Nigol, R.C. Heics, and H.J. Houston. Aeolian vibration of single conductors and its control. *IEEE Transactions on Power Apparatus and Systems*, PAS-104(11):3245–3254, November 1985.

[52] D.U. Noiseux. Similarity laws of the internal damping of stranded cables in transverse vibrations. *IEEE Transactions on Power Delivery*, 7:1574–1580, 1992.

[53] D.U. Noiseux, S. Houle, and R. Beauchemin. Transformation of wind tunnel data on aeolian vibrations for application to random conuctor vibrations in a turbolent wind. *IEEE Transactions on Power Delivery*, 3:265–271, 1988.

[54] WG 04 of Study Commitee 22. Guide for endurance tests of conductors inside clamps. *Electra*, 100:77–86, May 1989.

[55] A. Omrani, S. Langlois, and P. Van Dyke. Fretting fatigue life of individual wires in a wire-to-clamp contact configuration under uniaxial and biaxial laoding. In *Proceedings of the second International Symposium on Dynamics and Aerodynamics of Cables*, pages 225–231, Stavanger, Norway, September 2021.

[56] K.O. Papailiou. *Die Seilbiegung mit einer durch die innere Reibung, die Zugkraft und die Seilkrümmung veränderlichen Biegesteifigkeit*. PhD thesis, E.T.H. Zurich, Switzerland, 1995.

[57] K.O. Papailiou. On the bending stiffness of transmission line conductors. *IEEE Transactions on Power Delivery*, 12:1576–1588, October 1997.

[58] J. Paradis. *Étude de l'amortissement interne des conducteurs excités selon plusieurs fréquences simultanément*. PhD thesis, Université de Sherbrooke, Sherbrooke (Québec), Canada, April 2022.

[59] J.P. Paradis and F. Legeron. Modelling of the free bending behavior of a multilayer cable taking into account the tangential contact compliance of contact interfaces. In *Proceedings of the 9th International Symposium on Cable Dynamics*, Shangai, China, October 2011.

[60] C. B. Rawlins. *Analytical Elements of Overhead Conductor Fabrication.* Fultus Books, Palo Alto, 2005.

[61] C.B. Rawlins. Wind tunnel measurements of the power imparted to a model of a vibrating conductor. *IEEE Transactions on Power Apparatus and Systems*, 4:963–971, 1983.

[62] C.B. Rawlins. Flexural self-damping in overhead electrical transmission conductors. *Journal of Sound and Vibration*, 323:232–256, 2009.

[63] J. Redford, H.P. Lieurade, M. Gueguin, F. Hafid, C. Yang, and J.M. Ghidaglia. Modélisation numérique du phénomène de fretting-fatigue intervenant dans le vieillissement des conducteurs de lignes aériennes. *Matériaux et Techniques*, 106(3):1–12, 2018.

[64] P.E Rocha, S. Lalonde, J.A. Araújo, and S. Langlois. Failure zone prediction of all aluminium alloy conductor using the smith-watson-topper fatigue parameter. In *Proceedings of the second International Symposium on Dynamics and Aerodynamics of Cables*, pages 233–244, Stavanger, Norway, September 2021.

[65] S. Salavtori. Modellazione ad elementi finiti della risposta assiale-torsionale di funi metalliche. Master's thesis, Master of Science in Civil Engineering - Structures, Politecnico di Milano, Academic Year 2021–2022.

[66] J. Vecchiarelli. *Aeolian Vibration of a conductor with a stockbridge-type damper.* PhD thesis, Doctor of Philosophy Graduate Department of Mechanical and Industriai Engineering, University of Toronto, 1997.